Nonlinear Dynamics in Photonic Systems

Generic models for semiconductor ring lasers & dissipative solitons

Lendert Gelens

Promoters: prof. dr. Jan Danckaert, dr. ir Guy Van der Sande, dr. Damià Gomila Villalonga

Joint PhD
Vrije Universiteit Brussel
Universitat de les Illes Balears

May 2010

Nonlinear Dynamics in Photonic Systems:
Generic models for semiconductor ring lasers & dissipative solitons
PhD thesis by Lendert Gelens
E-mail: lendert.gelens@vub.ac.be

Vrije Universiteit Brussel
Pleinlaan 2
B-1050 Brussel
Belgium

Instituto de Física Interdisciplinar y Sistemas Complejos IFISC (UIB-CSIC)
Campus Universitat Illes Balears
E-07122 Palma de Mallorca
Spain

Proefschrift ingediend tot het behalen van de academische graad van Doctor in de Ingenieurswetenschappen
Thesis submitted in partial fulfilment of the requirements for the academic degree of Doctor in Engineering Sciences
Tesi presentada al Departament de Física de la Universitat de les Illes Balears, per optar al grau de Doctor en Física

Promoters: prof. dr. Jan Danckaert, dr. ir Guy Van der Sande, dr. Damià Gomila Villalonga
Jury members: prof. dr. ir J. Schoukens (chairman / Vrije Universiteit Brussel), prof. dr. ir R. Pintelon (vice-chairman / Vrije Universiteit Brussel), prof. dr. C. Van den Broeck (secretary / Universiteit Hasselt), prof. dr. E. Knobloch (University of California, Berkeley), prof. dr. C. Mirasso (Universitat de les Illes Balears), prof. dr. T. Erneux (Université Libre de Bruxelles)

Print: Silhouet, Maldegem

VUBPRESS is an imprint of ASP nv
(Academic and Scientific Publishers nv)
Ravensteingalerij 28
B-1000 Brussels
Tel. ++32 (0)2 289 26 50
Fax ++32 (0)2 289 26 59
E-mail: info@vubpress.be
www.vubpress.be

ISBN 978 90 5487 738 7
NUR 925 / 926 / 928
Legal Deposit D/2010/11.161/061

Acknowledgments

Dear reader,

If you are like me, these acknowledgment pages are probably the first thing you are looking at when opening my PhD thesis. For those of you for whom it is also the last thing you read, I have included several comics throughout my thesis in a perhaps desperate attempt to excite your interest in nonlinear dynamics. That being said, I would like to start these acknowledgments by explaining a bit the framework in which this thesis came to be.

During my master thesis I had worked on a topic called *cavity solitons*. This was a bit an exploratory topic as nobody in the department was really familiar with the subject. Therefore, for safety reasons, I was suggested to work on a different topic for my PhD: *semiconductor ring lasers*. As it is clear from the book you are holding now, I never really let go of the research on dissipative solitons and continued that work in collaboration with researchers from the UIB in Palma de Mallorca, from the ULB and from UC Berkeley in California. To be honest, the fact that I pursued this research on solitons was in the beginning also a bit motivated by me not quite knowing what to do with these ring lasers. Luckily I didn't stand alone in this journey and in the course of these last three to four years, many people joined the work on ring lasers, e.g. Guy VdS, Guy Versch., Stefano, Miquel Angel, Lilia, Werner, Sifeu, Ilya and myself.

"Elrond: Nine companions. So be it. You shall be the fellowship of the ring.
Pippin: Great! Where are we going?" — Lord of the Rings.

Good question! Well, as George Harrison said in a song of his: *"if you don't know where you're going, every road will take you there"*. And he's right, I guess after about one year we kind of found our way thanks to the Guys and Stefano, deriving a reduced model for ring lasers and interpreting the laser operation in that reduced phase space. I owe you a big one for getting us on the right track.

I would like to express my sincere gratitude to my promoter, thanks to whom I embarked on this PhD. Jan, thank you for giving me the opportunity to work in your group, for your scientific and more personal advice and — I know you don't want me to say it, but I'll do it anyhow — for giving me the freedom to explore the research topics in which I was interested in the places of my choosing (islands, California, ...). I truly enjoyed having you as a promoter and the nice atmosphere you have created in the group will not be forgotten.

Thank you Guy (VdS) for your encouragement, guidance and support both during my master thesis and my PhD thesis and for being interested and involved in all aspects of my work and personal life as well. I know you've got my back ... literally. I know that if necessary, from nowhere, you'll pop up behind me to give me a pat on the back ;-)

I am also very grateful to Stefano for sharing the office with me, for the shared passion for Nespresso and for our great collaboration on the ring lasers. I have much respect for the enthusiasm with which you stand in life and your ability to do excellent research despite the sometimes very difficult times.

All the theoretical work on the ring lasers would not have been nearly as interesting if not for the great experiments performed on the lasers. A very big thank you to Guy (Versch.), the great experimenter, and his disciples, Miquel Angel and Lilia!

Quisiera agradecer a Damià de quien también aprendí muchas cosas. Nuestra colaboración no sólo fue muy interesante y productiva, pero además he disfrutado un montón de tu compañía. Espero que podamos seguir con esta colaboración en el futuro. Gracias también a Pere y Manuel por las enriquecedoras discusiones que hemos tenido juntos. Marta, gracias a ti por tu ayuda administrativa. De la gente que conozco en Palma, quisiera agradecer en particular a Miki, Amaia, Adrian, Laura, Toni, Sandra y Roberta. Gracias a vosotros tuve un tiempo maravilloso en Palma!

Edgar, I find it an honor to have been able to work together with you in Berkeley. You were always accessible and willing to help me with the research. As a result, our collaboration has been very rewarding for me. Apart from teaching me a great deal about nonlinear dynamics and bifurcation theory, you have shown

me the importance of doing research in the most thorough and insightful way possible.

I would also like to thank Mustapha, Pascal, Thomas and Gregory from the ULB for interesting discussions and fruitful collaborations.

I am indebted to Marc Sorel and Gabor Mezosi for providing us with semiconductor ring laser devices in the framework of the EU-strep project IOLOS. In that framework, I thank Alessandro Sciré as well for collaborations.

I am honored that Johan Schoukens, Rik Pintelon, Christian Van den Broeck, Edgar Knobloch, Claudio Mirasso and Thomas Erneux accepted to be the jury of this work.

Above I already acknowledged the valuable support and help from several of my friends and colleagues. I would like to take this opportunity to also thank the entire TONA group. In particular, thank you Thomas G. (a cheap rip-off of our GG-factor has been stolen by the PhD comics — see p. 115), Thomas B., Gordon, Otti, Lennert, Lilia, Ilya, Vincent, Werner, Philippe, Sifeu, Miquel Angel, Guy VdS, Guy Versch., Stefano, Ingo, Michael, Lawrence, Sara, Els, Stefaan, Jana and Stijn. Undoubtedly I still have forgotten many people. Moreover I would find it appropriate to devote a few sentences of thanks to all of you personally, but in order to avoid making these acknowledgments an entire book in itself, I will refrain from doing so. I will only mention that I am indebted to Vincent for helping me out with 'Lendert zijn bol' in this thesis and to Tom and Werner for valuable research contributions in the context of their Master and PhD thesis.

Special thanks to Irina, Jan, Erik, Franklin and Hugo for the excellent education you have given us during our studies and to Majorie, Kenneth, An, Nadia, Nadine, Bernadette and Lobke for their administrative support over the years. Irina, thank you for the interest you have always shown in my work, for your involvement in so many things, and for being the first professor to raise my interest in physics. I also gratefully acknowledge support from the FWO-Vlaanderen for providing me with a fellowship.

A few words of gratitude to the WISK-TONA team as well. Krizzy Kris, G-meister Craggs, Josti and Isarius: you're damn fine chaps!

Ik zou vooral ook mijn familie en vrienden willen bedanken en dan in het bijzonder mijn moeder en Jan. Jullie hebben steeds onvoorwaardelijk voor me klaargestaan de laatste jaren (en heel mijn leven). Het is dan ook onmogelijk om in woorden uit te drukken hoe dankbaar ik ben voor jullie hulp, steun en liefde. Tambíen quisiera agradecer a quienes considero mi segunda familia en Pamplona. Gracias por haberme apoyado tan bien estas semanas.

Por fin, tengo que agradecer muchísimo a mi nena. Florcita, gracias por ser una persona tan cariñosa y por tu paciencia durante el período que yo estaba escribiendo mi tesis. Te quiero mucho!

Allow me to conclude on a lighter note using the words of George (Blackadder), Well tally ho! With a bing and a bong and a buzz buzz buzz!

Lendert Gelens
Brussels, Belgium
21 May 2010

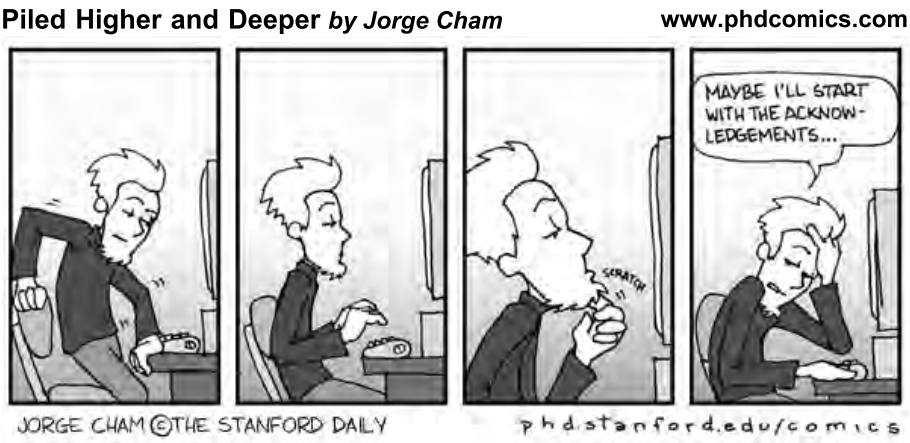

title: "Thesis writing" - originally published 11/5/1999

Contents

Titlepage **i**

Contents **vii**

Preface **xiii**

Voorwoord **xv**

Prefacio **xvii**

I Semiconductor Ring Lasers **1**

1 Introduction **3**
1.1 The laser 4
1.2 Semiconductor lasers 7
1.2.1 The semiconductor material 7
1.2.2 Semiconductor laser operation 9
1.2.3 Types of semiconductor lasers 11
1.3 Semiconductor ring lasers 12
1.3.1 Ring lasers throughout the years 12
1.3.2 Operating regimes 15
1.3.3 Technological applications 17
1.4 Modeling strategies 19
1.4.1 Rate-equation modeling 20

1.4.2 Symmetry-based modeling 22
1.4.3 Our modeling approach 23
1.5 Overview of Part I 24
References 24

2 An asymptotic rate-equation model for semiconductor ring lasers 33
2.1 Motivation 34
2.2 Asymptotic reduction 37
2.3 Special cases 40
2.3.1 Linear coupling 40
2.3.2 Nonlinear coupling 41
2.4 Linear stability analysis 41
2.4.1 Bidirectional solutions 41
2.4.2 Unidirectional solutions 42
2.5 Bifurcation diagrams 43
2.6 Intermezzo: spherical phase portraits 47
2.7 Basins of attraction in the bistable regime in the planar phase space 48
2.8 Conservative limit case 52
2.9 Conclusion 54
References 54

3 Deterministic switching mechanisms in the bistable regime 57
3.1 Phase space engineered switching 57
3.2 Optical injection 60
3.3 Current modulation 63
3.4 Phase modulation 65
3.5 Conclusion 67
References 68

4 Stochastic mode-hopping 71
4.1 Introduction 72
4.2 Experimental characterization of directional mode-hopping in the bistable regime 73
4.3 Topological interpretation 76
4.4 Multistable phase space portraits 79
4.5 Experimental exploration of stochastic mode-hopping in multistable regimes 82
4.6 Asymptotic analysis of the Fokker-Planck Equation 85
4.7 Optimal escape paths 89
4.8 Dependence of the activation energy on the parameters of the system 90
4.9 Conclusion 94
References 95

5 Breaking of the Z_2-symmetry **101**
5.1 Introduction . . . 101
5.2 Semiconductor ring laser rate-equation models with asymmetric linear coupling . . . 102
5.3 Bifurcation analysis . . . 104
5.4 Phase space portraits . . . 111
5.5 Conclusion . . . 112
References . . . 112

6 Excitability **117**
6.1 Introduction . . . 117
6.2 Origin of excitability in semiconductor ring lasers . . . 118
6.3 Deterministic analysis . . . 120
6.3.1 Long trigger pulses . . . 120
6.3.2 Short trigger pulses . . . 122
6.4 Stochastic analysis . . . 125
6.4.1 Pulse characterization . . . 125
6.4.2 Inter-spike-interval diagram . . . 130
6.5 Experiments . . . 132
6.5.1 Anatomy of the excited pulses . . . 132
6.5.2 Width-height correlation of single pulses . . . 135
6.6 Conclusion . . . 136
References . . . 137

7 Conclusions to Part I **141**

II Dissipative Solitons **147**

8 Introduction **149**
8.1 From integrable to dissipative solitons . . . 150
8.2 Generic models for dissipative solitons . . . 152
8.2.1 The Lugiato-Lefever equation . . . 153
8.2.2 The Swift-Hohenberg equation . . . 155
8.2.3 The Ginzburg-Landau equation . . . 157
8.3 Overview of Part II . . . 159
References . . . 160

9 One dimensional snaking of bright and dark cavity solitons **167**
9.1 Introduction . . . 167
9.2 Model . . . 171
9.3 Linear stability analysis . . . 172

9.4 Snaking of 1D bright cavity solitons . . . 174
9.5 Snaking of 1D dark cavity solitons . . . 178
9.5.1 Dark cavity solitons in the monostable regime . . . 179
9.5.2 Dark cavity solitons in the bistable regime . . . 181
9.6 Conclusion . . . 185
References . . . 186

10 Dynamical instabilities of two dimensional bright cavity solitons 191
10.1 Introduction . . . 192
10.2 Bifurcation diagrams and width of the localized structures . . . 193
10.3 Phase diagrams . . . 196
10.4 Dynamical behavior around the TB_1 point . . . 198
10.5 Dynamical behavior around the TB_2 point . . . 201
10.6 Excitability and conditional excitability . . . 204
10.7 Conclusion . . . 206
References . . . 206

11 Coarsening and faceting dynamics 209
11.1 Introduction . . . 210
11.2 Formulation of the problem . . . 210
11.3 The spatially homogeneous solutions . . . 212
11.3.1 Temporal stability . . . 213
11.3.2 Spatial stability . . . 214
11.4 The phase-winding states . . . 215
11.4.1 Temporal stability . . . 217
11.4.2 Spatial stability . . . 217
11.5 Coarsening dynamics: the Cahn-Hilliard equation . . . 217
11.5.1 Derivation of the Cahn-Hilliard equation . . . 218
11.5.2 Stationary solutions of the Cahn-Hilliard equation . . . 219
11.5.3 Derivation of the Cahn-Hilliard equation for phase-winding states . . . 220
11.5.4 Numerical verification of coarsening dynamics . . . 223
11.5.5 Transition from coarsening to Eckhaus dynamics . . . 225
11.6 Faceting of phase-winding states . . . 227
11.6.1 Origin of frozen facets . . . 227
11.6.2 Bifurcation structure of the frozen facets . . . 228
11.7 Transitions between coarsening, frozen faceted structures and Eckhaus dynamics . . . 233
11.7.1 Transition from coarsening to frozen faceted structures . . . 233
11.7.2 Transition from frozen faceted states to Eckhaus dynamics 235
11.8 Conclusion . . . 237

References . . . 238

12 Traveling wave dynamics **241**
12.1 Introduction . . . 241
12.2 Traveling wave solutions . . . 243
12.3 Numerical exploration . . . 243
12.3.1 Dynamics in the CSHE with a large intrinsic length scale (k_0 small) . . . 244
12.3.2 Dynamics in the CSHE with a finite intrinsic length scale ($k_0 = O(1)$) . . . 249
12.4 Derivation of a nonlinear phase equation . . . 252
12.5 Conclusion . . . 257
References . . . 257

13 Front interaction enhancement induced by nonlocal spatial coupling **261**
13.1 Introduction . . . 262
13.2 The nonlocal real Ginzburg-Landau equation . . . 263
13.2.1 Linear stability . . . 263
13.2.2 Spatial dynamics . . . 265
13.2.3 Front interaction . . . 267
13.2.4 Influence of the nonlocal kernel . . . 270
13.3 The nonlocal Parametrically forced complex Ginzburg Landau Equation . . . 273
13.3.1 Linear stability . . . 273
13.3.2 Spatial dynamics . . . 275
13.3.3 Nonlocal effects in two spatial dimensions . . . 277
13.4 Conclusion . . . 279
References . . . 279

14 Conclusions to part II **283**

Appendices **289**

A Nonlinear dynamics and bifurcation theory: a Toolbox **289**
A.1 Dynamics and bifurcations . . . 289
A.2 Linear stability . . . 292
A.3 Saddle-Node bifurcation . . . 294
A.4 Transcritical bifurcation . . . 295
A.5 Pitchfork bifurcation . . . 295
A.6 Hopf bifurcation . . . 296
A.6.1 Supercritical Hopf bifurcation . . . 297
A.6.2 Subcritical Hopf bifurcation . . . 297

References 298

B Numerical integration schemes **301**
B.1 Numerical integration of stochastic ordinary differential equations 301
B.2 Numerical integration of partial differential equations 303
References 304

List of Abbreviations **307**

List of Publications **309**
Published in international peer-reviewed journals 309
Contributions to international conferences 312
Contributions to Benelux conferences 314

Preface

Nonlinear dynamics in photonic systems is an effervescent field that has been continuously evolving during the last decades. The field of optical nonlinear dynamics can be divided in two subfields, namely the study of the temporal dynamics in nonlinear optical systems — assuming that the spatial structure of the light field does not change in time — and the study of spontaneous pattern formation in those systems. As an example of temporal dynamics, we refer to e.g. periodic or chaotic spike sequences that have been observed in the output of lasers. When considering the spatial extent of optical systems, a wealth of spatial patterns has been found in e.g. broad-area lasers and cells filled with sodium vapor. Most of these spatio-temporal phenomena encountered in optical systems can also be observed in a variety of other disciplines such as hydrodynamics, electrical discharges, chemical and biological systems, etc., because they refer to universal concepts and essentially share the same mathematical formalism. In this thesis, we address both temporal and spatial dynamics in optical systems. In Part I, we study the dynamical behavior of semiconductor ring lasers, while in Part II we examine nonlinear dynamics of spatially localized structures in extended systems.

(I) *Semiconductor ring lasers* (SRLs) and semiconductor disk lasers are particular types of semiconductor lasers where the laser cavity consists of a ring-shaped waveguide. SRLs are presently recognized to be promising sources in photonic integrated circuits. In particular, the possibility of bistable directional operation has paved the way for encoding digital information in the emission direction of SRLs with record low values for switching times and switching energies [M.

T. Hill *et al.*, Nature **432**, 206 (2004); L. Liu *et al.*, Nature Photon. **4**, 182 (2010)]. Apart from their technological applications in the field of photonics, SRLs are also optical prototypes for the large class of systems which are characterized by central reflection invariance. Such symmetry, known as Z_2 invariance, is one of the most common in nature, and besides in photonic systems it is also encountered in a wide number of bistable systems in different fields such as biology, aerodynamics, fluid mechanics and mechanics. Therefore, we conjecture that an in-depth study of SRLs based on a generic two-dimensional model will prove to be interesting for researchers working in other fields too.

(II) A spatial soliton is an example of an emergent structure in spatially-extended systems. Such a soliton can appear spontaneously and exists due to the interaction of each part with its immediate surroundings in space. In more mathematical terms, a soliton is a localized solution of a partial differential equation (PDE) describing the evolution of a (spatially) extended nonlinear system. Such localized solutions of real-world systems far from equilibrium are also referred to as *dissipative solitons* (DSs). These DSs are commonplace and have been shown to arise in a wide variety of pattern forming systems, such as e.g. chemical reactions, neural systems, granular media, binary-fluid convection, vegetation patterns and nonlinear optics. In Part II, we will study different types of DSs in (generalizations of) relevant universal model equations admitting DS solutions.

The connection between both parts of this thesis is the fact that we take advantage of particular symmetries in the different physical systems to derive and study generic models that are applicable in many fields of science. Bifurcation theory and nonlinear dynamics are employed to (I) understand how the underlying physical parameters of the SRL influence its experimentally observable dynamical behavior and (II) to unravel the fundamental principles and bifurcation structure of DSs.

We aspire that after reading this thesis, the reader will be — like us — intrigued by the nonlinear dynamical behavior that permeates our physical world. In particular, we will try to demonstrate that intricate systems can be understood amazingly well by combining quite simple models with general concepts of nonlinear dynamics.

Lendert Gelens
Brussels, Belgium
21 May 2010

Voorwoord

Niet-lineaire dynamica in fotonische systemen is een bruisend onderzoeksdomein dat continu geëvolueerd is gedurende de laatste tientallen jaren. Het domein van de optische niet-lineaire dynamica kan onderverdeeld worden in twee subdomeinen, namelijk de studie van de temporele dynamica in niet-lineaire optische systemen — veronderstellend dat de spatiale structuur van het lichtveld niet varieert in de tijd — en de studie van spontane patroonvorming in deze systemen. Als een voorbeeld van temporele dynamica refereren we naar bv. periodieke of chaotische sequenties van pulsen die geobserveerd zijn aan de uitgang van lasers. Als we ook de spatiale omvang van optische systemen in rekening brengen, dan heeft men ook een brede waaier van spatiale patronen geobserveerd in bv. brede lasers en cellen gevuld met natriumdamp. De meeste van deze spatiaal-temporele fenomenen die voorkomen in optische systemen kunnen ook geobserveerd worden in een variëteit van andere disciplines zoals hydrodynamica, elektrische ontladingen, chemische en biologische systemen, enz., omdat ze gebaseerd zijn op universele concepten en essentieel hetzelfde wiskundige formalisme delen. In deze thesis, adresseren we zowel temporele als spatiale dynamica in optische systemen. In Deel I, bestuderen we het dynamisch gedrag van halfgeleiderringlasers, terwijl we in Deel II de niet-lineaire dynamica van spatiaal gelokaliseerde structuren in uitgebreide systemen bestuderen.

(I) *Halfgeleiderringlasers* (HRLs) en halfgeleiderschijflasers zijn bijzondere types van halfgeleiderlasers waar de laserholte bestaat uit een ringvormige golfgeleider. HRLs worden momenteel erkend als beloftevolle bronnen in fotonisch geïntegreerde circuits. In het bijzonder heeft de mogelijkheid van bistabiele

directionele werking het pad geëffend om digitale informatie te coderen in de richting waarin de HRLs laseren met recordwaarden voor de schakeltijden en schakelenergiën [M. T. Hill *et al.*, Nature **432**, 206 (2004); L. Liu *et al.*, Nature Photon. **4**, 182 (2010)]. Buiten hun technologische toepassingen in het domein van de fotonica zijn HRLs ook optische prototypes voor de brede klasse van systemen die gekarakteriseerd zijn door een centrale reflectie invariantie. Zulke symmetrie, gekend als Z_2 invariantie, is één van de meest algemene in de natuur, en buiten in fotonische systemen komt ze ook voor in een groot aantal bistabiele systemen in verschillende domeinen zoals biologie, aërodynamica, stromingsleer en mechanica. Hierdoor stellen we dat een diepgaande studie van HRLs gebaseerd op een generisch tweedimensionaal model ook interessant zal blijken te zijn voor onderzoekers in andere domeinen.

(II) Een spatiaal soliton is een voorbeeld van een opkomende structuur in spatiaal uitgestrekte systemen. Zo een soliton kan spontaan verschijnen en bestaat dankzij de interactie van elk deel met zijn onmiddelijke omgeving in de ruimte. In meer wiskundige termen is een soliton een gelokaliseerde oplossing van een partiële differentiaalvergelijking die de evolutie van een (spatiaal) uitgebreid niet-lineair systeem beschrijft. Zulke gelokaliseerde structuren in realistische systemen ver van evenwicht worden ook *dissipatieve solitonen* (DSs) genoemd. Deze DSs komen vaak voor in vele verschillende patroonvormende systemen, zoals bv. chemische reacties, neurale systemen, granulaire media, binaire-vloeistof convectie, vegetatiepatronen en niet-lineaire optica. In Deel II bestuderen we verschillende types van DSs in (veralgemeningen van) relevante universele modelvergelijkingen die DS oplossingen hebben.

De connectie tussen beide delen van deze thesis is het feit dat we voordeel halen uit de bijzondere symmetriën in de verschillende fysische systemen om generische modellen, toepasbaar in vele wetenschapsdomeinen, af te leiden en te bestuderen. Bifurcatietheorie en niet-lineaire dynamica worden aangewend om (I) te begrijpen hoe de onderliggende fysische parameters van de HRL zijn experimenteel observeerbaar dynamisch gedrag beïnvloedt en (II) de fundamentele principes en bifurcatiestructuur van DSs te ontrafelen.

We streven ernaar dat na het lezen van deze thesis, de lezer — net zoals ons — geïntrigeerd zal zijn door het niet-lineaire gedrag dat onze fysische wereld doordringt. In het bijzonder zullen we trachten te tonen dat ingewikkelde systemen bijzonder goed begrepen kunnen worden door vrij eenvoudige modellen te combineren met algemene concepten van de niet-lineaire dynamica.

LENDERT GELENS

Prefacio

La dinámica no-lineal en sistemas fotónicos es un campo efervescente en continua evolución las últimas décadas. El campo de la dinámica en óptica no-lineal puede ser dividido en dos subcampos, a saber, el estudio de la dinámica temporal en sistemas ópticos no-lineales — en el supuesto de que la estructura espacial del campo electromagnético no cambia con el tiempo — y el estudio de la formación espontánea de patrones en estos sistemas. Como ejemplo de dinámica temporal, nos referimos, por ejemplo, a las secuencias periódicas o caóticas de picos que se observan a la salida de algunos láseres. Al considerar la extensión espacial de los sistemas ópticos, una gran cantidad de patrones espaciales puede ser encontrada, por ejemplo, en láseres de área ancha. La mayoría de estos fenómenos espacio-temporales que ocurren en sistemas ópticos también pueden ser observados en campos tan distintos como la hidrodinámica, las descargas eléctricas, los sistemas químicos y biológicos, etc., porque son una manifestación de fenómenos universales y, esencialmente, comparten el mismo formalismo matemático. En esta tesis nos ocupamos tanto de la dinámica temporal como espacial en sistemas ópticos. En la Parte I se estudia el comportamiento dinámico de los láseres de semiconductores de anillo, mientras que en la parte II se examina la dinámica no lineal de las estructuras localizadas en sistemas espacialmente extendidos.

(I) Los Láseres de Semiconductor de Anillo (LSAs) y los láseres de semiconductores de disco son tipos de láseres de semiconductor particulares, donde la cavidad del láser consiste en una guía de ondas en forma de anillo. A los LSAs se les reconoce actualmente como prometedoras fuentes de luz para circuitos in-

tegrados fotónicos. En particular, la posibilidad de operar en las dos direcciones de manera estable ha allanado el camino para la codificación de información digital en la dirección de emisión de los LSAs [M. T. Hill, et al., Nature 432, 206 (2004); L. Liu et al., Nature Photon. 4, 182 (2010)]. Además de sus aplicaciones tecnológicas en el campo de la fotónica, los LSAs son también prototipos ópticos para una gran clase de sistemas que se caracterizan por la invariancia de reflexión central. Tal simetría, conocida como la invariancia Z_2, es una de las más comunes en la naturaleza, y se encuentra en un gran número de sistemas biestables en campos tan diferentes como la biología, la aerodinámica, la mecánica de fluidos y la mecánica. Por lo tanto, creemos que un estudio en profundidad de los LSAs basado en un modelo de dos dimensiones genérico resultará interesante para los investigadores que trabajan en estos campos.

(II) Un solitón espacial es un ejemplo de una estructura emergente en un sistema espacialmente extendido. Estas estructuras pueden aparecer de forma espontánea y existen debido a la interacción de cada parte del sistema con su entorno inmediato en el espacio. En términos más matemáticos, un solitón es una solución localizada de una ecuación diferencial en derivadas parciales (PDE) que describe la evolución de un sistema no-lineal (espacialmente) extendido. Estas soluciones localizadas de sistemas lejos del equilibrio se denominan también solitones disipativos (SD). Estos SDs son comunes y se ha demostrado que surgen en una gran variedad de sistemas que forman patrones, como por ejemplo, reacciones químicas, sistemas neuronales, medios granulares, convección de fluidos binarios, patrones de vegetación y sistemas ópticos no lineales. En la segunda parte de esta tesis estudiaremos diferentes tipos de SDs en (generalizaciones de) ecuaciones de modelos universales relevantes.

La conexión entre las dos partes de esta tesis es el hecho de aprovechar las simetrías particulares de los diferentes sistemas físicos para obtener y estudiar modelos genéricos que son aplicables en muchos campos de la ciencia. La teoría de bifurcaciones y la dinámica no lineal se utilizan para (i) comprender cómo los parámetros físicos subyacentes de los LSAs influyen en su comportamiento dinámico observado experimentalmente y (II) para desentrañar los principios subyacentes y la estructura de las bifurcaciones de los SDs.

Aspiramos a que, tras leer esta tesis, el lector estará — como nosotros — intrigado por el comportamiento dinámico no-lineal que impregna nuestro mundo físico. En particular, vamos a tratar de demostrar que los sistemas complejos se pueden entender sorprendentemente bien mediante la combinación de modelos bastante sencillos con conceptos generales de dinámica no-lineal.

Lendert Gelens

Part I

Semiconductor Ring Lasers

The basins of attraction of both counter-propagating modes of a semiconductor ring laser plotted on a sphere (Courtesy of Vincent Ginis).

CHAPTER 1

Introduction

This year we are celebrating the 50th anniversary of the discovery of the laser by T. Maiman [1]. Moreover, it has been exactly ten years since the Nobel prize for physics was awarded for the discovery of the double hetero structure to Z.I. Alferov and H. Kroemer *"for developing semiconductor hetero structures used in high-speed- and opto-electronics"* and to J. S. Kilby *"for his part in the invention of the integrated circuit"*. Shortly after the fabrication of the very first laser in 1960 by T. Maiman after ideas by Schawlow and Townes in 1958 [2], the first semiconductor laser was developed by R.N. Hall in 1962. However, its efficiency was not very high such that continuous operation at room temperature was hampered. It is the discovery of the double hetero structure in 1963 [3] which would later allow to develop the first practical continuously operating lasers in Alferov's group (1970) [4]. The concept of the double hetero structure was conceived and published by H. Kroemer from Varian (USA), and, independently, also published and patented by Z. I. Alferov and R.F. Kazarinov at the Ioffe Physico-Technical Institute in the former Leningrad (USSR). Interestingly enough Kroemer mentioned the following anecdote concerning his discovery:

> *When I proposed to develop the technology for the double hetero structure laser, I was refused the resources to do so on the grounds that "this device could not possibly have any practical applications"* [5].

With hindsight, it is obvious just how wrong this assessment was. Nowadays, semiconductor lasers are by far the most fabricated lasers and have found their way to our everyday life. In telecommunications, they send signals for thousands

of kilometers along optical fibers at high speeds and bitrates. In consumer electronics, semiconductor lasers are used to read, write, erase and rewrite data on optical discs such as Compact Discs (CDs), Digital Versatile Discs (DVDs) and Blu-ray Discs (BDs). Other applications include, but are not limited to, laser pointers, laser printers, pollution monitoring, displays, surgical and welding equipment, and they are used in many different research fields. Semiconductor lasers can also exhibit highly nonlinear dynamical behavior and as such have proven to be ideal testbeds to study ideas from the universally applicable field of nonlinear dynamics. Dynamics in lasers is experimentally testable under controlled conditions and in a relatively short amount of time, which is not always the case for dynamical systems.
Since the advent of the semiconductor laser, many novel semiconductor lasers have been designed and developed into commercial products. One important research path is to use semiconductor lasers in all-optical switches in future optical fiber networks. At present the routing and switching in optical networks is mainly done electronically after converting the optical signals to electronic signals. The reason is that so far electronic switching is much more flexible than optical switching. Nevertheless, recent breakthroughs have been reported which make optical switching more competitive. The goal is to incorporate small and power efficient optical devices in photonic integrated circuits, implementing a variety of switching operations in the optical domain. An important step towards this direction was the demonstration of the bistable operation of a semiconductor ring laser (SRL) integratable on chip by M. Hill *et al.* in 2004 [6]. Low-energy switching in this bistable device possibly allows for all-optical information processing on chip. In view of the potential of SRLs, in this first part of the thesis, we will investigate in-depth how to model, physically understand and control the bistable operation of the SRL and its dynamical behavior.
In this introductory chapter, we start from the concept of a "laser", and explain how a pn-homojunction and a double hetero structure allow for semiconductor laser operation. Afterwards we focus on the birth of SRLs and how they have changed throughout the years, the possible applications SRLs have spawned and the theoretical concepts that have been introduced to model the behavior of SRLs. Finally, we conclude by giving an overview of the contents and goals of the Chapters to come in Part I "Semiconductor Ring Lasers".

1.1 The laser

The acronym *laser* stands for "light amplification by stimulated emission of radiation", which is a mechanism for emitting electromagnetic radiation, typically light, via the process of stimulated emission. It was Einstein, who already in

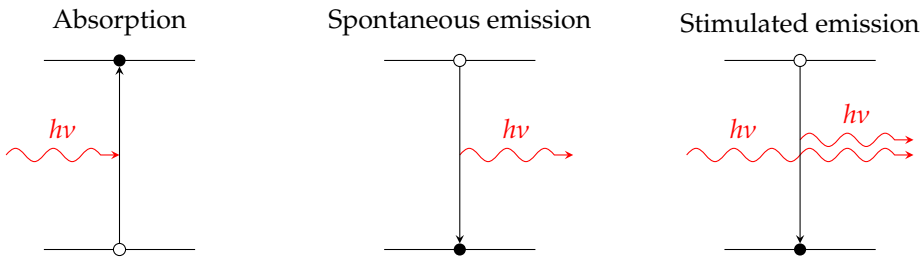

Figure 1.1: Illustration of absorption, spontaneous and stimulated emission in a two-level system with energy difference $\Delta E = h\nu$.

1916, proposed three different mechanisms of light-matter interaction: absorption, spontaneous emission and stimulated emission [7]. Einstein postulated that atoms can only occupy a discrete set of energy levels. When interacting with a photon, an atom can absorb it and as such be excited to a higher energy level (see Figure 1.1). When being in such an excited state, the atom can spontaneously emit a photon of light and fall back again to a lower energy level. Only photons with an energy equal to the energy difference $\Delta E = h\nu$ between both levels can be absorbed or emitted. The excited atom can not only spontaneously emit a photon, but can also be stimulated to do so. If a photon with the correct frequency ν hits an atom in the excited energy state, then it can stimulate the atom to emit an identical photon. Such an emitted photon is an exact replica of the incident photon and their associated electric fields have the same phase, frequency, polarization and propagation direction. In a material, absorption and stimulated emission are taking place with the same probability. It is the process of stimulated emission though that lies at the origin of the special properties of the emitted laser light, which can be generally described as a coherent and narrow beam. In order to take advantage of stimulated emission, the number of atoms in the excited state should exceed the number of atoms in the lower energy state. This situation is called *population inversion*. Unfortunately, when the system is in thermal equilibrium, this is never the case. Achieving population inversion therefore requires pushing the system into a non-equilibrated state. Armed with Einstein's principles of light-matter interaction, we can now understand why a laser essentially consists of three important ingredients determining its properties:

- A gain medium that can amplify light that passes through it. Such a gain medium is a material with properties that allow it to amplify light by stimulated emission.

- An energy pump source to create a population inversion in the gain medium.
- A resonant cavity confining the light.

The gain medium can be a solid, a liquid, or a gas and the pump source can be an electrical discharge, a flash lamp, or another laser. The gain medium absorbs pump energy, which raises some electrons into higher-energy excited quantum states creating population inversion. Hence, the light can be amplified[1]. In its simplest form, the laser cavity consists of two mirrors arranged such that light bounces back and forth, each time passing through the gain medium. Typically one of the two mirrors is partially transparent. The output laser beam is emitted through this mirror. Light of a specific wavelength is amplified as it passes through the gain medium. The surrounding mirrors ensure that most of the light stays in the gain medium for a long time, such that it gets amplified many times. If the chosen pump power is too small, the gain is not sufficient to overcome the resonator losses, and the laser will emit only very small light powers. The minimum pump power needed to begin laser action is called the lasing threshold[2]. Initially, photons will be emitted spontaneously in all directions with random phases and polarizations. The gain medium will amplify any photons passing through it, regardless of direction; but only the photons aligned with the cavity manage to pass more than once through the medium and so experience significant amplification. Therefore, not only does the laser cavity greatly increase the amount of amplification of light waves inside the cavity, but it also selects particular frequencies that are amplified and emitted in the laser. Such longitudinal modes of a resonant cavity are particular standing wave patterns formed by waves confined in the cavity.

[1]Population inversion is required for laser operation, but cannot be achieved in a system with two energy-levels as shown in Figure 1.1. Any method by which the atoms are directly and continuously excited from the ground state to the excited state (such as optical absorption) will eventually reach equilibrium with the de-exciting processes of spontaneous and stimulated emission. At best, an equal population of the two energy states can be achieved, resulting in optical transparency but no net optical gain. To achieve non-equilibrium conditions, an indirect method of populating the excited state must be used. Three-level or four-level laser are mostly used to explain how to achieve such population inversion.

[2]The *lasing threshold* is the lowest excitation level at which a laser's output is dominated by stimulated emission rather than by spontaneous emission. More in particular, the threshold is reached when the optical gain of the laser medium is exactly balanced by the sum of all the losses experienced by light in one round trip of the laser's optical cavity. Not taking into account the cavity losses, the laser is said to be *optically transparent* if the populations of the two energy states in Figure 1.1 are the same: the rate of absorption of light exactly balances the rate of emission. Below the lasing threshold, the laser's output power rises slowly with increasing excitation. Above threshold, the slope of power vs. excitation is orders of magnitude greater. The linewidth of the laser's emission also becomes orders of magnitude smaller above the threshold than it is below. Above the threshold, the laser is said to be lasing.

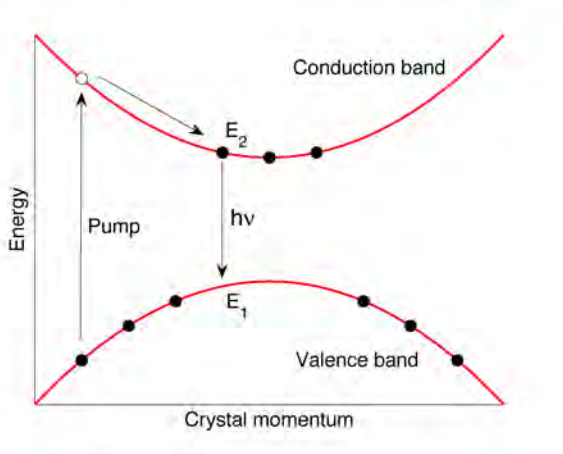

Figure 1.2: The conduction and valence energy band versus the crystal momentum in a semiconductor material. The pump excites electrons, which rapidly fall back to the bottom of the conduction band. Next, they recombine with a hole in the valence band, emitting a photon.

1.2 Semiconductor lasers

As explained in the previous Section, every laser consists of three vital parts: an active medium that allows for light amplification, a pump source and some form of feedback, e.g. realized in the form of an optical resonator. In a semiconductor laser, the gain medium is a semiconductor material. Gain is provided through recombination of electron-hole pairs in a suitable layer of a semiconductor medium embedded in a chip forming an optical cavity. Inversion of this medium may be achieved via an optical pump beam or by current injection via electrical contacts. Once the pump beam or the current exceeds a characteristic threshold spontaneous emission processes are exceeded by stimulated emission and lasing starts [8, 9].

1.2.1 The semiconductor material

Only electrons with an energy within a certain energy band can propagate through semiconductor materials. Due to the presence of such energy bands, lasing operation in semiconductor materials is very different from gas and solid-

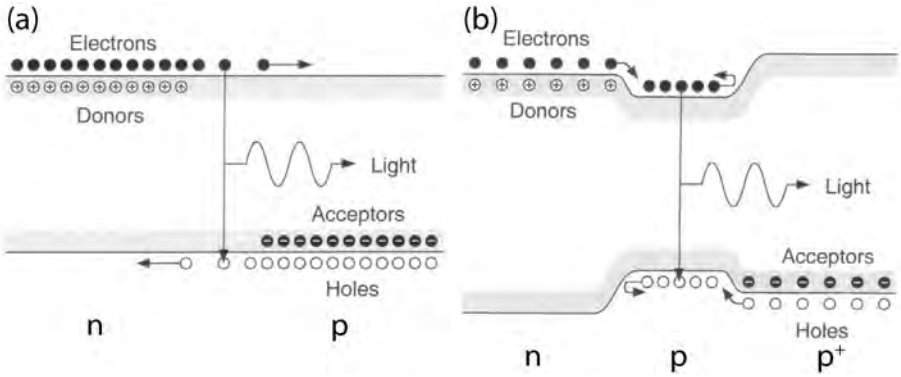

Figure 1.3: Schematic energy band diagram of a forward biased (a) p-n homojunction and (b) p^+-p-n double heterojunction. Taken from [5].

state lasers, where only discrete and well-defined energy levels are allowed. Figure 1.2 shows these allowed energy levels as a function of the electron's crystal momentum. At zero temperature, all electrons occupy the lowest possible states. The highest energy band that is still occupied by electrons is called the *valence band*, while the first unoccupied band is called the *conduction band*. The energy gap between these two bands is called the *band-gap*. Semiconductors typically have a relatively small band-gap of a few electron volts. The band-gap of a semiconductor is called a *direct* band-gap if the minimum of the conduction band and the maximum of the valence band have identical crystal momenta. If they have different crystal momenta, it is called an *indirect* band-gap.
At room temperature the conduction band is no longer unoccupied as some electrons can obtain enough energy to leave the valence band. The electrons in the conduction band move to the lowest energy states in this band, just as the remaining electrons in the valence band move to their lowest energy states. The net result is that both energy bands are not fully occupied and that the electrons are located at the bottom of each band. The top of the valence band is hence occupied by holes instead of electrons. An electron in the conduction band can spontaneously recombine with one of the available holes in the valence band, emitting photons with an energy near the bandgap energy (see Figure 1.2) [8, 9].

1.2.2 Semiconductor laser operation

Although recombination of electron-hole pairs can lead to the emission of photons in a semiconductor material, a single piece of semiconductor material can never operate as a laser. In order to induce population inversion in a semiconductor and thus get laser action, one needs *hetero structures*: heterogeneous semiconductor structures built from two or more different semiconductors. The layers of semiconductor are combined in such a way that the transition region or interface between the different materials plays an essential role in the laser operation, or even stronger it can be said that the interface is the actual laser medium.
The first and simplest hetero structure, the p-n homojunction, has been suggested by Bernard and Duraffourg in 1961 [10]. A p-n junction is a hetero structure consisting of two semiconductors placed next to each other. One of them is manipulated to have an enlarged number of free electrons in the conduction band and is referred to as *n-doped*. The other material is *p-doped* and has a larger amount of holes in the valence band. When bringing these two doped semiconductor in contact their energy bands start bending[3].
Consider the (highly oversimplified) energy band diagram of a p-n junction, heavily doped on both sides, and forward-biased to reach the band diagram shown in Figure 1.3(a). Electrons then diffuse from the n-type side to the p-type side, and holes diffuse in the opposite direction, creating a certain concentration of electron-hole pairs in the junction region. Their recombination causes light emission. However, in order to obtain laser action, a population inversion has to be achieved, which means that, in the active region (the interface), the occupation probability of the lowest states in the conduction band has to be higher than that of the highest states in the valence band. A necessary condition for such a population inversion is applying a forward bias voltage larger than the energy gap such that electrons and holes are injected in the active region. However, laser action in the p-n junction could only be achieved at either very low temperatures or short low-duty-cycle pulses, and usually both. The reason is twofold. First

[3]Band bending refers to the local change in energy of electrons at a semiconductor junction due to space charge effects. Because the common way to visualize the electron energy states and Fermi level in a material is to draw bands on an Energy vs. distance plot, band bending refers to bending in these diagrams and not in any physical form. Band bending can occur at a material/vacuum interface or when two materials with different local work functions are placed in contact. In general, bands will bend locally when materials come in contact, because the two Fermi levels of the materials will equilibrate to the same level through a local exchange of charge (either holes or electrons). This exchange of charge changes the energies of those charge carriers who have been exchanged, giving a curvature to the energy vs. distance diagram near the junction. Knowing how bands will bend when two different types of materials are brought in contact is key to understanding the operation of the device. The degree of band bending depends on the relative Fermi levels and carrier concentrations of the materials forming the junction.

of all, the electron concentration in the active region will always be lower than in the n-doped region, with an analogous limitation for the holes. Secondly, electrons and holes diffuse out of the active region into the adjacent oppositely doped region, preventing a population inversion from building up. Increasing the forward bias would not be very helpful either, as the rate of outflow would increase just as much as the rate of injection of electron-hole pairs.
The future of semiconductor laser devices operating in continuous wave was looking very cumbersome until, in 1963, H. Kroemer heard for the first time about such p-n junction lasers in a review talk on the topic by Dr. S. Miller. Miller and other experts had concluded that achieving continuous laser operation at room temperature was fundamentally impossible. Kroemer, however, immediately protested against this impossibility as follows

> *"but that is a pile of ..., all one has to do is give the injector regions a wider energy gap"* [5].

This suggestion provides the basis of Kroemer's discovery of the double hetero structure in the same year, for which he was awarded the Nobel prize in 2000. Figure 1.3(b) shows a sketch from such a double hetero structure, taken from Kroemer's Nobel lecture [5]. It becomes clear from Figure 1.3(b) that introducing an extra region with a higher doping (p^+) than the original p-doped region causes electrons and holes to be repelled at both sides. With a sufficiently high forward bias as in Figure 1.3(b) carrier confinement and population inversion is thus accomplished.
This layered p^+-p-n structure not only confines the carriers in the active region thus providing optical gain, but it can help to confine the optical mode in the vertical direction as well. The active layer in a p-n homojunction, as illustrated in Figure 1.3(a), only consists of the interface between the p-doped and n-doped region to both confine the optical field and to provide the optical gain. In a double hetero structure a semiconductor with the desired band gap, determining the emission wavelength of the laser, is sandwiched between materials with larger band-gaps. In this way, the injected electrons and holes crowd together in the narrow middle semiconductor layer, increasing the carrier density used in the radiative recombination needed to provide gain (see Figure 1.3(b)).
Moreover, if the middle layer in a double hetero structure is made thin enough, it acts as a quantum well (QW)[4]. Using one or more thin QW layers of active material has a number of advantages over using a more simple bulk laser. Such

[4]This means that the vertical variation of the electron's wavefunction, and thus a component of its energy, is quantized. The efficiency of a quantum well laser is greater than that of a bulk laser because the density of states function of electrons in the quantum well system has an abrupt edge that concentrates electrons in energy states that contribute to laser action. Lasers containing more than one quantum well layer are known as multiple quantum well lasers. Multiple quantum wells

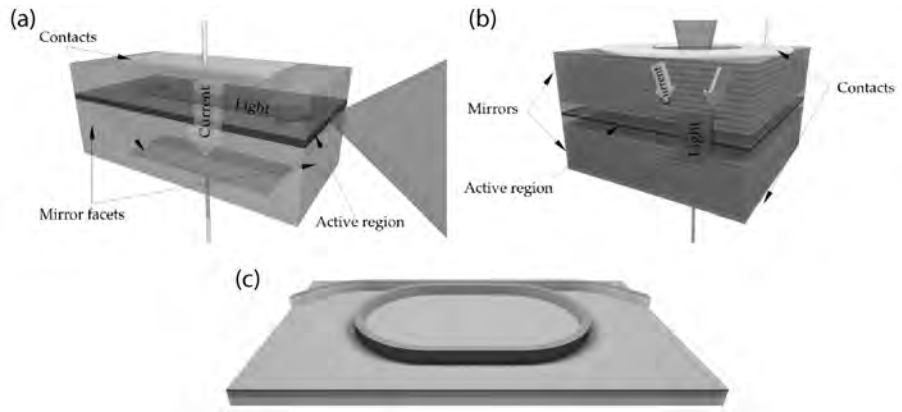

Figure 1.4: Different semiconductor lasers: (a) an edge-emitting laser (EEL), taken from [11], (b) a vertical-cavity surface-emitting lasers (VCSEL), taken from [11] and (c) a semiconductor ring lasers (SRL).

QW structures have a higher optical gain per injected carrier and thus a lower threshold current, a lower chirp, a polarization dependent gain and a higher differential gain as well. In view of these advantages, the SRLs studied in this thesis have been fabricated using a QW material.

1.2.3 Types of semiconductor lasers

Depending on the dimensions and geometry of the cavity, semiconductor lasers can be classified into several types of lasers. Here, we discuss the advantages and disadvantages of three main families of semiconductor lasers: edge-emitting lasers (EELs), vertical-cavity surface-emitting lasers (VCSELs) and semiconductor ring/disk lasers (SRLs).

In an EEL, the light is propagating in the plane of the active layer along a rectangular waveguide, while the mirrors are formed by cleaving the semiconductor wafer and by polishing the facets [see Figure 1.4(a)]. Although such EELs have been highly successful in consumer electronics, they have several shortcomings. The emitted beam is highly divergent and has an elliptical profile, which makes it hard to couple the light into an optical fiber. Multimode operation is easily obtained due to the long cavity length. Furthermore, the EELs have to be cleaved

improve the overlap of the gain region with the optical waveguide mode. Further improvements in the laser efficiency have also been demonstrated by reducing the quantum well layer to a quantum wire or to quantum dots.

and packaged before they can be tested. To improve on some of these disadvantages, novel semiconductor lasers have been developed.
The cavity of a VCSEL is oriented perpendicular to the active layer [12]. Hence, opposite to EELs, the light beam is emitted vertically and has a circular profile [see Figure 1.4(b)]. On-wafer testing is now possible, which is a considerable industrial advantage. The cavity length is also considerably shorter than in the case of EELs, such that they operate in a single-longitudinal mode, but due to the short cavity length the single pass gain is insufficient to achieve lasing. Therefore, extra layers of highly reflective dielectric mirrors are deposited on top and bottom of the VCSEL, making VCSELs difficult to grow. Furthermore, VCSELs cannot by integrated on a chip to perform e.g. switching operations.
Finally, semiconductor lasers with a circular cavity such as micro-ring and microdisk lasers [6, 13] encompass a wide variety of designs that share the common characteristic that optical feedback is achieved by circulating light around in a cavity that forms a loop [(see Figure 1.4(c)]. The modes supported by the cavity are traveling waves, rather than the standing waves that occur in devices where feedback is achieved by reflection between a pair of mirrors. Additionally, two such independent traveling waves can exist in the ring, one clockwise (CW) and one counterclockwise (CCW) propagating mode. The interaction between these counter-propagating modes leads to interesting dynamical behavior in SRLs, which will be studied in depth in this thesis. The fact that the SRL design is not based on reflection between mirrors leads to a number of advantages. As VCSELs, SRLs do not require cleaving of facets and thus allow for an accurate control of the cavity length and for an easy integration of SRLs with other functional elements in photonic integrated circuits (PICs). Typically, a coupler is used to transfer power from the cavity to an output waveguide.

1.3 Semiconductor ring lasers

1.3.1 Ring lasers throughout the years

Lasers with a circular cavity have attracted a lot of attention since the first conception of a ring laser in 1965 [14]. In the 70's, 80's and 90's ring lasers have especially been studied in the context of He-Ne ring lasers [15], CO_2 lasers [16, 17] and solid state lasers [18–20]. It was not until 1977 that the first semiconductor ring laser was reported [21]. The device had as an important limitation that its design did not incorporate any out-coupling of light from the ring. Lasing in the device was demonstrated by measuring light scattered from its sidewalls. The first design of a semiconductor laser with a circular symmetry and an output

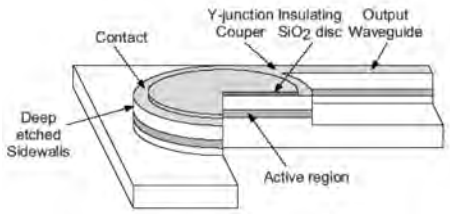

Figure 1.5: A micro-disk laser with y-junction output coupler, admitting *whispering gallery modes* [22].

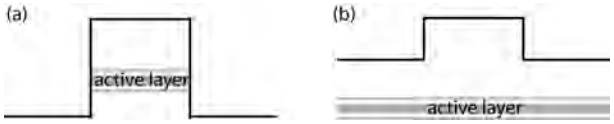

Figure 1.6: Schematic representation of (a) a rib waveguide and (b) a ridge waveguide.

waveguide has been realized in 1980 [22]. The micro-disk device was fabricated in GaAs/AlGaAs material and had a pillbox structure with a y-junction output coupler (see Figure 1.5). Although in principle such a disk-shaped resonator can support a large number of modes due to its lack of a clear wave-guiding ring, the modes with the lowest losses are often the *whispering gallery modes* propagating along the edge of the cavity. Thus as long as the micro-disk lasers can be characterized by two counter-propagating whispering gallery modes, their dynamics strongly resembles the one observed in SRLs. This design was followed by many different ones, where various choices were made for the semiconductor materials, waveguide designs and output coupler configurations.

Several types of waveguides have been designed to confine the light in the SRL, the most common of which are rib and ridge waveguides. For a *rib* waveguide, etching of the guiding ridge continues through the active layer [see Figure 1.6(a)]. The semiconductor/air interface that is created as such provides a strong confinement of the optical field, resulting in small bending losses and thus allowing for SRLs operating continuous wave with ring radii as small as 50μm [28]. Although bending losses are low when using a rib waveguide, scattering losses due to surface roughness of the waveguide side walls can be a serious problem. Such scattering loss has been demonstrated to be proportional to the intensity of light at the semiconductor/air interface. As waveguide bends push the optical mode towards the outside edge of the waveguide, scattering losses are enhanced in bended waveguides. Furthermore, backscattering due to surface roughness

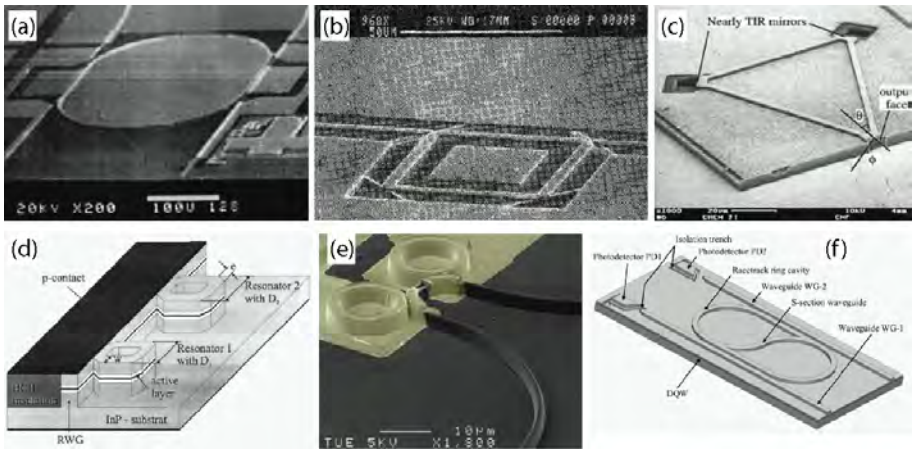

Figure 1.7: Semiconductor ring lasers with different geometries: (a) a racetrack cavity with evanescent out-coupling [23], (b) a square mirror based design [24], (c) a triangular mirror based design [25], (d) two coupled micro-squares [26], (e) two coupled rings [6], (f) a racetrack cavity with a S-bend coupler [27].

into the counter-propagating mode also increases this way [29]. The biggest downside of rib waveguides is the fact that the active layer gets exposed during the etching process, causing defects and surface states in the crystal lattice. As a consequence non-radiative recombination leads to a reduction of the quantum efficiency of the SRL and eventually to device failure.
Scattering due to waveguide roughness can be greatly reduced by using *ridge* waveguides, where one does not etch through the active layer [see Figure 1.6(b)]. In this case, however, the optical mode is confined much more weakly in the waveguide than with rib waveguides. Consequently these waveguides are more susceptible to bending losses and thus the ring radii cannot be as small.
Apart from the choice of the semiconductor material and the waveguide type, a lot of attention has been given to the type of coupler to extract light from the ring cavity. Especially in the earlier fabricated SRLs *y-junction* output couplers have been widely implemented [22, 24, 28, 30]. An example of such a y-coupler is shown in Figure 1.5 for a micro-disk laser. A y-junction coupler branches the waveguide in two, where one branch is the continuation of the ring itself and the other one is used as the output waveguide. The advantage of the coupler is that it is easy to fabricate, but unfortunately its performance is quite poor. Two other designs have been commonly used to improve on the y-junction: the *evanescent field* coupler and the *multimode interference* coupler. We limit ourselves here to

explaining the former one. Examples of the evanescent field coupler are shown in Figure 1.7(a),(e),(f). Two waveguides are brought close enough to each other such that the optical modes in both waveguides overlap and power is transferred between the waveguides. Because a larger coupler length leads to a higher overlap of the modes and thus a larger coupling ratio, racetrack geometries [Figure 1.7(a),(f)] are sometimes preferred over circular geometries [Figure 1.7(e)].
Several designs have taken advantage of the low scattering using ridge waveguides, while avoiding the associated size limitation imposed by bending losses by introducing Total Internal Reflection (TIR) mirrors. Figure 1.7(b)-(c) show a square and triangular shaped SRL [24, 25]. The rings are composed of straight ridge sections separated by deep etched TIR mirrors. One corner is cleaved and serves as the output facet.
Finally, one should remark that in several designs two SRLs are coupled to each other for all-optical flip-flop operation[5], see e.g. Figure 1.7(d)-(e) [6, 26]. Preliminary results have shown that coupling two SRLs can possibly lead to an increased stability in unidirectional operation. However, a device based on a single ring benefits from having a smaller footprint. In this thesis, we will focus on the dynamical instabilities occurring in such single SRLs.

1.3.2 Operating regimes

Figure 1.8(a) depicts a typical experimental SRL set-up. An In-P based multi-quantum-well SRL with a racetrack geometry is pumped with a current I_p and lases in a single-transverse, single-longitudinal mode at $\lambda = 1.56\mu m$. The power is extracted from the ring cavity by direct evanescently coupling the ring to a bus waveguide, and collected at the chip facets with a cleaved optical fiber. Figure 1.8(b) shows a typical cut of the double quantum well (DQW) structure, which can be fabricated in GaAs-AlGaAs[33] and InP-InGaAsP [31, 32].
An experimental measurement of the extracted modal power versus the pump current I_p of the SRL is shown in Figure 1.8(c). Several operating regimes can be distinguished, depending on the applied electrical pump current and internal parameters [34, 35]. Laser threshold is reached at an injection current of about 32 mA. Afterwards, the two counter-propagating modes in the SRL have approximately the same constant optical intensity. The SRL now operates in the so-called bidirectional regime [region BI in Figure 1.8(c)] for injection currents up to about 38 mA. From then on, one mode has a much stronger intensity than the other mode. This is the unidirectional regime which is of interest for memory element applications, since a bistability between both directional modes exists. The unidirectional regime corresponds to region U in Figure 1.8(c). In between

[5] All-optical flip-flop operation in SRLs will be discussed in more detail in Section 1.3.3.

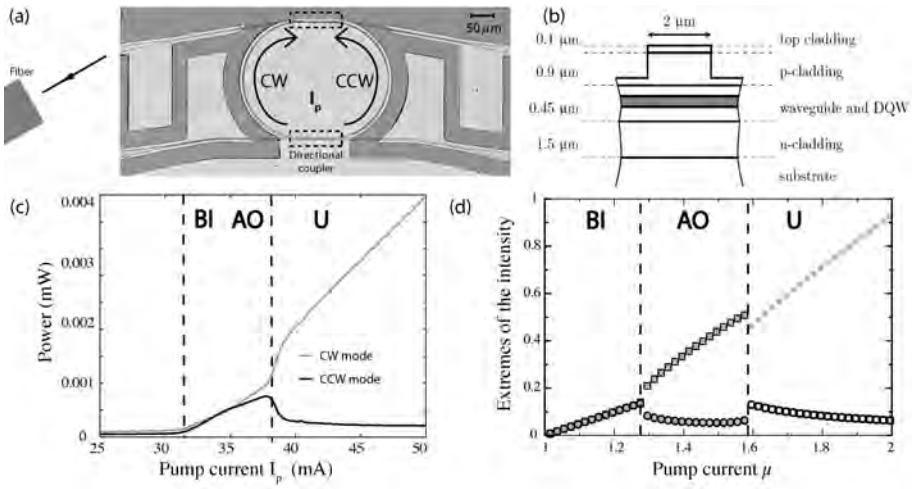

Figure 1.8: (a) Experimental SRL set-up. The ring is contacted through the pump current I_p [31, 32]. (b) A cut of the double quantum well (DQW) ring laser (after Ref. [33]). (c) Experimental PI-curve of a single mode InP-based DQW SRL. (d) Simulated PI-curve of a single mode SRL showing the extremes of the modal intensity using Eqs. (1.1)-(1.3) with $k = 0.44\text{ns}^{-1}$, $\phi_k = 1.5, c = 0.01, s = 0.005, \kappa = 100\text{ns}^{-1}, \gamma = 0.2\text{ns}^{-1}$ and $\alpha = 3.5$ [34]. The maxima (minima) of the CW mode are denoted by open black squares (circles), while the maxima (minima) of the CCW mode are denoted by gray crosses (dots).

these two operating regions, it is possible to also detect a regime of alternate oscillations [region AO in Figure 1.8(c)]. The intensities of the two modes start to oscillate out of phase at a frequency in the tens of megahertz range. As these oscillations are averaged out by the photodetector, this behavior is not visible in Figure 1.8(c). The oscillations become evident though when one looks at e.g. the oscilloscope in region AO during the experiment. One can also plot the extremes of the intensity as obtained from a simulation of a rate-equation model, which will be discussed in Section 1.4.1 [see Figure 1.8(d)].

As we will show in more detail in Chapter 2, the different operating regimes are a result of the competition between the linear and nonlinear coupling between both counter-propagating modes. The linear coupling can have multiple origins: a) reflections due to surface roughness in the ring itself, b) reflections at the point of coupling between the bus waveguide and the ring cavity, c) reflections at the out-coupling facet from the chip and d) reflections at the fiber that collects the output power of the light coupled out of the ring. This coupling is

linear as it does not depend on the optical intensity and the different reflections mentioned above will be lumped together in a single backscattering contribution throughout this thesis. Nonlinear coupling is present through the fact that both counter-propagating modes saturate their own and each others gain through spectral hole burning and carrier heating effects. These are believed to be two of the major physical processes underlying nonlinear gain saturation in SRLs [36][6]. At low injection currents, the intensities of the directional modes are low. Because saturation effects are negligible at low intensities, the backscattering is the dominant coupling mechanism. It will tend to equalize the intensities of both modes, leading to the bidirectional regime. Oppositely, for high injection currents and the associated high intensities, saturation effects become the dominant process. Cross saturation now causes the gain of one mode to become larger than the one of the counter-propagating mode. Therefore, one mode is suppressed, making the SRL operate unidirectionally. In the region where coupling through backscattering and cross saturation have comparable strengths, there exists a wealth of dynamical behavior, which is the subject of this first part of the thesis. While alternate oscillations are a part of the possible dynamics in this operating region and they have been observed before (see Ref. [33]), the other dynamical features discussed in this thesis are — to the best of our knowledge – novel in SRLs.

1.3.3 Technological applications

Due to the fact that SRLs do not require cleaved facets or gratings for optical feedback and are thus particularly suited for monolithic integration [30], several practical applications have been suggested [6, 37–42]. Unidirectional bistable operation as shown in Sect. 1.3.2 is often desirable in a SRL being used as a photonic element integrated on chip. If the unidirectional lasing can be stably switched between the two counter-propagating directions then functions such as optical memories can be implemented with a SRL. Such all optical flip-flops based on a single or on two coupled micro-rings have been fabricated and can be switched between counter-propagating modes by injection of a signal counter-propagating to the lasing mode [6, 43, 44]. The bistability of the SRLs also

[6]Spectral hole burning is the formation of a dip in the gain spectrum due to stimulated emission. The dip occurs by the recombination of electrons and holes at a specific energy and the subsequent redistribution of carrier energies due to carrier-carrier scattering. The scattering process takes place on a time scale of the order of 50-100 fs. Carrier heating describes the fact that the carrier temperatures may be different from the lattice temperature. The carrier temperatures relax towards the lattice temperature by electron-phonon scattering with a relaxation time of 0.5-1 ps. As these saturation phenomena occur on faster time scales than the photon life time of the SRL, they can be added phenomenologically.

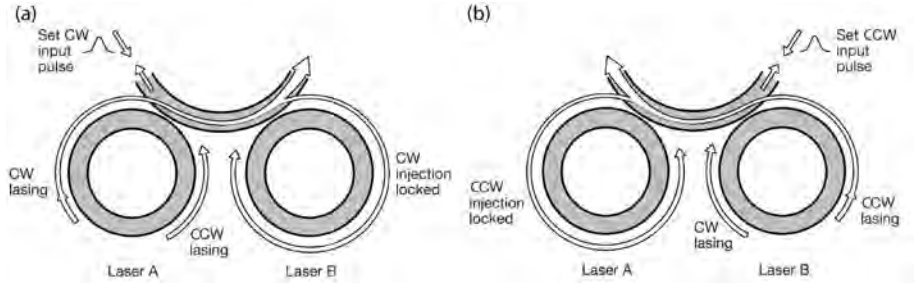

Figure 1.9: Demonstration of all-optical switching in two coupled semiconductor micro-ring lasers. (a) State I where the laser is injection locked in the CW mode. (b) State II where the laser is injection locked in the CCW mode. Taken from [6].

opens the possibility of using them in systems for all-optical switching, gating, wavelength-conversion functions, and optical memories [6, 38, 41, 45, 46]. We have proposed optical switching schemes based on injecting only on one side of the SRL [35, 47]. Monolithic SRLs exhibiting unidirectional operation are also potentially useful in applications because of their wavelength stability [37–39, 48, 49]. Finally, He-Ne [15], solid state [50] and semiconductor [51] ring lasers have been demonstrated to operate as optical gyroscopes.

In order to provide some more insight into the operation of a SRL as an optical memory element, we focus on the first demonstration of a bistable memory in a SRL integrated on chip. In 2004, in their Nature paper [6], M. Hill *et al.* experimentally demonstrated low-energy switching in the bistable unidirectional regime, which thus allows to encode digital information in the direction of emission of SRLs. Figure 1.9, taken from [6], demonstrates how bits of information can be stored in two coupled semiconductor micro-ring lasers[7] and how to switch between both stable states. In state I, CW light from laser A is injected via the waveguide into laser B [see Figure 1.9(a)]. The light from laser A will undergo significant resonant amplification in laser B if the resonant frequencies of the two laser cavities are close. If sufficient light is injected into laser B, then laser A captures or injection-locks[8] laser B, forcing light to circulate only in the CW direction. Only small amounts of light need to enter the laser cavity to achieve injection locking, owing to the strong resonant amplification. The reverse situation, state II, with laser B injection-locking laser A is also a stable state of the system when the lasers are equally pumped [see Figure 1.9(b)]. To set the system

[7] The SRL device in Ref. [6] occupies an area of 18 x 40 μm^2 on an InP/InGaAsP photonic integrated circuit,

[8] More information about injection-locking can be found in Section 3.2.

in one state or another, light close to the lasing wavelength and polarization can be injected into the waveguide connecting the lasers. This light will set both lasers simultaneously lasing in either the CW or the CCW direction. The different states can be distinguished by the different power levels at the two outputs. Similar optical memory operation can be obtained in the bistable region of a single SRL (see region **U** in Figure 1.8).
As discussed in Sect. 1.3.2, the directionality of the SRL depends critically on the relative strength of the linear coupling between the directional modes through backscattering and their nonlinear coupling through gain saturation processes. Unidirectional operation can thus be obtained by reducing the amount of backscattering, such that gain competition can suppress one of both modes. By reducing the linear coupling between whispering gallery modes in an In-P based micro-disk laser on silicon-on-insulator, low-power optical flip-flop operation has recently also been obtained in micro-disks by researchers of Ghent university [13].
While in the above applications bistability was a key element for designing e.g. an optical memory, for other applications a highly unidirectional, yet monostable SRL can be desirable. Such monostable unidirectional operation in ring lasers and disk lasers is often obtained by breaking the cavity symmetry in the laser through preferential scattering into one direction. In Ref. [27], an extra S-bend waveguide was incorporated into an SRL with a racetrack geometry such that more power is coupled in one directional mode than in the other one [see Figure 1.7(f)]. Another design that allows for a preferential linear coupling was introduced in Ref. [38] and were termed triangular *diode* lasers. More recently, a *snail*-type SRL has also been introduced to obtain a highly directional output [52]. The laser has one cleaved output facet, and the input waveguide is curved until it couples with itself, forming a ring cavity. The waveguide is then terminated inside the ring with a second, etched, facet. Further discussions of the importance of asymmetries in the design and modeling of semiconductor micro-ring and micro-disk lasers have been addressed in Refs. [53–57]. The importance and consequences (such as excitable behavior) of a broken cavity symmetry will be further discussed in Chapters 5-6.

1.4 Modeling strategies

In this Section, we will introduce several types of modeling that can be used to describe the dynamical behavior of a SRL. A first approach focuses on a description of the time evolution of the slowly varying envelopes of the electric fields and the carrier density in terms of rate equations. Secondly, a more

generic description of dynamics occurring near a bifurcation point of the SRL system is possible. Here, the underlying circular symmetry of the SRL can be used to predict universal dynamical behavior encountered in a wide variety of such bistable systems with that symmetry. We discuss the advantages and disadvantages of both approaches and lay out the modeling strategy that we will use in this thesis.

1.4.1 Rate-equation modeling

Different theoretical models have been proposed for the analysis of generalized rings and two-mode laser systems. These theories focus on the interplay between the two counter-propagating modes and their interaction with the active medium. A particular treatment for the SRL was devised by Sargent, who has derived a simple model for the intensities of the two modes starting from first principles [19]. This work has pointed out the relevance of self- and cross-gain saturation processes in the dynamical operation of the device. Specifically, Sargent has found that SRLs operate preferably unidirectionally due to gain saturation. Etrich *et al.* have proposed a model based on the time evolution of the electric fields [20]. They have addressed the effect on the device operation of the carrier induced grating originating from the interference of the two counter-propagating modes. These works highlight the emergence of intensity oscillations induced by mode to mode phase-coupling [58, 59].
The current revived interest in SRLs has not only lead to numerous technological publications, but it has also spawned renewed interest in the theoretical modeling of SRLs. A general rate-equation approach has been suggested by Sorel *et al.* in Ref. [37]. The model consists of two mean-field equations for the counter-propagating modes in the SRL, and a third rate equation for the carriers. The model accounts for self- and cross-gain saturation effects and includes backscattering contributions originating at the coupler to the output-waveguide. In the same work, bidirectional and unidirectional regimes of continuous-wave mode operation, and a bidirectional regime where the two counter-propagating modes experience harmonic alternate oscillations have been observed. These different features are adequately described by the rate-equation model for SRLs in Ref. [37]. Although this rate-equation approach explains certain experimentally observed features, problems involving e.g. wavelength changes fall outside the scope of such rate-equation models and this thesis, and a traveling wave model would be more suited to tackle such questions [60, 61].

Symbol	Physical meaning	Simulation value
κ	Field decay rate	100ns^{-1}
γ	Decay rate of the carrier population	0.2ns^{-1}
α	Linewidth enhancement factor	3.5
μ	Renormalized bias current	1.704
s	Self-saturation coefficient	0.005
c	Cross-saturation coefficient	0.01
k	Backscattering parameter	0.44ns^{-1}
ϕ_k	Backscattering phase	1.5
τ_{in}	Round trip time	0.6ps

Table 1.1: Summary of the physical meaning of the parameters in the rate equations (1.1)-(1.3) and their typical values used throughout this thesis, unless stated otherwise.

The rate-equation model from Ref. [37] is given by:

$$\dot{E}_{cw} = \kappa(1+i\alpha)\left[g_{cw}N-1\right]E_{cw} - ke^{i\phi_k}E_{ccw}, \tag{1.1}$$

$$\dot{E}_{ccw} = \kappa(1+i\alpha)\left[g_{ccw}N-1\right]E_{ccw} - ke^{i\phi_k}E_{cw}, \tag{1.2}$$

$$\dot{N} = \gamma\left[\mu - N - g_{cw}N|E_{cw}|^2 - g_{ccw}N|E_{ccw}|^2\right], \tag{1.3}$$

with $E_{cw,ccw}$ the slowly varying amplitudes of clockwise and counter-clockwise propagating waves and one rate equation for the carrier number N. The dot represents differentiation with respect to time. In Eqs. (1.1)-(1.3), κ is the field decay rate, and γ is the decay rate of the carrier population. α is the linewidth enhancement factor, $g_{cw} = 1 - s|E_{cw}|^2 - c|E_{ccw}|^2$, $g_{ccw} = 1 - s|E_{ccw}|^2 - c|E_{cw}|^2$, μ is the renormalized injection current ($\mu \approx 0$ at transparency, $\mu \approx 1$ at lasing threshold). The two counter-propagating modes are considered to saturate both their own and each other's gain due to e.g. spectral hole burning and carrier heating effects as mentioned in Sect. 1.3.2. Self- and cross-saturation effects are added phenomenologically and are modeled by s and c. For a realistic device, cross saturation is stronger than self-saturation (c =2 s). The ring geometry, in principle, allows for the two counter-propagating waves to form a carrier grating [18]. Nevertheless, due to the high electron mobility in semiconductors, this carrier grating is washed out on a timescale faster than the photon lifetime [61, 62]. Therefore the effect of the grating can be included in the saturation coefficients through an adiabatic elimination. As this change in saturation coefficients is negligible, we will consider the cross-saturation to be twice the self-saturation coefficient. Reflection of the counter-propagating modes occurs at the point where light is coupled out of the ring cavity into a coupling waveguide and can also occur at the end facets of the coupling waveguide. These localized

reflections result in a linear coupling between the two fields characterized by an amplitude k and a phase shift ϕ_k.
A numerical simulation of a PI-curve using Eqs. (1.1)-(1.3) is shown in Figure 1.8(d) choosing the parameters as in Table. 1.1. The simulation shows that the model contains all necessary ingredients to adequately model the different experimentally observed operating regimes in a SRL. Nonetheless, such a high-dimensional model needs to be simplified in order to allow for a clear bifurcation analysis[9] and to understand more deeply the influence of the different device parameters on the underlying phase space of the SRL.

1.4.2 Symmetry-based modeling

A modeling approach based on rate equations derived from first principles has as a big advantage that a direct connection with physically meaningful system parameters is retained. A different and more generic approach is to analyze the SRL properties based on the symmetries present in the system. Due to their circular symmetry, SRLs can be seen as ideal optical prototypes for the large class of equivariant systems which are characterized by an O(2) symmetry group of rotations and reflections of a circle[10]. Perfectly symmetric systems are rare and are often influenced by imperfections. Sometimes such imperfections do not break the symmetry, and thus do not affect the generic problem. They can, however, also break the O(2) symmetry, but e.g. keep a Z_2 symmetry under reflections. Such Z_2 invariance is one of the most common in nature, encountered in a wide number of bistable systems. General Z_2-symmetric systems, such as e.g. Duffing-Van der Pol oscillators, have been studied in depth [63–67]. In particular, insight into the bifurcation structure of Z_2-invariant systems has been proven useful in biology [68, 69], aerodynamics [70], fluid mechanics [71, 72], laser systems [16, 17, 73] and mechanics [74].
A lot of knowledge can be inferred from studying normal forms close to a certain type of bifurcation. In the context of laser systems, such an approach has especially proven to be insightful in the analysis of the dynamical behavior in CO_2-lasers [16, 17]. The nonlinear interaction of two transverse modes in a CO_2-laser

[9] Bifurcation theory is the mathematical study of changes in the qualitative or topological structure of a given family. Examples of such families are the integral curves of a family of vector fields, and the solutions of a family of differential equations. Most commonly applied to the mathematical study of dynamical systems, a bifurcation occurs when a small smooth change made to the parameter values (the bifurcation parameters) of a system causes a sudden 'qualitative' or topological change in its behavior. Bifurcations occur in both continuous systems (described by ODEs, DDEs or PDEs), and discrete systems (described by maps). For more information on bifurcation theory, we refer to [63, 64].

[10] The symmetry group O(2) consists of all rotations about a fixed point and reflections in any axis through that fixed point. This is the symmetry group of a circle.

is symmetrically similar to the interaction of the counter-propagating modes in a SRL. In both cases, the system has a basic $O(2)$ symmetry admitting traveling wave solutions. This symmetry is then perturbed by symmetry-breaking effects that still preserve the Z_2-symmetry, creating a mixture of standing waves, traveling waves and modulated waves. In a SRL, this $O(2)$ symmetry is broken by introducing a output-coupler to extract power. The unfolding of general dynamics near a Takens-Bogdanov (TB) codimension-two bifurcation point[11] allows to understand experimentally observable dynamical features, albeit only in the neighborhood of this codimension-two bifurcation point. How the SRL dynamics unfolds from such a TB point will be shown in Chapter 2.

1.4.3 Our modeling approach

In this thesis, we prefer to follow an approach which lies somewhat in the middle of both the rate-equation approach and the symmetry-based modeling. We will introduce a simplified Z_2-symmetric two-dimensional SRL model and use the combination of both the full [Eqs. (1.1)-(1.3)] and a reduced rate-equation model to gain much more insight into different novel dynamical operating regimes of the SRL. Such a Z_2-symmetric SRL model retains the connection with the different physical parameters. However, as the rate-equation is greatly simplified, we are still able to analyze the presence of all codimension-two bifurcation points in function of the device parameters such that the full bifurcation diagram can be explored. Access to Z_2-symmetric phase space portraits also remains possible. Such approach has the advantage that the model remains valid both close to and far from the first instability, while avoiding the necessity to perform most of the analysis numerically. Such purely numerical analysis is necessary for higher dimensional rate equations, which means in practice that significant dynamical phenomena are overlooked.
Finally, we would like to point out that the study presented for SRLs in this thesis is general for lasers with a circular symmetry that admit two counter-propagating modes that are coupled both linearly and nonlinearly. Therefore, the presented results can readily be translated to e.g. the dynamical interaction of whispering gallery modes in micro-disk lasers as well.

[11] A Takens-Bogdanov bifurcation is a well-studied example of a bifurcation with codimension-two, meaning that two parameters must be varied for the bifurcation to occur. A system undergoes a Takens-Bogdanov bifurcation if it has a fixed point and the linearization of the system function around that point has a double eigenvalue at zero. Three codimension-one bifurcations occur nearby: a saddle-node bifurcation, an Andronov-Hopf bifurcation and a homoclinic bifurcation. All associated bifurcation curves meet at the Takens-Bogdanov bifurcation. [63, 64]

1.5 Overview of Part I

In **Chapter 2**, a singular perturbation technique is applied to reduce the set of original rate equations (1.1)-(1.3) for a SRL to two equations. The analysis takes advantage from the different timescales present in the system. Not only do these reduced equations simplify the bifurcation analysis of the possible steady-state solutions considerably, they also allow for a two-dimensional phase space description of the laser. In particular, the shape of the invariant manifolds of the saddle point in the system is studied and a full bifurcation analysis of this two-dimensional laser system is carried out.
Chapter 3 demonstrates that a topological investigation of the phase space of a SRL can be used to devise switching schemes which are alternative to optical pulse injection of counter-propagating light. To provide physical insight in these switching mechanisms, the specific topological structure of the two-dimensional phase space is shown to be of great importance. Numerical simulations confirm the topological predictions.
In **Chapter 4**, we investigate both theoretically and experimentally the stochastic switching between two counter-propagating lasing modes of a SRL. Experimentally, the residence time distribution cannot be described by a simple one parameter Arrhenius exponential law and reveals the presence of two different mode-hop scenarios with distinct time scales. The topological phase space picture of the two-dimensional dynamical system introduced in Chapter 2 allows to understand the observed features. Expanding on the mode-hopping study in the bistable region, we also show how the operation of the device can also be steered to multistable dynamical regimes, predicted by the two-dimensional model. By analyzing the phase space in this model, we predict how the stochastic transitions between multiple stable states take place and confirm it experimentally. Furthermore, in the limit of small noise intensity, the initial stochastic rate equations can be reduced to an auxiliary Hamiltonian system and the optimal escape paths can be calculated. This approach also allows to investigate the dependence of the activation energy on the principal laser parameters.
Chapter 5 shows the bifurcation scenario and the evolution of the counter-propagating modes in a SRL when the Z_2-symmetry of the laser is broken. Theoretical predictions and insights in the different dynamical regimes of this asymmetric SRL are obtained.
In **Chapter 6** the knowledge of the bifurcation structure obtained in Chapter 5 is used to characterize theoretically and experimentally excitability in SRLs. The global shapes of the invariant manifolds of a saddle in the vicinity of a homoclinic loop are shown to determine the origin of excitability and the features of the excitable pulses. Finally, in **Chapter 7**, we summarize the results obtained in Part I of this thesis.

References

[1] T. Maiman, "Stimulated optical radiation in ruby," *Nature* **187**, 493–494, 1960.

[2] A. Schawlow and C. Townes, "Infrared and optical masers," *Phys. Rev.* **112**, 1940, 1958.

[3] H. Kroemer, "A proposed class of heterojunction injection lasers," *Proc. IEEE* **51**, 1782, 1963.

[4] Z. Alferov, V. Andreev, D. Garbuzov, Y. Zhilyaev, E. Morozov, E. Portnoi, and V. Trofim, "Investigation of influence of AlAs-GaAs heterostructure parameters on laser threshold current and realization of continuous emission at room temperature," *Sov. Phys. - Semicond.* **4**, 1573–1575, 1971.

[5] H. Kroemer, "Quasi-electric fields and band offsets: teaching electrons new tricks," *Nobel lecture* , 2000.

[6] M. T. Hill, H. Dorren, T. de Vries, X. Leijtens, J. den Besten, B. Smalbrugge, Y. Oei, H. Binsma, G. Khoe, and M. Smit, "A fast low-power optical memory based on coupled micro-ring lasers," *Nature* **432**, 206–209, 2004.

[7] A. Einstein, "Zur quantentheorie der strahlung," *Physik. Zeitschr.* **18**, 121, 1917.

[8] W. W. Chow and S. W. Koch, *Semiconductor - Laser Fundamentals*, Springer-Verlag, Berlin, 1999.

[9] J. Singh, *Semiconductor Optoelectronics*, McGraw-Hill, Inc., Singapore, 1995.

[10] M. Bernard and G. Duraffourg, "Laser conditions in semiconductors," *Phys. Status Solidi* **1**, 669–703, 1961.

[11] M. Peeters, *Polarization switching in vertical-cavity surface-emitting lasers: a modeling perspective*, PhD thesis, Vrije Universiteit Brussel, 2003.

[12] K. Iga, "Surface-emitting laser — its birth and generation of new optoelectronics fields," *IEEE J. Quant. Electron.* **6**, 1201–1215, 2000.

[13] L. Liu, R. Kumar, K. Huybrechts, T. Spuesens, G. Roelkens, E.-J. Geluk, T. de Vries, P. Regreny, D. Van Thourhout, R. Baets, and G. Morthier, "An ultra-small, low-power, all-optical flip-flop memory on a silicon chip," *Nature Photon.* **4**, 182–187, 2010.

[14] F. Aronowitz, "Theory of a traveling-wave optical maser," *Phys. Rev. A* **139**, 635, 1965.

[15] L. N. Menegozzi and W. E. Lamb, "Theory of a ring laser," *Phys. Rev. A* **8**, 2103–2125, 1973.

[16] E. D'Angelo, E. Izaguirre, G. Mindlin, G. Huyet, L. Gil, and J. R. Tredicce, "Spatiotemporal dynamics of lasers in the presence of an imperfect O(2) symmetry," *Phys. Rev. Lett.* **68**, 3702–3705, 1992.

[17] R. Lopez-Ruiz, G. B. Mindlin, C. Perez-Garcia, and J. R. Tredicce, "Nonlinear-interaction of transverse-modes in a CO_2-laser," *Phys. Rev. A* **49**, 4916–4921, 1994.

[18] H. Zeghlache *et al.*, "Bidirectional ring laser: Stability analysis and time-dependent solutions," *Phys. Rev. A* **37**, 470, 1988.

[19] M. Sargent III, "Theory of a multimode quasiequilibrium semiconductor laser," *Phys. Rev. A* **48**, 717–726, 1993.

[20] C. Etrich, P. Mandel, N. B. Abraham, and H. Zeghlache, "Dynamics of a two-mode semiconductor laser," *IEEE J. Quantum Electron.* **28**, 811–821, 1992.

[21] N. Matsumoto and K. Kumabe, "AlGaAs-GaAs semiconductor ring laser," *Japanese J. of Appl. Phys.* **16**, 1395, 1977.

[22] A. Liao and S. Wang, "Semiconductor injection-lasers with a circular resonator," *Appl. Phys. Lett.* **36**, 801, 1980.

[23] G. Griffel, "Synthesis of optical filters using ring resonator arrays," *Photon. Technol. Lett.* **12**, 810, 2000.

[24] H. Han, D. Forbes, and J. Coleman, "InGaAs-AlGaAs-GaAs strained-layer quantum-well heterostructuresquare ring lasers," *IEEE J. Quantum Electron.* **31**, 1994, 1995.

[25] C. Ji, M. Leary, and J. Ballantyne, "Long-wavelength triangular ring laser," *Photon. Technol. Lett.* **9**, 1469, 1997.

[26] L. Bach, "Wavelength stabilized single-mode lasers by coupled micro-square resonators," *Photon. Technol. Lett.* **15**, 377, 2003.

[27] H. Cao and M. Osinski, "Large S-section-ring-cavity diode lasers: directional switching, electrical diagnostics, and mode beating spectra," *Photon. Technol. Lett.* **17**, 282, 2005.

[28] J. Hohimer, D. Craft, and G. Vawter, "Effect of the y-junction output coupler on the lasing threshold of semiconductor ring lasers," *App. Phys. Lett.* **63**, 1325, 1993.

[29] B. E. Little, J. Laine, and S. T. Chu, "Surface-roughness-induced contradirectional coupling in ring and disk resonators," *Opt. Lett.* **22**, 4, 1997.

[30] T. Krauss, P. J. R. Laybourn, and J. S. Roberts, "CW operation of semiconductor ring lasers," *Electron. Lett.* **26**, 2095–2097, 1990.

[31] S. Beri, L. Gelens, M. Mestre, G. Van der Sande, G. Verschaffelt, A. Sciré, G. Mezosi, M. S. M, and J. Danckaert, "Topological insight into the non-Arrhenius mode hopping of semiconductor ring lasers," *Phys. Rev. Lett.* **101**, 093903, 2008.

[32] L. Gelens, S. Beri, G. Van der Sande, G. Mezosi, M. Sorel, J. Danckaert, and G. Verschaffelt, "Exploring multistability in semiconductor ring lasers: Theory and experiment," *Phys. Rev. Lett.* **102**, 193904, 2009.

[33] M. Sorel, G. Giuliani, A. Sciré, R. Miglierina, S. Donati, and P. Laybourn, "Operating regimes of GaAs-AlGaAs semiconductor ring lasers: experiment and mode," *IEEE J. Quantum Electron.* **39**, 1187–1195, 2003.

[34] G. Van der Sande, L. Gelens, P. Tassin, A. Sciré, and J. Danckaert, "Two-dimensional phase-space analysis and bifurcation study of the dynamical behavior of a semiconductor ring laser," *J.Phys.B* **41**, 095402, 2008.

[35] L. Gelens, G. Van der Sande, S. Beri, and J. Danckaert, "Phase-space approach to directional switching in semiconductor ring lasers," *Phys. Rev. E* **79**, 016213, 2009.

[36] M. Willatzen, A. Uskov, J. Mork, H. Olesen, B. Tromborg, and A.-P. Jauho, "Nonlinear gain suppression in semiconductor lasers due to carrier heating," *IEEE Phot. Techn. Lett.* **3**, 606, 1991.

[37] M. Sorel, P. Laybourn, A. Sciré, S. Balle, G. Giuliani, R. Miglierina, and S. Donati, "Alternate oscillations in semiconductor ring lasers," *Opt. Lett.* **27**, 1992–1994, 2002.

[38] J. J. Liang, S. Lau, M. Leary, and J. Ballantyne, "Unidirectional operation of waveguide diode ring lasers," *Appl. Phys. Lett.* **70**, 1192–1194, 1997.

[39] V. R. Almeida and M. Lipson, "Optical bistability on a silicon chip," *Opt. Lett.* **29**, 2387–2389, 2004.

[40] B. Li, M. I. Memon, G. Mezosi, G. Yuan, Z. Wang, M. Sorel, and S. Yu, "All-optical response of semiconductor ring laser to dual-optical injections," *IEEE Photon. Technol. Lett.* **20**, 770–772, 2008.

[41] Z. Wang, G. Yuan, G. Verschaffelt, J. Danckaert, and S. Yu, "Storing 2 bits of information in a novel single semiconductor microring laser memory cell," *IEEE Photon. Technol. Lett.* **20**, 1228–1230, 2008.

[42] S. Fürst and M. Sorel, "Cavity-enhanced four-wave mixing in semiconductor ring lasers," *IEEE Photon. Technol. Lett.* **20**, 366–368, 2008.

[43] T. Pérez, A. Sciré, G. Van der Sande, P. Colet, and C. Mirasso, "Bistability and all-optical switching in semiconductor ring lasers," *Opt. Expr.* **15**, 12941–12948, 2007.

[44] G. Yuan and S. Yu, "Bistability and switching properties of semiconductor ring lasers with external optical injection," *IEEE J. Quantum Electron.* **44**, 41, 2008.

[45] M. Waldow, T. Plotzing, M. Gottheil, M. Först, J. Bolten, T. Wahlbrink, and H. Kurz, "25ps all-optical switching in oxygen implanted silicon-on-insulator microring resonator," *Opt. Express* **16**, 7693–7702, 2008.

[46] S. J. Chang, C. Y. Ni, Z. P. Wang, and Y. J. Chen, "A compact and low power consumption optical switch based on microrings," *IEEE Photonic Techn. L.* **20**, 1021–1023, 2008.

[47] L. Gelens, S. Beri, G. Van der Sande, J. Danckaert, N. Calabretta, H. Dorren, R. Nötzel, E. Bente, and M. Smit, "Optical injection in semiconductor ring lasers: backfire dynamics," *Opt. Expr.* **16**, 16968–16974, 2008.

[48] S. Zhang, Y. Liu, D. Lenstra, M. Hill, H. Ju, G. Khoe, and H. Dorren, "Ring-laser optical flip-flop memory with single active element," *IEEE J. Sel. Top. Quantum Electron.* **10**, 1093–1100, 2004.

[49] V. R. Almeida, C. Barrios, R. Panepucci, M. Lipson, M. Foster, D. Ouzounov, and A. Gaeta, "All-optical switching on a silicon chip," *Opt. Lett.* **29**, 2867–2869, 2004.

[50] S. Schwartz, F. Gutty, G. Feugnet, E. Loil, and J. Pocholle, "Solid-state ring laser gyro behaving like its helium-neon counterpart at low rotation rates," *Opt. Lett.* **34**, 24, 2009.

[51] T. Numai, "Analysis of signal voltage in a semiconductor ring laser gyro," *IEEE J. Quant. Electron.* **36**, 1161, 2000.

[52] M. Strain, G. Mezosi, J. Javaloyes, M. Sorel, A. Perez-Serrano, A. Sciré, S. Balle, G. Verschaffelt, and J. Danckaert, "Semiconductor snail lasers," *App. Phys. Lett.* **96**, 121105, 2010.

[53] J. Y. Lee, X. S. Luo, and A. W. Poon, "Reciprocal transmissions and asymmetric modal distributions in waveguide-coupled spiral-shaped microdisk resonators," *Opt. Express* **15**, 14650–14666, 2007.

[54] C. M. Kim, J. Cho, J. Lee, S. Rim, S. H. Lee, K. R. Oh, and J. H. Kim, "Continuous wave operation of a spiral-shaped microcavity laser," *Appl. Phys. Lett.* **92**, 131110, 2008.

[55] J. Wiersig, S. W. Kim, and M. Hentschel, "Asymmetric scattering and nonorthogonal mode patterns in optical microspirals," *Phys. Rev. A* **78**, 053809, 2008.

[56] L. Shang, L. Y. Liu, and L. Xu, "Single-frequency coupled asymmetric microcavity laser," *Opt. Lett.* **33**, 1150–1152, 2008.

[57] M. Hentschel and T. Y. Kwon, "Designing and understanding directional emission from spiral microlasers," *Opt. Lett.* **34**, 163–165, 2009.

[58] R. C. Neelen, M. P. V. Exter, D. Bouwmeester, and J. P. Woerdman, "Mode competition in a semiconductor ring laser," *J. Mod. Opt.* **39**, 1623–1641, 1992.

[59] R. J. C. Spreeuw, R. C. Neelen, N. J. van Druten, E. R. Eliel, and J. P. Woerdman, "Mode coupling in a He-Ne ring lasers with backscattering," *Phys. Rev. A* **42**, 4315–4324, 1990.

[60] R. Ciegis, M. Radziunas, and M. Lichtner, "Numerical algorithms for simulation of multisection lasers by using traveling wave model," *Mathematical modelling and analysis* **13**, 327–348, 2009.

[61] J. Javaloyes and S. Balle, "Emission directionality of semiconductor-ring lasers: a travelling-wave description," *IEEE J. Quantum Electron.* **45**, 431–438, 2009.

[62] P. A. Khandokhin, I. Koryukin, Y. Khanin, and P. Mandel, "Influence of carrier diffusion on the dynamics of a two-mode laser," *IEEE J. Quantum Electron.* **31**, 647, 1995.

[63] Y. Kuznetsov, *Elements of Applied Bifurcation Theory*, Springer, 3rd edition, New York, 2004.

[64] J. Guckenheimer and P. Holmes, *Nonlinear Oscillations, Dynamical Systems, and Bifurcations of Vector Fields*, Springer-Verlag, New York, 2002.

[65] K. A. Wiesenfeld and E. Knobloch, "Effect of noise on the dynamics of a nonlinear oscillator," *Phys. Rev. A* **26**, 2946–2953, 1982.

[66] G. Dangelmayr and E. Knobloch, "Hopf bifurcation with broken circular symmetry," *Nonlinearity* **4**, 399, 1991.

[67] K. R. Schenk-Hoppe, "Bifurcation scenarios of the noisy Duffing-van der Pol oscillator," *Nonlinear Dynamics* **11**, 255–274, 1996.

[68] J. H. P. Dawes and J. R. Gog, "The onset of oscillatory dynamics in models of multiple disease strains," *J. Math. Biol.* **45**, 471–510, 2002.

[69] G. Schöner, "A dynamic theory of coordination of discrete movement," *Biol. Cybern.* **63**, 257–270, 1990.

[70] E. H. Dowell, "Nonlinear oscillations of a fluttering plate," *AIAA J.* **4**, 1267, 1966.

[71] E. Knobloch and M. R. E. Proctor, "Non-linear periodic convection in double-diffusive system," *J. Fluid Mech.* **108**, 291–316, 1981.

[72] G. Dangelmayr, E. Knobloch, and M. Wegelin, "Dynamics of traveling waves in finite containers," *Europhys. Lett.* **16**, 723–729, 1991.

[73] D. Chillingworth, G. D'Alessandro, and F. Papoff, "Explicit centre manifold reduction and full bifurcation analysis for an astigmatic Maxwell-Bloch laser," *Physica D* **177**, 175, 2003.

[74] P. Holmes and D. Rand, "Phase portraits and bifurcations of the non-linear oscillator," *Int. J. Non-Linear Mech.* **15**, 449–458, 1980.

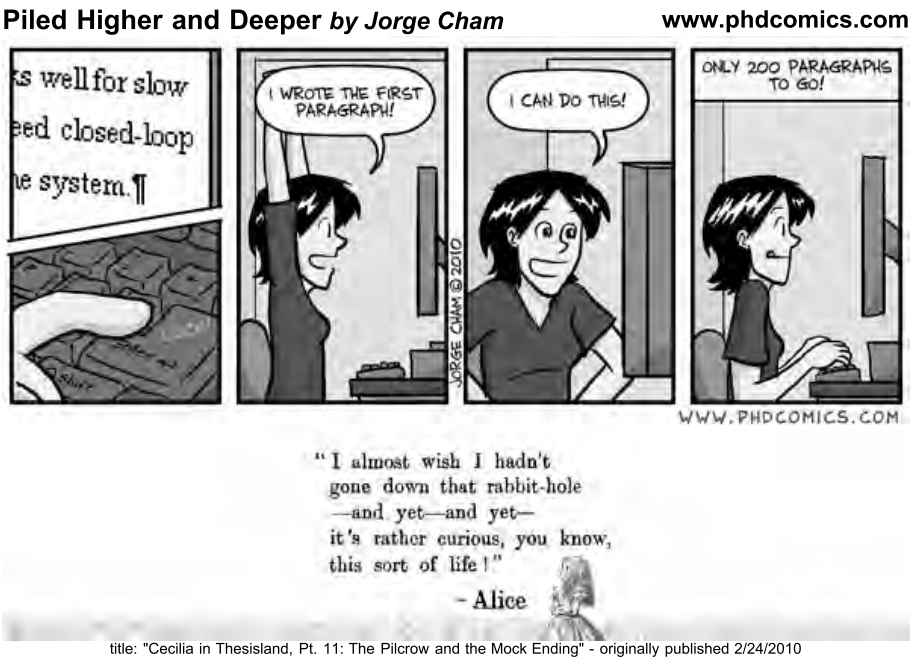

title: "Cecilia in Thesisland, Pt. 11: The Pilcrow and the Mock Ending" - originally published 2/24/2010

CHAPTER 2

An asymptotic rate-equation model for semiconductor ring lasers

"I'm absolutely top-hole, sir, with a ying and yang and yippiedeedoo." — Hugh Laurie as George in Blackadder

In this chapter, we apply a singular perturbation technique to reduce the original five dimensional set of rate equations for a semiconductor ring laser to two equations. The analysis takes advantage of the different timescales present in the system. More specifically, the asymptotic analysis is valid on timescales slower than the relaxation oscillations. Not only do these reduced equations simplify the bifurcation analysis of the possible steady-state solutions considerably, they also allow for a two-dimensional phase space description of the laser. In particular, the shape of the invariant manifolds of the saddle point in the system is studied and a full bifurcation analysis of this two-dimensional laser system is carried out.[1]

[1]The work presented in this Chapter has been published in the following journal papers: [1, 2].

2.1 Motivation

In this Chapter, we will introduce an asymptotic Z_2-symmetric two-dimensional SRL model. Combining the full rate-equation model [Eqs. (1.1)-(1.3)] and this asymptotic one will allow us to gain much more insight into different novel dynamical operating regimes of the SRL, which is discussed in the following Chapters. In this 2D SRL model we are able to determine analytically all local bifurcation points and determine with relative ease all global bifurcations as well[2]. Calculating the loci of the bifurcations in the parameter space of the reduced SRL model has the advantage that it keeps a direct connection with the different physical device parameters (present in the original set of equations (1.1)-(1.3)). Furthermore, as the asymptotic model has only two system variables, the time evolution of the laser can be easily depicted in a simple two-dimensional plot. Additionally, all attractors and invariant manifolds of the saddle points in the system can be determined and analyzed as well in the plane.
The rate-equation model for SRLs can be derived from first principles using a semi-classical approach. An exact description of the dynamical behavior of semiconductor lasers requires a study of the electromagnetic fields in the laser cavity and of the gain medium using electromagnetics and quantum mechanics. To reduce the complexity of the problem, rate equations have been introduced, which describe the evolution in time of the optical field and the carrier density through a set of ordinary differential equations. They have proven to be successful in describing the steady-state behavior and the dynamics of lasers on time scales slower than the cavity round trip time. The appropriate rate equations (2.1)-(2.3) for a SRL, already introduced in Section 1.4 of the previous introductory Chapter, can be found by applying a semiclassical approach, obtaining the field dynamics in a classical way and describing the gain dynamics on a quantum mechanical level [3, 4]. This model consists of two mean-field equations for the counter-propagating modes in the SRL, and a third rate equation for the carriers. The model accounts for self- and cross-gain saturation effects and includes backscattering contributions originating e.g. at the coupler to the

[2]One can divide bifurcations into two principal classes:

- Local bifurcations: they can be analyzed entirely through changes in the local stability properties of equilibria, periodic orbits or other invariant sets as parameters cross through critical thresholds.
- Global bifurcations: they often occur when larger invariant sets of the system 'collide' with each other, or with equilibria of the system. They cannot be detected purely by a stability analysis of the equilibria (fixed points).

For the reader not familiar with bifurcation theory and nonlinear dynamics, an introduction to this topic has been included in Appendix A.

output-waveguide. The rate-equation model from Ref. [5] is given by:

$$\dot{E}_{cw} = \kappa(1+i\alpha)\left[g_{cw}N-1\right]E_{cw} - ke^{i\phi_k}E_{ccw}, \quad (2.1)$$

$$\dot{E}_{ccw} = \kappa(1+i\alpha)\left[g_{ccw}N-1\right]E_{ccw} - ke^{i\phi_k}E_{cw}, \quad (2.2)$$

$$\dot{N} = \gamma\left[\mu - N - g_{cw}N|E_{cw}|^2 - g_{ccw}N|E_{ccw}|^2\right], \quad (2.3)$$

with $E_{cw,ccw}$ the slowly varying amplitudes of clockwise and counter-clockwise propagating waves and one rate equation for the carrier number N. The dot represents differentiation with respect to time t. In Eqs. (2.1)-(2.3), κ is the field decay rate, and γ is the decay rate of the carrier population. α is the linewidth enhancement factor, $g_{cw} = 1 - s|E_{cw}|^2 - c|E_{ccw}|^2$, $g_{ccw} = 1 - s|E_{ccw}|^2 - c|E_{cw}|^2$, μ is the renormalized injection current ($\mu \approx 0$ at transparency, $\mu \approx 1$ at lasing threshold). Self- and cross-saturation effects are modeled by s and c. Backscattering results in a linear coupling between the two fields via $k\exp(i\phi_k)$.

We will use Eqs. (2.1)-(2.3) as the starting point of our analysis of the dynamical behavior in SRLs. These rate equations have been shown to explain the occurrence of bidirectional and unidirectional regimes of continuous-wave mode operation, and a bidirectional regime where the two counter-propagating modes experience harmonic alternate oscillations has been observed [5, 6]. Although numerical simulations of Eqs. (2.1)-(2.3) can correctly reproduce the observed SRL dynamics, analytical and topological insight into the mechanisms that lead to the different instabilities are lacking, as is a clear picture of the influence of the different device parameters. Due to the too high dimensionality of the model only a purely numerical analysis can be used. Therefore, in the next Section, relying on asymptotic methods we will derive a reduced model to describe the SRL dynamics.

Using the rate-equation model Eqs. (2.1)-(2.3), we will now briefly revisit the main operating regimes in the SRL (as also shown in Section 1.3.2 of the previous Chapter), putting emphasis on the primary bifurcations that occur in the system. Introducing an amplitude/phase decomposition

$$E_{cw,ccw} = Q_{cw,ccw}e^{i\phi_{cw,ccw}}, \quad (2.4)$$

it is possible to rewrite Eqs. (2.1)-(2.3)

$$\dot{Q_{cw}} = \kappa\left[g_{cw}N-1\right]Q_{cw} - k\cos\phi_k Q_{ccw}\cos\psi + k\sin\phi_k Q_{ccw}\sin\psi, \quad (2.5)$$

$$\dot{Q_{ccw}} = \kappa\left[g_{ccw}N-1\right]Q_{ccw} - k\cos\phi_k Q_{cw}\cos\psi - k\sin\phi_k Q_{cw}\sin\psi, \quad (2.6)$$

$$\dot{\psi} = \kappa\alpha N(c-s)(Q_{ccw}^2 - Q_{cw}^2) + k\cos\phi_k\sin\psi\left(\frac{Q_{ccw}}{Q_{cw}} + \frac{Q_{cw}}{Q_{ccw}}\right) + k\sin\phi_k\cos\psi\left(\frac{Q_{ccw}}{Q_{cw}} - \frac{Q_{cw}}{Q_{ccw}}\right), \quad (2.7)$$

$$\dot{N} = \gamma\left[\mu - N - g_{cw}NQ_{cw}^2 - g_{ccw}NQ_{ccw}^2\right], \quad (2.8)$$

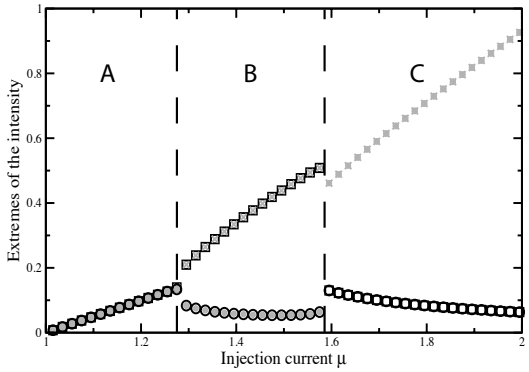

Figure 2.1: Bifurcation diagram of Eqs. (2.1)-(2.3) depicting the extremes of the modal intensity vs. injection current μ. Three regimes of operation are distinguished: A: bidirectional CW operation, B: alternate oscillations, C: bistable unidirectional operation. $\kappa = 100\text{ns}^{-1}$, $\gamma = 0.2\text{ns}^{-1}$, $\alpha = 3.5$, $s = 0.005$, $c = 0.01$ $\phi_k = 1.5$, $k = 0.44\text{ns}^{-1}$. The maxima (minima) of Q_{cw}^2 are denoted by open black squares (circles). The maxima (minima) of Q_{ccw}^2 are denoted by gray crosses (dots).

where the relative phase ψ is defined by

$$\psi = \phi_{ccw} - \phi_{cw}. \tag{2.9}$$

Performing a numerical bifurcation analysis, the following scheme can be found (see Figure 2.1)[3]. At the threshold current, $\mu \approx 1$, laser action starts. Although the counter-propagating modes experience nonlinear gain saturation, backscattering $[k \exp(i\phi_k)]$ favors bidirectional emission (regime A in Figure 2.1) just above threshold. In Ref. [5], Sorel *et al.* studied the steady state solutions in the bidirectional regime. We quickly review these results here. The bidirectional regime corresponds to two symmetric solutions ($Q_{cw} = Q_{ccw} = Q_0$ and $N = N_0$) with

$$Q_0^2 = \frac{N_0 - 1 - k\cos\phi_k \cos\psi}{(c+s)N_0}, \tag{2.10}$$

$$N_0 = \frac{\mu}{1 + 2Q_0^2 - 2(c+s)Q_0^4}. \tag{2.11}$$

These two solutions differ in their relative phase difference ψ. One of them has $\psi = 0$ and is referred to as the *In-Phase Symmetric Solution* (IPSS), while the *Out-of-Phase Symmetric Solution* (OPSS) is characterized by $\psi = \pi$. For the parameter

[3] An explanation of the numerical integration schemes that we use can be found in Appendix B.

set given in Figure 2.1, in regime A, the OPSS is found to be the stable solution due to the positive value of $\cos\phi_k$, while the IPSS is unstable. Therefore, in this case, the IPSS is of no further importance and all further bifurcations emerge from the OPSS.
Regime B is characterized by alternate intensity oscillations between the two counter-propagating modes. At $\mu \approx 1.3$, the IPSS loses its stability through a Hopf bifurcation when

$$4k\cos\phi_k = \kappa N_0 Q_0^2(c-s), \tag{2.12}$$

with a Hopf frequency

$$\omega_H = 2k\sqrt{-(\cos(2\phi_k) + \alpha\sin(2\phi_k))}. \tag{2.13}$$

At this point, a limit cycle representing a dynamic competition between the two counter-propagating modes appears. From Eqs. (2.12) and (2.13), it is clear that this regime is induced by backscattering, weak as it may be.
For injection currents larger than $\mu \approx 1.6$, in regime C, the optical output power is mainly concentrated in one propagation direction. This regime corresponds to two out-of-phase asymmetric solutions (OPAS) emerging from a pitchfork bifurcation of the unstable OPSS. Because of the device symmetry two OPAS exist: one where $Q_{cw} > Q_{ccw}$ and vice versa. In this regime, the device exhibits bistability.
The bidirectional regime and its corresponding Hopf point can be found by solving Eqs. (2.10)-(2.12). However, the unidirectional regime can only be found by solving Eqs. (2.5)-(2.8) numerically for its steady-state values using a Newton-Raphson method. This complicates the analysis of its bifurcation points, making a physical interpretation of the bifurcation schemes not straightforward. In the next Section, we will show that it is possible to simplify the dynamical equations such that analytical results can be obtained for the unidirectional regime. Also, this analysis provides easier expressions for the bidirectional regime, eliminating the need for solving Eqs. (2.10)-(2.12).

2.2 Asymptotic reduction

Our numerical investigations of Eqs. (2.1)-(2.3) show that (for the given parameter set) the quantity $N - 1$ remains small. The parameter values suggest to investigate the limit

$$\kappa/\gamma \to \infty \tag{2.14}$$

assuming $N-1$, s and c smaller than 1, and k smaller than κ. The approach that we will follow here has already proven itself very successful in understanding the dynamical behavior of other semiconductor laser devices such as VCSELs [7].
To be able to define the order of magnitude of all parameters and to be able to determine the leading order approximation to Eqs. (2.5)-(2.8), we need to introduce a dimensionless time τ and a smallness parameter ρ as

$$\tau = \gamma t, \tag{2.15}$$

$$\rho = \frac{\gamma}{\kappa}. \tag{2.16}$$

From numerical simulations, we have seen that N always evolves close to the threshold value. Hence, we define a new carrier variable

$$N - 1 = \rho n \tag{2.17}$$

where n is assumed to be $O(1)$. Please note that in this analysis, the carrier number N is assumed close to its steady-state value, whereas the field variables are allowed to evolve arbitrarily. We further assume that

$$s = \rho S, \tag{2.18}$$

$$c = \rho C, \tag{2.19}$$

$$k/\kappa = \rho K, \tag{2.20}$$

with S, C and K of $O(1)$. After substituting Eqs. (2.15)-(2.20) into Eqs. (2.5)-(2.8) and taking the limit $\rho \to 0$, we obtain the following leading order system:

$$\begin{aligned} Q'_{cw} &= \left(n - SQ_{cw}^2 - CQ_{ccw}^2\right) Q_{cw} \\ &\quad -K\cos\phi_k Q_{ccw}\cos\psi + K\sin\phi_k Q_{ccw}\sin\psi, \end{aligned} \tag{2.21}$$

$$\begin{aligned} Q'_{ccw} &= \left(n - SQ_{ccw}^2 - CQ_{cw}^2\right) Q_{ccw} \\ &\quad -K\cos\phi_k Q_{cw}\cos\psi - K\sin\phi_k Q_{cw}\sin\psi, \end{aligned} \tag{2.22}$$

$$\begin{aligned} \psi' &= \alpha(C-S)(Q_{ccw}^2 - Q_{cw}^2) + K\cos\phi_k\sin\psi\left(\frac{Q_{ccw}}{Q_{cw}} + \frac{Q_{cw}}{Q_{ccw}}\right) \\ &\quad +K\sin\phi_k\cos\psi\left(\frac{Q_{ccw}}{Q_{cw}} - \frac{Q_{cw}}{Q_{ccw}}\right), \end{aligned} \tag{2.23}$$

$$1 - \mu + Q_{cw}^2 + Q_{ccw}^2 = 0, \tag{2.24}$$

where prime now denotes derivation with respect to the dimensionless time τ. The first three equations (2.21)-(2.23) are a simplified form of the original rate

equations Eqs. (2.5)-(2.7). However, Eq. (2.24) is not a rate equation and does not give us an expression for n. At this point, it is clear that our analysis differs considerably from an adiabatic elimination of the carrier dynamics. Instead, we have derived a conservation law for the total intensity valid on the timescale τ:

$$Q_{cw}^2 + Q_{ccw}^2 = \mu - 1 > 0. \tag{2.25}$$

Practically, this means that when reaching the conservation relation dynamically (e.g. after a step in the injected current) the typical relaxation oscillations are observed on a faster timescale with typical frequency $\sim \sqrt{(\mu-1)/\rho}$. On the slow timescale, however, this transition will seem to have appeared instantaneously. So, on the slow time τ, in all different operating regimes of the SRL – steady-state bidirectional (A) and unidirectional (C) behavior as well as the alternate oscillations (B) between the two counter-propagating modes – the total power will remain conserved. As a result, the carrier number n will become a slaved variable. We can now use this property to determine n from the equations for the amplitudes $Q_{cw,ccw}$. Combining Eqs. (2.21) and (2.22), we can find a dynamical equation for the total power. Furthermore, because of the conservation law in Eq. (2.25), this equation for the total power reduces to a algebraic equation relating n to Q_{cw}, Q_{ccw} and ψ. Combining the resulting equation with the relation $Q_{ccw}^2 = \mu - 1 - Q_{cw}^2$ results in an expression for the carriers $n(Q_{cw}, \psi)$. Finally, substituting the latter equation into Eqs. (2.21)-(2.23), leads to a closed set of two rate equations

$$\begin{aligned} Q_{cw}' &= \left[n(Q_{cw},\psi) - SQ_{cw}^2 - CQ_{ccw}^2(Q_{cw})\right] Q_{cw} - K\cos\phi_k Q_{ccw}(Q_{cw})\cos\psi \\ &\quad + K\sin\phi_k Q_{ccw}(Q_{cw})\sin\psi, \end{aligned} \tag{2.26}$$

$$\begin{aligned} \psi' &= \alpha(C-S)\left[Q_{ccw}^2(Q_{cw}) - Q_{cw}^2\right] + K\cos\phi_k \sin\psi\left[\frac{Q_{ccw}(Q_{cw})}{Q_{cw}} + \frac{Q_{cw}}{Q_{ccw}(Q_{cw})}\right] \\ &\quad + K\sin\phi_k\cos\psi\left[\frac{Q_{ccw}(Q_{cw})}{Q_{cw}} - \frac{Q_{cw}}{Q_{ccw}(Q_{cw})}\right]. \end{aligned} \tag{2.27}$$

These two coupled rate equations represent the leading order approximation to the original four equations.
Using the conservation law of Eq. (2.25) for one last time, Eqs. (2.26)-(2.27) can be rewritten in a more appealing form. We define the dynamical variable θ as a measure for the relative modal intensity by

$$Q_{cw} = \sqrt{\mu-1}\cos\left(\frac{\theta+\pi/2}{2}\right), \tag{2.28}$$

$$Q_{ccw} = \sqrt{\mu-1}\sin\left(\frac{\theta+\pi/2}{2}\right), \tag{2.29}$$

with $\theta \in [-\pi/2, \pi/2]$. Redefining the current

$$J = (C - S)(\mu - 1)/K, \tag{2.30}$$

and rescaling time to the backscattering $\tau \to K\tau$, the reduced equations now read

$$\theta' = -2\sin\phi_k \sin\psi + 2\cos\phi_k \cos\psi \sin\theta + J\sin\theta\cos\theta, \tag{2.31}$$

$$\cos\theta\psi' = \alpha J \sin\theta\cos\theta + 2\cos\phi_k \sin\psi + 2\sin\phi_k \cos\psi \sin\theta. \tag{2.32}$$

Note that the renormalized injection current J can be either positive or negative depending on the sign of $C - S$. Before performing a linear stability analysis and giving analytical expressions of the different local bifurcations, we will first consider the SRL behavior in two limiting cases.

2.3 Special cases

Eqs. (2.31)-(2.32) can be studied in two extreme cases offering a lot of physical insight into the operation of the SRL. In the first case, we will assume that the coupling between the two counter-propagating waves is purely linear. This means that all effects of saturation are neglected ($C = S$). In the second case, we will briefly study the effect of the nonlinear coupling, when no linear backscattering is present ($K = 0$).

2.3.1 Linear coupling

Only linear coupling ($C = S$) implies that for every injection current μ the renormalized current $J = 0$. This gives:

$$\theta' = -2\sin\phi_k \sin\psi + 2\cos\phi_k \cos\psi \sin\theta, \tag{2.33}$$

$$\cos\theta\psi' = 2\cos\phi_k \sin\psi + 2\sin\phi_k \cos\psi \sin\theta. \tag{2.34}$$

Solving Eqs. (2.33)-(2.34) for their steady states, we find:

$$\theta = 0 \text{ and } \sin\psi = 0, \tag{2.35}$$

which corresponds to bidirectional emission. Backscattering effects will thus force the SRL to emit in both directions. This is a good point to remark that these bidirectional solutions are independent from the injection current J. On the slow timescale τ, rapidly changing the current will therefore make the intensity of this solution jump infinitely fast [see Eqs. (2.28)-(2.29)]. Of course, in the original model, such a switch would be accompanied by an initial fast layer of relaxation oscillations.

2.3.2 Nonlinear coupling

When $K = 0$, $J \to \infty$, such that Eqs. (2.31)-(2.32) reduce to

$$\theta' = J \sin\theta \cos\theta, \tag{2.36}$$
$$\cos\theta\psi' = \alpha J \sin\theta \cos\theta, \tag{2.37}$$

which also has bidirectional emission as steady-state solution. A second steady-state solution,

$$\theta = \pm\frac{\pi}{2}, \tag{2.38}$$

corresponds to pure unidirectional emission. The sign of J will determine which of the two solutions is stable. For positive J, it will always be the unidirectional emitting one, whereas for negative J, the SRL would still be emitting in both directions. We can conclude that stronger cross-saturation then self-saturation ($C > S$) gives preference to unidirectional emission.

2.4 Linear stability analysis

In this Section, we will perform the steady-state analysis of the reduced equation set (2.31)-(2.32) describing the slow time dynamics of SRLs. This will show us how the linear and nonlinear coupling compete. Thanks to the two-dimensionality of the given problem, the linear stability can be studied analytically. The bifurcation diagrams of the periodic solutions still need to be constructed numerically. Moreover, Eqs. (2.31)-(2.32) motivate that the slow time dynamical behavior of the system is limited to the phase plane (θ, ψ).

2.4.1 Bidirectional solutions

Equating Eqs. (2.31)-(2.32) to zero, it is clear that the steady-state (bidirectional) symmetric solutions are given by

$$\theta = 0, \tag{2.39}$$
$$\sin\psi = 0, \tag{2.40}$$

with $\psi = 0$ for the IPSS and $\psi = \pi$ for the OPSS. Using Eqs. (2.31)-(2.32), we can study the linear stability of these steady-state solutions. Considering small

Type of bifurcation	Bifurcation current
Hopf IPSS	$J^H_{IPSS} = -4\cos\phi_k$
Hopf OPSS	$J^H_{OPSS} = 4\cos\phi_k$
Pitchfork IPSS	$J^P_{IPSS} = -\frac{2}{\cos\phi_k+\alpha\sin\phi_k}$
Pitchfork OPSS	$J^P_{OPSS} = \frac{2}{\cos\phi_k+\alpha\sin\phi_k}$

Table 2.1: The Hopf and pitchfork bifurcation currents of the bidirectional IPSS, OPSS solutions

perturbations around the steady-state values, we find the following characteristic equation:

$$\lambda^2 - \lambda\left(J \pm 4\cos\phi_k\right) \pm 2J\left(\cos\phi_k + \alpha\sin\phi_k\right) + 4 = 0, \tag{2.41}$$

where the upper (lower) sign corresponds to the IPSS (OPSS).
Analyzing this characteristic equation immediately gives us the condition for the Hopf bifurcations $J^H_{IPSS,OPSS}$ of the IPSS and OPSS with the corresponding frequency $\Omega^H_{IPSS,OPSS} = 2\sqrt{-(\cos(2\phi_k) + \alpha\sin(2\phi_k))}$ at onset of this oscillatory instability . Moreover, the static bifurcation point of the IPSS and OPSS provide us with the locus of the pitchfork bifurcation that occurs in the SRL system. For analytical expressions of these local bifurcations, we refer to Table 2.1.

2.4.2 Unidirectional solutions

The unidirectional asymmetric solutions are less straightforward to obtain. An elegant approach to writing an analytical expression for these solutions is to parametrize them in ψ. The solution is then of the form $\{\theta(\psi), J(\psi)\}$:

$$\theta_{AS}(\psi) = \arcsin\left(\frac{\alpha\sin\phi_k + \cos\phi_k}{\alpha\cos\phi_k - \sin\phi_k}\tan\psi\right), \tag{2.42}$$

$$J(\psi) = 2\csc\theta(\psi)\sec\theta(\psi)\left(\sin\phi_k\sin\psi - \cos\phi_k\cos\psi\sin\theta(\psi)\right). \tag{2.43}$$

Four asymmetric solutions exist: two that originate at a pitchfork bifurcation from the IPSS ($\theta = 0$, $\psi = 0$), and two from the OPSS ($\theta = 0$, $\psi = \pi$). We will refer to them as IPAS and OPAS, respectively. The pitchfork bifurcation currents are given in Table 2.1. When increasing the current J, these asymmetric solutions

are stabilized at a Hopf bifurcation point:

$$\tan^2 \psi_{AS}^H = \left(\frac{\sin\phi_k - \cos\phi_k\alpha}{\cos\phi_k + \sin\phi_k\alpha}\right)^2 \times \frac{\sin^2\phi_k - \cos^2\phi_k - \alpha\sin 2\phi_k}{3\sin^2\phi_k + \cos^2\phi_k - \alpha\sin 2\phi_k}. \quad (2.44)$$

For every value of α, there exists a point in parameter space (J, ϕ_k) for which the pitchfork bifurcation and the above Hopf bifurcations coincide. Such a point is called a Takens-Bogdanov (TB) codimension-two point[4]. It is known that from these points there should also be global bifurcations emerging [8]. Therefore, in the next Section we complement our analytical analysis of the bifurcations in the reduced system, with a numerical approach using the continuation software package AUTO [10]. As the TB point involves local bifurcations for which we have obtained analytical expressions, we can determine the critical phase $\phi_k^{TB_2}$ of the TB_2 point:

$$\sin^2(\phi_k^{TB_2}) = \frac{1}{2} \pm \frac{\alpha}{2\sqrt{\alpha^2+1}}, \quad (2.45)$$

$$J^{TB_2} = \pm 4\cos\phi_k^{TB_2}. \quad (2.46)$$

Moreover, we mention that for a certain parameter regime, the IPAS (OPAS) can be born in a saddle-node bifurcation or fold bifurcation before the pitchfork bifurcation has occurred. This fold bifurcation is given analytically by:

$$\cos^2\psi^F = \pm 2\frac{\cos\phi_k + \alpha\sin\phi_k}{1+\alpha^2} \quad (2.47)$$

2.5 Bifurcation diagrams

In Figure 2.2, we summarize the previous results and study the stability of the SRL system in a two parameter plane defined by J and ϕ_k with a fixed α. Apart from local bifurcations which can be obtained analytically, we also numerically determine the global bifurcations of the system.

If we choose a polar representation where $x = J\cos\phi_k$ and $y = J\sin\phi_k$, the

[4] As also mentioned in Section 1.4.2, a Takens-Bogdanov bifurcation is a well-studied example of a bifurcation with codimension-two, meaning that two parameters must be varied for the bifurcation to occur. A system undergoes a Takens-Bogdanov bifurcation if it has a fixed point and the linearization of the system function around that point has a double eigenvalue at zero. Three codimension-one bifurcations occur nearby: a fold (saddle-node) bifurcation, an Andronov-Hopf bifurcation and a homoclinic bifurcation. All associated bifurcation curves meet at the Takens-Bogdanov bifurcation. [8, 9]

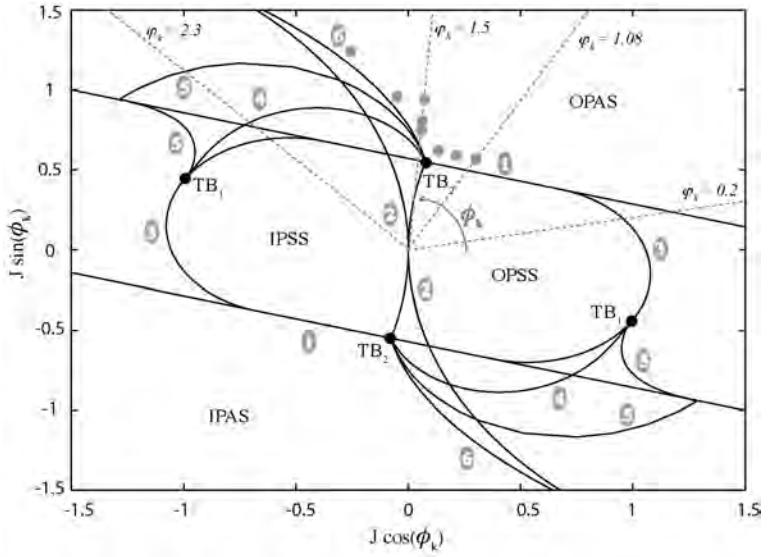

Figure 2.2: Stability diagram for a fixed value $\alpha = 3.5$ showing the different stable operation regimes for $J > 0$. The different black solid lines indicate the different bifurcation currents, and are depicted in a polar plot (J, ϕ_k). The dotted lines depict four cuts for four different values of ϕ_k, for which we show the corresponding PI-curves in Figure 2.3. The eight solid gray dots denote the different operating points of which we plot the invariant manifolds in Figs. 2.5-2.7. Finally, the denotations 1-6 correspond to ① the pitchfork bifurcation of the OPSS (IPSS), ② Hopf bifurcation of the OPSS (IPSS), ③ fold bifurcation of the OPSS (IPSS), ④ subcritical Hopf bifurcation the OPAS (IPAS), ⑤ a double homoclinic bifurcation with gluing and ⑥ a fold of cycles. Multiple Takens-Bogdanov (TB) co-dimension two points are also depicted.

pitchfork bifurcation (see Table 2.1) denoted by ① in Figure 2.2 is a straight line $x + \alpha y = \pm 2$. For a certain parameter regime, the IPAS (OPAS) are born in a fold bifurcation before the pitchfork bifurcation has occurred, denoted by ③ in Figure 2.2. The symmetric solutions can also change stability through a Hopf bifurcation at $J = J_H(\phi_k)$ of the symmetric solutions (OPSS, IPSS) as described by the expressions in Table 2.1. In Figure 2.2, these Hopf bifurcations lines are segments of the circles $[(x \pm 2)^2 + y^2 = 4]$ denoted by ②. The Hopf bifurcations lines end at the pitchfork bifurcations in a Takens-Bogdanov point with symmetry (TB_2) [9]. The asymmetric solutions can change stability through a subcritical Hopf bifurcation given by Eq. (2.44) (④ in Figure 2.2), emerging from a Takens-

Bogdanov point (TB_1) at the fold bifurcation line. For a generic in-depth analysis of all possible bifurcation scenarios close to Takens-Bogdanov points in the wide class of systems with a broken $O(2)$-symmetry, we refer to Refs. [11, 12] (and references therein).
The global bifurcations emerging from the two Takens-Bogdanov points of co-dimension two have been tracked numerically using the continuation software package AUTO [10] and using brute force numerical simulations. From TB_1, the point where the fold bifurcation line ③ and the subcritical Hopf line ④ meet, emerges a double homoclinic bifurcation line with gluing[5] ⑤. From TB_2, the point where the supercritical Hopf bifurcation line ② and the pitchfork bifurcation ① meet, emerges a double homoclinic connection with a gluing bifurcation ⑤ and a fold of cycles ⑥. Finally, also the supercritical Hopf bifurcation and the fold of cycles coincide in a co-dimension 2 point called a Bautin bifurcation point (not shown)[6].
We point out that Figure 2.2 provides a complete picture of the different dynamical regimes for $\alpha = 3.5$, but only for positive values of J, meaning that $c > s$, being the physically relevant parameter region. The bifurcation lines for negative values of J, however, are exactly the same, but due to the following particular invariance of the reduced system (Eqs. 2.31-2.32) the stability is reversed:

$$\phi_k \quad \rightarrow \phi_k + \pi, \tag{2.48}$$
$$J \quad \rightarrow -J, \tag{2.49}$$
$$t \quad \rightarrow -t. \tag{2.50}$$

While performing a bifurcation analysis, both analytically and numerically, many different dynamical regions of operations can be found in the reduced system Eqs. (2.31)-(2.32), as can be seen from the different PI-curves in Figure 2.3. Three different regions of operation A,B,C can be identified in Figure 2.3(a)-(d) according to the relative magnitude of the linear and nonlinear coupling terms between CW and CCW mode [see also Figure 2.1]. These three main regions of operation have been already introduced to the reader in Section 1.3.2 and Section 2.1. However, we will revisit these operating regimes now and demonstrate that depending on the physical parameters of the system the behavior of the SRL can largely vary in region B where linear and nonlinear coupling are of similar

[5]We use the terminology *gluing* for bifurcations in which two limit cycles merge together to form one limit cycle. In this case, this happens through a double homoclinic bifurcation.

[6]The Bautin bifurcation is a bifurcation of an equilibrium in a two-parameter family of autonomous ODEs at which the critical equilibrium has a pair of purely imaginary eigenvalues and the first Lyapunov coefficient for the Hopf bifurcation vanishes. This phenomenon is also called the generalized Hopf (GH) bifurcation. The bifurcation point separates branches of sub- and supercritical Hopf bifurcations in the parameter plain. For nearby parameter values, the system has two limit cycles which collide and disappear via a fold bifurcation of periodic orbits. [8, 9]

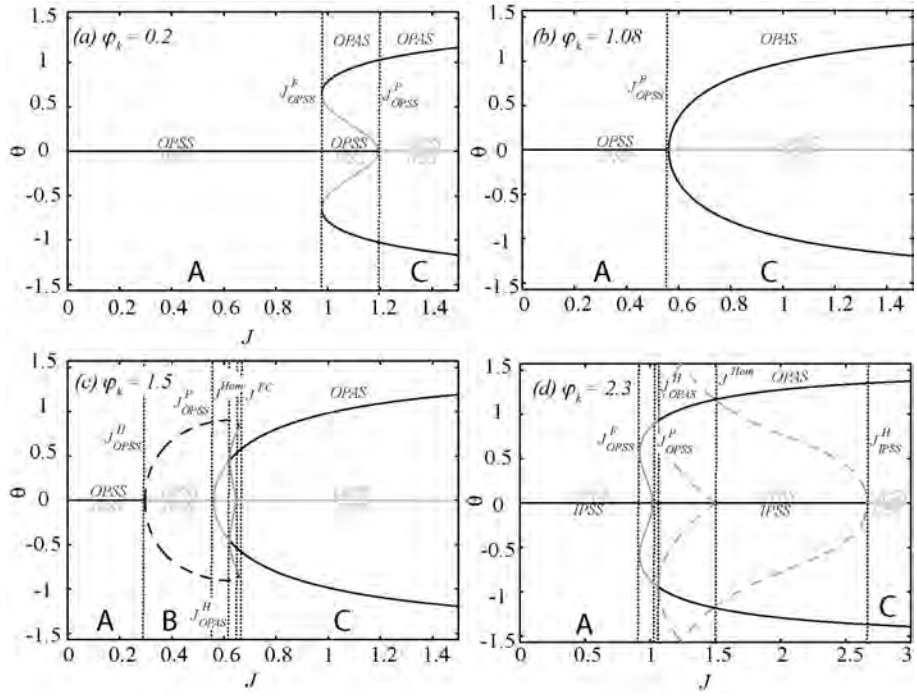

Figure 2.3: Bifurcation diagrams of Eqs. (2.31)-(2.32) depicting the extremes of θ vs. injection current J. The steady state values of θ are denoted by full lines, while the extrema of periodically oscillating θ are indicated with dashed lines. Black (gray) color is used for stable (unstable) fixed points or limit cycles. The dotted lines represent the different bifurcation currents, and are denoted as explained in the text. Black (gray) OPSS/IPSS/OPAS denotations correspond to stable (unstable) OPSS/IPSS/OPAS. From (a) to (d), we have ϕ_k = 0.2, 1.08, 1.5 and 2.3, respectively. α = 3.5.

magnitude.

At the threshold current, $J \approx 0$, laser action starts. When operating close to the threshold, at low power, the nonlinear coupling between CW and CCW is negligible when compared to the linear coupling induced by the backscattering. The resulting operation is bidirectional with CW and CCW operating either in-phase or out-of-phase according to ϕ_k. (see region A in Figure 2.3).

For large values of the pump parameter J, the nonlinear gain saturation becomes the dominant coupling mechanism between the modes and two out-of-phase (in-phase) asymmetric OPAS (IPAS) solutions become possible. The optical output power is mainly concentrated in one propagation direction, called unidi-

rectional operation. Because of the device symmetry two OPAS exist: one where $|E_{cw}|^2 > |E_{ccw}|^2$ and vice versa. In this regime, the device exhibits bistability (See Regime C in Figure 2.3).
For intermediate values of J, the linear and nonlinear coupling are comparable (Region B) and the dynamics of the system as well as the shape of the P-I curve depend on the value of ϕ_k. A SRL aimed to applications such as all-optical information storage is expected to be operated at the edge between region B and C if you want to reduce the switching energy. Depending on the linear coupling phase ϕ_k, the dynamical behavior that the SRL exhibits at the transition between bidirectional and unidirectional operation, originates from instabilities of either the out-of-phase or in-phase solutions. The stable bidirectional solution can be destabilized, immediately going to stable unidirectional operation [see Figure 2.3(b)], but there can be many other possibilities of which we show a couple of examples in the other panels of Figure 2.3. E.g. in Figure 2.3(a), there exists a region where both the stable bidirectional solution as the stable unidirectional solution coexist. In Figure 2.3(c), the destabilisation of the bidirectional solution leads to region B, characterized by stable alternate intensity oscillations between the two counter-propagating modes, which has been observed experimentally [5]. At this Hopf bifurcation point, a limit cycle representing a dynamic competition between the two counter-propagating modes appears. Furthermore, a combination of the above situations is also possible. For instance, in Figure 2.3(d), there exists tristability between the stable IPSS and the stable OPAS, with the presence of different unstable limit cycles separating the different basins of attraction of these stable solutions. We will go into further detail on the possible bi- and multi-stable operation regions in Chapter 4. Both theoretical and experimental results will be discussed there.

2.6 Intermezzo: spherical phase portraits

Because we have reduced the dynamics of the system to a phase space consisting of two angles θ and ψ, it is possible to study the properties of the solutions on a sphere. If the angles would be defined as the spherical coordinates [as in Figure 2.4(a)], then bidirectional emission fixed points ($\theta = 0$) would be situated along the equator with the IPSS and the OPSS opposite to each other. Purely unidirectional emission ($\theta = \pm\pi/2$) can be found on the North ($\theta = +\pi/2$) and South Pole ($\theta = -\pi/2$). We can e.g. use this representation to study the transient behavior exhibited by the SRL. We focus on the bifurcation scheme as presented in Figure 2.3(c) ($\phi_k = 1.5$ and $\alpha = 3.5$). In this case, the IPSS is always unstable and we will use it as our initial condition. In Figures 2.4(b)-(d), we let the system evolve from this point for different values of the injection current

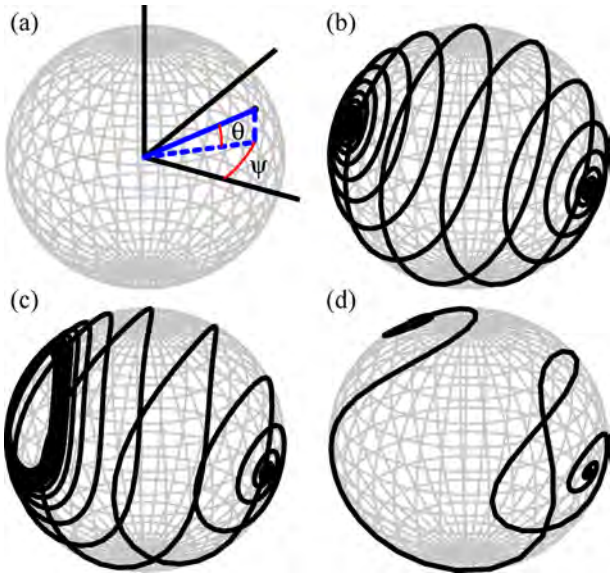

Figure 2.4: Examples of phase space portraits in the spherical phase space for $\phi_k = 1.5$ and $\alpha = 3.5$. The angles θ and ψ are defined as in (a). (b) Time evolution from the unstable IPSS to the stable OPSS ($J = 0.23$). (c) Time evolution from the unstable IPSS to the stable oscillations ($J = 0.34$). (d) Time evolution from the unstable IPSS to one of the stable OPAS ($J = 0.91$).

J. In Figure 2.4(b), the current is fixed such that the only other attractor in the phase space is the stable OPSS. As it is clear from this Figure, the system spirals along the sphere in a specific way from the IPSS to the diametrically opposed OPSS. In Figure 2.4(c), a limit cycle is the stable attractor. This limit cycle clearly distorts the spiral. When the OPAS have become stable [Figure 2.4(d)], the spiral disappears and the system snakes from the IPSS to one of the OPAS which is now close to the North Pole.

2.7 Basins of attraction in the bistable regime in the planar phase space

In the previous Section we have studied in depth the different possible bifurcation scenarios of the SRL. The main question that still remains to be answered to have a full understanding of the SRL dynamics is what the basins of attraction of

the different attractors look like in the phase space (θ, ψ) of the SRL. Therefore, in this Section, we investigate the 2D phase space for a SRL operating in the bistable unidirectional regime. As this operating region is the most interesting for all-optical processing applications, we will characterize the basins of attraction of both directional modes in this region. Such basins of attraction determine which regions in the SRL state space (θ, ψ) evolve towards the *CCW* solution and which ones go to the *CW* mode when time evolves. Such a picture provides useful insight into how the SRL operates. Therefore we will use the phase portraits of the basins of attraction to explain several theoretical and experimental observations in the following Chapters of this first Part of the thesis.
In the bistable regime, Eqs. (2.31)-(2.32) have four stationary solutions: an unstable in-phase (out-of-phase) bidirectional state in $(0, 0)$ $[(0, \pi)]$; two symmetric stable states *CW* (clockwise) and *CCW* (counter-clockwise) at $\psi \approx \pi$ ($\psi \approx 0$) both corresponding to undirectional operation, and a saddle point **S** in $(0, \pi)$ $[(0, 0)]$ which is the unstable out-of-phase (in-phase) bidirectional solution. As we are interested in operating regimes which are relevant for optical information storage, we consider here parameter values such that we are at the edge between region B and C (see Figure 2.3). In particular, we focus on parameters such that we are relatively close to the fold of cycles bifurcation line ⑥ (see Figure 2.2).
We are interested in the qualitative shape of the invariant manifolds of the saddle-point **S** and their dependence on the principal parameters of the system. In particular, we focus on the stable manifold of **S** separating the basins of attractions of the *CW* and *CCW* mode, shown in black and white in Figs. 2.5, 2.6, 2.7 (The parameter sets under study in these figures are depicted by gray dots in Figure 2.2). The invariant manifolds are depicted in the plane instead of using the spherical phase portraits as before. Throughout the remainder of this work, we will prefer the planar phase space pictures due to their greater ease in graphical manipulations.

Influence of J

We study first the dependence of the phase space structures on the pump parameter J [see Eq. (2.30)]. J measures the ratio of nonlinear and linear coupling between *CW* and *CCW* modes. Consider here $(\phi_k, \alpha) = (1.5, 3.5)$; when varying the parameter J, one observes three different regions of operation: bidirectional operation (A), bidirectional operation with alternating oscillations (B) and unidirectional operation (C) [see Figure 2.3] as has been experimentally observed [5]. The shape of the stable manifold of **S**, and the basins of attraction of *CW* and *CCW* are depicted in Figure 2.5. The basins of attraction of *CW* and *CCW* fold into each-other as the stable manifold of *S* spirals inwards. As J increases, the stable manifold unfolds and the basins of attraction separate. Therefore, a large

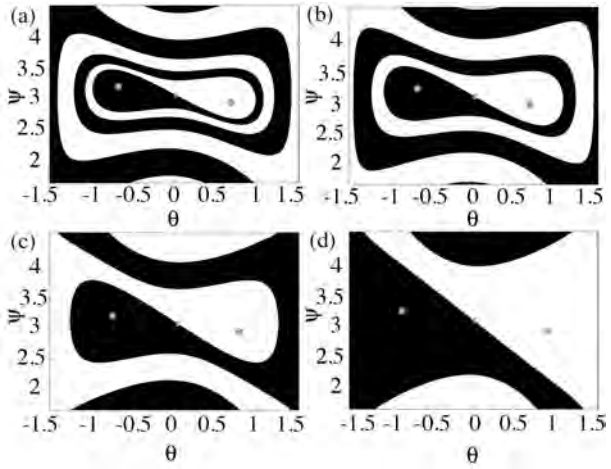

Figure 2.5: Stable manifold at $\phi_k = 1.5$, and $\alpha = 3.5$ for three increasing different values of the normalized current J: $J = 0.71, 0.739, 0.8, 0.93$, from (a) to (d). The basins of attractions of the *CW* and *CCW* mode are given by the black and white region.

bias current μ or a small coupling amplitude k correspond to unfolded basins of attraction.

Influence of ϕ_k

It is very hard to determine the value of ϕ_k for a SRL device as this parameter describes the phase of the backscattering that arises due to different phenomena: localized backscattering at the output coupler region, at the end facets of the output waveguides and distributed backscattering originating from e.g. sidewall surface roughness in the ring itself. Therefore, it is useful to gain insight in the effect of the linear coupling phase ϕ_k in the entire region from zero to 2π. In order to study the influence of ϕ_k on the shape of the manifold, we will focus on the region having the stable OPAS at higher current ($\phi_k \in [0, \pi]$). The region $\phi_k \in [\pi, 2\pi]$ is exactly the same if one interchanges everywhere in-phase (IP) and out-of-phase (OP).
One could wonder whether this folded shape of the stable manifold is only present if one has a region of alternating oscillations in the PI scan, as was the case in Figure 2.5. We have checked the evolution of the manifold shape in the region $\phi_k \in [0, \phi_k^{TB_2}]$ where one does not have a Hopf bifurcation [See Figure 2.6(d)-(f)]. $\phi_k^{TB_2}$ defines the phase ϕ_k where the second Takens-Bogdanov

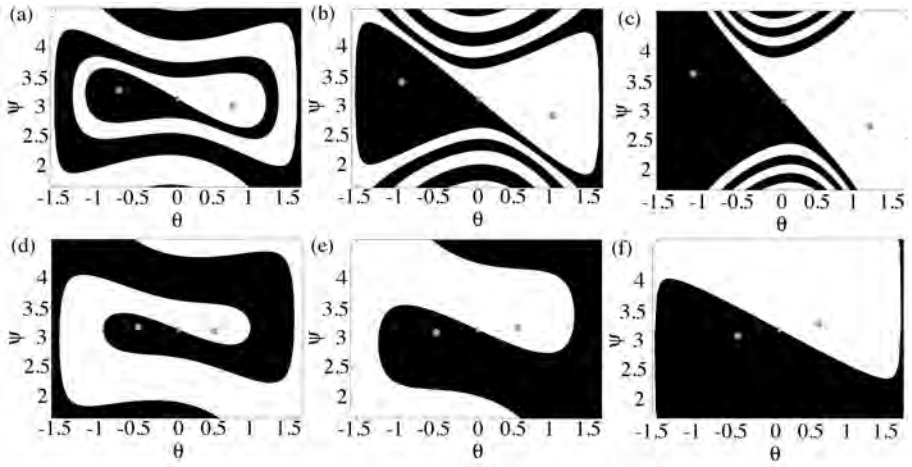

Figure 2.6: Stable manifold at $\alpha = 3.5$ for different values of the linear coupling phase ϕ_k: from (a) to (f) $(\phi_k, J) = (1.5, 0.739), (1.64, 0.972), (1.78, 1.260), (1.36, 0.625), (1.22, 0.625), (1.08, 0.636)$. The basins of attractions of the *CW* and *CCW* mode are given by the black and white region.

bifurcation point lies. For $\phi_k \in [0, \phi_k^{TB_2}]$, one can notice in Figure 2.6(d)-(f) that although one does not observe oscillations in a PI scan, the manifold can still have a folded shape. It unfolds continuously with decreasing values of ϕ_k. In the region $\phi_k > \phi_k^{TB_2}$, many different bifurcation scenarios can take place in a PI scan. However, the bifurcation scheme always ends in a fold of cycles where a stable limit cycle (originating from either the OPSS or the IPSS) touches the unstable limit cycle formed in the gluing bifurcation. As becomes clear from Figure 2.6(a)-(c), the manifold unfolds itself with increasing values of ϕ_k. Due to the fact that the distance between the gluing bifurcation and the fold of cycles also increases, the stable manifold is already more unfolded by the time the fold of cycles occurs.

Influence of α

The linewidth enhancement factor α is a difficult parameter to estimate experimentally [13]. Therefore, as α is often unknown in the SRL, we study how α affects the dynamical system [Eqs. (2.31)-(2.32)]. The results are illustrated in Figure 2.7. We have plotted the manifold shapes for different values of the linewidth enhancement factor α, while keeping (ϕ_k, J)=(1.64, 0.972). We find that increasing values of α lead to an unfolding of the stable manifold for $\phi_k > \phi_k^{TB_2}$,

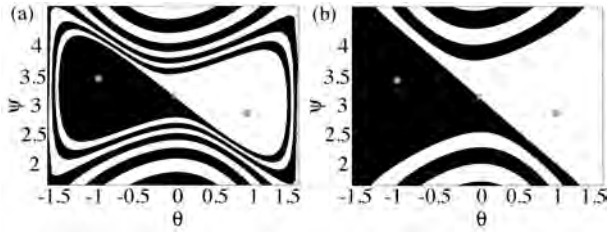

Figure 2.7: Stable manifold at (ϕ_k, J) = (1.64, 0.972) for different values of the linewidth enhancement factor α: (a) 3.3, (b) 3.7. The basins of attractions of the *CW* and *CCW* mode are given by the black and white region.

while for $\phi_k \in [0, \phi_k^{TB_2}]$, the reverse behavior is observed. This can be explained with the analytical expression for the pitchfork bifurcation given in table 2.1. This pitchfork bifurcation is a straight line in Figure 2.2 with a slope given by $-1/\alpha$. Thus, on the one hand increasing the value of α for $\phi_k > \phi_k^{TB_2}$ will shift all the bifurcation lines further away from the operating point (ϕ_k, J) = (1.64, 0.972), such that the manifold unfolds itself. On the other hand, increasing the value of α for $\phi_k \in [0, \phi_k^{TB_2}]$, the pitchfork bifurcation will come closer to the chosen (ϕ_k, J) point in the bistable regime, such that the manifold will spiral more into itself.

Similar folded shapes of the basins of attraction in the bistable regime have been found theoretically in the context of dissipative perturbations of strongly nonlinear oscillators that correspond to slowly varying double-well potentials [14, 15]. In the next Section, we try to make this possible connection of the particular shape of the basins of attraction with a weakly perturbed conservative system more explicit.

2.8 Conservative limit case

From the previous analysis of the phase space picture of the reduced set of equations (2.31)-(2.32) it becomes clear that the folded shape of the basins of attraction of the two counter-propagating modes exists solely when close enough to the homoclinic bifurcation, and i.e. close to the Takens-Bogdanov point.
We suggest to consider the limit $\alpha \to \infty$. In this case, the Takens-Bogdanov point TB_2 is located exactly at $\phi_k \to 1.5$ and $J \to 0$ [see Eq. (2.46)]. In this limit, Eqs. (2.31)-(2.32) reduce to the following system:

$$\theta' = -2\sin(\psi), \tag{2.51}$$

$$\cos(\theta)\psi' = \alpha J \sin(\theta)\cos(\theta) + 2\cos(\psi)\sin(\theta), \tag{2.52}$$

or when introducing $\phi = \psi - \pi$ and rewriting Eqs. (2.51) and (2.52) in terms of θ and ϕ:

$$\theta' = 2\sin(\phi), \tag{2.53}$$
$$\phi' = \alpha J \sin(\theta) - 2\cos(\phi)\tan(\theta). \tag{2.54}$$

We next expand all trigonometric functions near $(\theta, \phi) = (0, 0)$. From Eqs. (2.53) and (2.54), we find

$$\theta' = 2(\phi - \frac{1}{6}\phi^3 + ...), \tag{2.55}$$
$$\phi' = \alpha J(\theta - \frac{\theta^3}{6} + \frac{\theta^5}{120} + ..) - 2(1 - \frac{1}{2}\phi^2 + ...)(\theta + \frac{1}{3}\theta^3 + \frac{2x^5}{15} + ...). \tag{2.56}$$

We assume $\phi = O(\theta^2)$ and reorganize Eqs. (2.55) and (2.56) as

$$\theta' = 2\phi + O(\phi^3), \tag{2.57}$$
$$\phi' = (\alpha J - 2)\theta - (\frac{\alpha J}{2} + 2)\frac{\theta^3}{3} + \phi^2\theta + \frac{\theta^5}{15}(\frac{\alpha J}{8} - 4) + O(\theta^7, \theta^3\phi^2). \tag{2.58}$$

We now introduce the following parameters and scaled variables

$$\varepsilon^2 \equiv \alpha J - 2, \tag{2.59}$$
$$\theta = \varepsilon x, \tag{2.60}$$
$$s = \varepsilon t, \tag{2.61}$$

with ε a small variable, such that from Eqs. (2.57)-(2.58), we find

$$x'' = 2x - 2x^3 + \varepsilon^2\left[-\frac{x^3}{3} + \frac{x'^2 x}{2} - \frac{x^5}{2}\right] + O(\varepsilon^4). \tag{2.62}$$

We recognize a weakly perturbed conservative system which reminds us of the normal form of the TB bifurcation point with symmetry, or equivalently, it is similar to the expression of a Duffing - Van der Pol oscillator [8, 9]. The first integral of the leading conservative equation ($\varepsilon = 0$) is

$$\frac{x'^2}{2} - x^2 + \frac{x^4}{2} = E \tag{2.63}$$

where $E \geq 0$ is the constant of integration (energy). This is nothing else than the classical movement of a particle in a double potential well.
Due to resemblance of the reduced SRL model with that of a Duffing - Van der Pol oscillator in certain parameter regions, the broad knowledge about such weakly perturbed conservative systems can be potentially useful to gain insight into the dynamical behavior of the SRL as well.

2.9 Conclusion

In this Chapter, motivated by the different orders of magnitude of the parameters, we have used asymptotic methods to derive a two-variable reduced model for the dynamical behavior of a semiconductor ring laser. The model accounts for both backscattering processes and gain saturation effects. Thanks to this analysis, we have been able to perform a systematic and largely analytical bifurcation study of all the steady states and time-periodic states of the model. Together with the bifurcation analysis, the two-dimensionality of the reduced model has eased the understanding of the appearance of the different operating regimes. We have revealed a non-trivial shape of the basin of attraction of the system. In the following Chapters, this particular intertwining shape of the basins of attraction will be shown to be at the origin of interesting dynamical behavior of the SRL.

References

[1] G. Van der Sande, L. Gelens, P. Tassin, A. Sciré, and J. Danckaert, "Two-dimensional phase-space analysis and bifurcation study of the dynamical behavior of a semiconductor ring laser," *J.Phys.B* **41**, 095402, 2008.

[2] L. Gelens, G. Van der Sande, S. Beri, and J. Danckaert, "Phase-space approach to directional switching in semiconductor ring lasers," *Phys. Rev. E* **79**, 016213, 2009.

[3] G. Van der Sande, *Simple models for complex photonic systems*, PhD, Vrije Universiteit Brussel, Brussel, 2006.

[4] M. Sargent III, M. O. Scully, and W. J. Lamb, *Laser physics*, Westview Press, 1978.

[5] M. Sorel, P. Laybourn, A. Sciré, S. Balle, G. Giuliani, R. Miglierina, and S. Donati, "Alternate oscillations in semiconductor ring lasers," *Opt. Lett.* **27**, 1992–1994, 2002.

[6] M. Sorel, G. Giuliani, A. Sciré, R. Miglierina, S. Donati, and P. Laybourn, "Operating regimes of GaAs-AlGaAs semiconductor ring lasers: experiment and mode," *IEEE J. Quantum Electron.* **39**, 1187–1195, 2003.

[7] T. Erneux, J. Danckaert, K. Panajotov, and I. Veretennicoff, "Two-variable reduction of the San Miguel - Feng - Moloney model for vertical-cavity surface-emitting lasers," *Phys. Rev. A* **59**, 4660–4667, 1999.

[8] Y. Kuznetsov, *Elements of Applied Bifurcation Theory*, Springer, 3rd edition, New York, 2004.

[9] J. Guckenheimer and P. Holmes, *Nonlinear Oscillations, Dynamical Systems, and Bifurcations of Vector Fields*, Springer-Verlag, New York, 2002.

[10] E. Doedel *et al.*, "Auto 97," *http://indy.cs.concordia.ca/auto/main.html* , 1997.

[11] G. Dangelmayr, E. Knobloch, and M. Wegelin, "Dynamics of traveling waves in finite containers," *Europhys. Lett.* **16**, 723–729, 1991.

[12] G. Dangelmayr and E. Knobloch, "Hopf bifurcation with broken circular symmetry," *Nonlinearity* **4**, 399, 1991.

[13] C. H. Henry, "Theory of the linewidth of semiconductor lasers," *IEEE J. Quantum Electron.* **18**, 259, 1982.

[14] F. Bourland and R. Haberman, "Separatrix crossing - time-invariant potentials with dissipation," *SIAM J. Appl. Math.* **50**, 1716–1744, 1990.

[15] F. Bourland and R. Haberman, "Connection across a separatrix with dissipation," *Stud. Appl. Math.* **91**, 95–124, 1994.

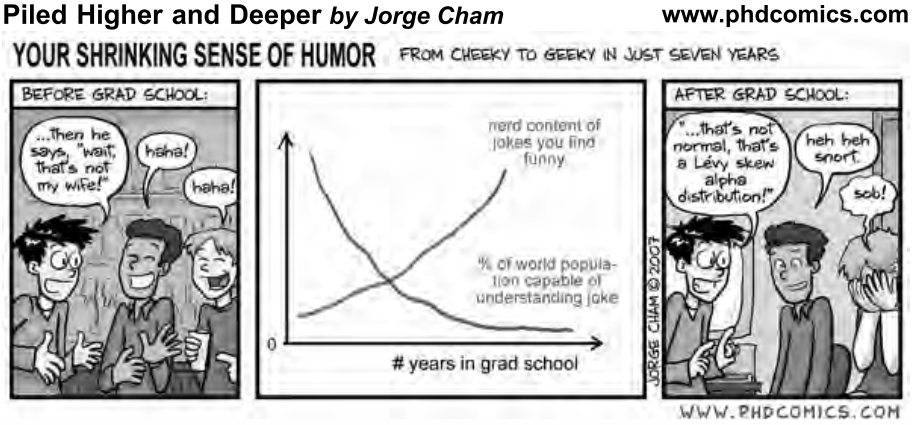

title: "Your Shrinking Sense of Humor" - originally published 5/30/2007

CHAPTER 3

Deterministic switching mechanisms in the bistable regime

"Don't follow the lights." — Gollum in Lord of the Rings

This chapter demonstrates that the topological investigation of the phase space of a semiconductor ring laser, introduced in the previous Chapter, can lead to switching schemes which are an alternative to optical pulse injection of counter-propagating light. Numerical simulations confirm the topological predictions.[1]

3.1 Phase space engineered switching

The standard approach to switch the direction of operation of a SRL operating in the unidirectional regime consists of injecting an optical signal counter-propagating to the lasing mode. Once the external signal is removed, the SRL remains stable in this direction [3–5]. This is illustrated in phase space in Figure 3.1(a). A full understanding of the dynamical stability properties of a SRL as well as an in depth knowledge of the phase space structure, acquired in Chapter 2, allows for alternative switching schemes which rely on the topological properties of the system [1, 2]. Figure 3.1(b) demonstrates e.g. that injecting more energy in

[1] The work presented in this Chapter has been published in the following journal papers: [1, 2]

the lasing CW state can induce a successful switch to the counter-propagating CCW state, which is at first sight rather counter-intuitive. We propose three such novel schemes, based on the particular topology of the phase space, to switch the operation of the ring from clockwise (CW) to counter-clockwise (CCW) mode (or vice versa). Such schemes are based on externally steering the system in the phase space and have been applied e.g. to increase the speed of turn-on in semiconductor lasers in Ref. [6].

An investigation of the dependence on device parameters of the phase space (θ, ψ) for a SRL operating in the bistable regime has been carried out in the previous Chapter 2. In this bistable unidirectional regime, the two-dimensional reduced model [Eqs. (2.31)-(2.32)] has four stationary solutions (see Figure 3.1): an unstable in-phase bidirectional state in $(0, 0)$ (IPSS); two symmetric stable states CW and CCW at $\psi \approx \pi$ both corresponding to undirectional operation (OPAS), and a saddle point **S** in $(0, \pi)$ which is the unstable out-of-phase bidirectional solution (OPSS)[2]. The stable manifold of the saddle-point **S** separates the basins of attractions of the CW and CCW mode. The unstable bidirectional state in $(0, 0)$ is not shown in Figure 3.1.

Consider now for instance a SRL operating in the CW mode. In order to switch operating direction, one needs to steer the system to the basin of attraction of the CCW state with an external perturbation such as e.g. an optically injected pulse. One can engineer switches in the following way. Consider the laser operating stationary in the unidirectional regime, for instance CW (θ_{CW}, ψ_{CW}), and introduce a perturbation in the system which shifts the system away from this CW state. It is possible to use such a perturbation to drive the system into the basin of attraction of the opposite (CCW) state. Once the perturbation is removed, the system will deterministically relax to CCW operation. We propose to induce such a switch by:

1. optically injecting an external field,

2. modulation of the pump current μ,

3. external modulation of the linear coupling phase ϕ_k.

[2]For different values of ϕ_k, it is also possible to have an unstable out-of-phase bidirectional state in $(0, \pi)$ (OPSS); two symmetric stable states CW and CCW at $\psi \approx 0$ both corresponding to undirectional operation (IPAS), and a saddle point **S** in $(0, 0)$ which is the unstable out-of-phase bidirectional solution (IPSS).

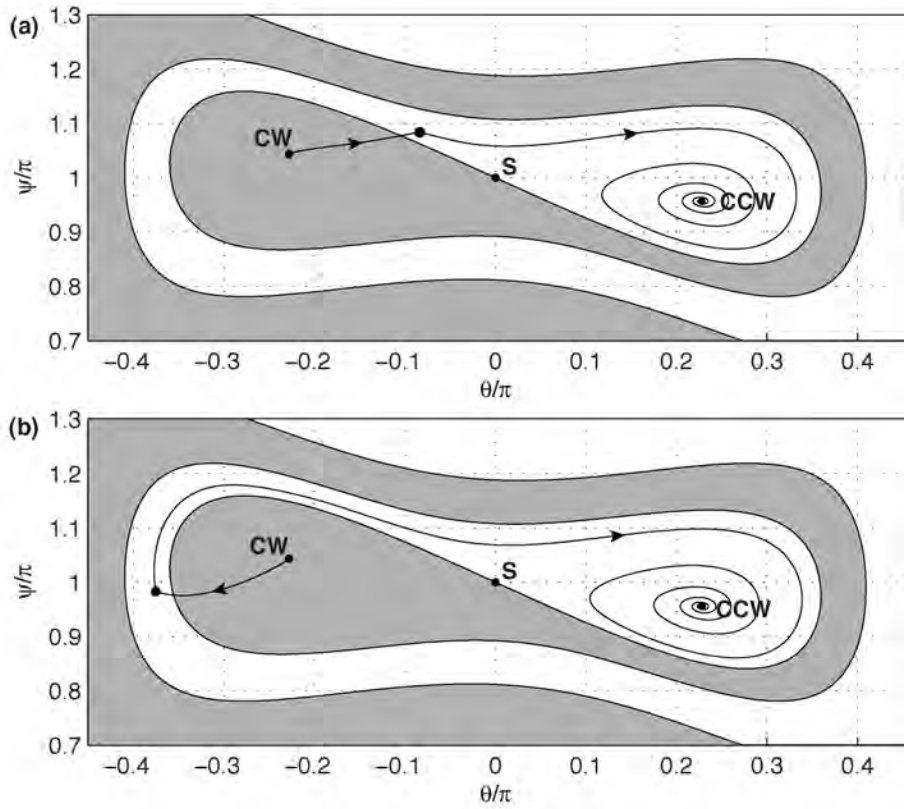

Figure 3.1: Principle of using the topology of the SRL phase space to devise different switching schemes. The stable manifold of the saddle **S** in Eqs. (2.31)-(2.32) is shown for $\phi_k = 1.5$, $J = 0.739$ and $\alpha = 3.5$. The basins of attractions of the CW and CCW mode are given by the gray and white region. (a) demonstrates the standard way to switch by crossing the barrier close to the saddle point, while (b) shows that also increasing the energy in the CW mode can induce a switch to CCW operation.

3.2 Optical injection

We consider a rate-equation model for SRLs operating in a single-longitudinal, single-transverse mode, presented in Chapter 2, now adjusted to take into account an optical injection term [1, 7]:

$$\begin{aligned}\dot{E}_{cw,ccw} &= \kappa(1+i\alpha)\left[N\left(1-s|E_{cw,ccw}|^2-c|E_{ccw,cw}|^2\right)-1\right]E_{cw,ccw} \\ &\quad -ke^{i\phi_k}E_{ccw,cw}+\tfrac{1}{\tau_{in}}F_{cw,ccw}(t), \qquad (3.1)\\ \dot{N} &= \gamma[\mu-N-N\left(1-s|E_{cw}|^2-c|E_{ccw}|^2\right)|E_{cw}|^2 \\ &\quad -N\left(1-s|E_{ccw}|^2-c|E_{cw}|^2\right)|E_{ccw}|^2], \qquad (3.2)\end{aligned}$$

with the parameters and variables defined as in Table 1.1. The term $F_{cw,ccw}(t) = E_{inj}e^{i\Delta t}$ represents the optically injected field in one of the two modes. τ_{in} is the flight time in the ring cavity, $|E_{inj}|^2$ the injected power, and Δ represents the detuning between both lasers.

When no external signal is present, the system will relax to either *CW* or *CCW*. However, when a signal is injected, the system is shifted away from *CW*/*CCW* outside of the asymptotic phase plane. In particular, when injecting a signal strong enough to lock the laser, the relative modal intensity θ and the modal phase difference ψ will converge to new stationary values. The absolute value of θ increases due to the change in the suppression ratio of the two modes, whereas ψ changes due to the new phase relation between E_{cw} and E_{ccw}. When the injected signal is then removed, the system relaxes back to either *CW* or *CCW* according to the basins of attraction.

For instance, when the system is prepared in the steady state *CW* ($\theta < 0$) and one injects a counter-propagating optical field, the relative modal intensity θ will increase. For a strong enough signal, this can even rise above the barrier created by the stable manifold of *S*. When the injection is removed, the system finds itself in the basin of attraction of *CCW* and will relax to it. This is the intuitive switching scenario of a switch induced by a counter-propagating signal.

When injecting a co-propagating signal, the value of θ is expected to decrease further. Due to the folded shape of the stable manifold of *S*, the system can eventually be driven outside the basin of attraction of *CW*. In this case, when the injection is removed, the system will relax to *CCW*, the counter-propagating stationary operation. This mechanism is counter-intuitiveas the mode, which receives the least energy from the optical injection, prevails after the injection pulse. In that sense, the laser has "backfired" after the optical injection.

This prediction has been checked by numerical integration of the full set of rate

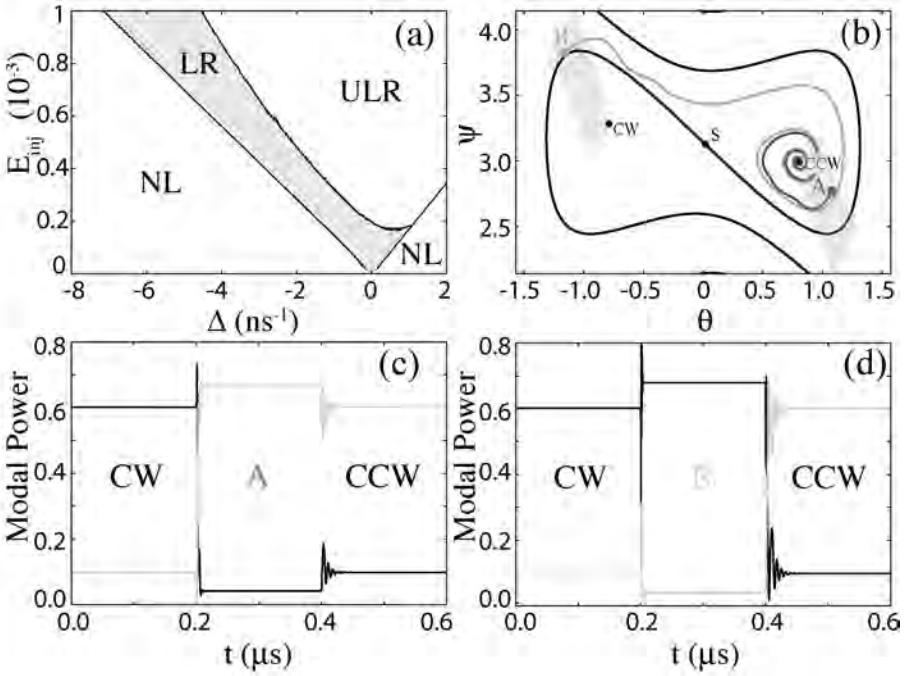

Figure 3.2: Results obtained from numerical simulations of Eqs. (3.1)-(3.2). In (a) the different regimes of operation of the optically injected SRL are indicated in the plane (Δ, E_{inj}). LR marks the stable locking region in gray, ULR the unstable locking region, and NL the regime without locking. Δ represents the detuning with the injected master laser, and E_{inj} the amplitude of the injected signal. (b) shows the phase portrait of the system. *CW* and *CCW* are the stable states of the system; *S* is the saddle. The stable manifold of *S* is indicated with a black solid line. *A* and *B* indicate the equilibrium positions of the system when the counter-propagating (A) or co-propagating (B) signal is injected starting from the *CW* state. The possible locked states from panel (a) by co-propagating injection are again depicted by the gray region. The external field is injected in the co-propagating direction at t_{in} = 200ns and removed at t_{fin} = 400ns. The relaxation trajectories from *A*-*B* towards the corresponding equilibrium are marked in gray solid lines. Finally, (c)-(d) depict the time-series for $|E_{cw}|^2$ (gray) and $|E_{ccw}|^2$ (black) corresponding to the switches in (b). The injection amplitude and detuning are ($E_{inj} = 3\,10^{-4}$, $\Delta = -1.2ns^{-1}$) in (c) and ($E_{inj} = 6\,10^{-4}$, $\Delta = -4.2ns^{-1}$) in (d). $\mu = 1.704$ ($J = 0.8$), $k = 0.44ns^{-1}$, $\phi_k = 1.5$, $\kappa = 100ns^{-1}$, $\gamma = 0.2ns^{-1}$, $s = 0.005$, $c = 0.01$, $\alpha = 3.5$.

equations [Eqs. (3.1)-(3.2)], including $F_{cw,ccw}(t) \neq 0$ to model optical injection[3]. The results are shown in Figure 3.2. The system is initially prepared in the state *CW* at $t_0 = 0$; a counter-propagating [See Figure 3.2(b)-(c)] or co-propagating [See Figure 3.2(b)-(d)] signal is injected in the system at $t_{in} = 200$ns and removed at $t_{fin} = 400$ns. The parameter values have been chosen such that the system can lock to the injected laser field. The locking region (LR), shown in grayscale in Figure 3.2(a)-(b), mainly exists for negative values of the detuning Δ. This asymmetry in the locking region with respect to the detuning Δ is typical for semiconductor lasers having a certain linewidth enhancement factor α [8, 9]. Furthermore, we point out that, in Figure 3.2(a), Δ represents the actual detuning of the free running laser frequency with the injected master laser frequency. In fact, the linear coupling term $k \exp(i\phi_k)$ introduces a splitting of the lasing frequency of the SRL into a doublet structure. This frequency shift — for the chosen parameters here $\approx 0.2\text{ns}^{-1}$ — has been taken into account in Figure 3.2(a) by shifting the detuning Δ used in Eqs. (3.1)-(3.2) over 0.2ns^{-1}. For an elaborate study of the locking regions of the optically injected SRL and the possible dynamical regimes that can be induced by optical injection, we refer to our study presented in Ref. [10].

Our simulations show that for $t_{in} < t < t_{fin}$, the system locks to the external signal after an initial transient. The corresponding locked states are indicated as *A* and *B* in Figure 3.2(b). Both states *A* and *B* belong to the basin of attraction of *CCW*. When the injection is removed ($t > 400$ns), the system follows the slow time-scale dynamics of the two-dimensional phase plane. Therefore, it relaxes towards *CCW* following the stable manifold of *S*. A successful switch to the counter-propagating direction has been achieved in both cases.

Note that in Figure 3.2, we have given the system enough time to lock to the injected laser light. Since this process can take several ns, injecting light pulses with a longer pulse duration than this locking time will all have the same effect. On the contrary, we have checked that when shorter injection pulses are used, pulse duration will clearly influence the switching scenario. Since in that case the stationary locking state will not be reached yet, the pulse duration time critically determines the initial point in phase space when removing the optical pulse. Depending on this pulse duration, the SRL will switch its direction of operation or relax back to the same directional lasing mode. The effect of pulse duration on directional switches with resonant injection counter-propagating to the lasing mode has been investigated in Ref. [5]. No backfiring events have been observed in that work though. This is due to the fact that the authors have investigated the switching behavior at higher values of the current. In that case the stable manifold of the saddle point is completely unfolded (see Figure 2.5) and no backfiring can occur.

[3] An explanation of the numerical integration schemes that we use can be found in Appendix B.

Also, we have observed in the numerics that the switching process can become random in the presence of noise. The randomness of the directional switches due to noise is especially large when the injected power and detuning are such that the locking state is close to the stable manifold of the saddle point in the two-dimensional system without injection, shown in Figure 3.2(b).
In Ref. [1], preliminary experiments performed on a SRL have shown the possibility to switch the laser using co-propagating pulse injection. However, a detailed experimental characterization of switching behavior in SRLs due to both counter-propagating and co-propagating injection remains to be carried out. Such an experimental study should then be compared with the theoretical concepts based on the two-dimensional SRL model discussed in this Section.

3.3 Current modulation

Knowing that the OPAS separate for increasing values of the normalized pump current J, one possibility to induce a switch is by increasing the pump current for a certain time, such that the system relaxes to the new OPAS state with higher intensity. If one then decreases the current fast enough, the system will find itself in the basin of attraction of one of the original lower intensity OPAS modes. It will follow the deterministic trajectories of this last current value and relax to the targeted OPAS state. Which OPAS state depends on the amplitude of the current modulation determining where in the stable manifold one ends up.
A confirmation of this behavior can be seen in Figure 3.3, where the full SRL rate equation model [Eqs. (2.1)-(2.3)] is simulated in the unidirectional regime. A time-varying square-wave modulation $\mu(m) = \mu_{bias} + \Delta\mu(m)$ is applied with a period $T = 100ns$. $\Delta\mu(m)$ is given by $0.044m$, where m is an integer describing the m^{th} modulation step. This $\Delta\mu$ corresponds to $\Delta J = 0.05m$. In Figure 3.3, one can clearly see that there exist regions of $\Delta\mu$ inducing a switch, and others that do not, confirming the relevance of the two-dimensional stable manifold.
The insets I, II, III in Figure (3.3) depict the evolution of the system projected in the two-dimensional phase plane (θ, ψ) for three values of the current modulation, respectively for $m = 4, 12$ and 19. These insets demonstrate that depending on your initial condition (determined by $\Delta\mu$), you either switch to the opposite mode or not. More importantly, one can see that the invariant manifolds of the saddle point as obtained from the reduced 2D model are followed by the system described with the full SRL rate equation model, confirming the validity of the asymptotically reduced system. However, one should note that this good correspondence between the full rate-equation system and the reduced one is only obtained after a certain transient time, determined by the damping rate of

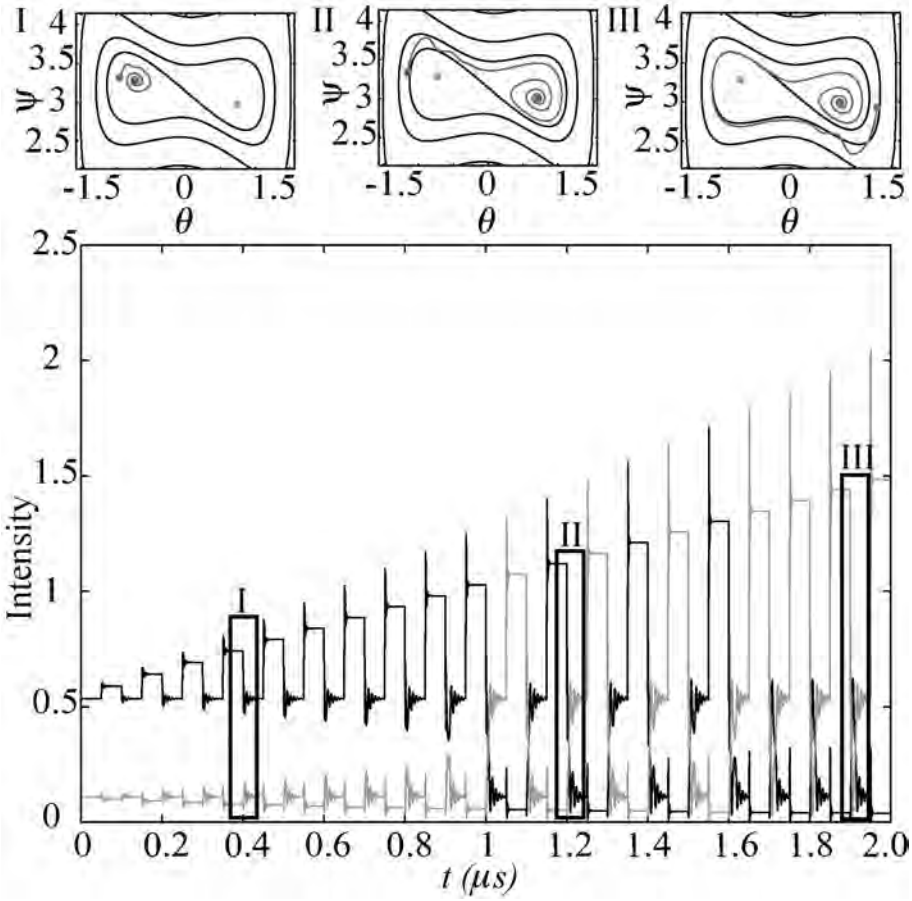

Figure 3.3: Numerical simulations of Eqs. (2.1)-(2.3), where the current is modulated around $\mu_{bias} = 1.65$ ($J_{bias} = 0.739$). The current modulation $\mu(m) = \mu_{bias} + \Delta\mu(m)$ is continuously changed in time by $\Delta\mu(m) = 0.044m$ with a period of $T = 100ns$, where m is an integer describing the m^{th} modulation step. The insets I, II, III depict the evolution of the system projected in the two-dimensional phase plane (θ, ψ) for three values of the current modulation, respectively for $m = 4, 12$ and 19. Other parameters as in Figure 3.2.

the relaxation oscillations (ROs). We have already mentioned before that the two-dimensional system [Eqs. (2.31)-(2.32)] is only valid on a slow time scale ($\tau = \gamma t$), such that the faster ROs should have first damped out before one can adequately predict the evolution of the SRL with the reduced model.
In Figure 3.3, we have taken an infinitely fast rise and fall time for the current modulation, which is not realistic from an experimental point of view. In order to understand the effect of a finite rise/fall time, we have investigated the case of $\Delta\mu = 0.0528$ (Inset II in Figure 3.3) for different values of the fall time. Our simulations (not shown) reveal that fall times which are longer that a critical $t_{fall} \approx 1.35ns$ do not result in a switch, and the system returns to the original state by following the instantaneous equilibrium states.

3.4 Phase modulation

An important drawback of using current modulation to induce directional switches in a SRL, is that it should be feasible to electrically modulate the pump current with fall times of the order of *ns*. Modulating the linear coupling phase could help to circumvent this issue, since the modulation could be done optically. Consider for instance injection of a non-resonant external optical signal in the coupler. Far from the resonance condition, the main effect of such signal would be to alter the refractive index of the coupler without altering the field inside the ring cavity. In first approximation, for a standard semiconductor, we can disregard the changes in k and consider only changes in ϕ_k. Moreover, it is clear from Figure 2.2, that one can induce larger effects by modulating the phase as compared with current modulation and therefore it is more flexible. In what follows, we propose two switching schemes that are both based on steering induced by phase modulation.
In Figure 3.4, we show numerical simulations of the full rate-equation system [Eqs. (2.1)-(2.3)], where the linear coupling phase is modulated between $\phi_{k,i} = 0.7$ and $\phi_{k,f} = 1.5$ [Figure 3.4(a),(c)], $\phi_{k,f} = 4.3$ [Figure 3.4(b),(d)] with a period $T = 200ns$. Figure 3.4(a)-(b) depict a timetrace demonstrating the possibility to switch the SRL between the two OPAS. Figure 3.4(c)-(d) show the projection of Figure 3.4(a)-(b) in the two-dimensional phase space of the reduced system in a solid black line. *CW* and *CCW* denote the stable unidirectional states of the system; *S* is the saddle. The stable (unstable) manifold of *S* is indicated with a gray solid (dashed) line for the two values of the phase $\phi_{k,i}$ and $\phi_{k,f}$, respectively in dark gray and light gray.

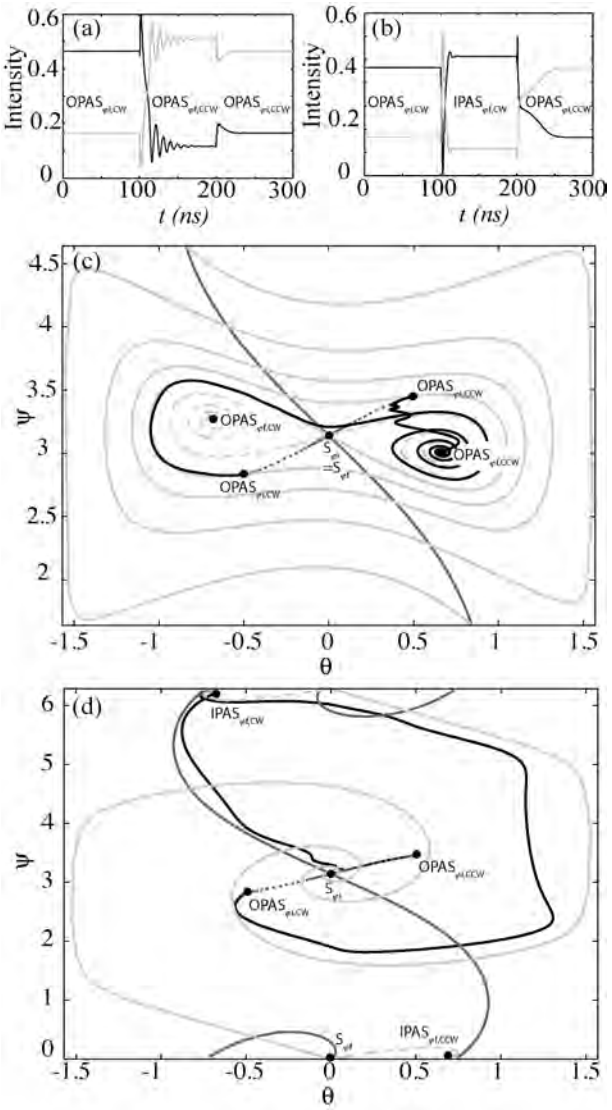

Figure 3.4: Numerical simulations of Eqs. (2.1)-(2.3), where the linear coupling phase is modulated between $\phi_{k,i} = 0.7$ and (a,c) $\phi_{k,f} = 1.5$, (b,d) $\phi_{k,f} = 4.3$ with a period $T = 200ns$. (a,b) depict a timetrace demonstrating the possibility to switch the SRL between the two OPAS. (c,d) show the projection of (a,b) in the phase portrait of the system in a solid black line. The stable (unstable) manifold of S is indicated with a gray solid (dashed) line for the two values of the phase $\phi_{k,i}$ and $\phi_{k,f}$, respectively in dark gray and light gray. $\mu = 1.63$ ($J = 0.716$) and other parameters as in Figure 3.2.

One can distinguish between two possible methods to switch the laser between two OPAS (IPAS) states through phase modulation. The first one is based on changes in ϕ_k smaller than π ($\Delta\phi_k < \pi$) and do not largely affect the variable ψ. Therefore, they involve only the areas of phase space which are close to the initial modal phase difference $\psi = \pi$ ($\psi = 0$). The second method takes advantage of a phase modulation $\Delta\phi_k > \pi$ which affects the complete two-dimensional phase-plane (θ, ψ). While the first method depends on the folded shape of the stable manifold of S as discussed in Chapter 2, the second one does not and has a operating region which can be ten times as large.
Method 1 is shown in Figure 3.4(a)-(c). Starting from the clockwise (CW) OPAS solution for $\phi_{k,i} = 0.7$ ($OPAS_{\phi i,CW}$), we change the linear coupling phase to $\phi_{k,f} = 1.5$, such that $OPAS_{\phi i,CW}$ now finds itself in the basin of attraction of the counter-clockwise (CCW) OPAS state ($OPAS_{\phi f,CCW}$) for the dynamical phase picture with $\phi_{k,f} = 1.5$. In this new situation, the system follows first the stable and then the unstable manifold of the saddle point $S_{\phi f}$, such that it finally relaxes to the stable $OPAS_{\phi f,CCW}$ state. If we then remove the modulation of the coupling phase, the system feels again the manifolds of the original phase space picture ($\phi_{k,i} = 0.7$). Since the $OPAS_{\phi f,CCW}$ state finds itself in the basin of attraction of the CCW OPAS state for $\phi_{k,i} = 0.7$, it relaxes to this $OPAS_{\phi i,CCW}$ state, such that we have accomplished a successful switch.
Since we have seen in the previous Chapter 2 that the spiraling shape of the stable manifold is quite sensitive to parameter variations, the necessity of this folded shape for the directional switching to occur can be a drawback of this method. Therefore, we propose a second scheme, which is less demanding on the particular phase space structure of the reduced dynamical system. In Figure 3.4(b)-(d), we again prepare the system in the $OPAS_{\phi i,CW}$ state with $\phi_{k,i} = 0.7$, but now we change the coupling phase to $\phi_{k,f} = 4.3$. In doing this, the $OPAS_{\phi i,CW}$ state is now located in the basin of attraction of the in-phase asymmetric solution $IPAS_{\phi f,CW}$, such that it relaxes to that state. Furthermore, this $IPAS_{\phi f,CW}$ state finds itself in the basin of attraction of the counter-propagating mode $OPAS_{\phi i,CCW}$. By removing the modulation ($\phi_{k,i} = 0.7$), the system thus follows first the stable and then the unstable manifold of the saddle $S_{\phi i}$ to end up having successfully switched to the CCW mode $OPAS_{\phi i,CCW}$. It is important to note that this second method works for $\phi_{k,f} \in [4.27 - 4.47]$ (for this particular $\phi_{k,f}$ and current J), which is a more than ten times bigger operating region than for method 1.

3.5 Conclusion

We have proposed three novel schemes to switch the operation of the ring from clockwise (CW) to counter-clockwise (CCW) or vice versa. Such schemes relying

on the folded shape of the invariant manifolds of the system, are alternative to the standard approach of injecting a counter-propagating signal [1, 4, 5] and would be unexpected if the topology of the SRL phase space is unknown.
The first of such schemes shows that the operation direction of a semiconductor ring laser can be controlled by injecting a signal from only one port. We have predicted the counter-intuitive phenomenon of inducing a switch by injecting a signal which is co-propagating with the field in the ring. Such a scheme could provide practical advantages as only one master laser is needed for the switching back and forth.
The second scheme consists of a modulation in the bias current, which drags the system outside the basin of attraction of the initial state and releases it when inside the basin of attraction of the final state. Such scheme might be considered counter-intuitive as the system is perfectly bistable. Our simulations reveal the existence of a limiting fall time t_{fall} for the applicability of the scheme. Although the switching speed, obtainable with this scheme, is of course limited by the electrical bandwidth of the modulation source, all-optical methods relying on phase space steering [6] can be applied to increase the performance.
Finally a third scheme has been proposed which consists of modulating the backscattering phase ϕ_k. Switching takes place in two different ways when the amplitude of the phase modulation is larger or smaller than π. Numerical simulations have demonstrated the applicability of the scheme in both cases.
As a final remark, we want to state that this phase space topology is common for optical systems, for instance a nonlinear ring resonator described by the Ikeda map [11]. Our proposed switching schemes are based on the folded shape of the basins of attraction. Folded basins of attractions are expected for a large class of symmetric systems [12]. A similar switching scheme can therefore be expected to be valid in other systems with similar symmetry such as e.g. micro-disk lasers [13] and CO_2-lasers [14].

References

[1] L. Gelens, S. Beri, G. Van der Sande, J. Danckaert, N. Calabretta, H. Dorren, R. Nötzel, E. Bente, and M. Smit, "Optical injection in semiconductor ring lasers: backfire dynamics," *Opt. Expr.* **16**, 16968–16974, 2008.

[2] L. Gelens, G. Van der Sande, S. Beri, and J. Danckaert, "Phase-space approach to directional switching in semiconductor ring lasers," *Phys. Rev. E* **79**, 016213, 2009.

[3] M. T. Hill, H. Dorren, T. de Vries, X. Leijtens, J. den Besten, B. Smalbrugge, Y. Oei, H. Binsma, G. Khoe, and M. Smit, "A fast low-power optical memory based on coupled micro-ring lasers," *Nature* **432**, 206–209, 2004.

[4] G. Yuan and S. Yu, "Bistability and switching properties of semiconductor ring lasers with external optical injection," *IEEE J. Quantum Electron.* **44**, 41, 2008.

[5] T. Pérez, A. Sciré, G. Van der Sande, P. Colet, and C. Mirasso, "Bistability and all-optical switching in semiconductor ring lasers," *Opt. Expr.* **15**, 12941–12948, 2007.

[6] G. Lippi, S. Barland, N. Dokhane, F. Monsieur, P. Porta, H. Grassi, and L. Hoffer, "Phase space techniques for steering laser transients," *J. Opt. B: Quantum Semiclass. Opt.* **2**, 375–381, 2000.

[7] M. Sorel, P. Laybourn, A. Sciré, S. Balle, G. Giuliani, R. Miglierina, and S. Donati, "Alternate oscillations in semiconductor ring lasers," *Opt. Lett.* **27**, 1992–1994, 2002.

[8] G. H. M. Tartwijk and D. Lenstra, "Semiconductor lasers with optical injection and feedback," *Quantum. Semiclass. Opt.* **7**, 87, 1995.

[9] V. Annovazzi-Lodi, A. Sciré, M. Sorel, and S. Donati, "Dynamic behavior and locking of a semiconductor laser subjected to external injection," *IEEE J. Quantum Electron.* **34**, 2350, 1998.

[10] W. Coomans, S. Beri, G. Van der Sande, L. Gelens, and J. Danckaert, "Optical injection in semiconductor ring lasers," *Phys. Rev. A* **81**, 033802, 2010.

[11] S. M. Hammel, C. K. R. T. Jones, and J. V. Moloney, "Global dynamical behavior of the optical field in a ring cavity," *J. Opt. Soc. Am. B* **2**, 552, 1985.

[12] Y. Kuznetsov, *Elements of Applied Bifurcation Theory*, Springer, 3rd edition, New York, 2004.

[13] L. Liu, R. Kumar, K. Huybrechts, T. Spuesens, G. Roelkens, E.-J. Geluk, T. de Vries, P. Regreny, D. Van Thourhout, R. Baets, and G. Morthier, "An ultra-small, low-power, all-optical flip-flop memory on a silicon chip," *Nature Photon.* **4**, 182–187, 2010.

[14] E. D'Angelo, E. Izaguirre, G. Mindlin, G. Huyet, L. Gil, and J. R. Tredicce, "Spatiotemporal dynamics of lasers in the presence of an imperfect O(2) symmetry," *Phys. Rev. Lett.* **68**, 3702–3705, 1992.

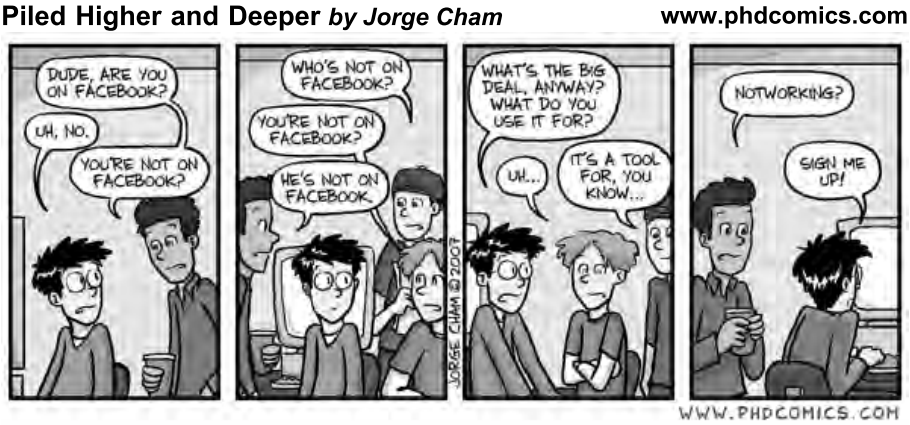

title: "Facebook" - originally published 6/23/2007

CHAPTER 4

Stochastic mode-hopping

"Jesus did. I was hopping along, when suddenly he comes and cures me. One minute I'm a leper with a trade, next moment me livelihood's gone. Not so much as a by your leave. Look. I'm not saying that being a leper was a bowl of cherries. But it was a living. I mean, you try waving muscular suntanned limbs in people's faces demanding compassion. It's a bloody disaster." — Monty Python

"Not all those who wander are lost." — J.R.R. Tolkien - Lord of the Rings

We investigate both theoretically and experimentally the stochastic switching between two counter-propagating lasing modes of a semiconductor ring laser. Experimentally, the residence time distribution cannot be described by a simple one parameter Arrhenius exponential law and reveals the presence of two different mode-hop scenarios with distinct time scales. In order to elucidate the origin of these two time scales, we apply the topological approach based on the two-dimensional dynamical system presented in Chapter 2. Stimulated by the good correspondence between the experiments and the predictions based on the two-dimensional semiconductor ring laser model, we experimentally search for multistable regimes, present in the model. We observe that monostable, bistable and multistable dynamical regimes are organized in well reproducible sequences that match the bifurcation diagrams of the two-dimensional model. Finally, in the limit of small noise intensity, the initial stochastic rate equations can be reduced to an auxiliary Hamiltonian system and the optimal escape paths can be calculated. This approach also

allows one to investigate the dependence of the activation energy on the principal laser parameters.[1]

4.1 Introduction

Fluctuations in active optical systems such as lasers are one of today's technological challenges as well as a fundamental problem of modern physics as they are the result of the quantum nature of the interaction between light and matter [4]. Fluctuations are e.g. responsible for longitudinal mode switching in semiconductor lasers [5], polarization mode-hopping in Vertical Cavity Surface Emitting Lasers (VCSELs) [6–8], and they play a fundamental role in stochastic and coherence resonances of optical systems [9–11]. SRLs are a particular class of lasers whose operation is strongly affected by stochastic fluctuations.
Fluctuations induce spontaneous abrupt changes in the SRL's directional operation from CW to CCW and vice versa, and therefore represent a major limitation to their successful applications, for instance as optical memories. An in-depth understanding of the mode-hopping in SRLs would shed light on the stochastic properties of the large class of Z_2-symmetric systems. The problem of spontaneous directional switches in SRLs has remained unaddressed for a long time, partly due to the high dimensionality of the models that have been proposed for SRLs [12, 13].
We study stochastic mode-hopping in SRLs in two independent limits. First, we consider the asymptotic reduction of the full set of rate equations in the limit of slow time scales as described in Chapter 2 [14]. Monostable, bistable and multistable phase space portraits of the reduced variable set in this asymptotic model allow us to explain experimental features of directional mode-hopping in the SRL (see Sections 4.2-4.5). Secondly, the asymptotic limit of vanishing noise intensity is considered [15]. As a result, we obtain an auxiliary Hamiltonian system which describes the mode-hopping process and contains the dependence on the original parameters of the system without any fitting or any further phenomenology (see Sections 4.6-4.8). We investigate the role of the bias current and the phase of the linear coupling between the CW and CCW modes. The limit of a small linear coupling amplitude is addressed numerically and analytically. A different approach would be to use a phenomenological model such as a double-well potential, but as it would require the fitting of a large number of parameters, a direct connection with the physically meaningful parameters of the system would be lost. A similar problem has been investigated in solid-state

[1] The work presented in this Chapter has been published in the following journal papers: [1–3].

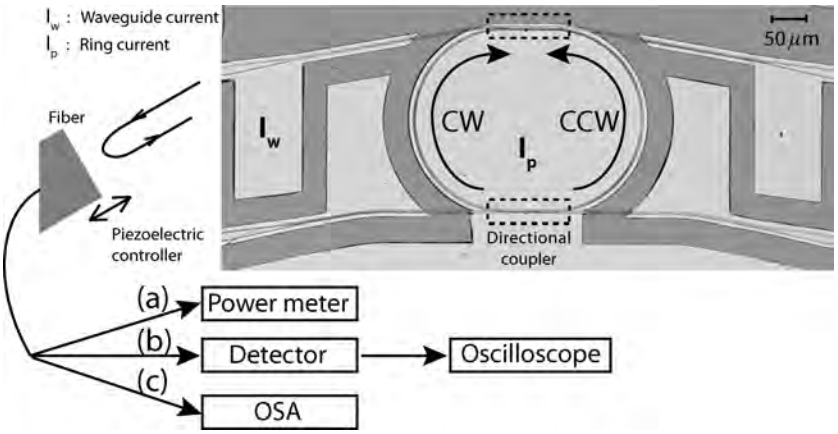

Figure 4.1: Experimental SRL set-up. Four waveguide contacts are depicted of which only the one denoted by I_w is biased. I_p represents the bias current on the ring. The light is collected out from the chip by a fiber that can be positioned by a piezoelectric controller. The light in the fiber can be analyzed by (a) a power meter, (b) a detector connected to an oscilloscope, (c) an optical spectrum analyzer (OSA).

ring lasers [11] to reveal stochastic resonance, but it relied on a phenomenological double-well potential which kept the real parameters of the system hidden.

4.2 Experimental characterization of directional mode-hopping in the bistable regime

The experimental set-up is exemplified in Figure 4.1. We consider here an InP-based multiquantum-well SRL with a racetrack geometry and a free-spectral-range of 53.6 GHz. The device operates in a single-transverse, single-longitudinal mode regime at wavelength $\lambda = 1.56\mu$m. A bias current I_p is applied to the SRL using a current source [Thorlabs, model LDC8002] with a resolution of 3μA. The chip containing the SRL is mounted on a copper mount and thermally controlled by a Peltier element with a 10 kΩ thermistor and a PID control loop. The Peltier element is stabilized at a temperature of 28.57°C with an accuracy of 0.01°C. A bus waveguide made of the same active material as the ring has been integrated on the chip in order to couple power out from the ring. To this waveguide, an independent electrical contact has been applied. Sending a current I_w through the waveguide reduces the absorption. The power emitted from the chip is collected

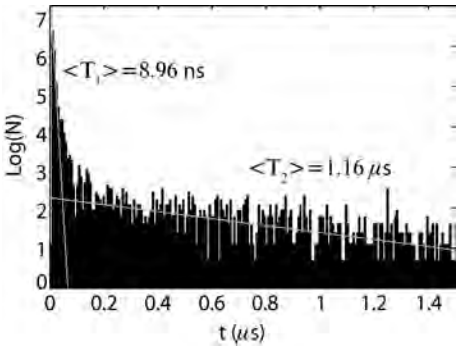

Figure 4.2: Measured RTD in the CCW mode for a laser current of J_{ring} = 39.92mA; the waveguide is biased at 8.22mA and the temperature is 21.55°C. The best fitting lines are shown in white.

with a multimode fiber. The light in the fiber can be coupled to a power meter [Newport, model 2832] with a Germanium detector and a resolution of 0.1nW. Time series of the SRL can be measured by detecting the light in the fiber with a 2.4GHz photodiode detector connected to an oscilloscope [Tektronix, model CSA7404] with a bandwidth of 4 GHz. To verify e.g. the single longitudinal mode operation of the SRL, we have coupled the fiber to an optical spectrum analyzer (OSA) [ANDO, model AQ6317] with a resolution of 0.01nm. The strength K and phase ϕ_k of the coupling between CW and CCW modes are not controllable during the fabrication process and they are *a priori* unknown. However, by using the cleaved facet of the fiber as a mirror, we are able to reflect power from one mode (for instance CCW) back into the waveguide and finally to the counter-propagating mode in the ring. The amount of power that is coupled to the CW mode can then be controlled by tuning the current I_w on the waveguide, whereas its phase can be tuned by positioning the fiber facet with a piezoelectric controller. With this technique, we achieve control of the coupling parameter ϕ_k as well as the coupling strength K.

We forward-bias the waveguide at a fixed current of 8.22 ± 0.01 mA in order to achieve transparency, and we bias the device with increasing DC current until it reaches the threshold at ≈ 31.5 mA. The stochastic mode-hopping starts at approximately 39 mA. In the mode-hopping region, the time series of the power emitted in the CCW mode have been digitally recorded with the oscilloscope for different values of the bias current. Due to the anti-correlation of the two counter-propagating modes [12], a direct result of the conservation law derived in Chapter 2, a drop in power in the CW mode corresponds to an increase in power emitted in the CCW mode. The CCW mode's *Residence Time Distribution*

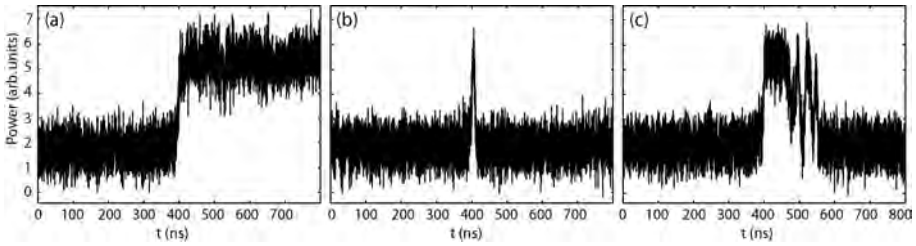

Figure 4.3: Experimentally measured time series showing different kinds of transitions. The ring was biased at I_p = 39.86mA; the waveguide was biased at 8.22mA and the temperature was 21.55°C.

(RTD) has been obtained from the time series and is plotted in Figure 4.2. It is evident from Figure 4.2 that two well-separated time scales are present in the RTD. The white lines depict the best linear fit in this logarithmic plot of the regions where the residence times are exponentially distributed with one of both characteristic time scales [$\propto \exp(-t/\langle T_{1,2}\rangle)$]. The fast time scale corresponds to an average residence time $\langle T_1\rangle$ of 10ns, whereas the slow time scale events have an average residence time $\langle T_2\rangle$ of approximately 1μs. An increase in the bias current affects the time scales in different ways: $\langle T_1\rangle$ remains almost constant, whereas $\langle T_2\rangle$ increases with bias current. The appearance of the short time scale is a characteristic feature of SRLs: similar experiments performed in VCSELs [7, 8] or in Dye ring lasers [16] lead to RTDs that are well fitted by a one-parameter Arrhenius distribution. A spectral analysis of the time series reveals a relaxation-oscillation (RO) frequency between 1.0 and 2.0 GHz and therefore rules out ROs as the origin of the non-Arrhenius features of the RTD.
In order to clarify the origin of the two separate time scales, we have directly investigated the recorded time traces. Qualitatively different switches are revealed in these time traces as shown in Figure 4.3(a)-(c). Figure 4.3(a) shows the system leaving the initially lasing CW mode and settling into the CCW mode. Short excursions of the duration of approximately 10ns to the opposite mode have also been observed as shown in Figure 4.3(b). Opposite to the case of Figure 4.3(a), during these short excursions, the system does not settle in the other mode. The durations of such events match the fast time scale $\langle T_1\rangle$ in the RTD. Instead, the second time scale in the RTD is related to long residences in one mode such as depicted in Figure 4.3(a). The long residences are distributed in an exponential way with a mean-residence-time of 1.16μs. We would like to stress here that the RTD is not a simple superposition of independent events such as those in Figure 4.3(a),(b), but that more complex transitions are also present in the system, such as the one depicted in Figure 4.3(c). In the latter, a number of consecutive,

correlated short time excursions are performed before the system settles in the counter-propagating mode.

4.3 Topological interpretation

In order to explain our experimental results, we start again from the classical rate-equation model introduced in Chapter 2, accounting for both saturation and backscattering effects, as given by Eqs. (2.1)-(2.3). Although perfectly adequate to model the SRL's operation, to allow for a clear topological analysis, we will also take advantage of the reduced two-dimensional model (2.31)-(2.32) derived in Chapter 2. The dynamical system (2.31)-(2.32) describes the asymptotic behaviour of the ring laser in the phase space (θ, ψ) on time scales that are slower than the relaxation oscillations. As explained in detail in Chapter 2, $\theta \in [-\pi/2, \pi/2]$ represents the relative modal intensity and $\psi \in [0, 2\pi]$ is the phase difference between the counter-propagating modes.
When the SRL operates in a unidirectional regime, the phase portrait of the system is exemplified in Figure 4.4(d)-(f). Two symmetric stable states CW and CCW at $\psi \approx \pi$, both corresponding to unidirectional operation, are shown. The basins of attractions of the CW and CCW mode are separated by a saddle point S in $(0, \pi)$ which is the unstable out-of-phase bidirectional solution. At a critical value J_{hom} of the current, a homoclinic bifurcation takes place in the system and the stable and unstable manifold of S coincide [17]. When $J > J_{hom}$ the stable manifold spirals around S and the basins of attraction of CW and CCW fold around each-other. Increasing the parameter J continuously unfolds the stable manifold, as shown in Chapter 2.
When noise is present in the system, a rare, large fluctuation may drag the system away from an initial stationary state to the basin of attraction of the opposite mode. It is known from the theory of stochastic transitions in nonlinear systems that in the limit of small noise strength a transition takes place in a ballistic way along a *most probable escape path* (MPEP) which can be calculated by solving an auxiliary Hamiltonian system [18]. As our arguments rely only on the topological features of the system, an exact calculation of the MPEP is not required. In a system such as Eqs. (2.31)-(2.32), it is known that the MPEP connects a stationary state with the saddle S [19]. More specifically, the MPEP approaches S along its stable manifold (for a more detailed discussion on the MPEP, we refer to Section 4.7). Once the saddle is reached, the transition to the opposite equilibrium state is completed by following the unstable manifold of the saddle. However, when the system's parameters are close to the homoclinic bifurcation, the folds of the stable manifold cluster very tightly around each other, and the stable and unstable manifolds of the saddle get very close to each other. Therefore, even

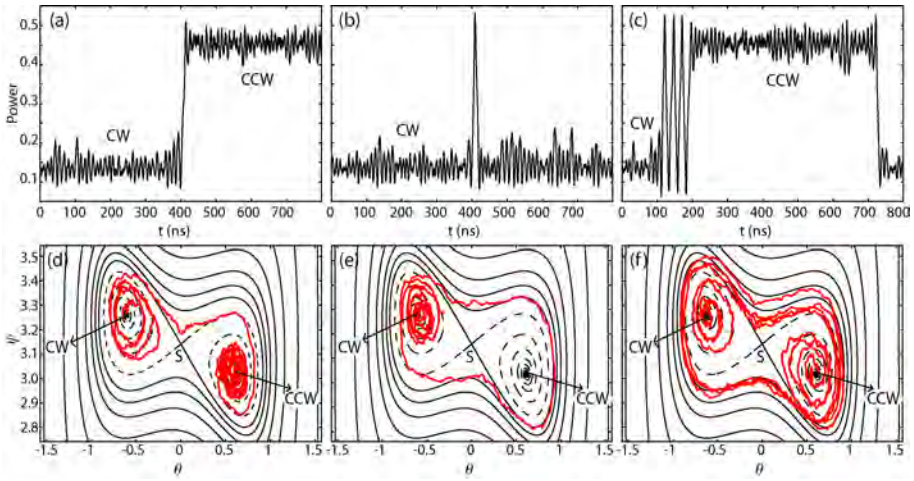

Figure 4.4: Numerical simulation of Eqs. (2.1)-(2.3) showing time series (a)-(c) and phase space trajectories (d)-(f) for different kinds of transitions. The following parameters were used: $\mu = 1.59$, $\alpha = 3.5$, $s = 0.005$, $c = 0.01$ $k = 0.44\text{ns}^{-1}$, $\phi_k = 1.5$, $D' = 6.5 \cdot 10^{-5}$ ns^{-1}. The notation of (d)-(f) is as follow: CW, CCW are the stable states, S is the saddle; solid line: stable manifold of S, dashed line: unstable manifold of S, red: projection of the time series (a)-(c).

at very low noise intensities, the system can diffuse between the folds of the stable manifold or between the stable and the unstable manifold. Such topological considerations can explain the separated time scales $\langle T_{1,2} \rangle$ as well as the features of the transitions shown in Figure 4.3(a)-(c). A noise induced activation is responsible for the slow time scale $\langle T_1 \rangle$, whereas a noise-sustained rotation along the folds of the stable manifold of S produces the short excursion shown in Figure 4.3(b).

In order to confirm our topological arguments, we perform numerical simulations of Eqs. (2.1)-(2.3) using relevant parameters [12][2]. The spontaneous emission noise has been introduced in Eqs. (2.1)-(2.2) phenomenologically as complex uncorrelated zero-mean stochastic terms described by the correlation terms: $\langle \xi_i(t+\tau)\, \xi_j^*(t) \rangle = 2D'N\delta_{ij}\delta(\tau)$ where $i, j = 1, 2$ and D' is the noise intensity. For simplicity, carrier noise has been disregarded.

Three examples of numerically obtained stochastic transitions are reported in

[2] An explanation of the numerical integration schemes that we use can be found in Appendix B.

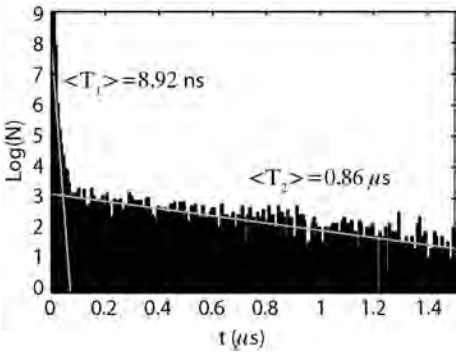

Figure 4.5: RTD obtained by simulating Eqs. (2.1)-(2.3) with the parameters chosen as in Figure 4.4. Best fitting lines are shown in white.

Figure 4.4(a)-(c) and compared with the experimental ones [3]. The same trajectories projected in the $\theta - \psi$ plane are shown in Figure 4.4(d)-(f) together with the invariant manifolds. The trajectory in Figure 4.4(a) shows a simple mode-hop from the CW to the CCW mode as in Figure 4.3(a). In phase space [Figure 4.4(d)] such a trajectory corresponds to a stochastic path originating at the CW state which approaches the saddle and relaxes to the opposite CCW state along the unstable manifold of S. When lasing in the CW mode, a short excursion to the opposite CCW direction is possible and shown in Figure 4.4(b), corresponding to the experimental time trace shown in Figure 4.3(b). In phase space [Figure 4.4(e)] the trajectory rotates around the saddle, but remains inside the basin of attraction of the initial CW mode. In Figure 4.4(c), we show an example of a more complicated transition similar to the experimental trajectory shown in Figure 4.3(c). In phase space [Figure 4.4(f)] the system escapes from the CW state and afterwards rotates three times around S before settling in the opposite CCW state. The simulations shown in Figure 4.4(a)-(c) are in good qualitative agreement with the experiments in Figure 4.3(a)-(c). A direct simulation of the reduced model Eqs. (2.31)-(2.32) leads to similar results. We remark that the described effect takes place in regions of the parameter space $\left(J, \alpha, \phi_k\right)$ which are close to the homoclinic bifurcation. In the unphysical case of $k = 0$ (no backscattering) the manifolds are completely unfolded for every value of ϕ_k and J and the effect disappears.
Finally, we have extracted the RTD from the simulated time series [Figure 4.3(c)]. The simulations show the same non-Arrhenius structure as in the experimental

[3] One should be aware that the RMS for the noise background observed in the experimental time series is dominated by the electrical noise floor of the oscilloscope and the detector.

RTD, and quantitatively reproduce the time scales $\langle T_{1,2} \rangle$ (see Figure 4.5).
In the following two Sections, we will extend the analysis of the problem of fluctuations from bistable regimes of operation to multistable ones in SRLs. Such multistable regions of operation have been predicted in Chapter 2. Here, we will elaborate on the 2D phase space of the multistable SRL and experimentally demonstrate the existence of such multiple stable attractors in the SRL.

4.4 Multistable phase space portraits

Multistability is a general feature of nonlinear systems which attracts attention in a broad set of subjects including hydrodynamics [20], plasma physics [21], biology [22], neural networks [23, 24], chemical reactions [25] and optical systems [26–28]. The phase space of a multistable system is in general very intricate due to the strongly interwoven basins of attractions of the coexisting stable structures, and is often further complicated by the presence of structures such as chaotic saddles [29, 30]. For this reason, the dynamics of a multistable system is characterized by a larger complexity than their bistable counterpart, leading to phenomena such as attractor hopping [30, 31] or chaotic itineracy [24]. While being of broad interdisciplinary interest, multistability is especially interesting in the case of semiconductor lasers, due to their large number of applications and their wealth of dynamical regimes (see [32] and references therein). However, the fast time scales involved, the blurring of the different attractors due to the presence of spontaneous emission of photons, the difficulty to control the internal parameters, the inaccessibility of some dynamical variables, all make the experimental reconstruction of the phase space of semiconductor lasers an extremely challenging task. Therefore, despite the large number of theoretical work [28, 30, 32–35], the dynamical complexity of multistable semiconductor lasers remained experimentally unaddressed.
From the theoretical point of view, we have predicted many dynamical regimes including multistable ones in Chapter 2. These dynamical regimes can be understood in a more general context from the unfolding of a Takens-Bogdanov bifurcation with Z_2-symmetry (see Chapter 2 and Ref. [36]). From the technological point of view, an understanding of the phase space of SRLs in these different dynamical regimes would be highly desirable to improve performance in applications such as all-optical memories [37] and allow for a better control of the device [34, 38]. In this Section, we thus start by investigating the bifurcation diagrams and the corresponding 2D phase space when multiple stable attractors are present. In the following Section, we will then show how we can explore the parameter space in a SRL experimentally and compare the results with the corresponding theoretical phase space portraits.

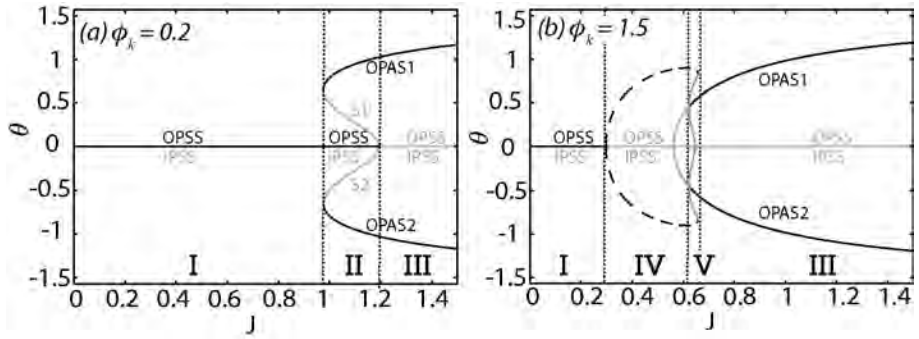

Figure 4.6: Bifurcation diagrams of Eqs. (2.31)-(2.32) for (a) $\phi_k = 0.2$ and (b) $\phi_k = 1.5$ Stable solutions of Eqs. (2.31)-(2.32) are marked in black, unstable ones in grey. Dashed lines are used to indicate periodic solutions. The Roman numbers **I** - **V** indicate different dynamical regimes.

Consider $\phi_k = 0.2$ in the reduced SRL model Eqs. (2.31)-(2.32). The bifurcation diagram for such value of ϕ_k is shown in Figure 4.6(a) while representative examples of its phase space are shown in Figure 4.7. For small values of the bias current, the system operates in the bidirectional regime and the phase space of the system (not shown) consists of a stable state OPSS (out-of-phase symmetric solution) coexisting with an unstable IPSS (in-phase symmetric solution)[4]. This is denoted as Region **I**. An increase of the bias current J leads to the appearance of two more stable states corresponding to unidirectional CW and CCW rotating solutions ($OPAS_{1,2}$ — out-of-phase asymmetric solution). The SRL therefore operates in a tristable regime (Region **II**). The corresponding phase space is shown in Figure 4.7(a). Three stationary states $OPAS_1$, $OPAS_2$ and OPSS coexist. An unstable state IPSS corresponding to bidirectional in-phase lasing and two saddles $S_{1,2}$ are also present in the system. The basins of attraction of the three states are separated by the stable manifolds of S_1 and S_2 in such a way that the basin of attraction of OPSS lies in between the basins of attraction of $OPAS_1$ and $OPAS_2$. When spontaneous emission noise is introduced in the system, spontaneous attractor hopping may appear. In the limit of vanishing noise intensity, the topology of the phase space predicts only transitions between a unidirectional mode and the bidirectional mode. Direct transitions between $OPAS_1$ and $OPAS_2$ are possible only for larger values of the noise intensity. Increasing the value of the bias current J, the saddles $S_{1,2}$ migrate towards OPSS making the basin of attraction of OPSS shrink. Therefore the residence time in the bidirectional lasing mode is expected to decrease and the laser to operate most of its time in

[4]See Chapter 2 for more information on these solutions, their stability and notation.

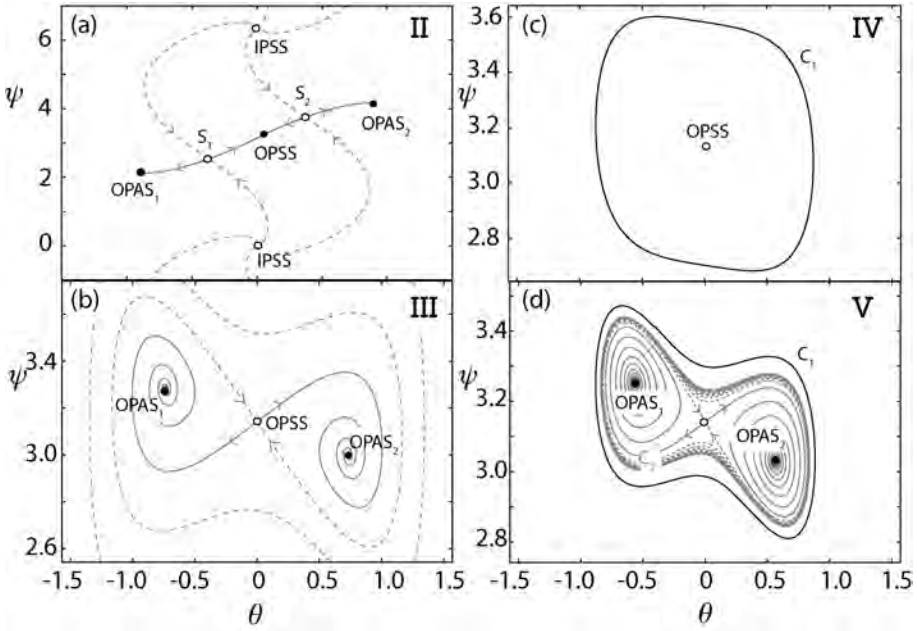

Figure 4.7: Phase space portraits of Eqs. (2.31)-(2.32) for different values of J and ϕ_k. The notation is as defined in the text. (a) $\phi_k = 0.2$, $J = 1.05$, (b) $\phi_k = 1.5$, $J = 0.75$, (c) $\phi_k = 1.5$, $J = 0.5$, (d) $\phi_k = 1.5$, $J = 0.66$.

either one of the unidirectional modes. When the bias current is increased above a critical value, the saddles collide with OPSS and the bidirectional out-of-phase mode become unstable. The SRL is then operating in a bistable regime with two stable unidirectional modes $OPAS_{1,2}$ (Region **III**). The corresponding phase space is shown in Figure 4.7(b). Here $OPAS_1$ and $OPAS_2$ are the unidirectional modes whereas OPSS is a saddle point. The stable manifold of OPSS separates the basins of attraction of $OPAS_1$ and $OPAS_2$. In this regime, noise-induced hopping is expected between the two unidirectional modes, whereas we do not expect to observe any residence in the bidirectional regime. A further increase of the current leads to longer residence times in $OPAS_{1,2}$ but no further bifurcations are expected.

When $\phi_k = 1.5$ the bifurcation curve as shown in Figure 4.6(b) is qualitatively different from the previous case. For small values of the bias current, the system operates in the bidirectional regime, similar to Region **I** for $\phi_k = 0.2$. Increasing the current above a critical value, the bidirectional operation loses its stability and the SRL exhibits periodic oscillations known as alternate oscillations [12]

between CW and CCW modes (Region **IV**). In the phase space [Figure 4.7(c)] the alternate oscillations are a stable limit cycle C_1 which surrounds the unstable bidirectional state OPSS. When the bias current J is increased, two unidirectional solution $OPAS_{1,2}$ appear, and tristability between the latter and C_1 is possible (Region **V**). This scenario corresponds to Figure 4.7(d). The basins of attraction of $U_{1,2}$ are separated by the stable manifold of the saddle OPSS. A second unstable cycle C_2 separates the basin of attraction of C_1 from the basins of attraction of $OPAS_{1,2}$. When noise is present in the system hopping between $OPAS_1$ and $OPAS_2$ as well as hopping between $OPAS_{1,2}$ and the alternate oscillations are possible, allowing the system to burst into periodic oscillations. A further increase of the current leads to the disappearance of C_1 and the SRL operates in a bistable regime between the two unidirectional modes $OPAS_{1,2}$ (Region **III**). The phase space corresponding to this regime is shown in Figure 4.7(b), similar to the case of $\phi_k = 0.2$. Spontaneous emission noise induces hopping between $OPAS_1$ and $OPAS_2$, elaborately discussed in the previous two Sections, but no periodic oscillations can appear.

4.5 Experimental exploration of stochastic mode-hopping in multistable regimes

The experimental set-up (see Figure 4.1) is the same one as used to study the stochastic mode-hopping in the bistable region ($OPAS_1$ and $OPAS_2$) in Section 4.2. We have fixed the waveguide current $I_w = 9.81$mA and as in Section 4.2 we have tuned the voltage on the piezoelectric controller until a symmetric operation of the SRL was achieved. This corresponds to fixing the ϕ_k parameter of the SRL. We now tune the bias current I_p on the ring, in order to reproduce the dynamical regimes predicted by the theory. We choose here to measure with the oscilloscope the emission in the CCW mode. Like before, due to the anti-correlated dynamics of the counter-propagating modes [12], any change in the power in the CCW mode corresponds to an opposite change in the emission in the CW mode. A high (low) amplitude signal on the scope thus corresponds to operation in the CCW (CW) mode, whereas bidirectional operation appears as an intermediate amplitude signal. Examples of time traces of the CCW mode are shown in Figure 4.8 (a)-(f). The ring reaches its lasing threshold at 34mA[5]. For current values close to threshold, bidirectional lasing is observed (not shown).

[5]One can notice that the lasing threshold here is different than in the experiments discussed in Section 4.2. The reason for this is that we now measure a different ring on the same chip containing six SRLs. All these SRLs show qualitatively the same behavior, but have slightly different lasing thresholds.

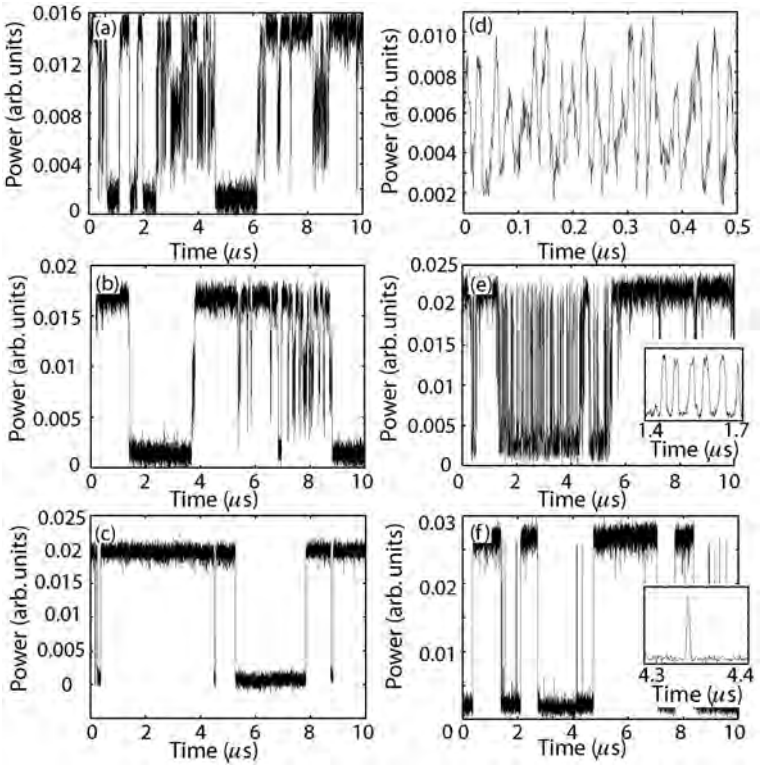

Figure 4.8: Experimentally measured time series for different bias currents I_p and I_w corresponding to the dynamical regimes of Figure 4.7. (a) I_w = 9.81mA, I_p = 44.35mA; (b) I_w = 9.81mA, I_p = 45.21mA; (c) I_w = 9.81mA, I_p = 46.39mA; (d) I_w = 12.0mA, I_p = 40.23mA; (e) I_w = 12.0mA, I_p = 44.34mA; (f) I_w = 12.0mA, I_p = 45.94mA. The insets show a zoom on relevant segments of the time series.

When increasing the current above a critical value $I_p \sim 44$mA, hopping between the bidirectional regime and the two unidirectional modes appears. Segments of time traces for I_p = 44.35mA and I_p = 45.21mA are shown in Figure 4.8(a)-(b). The average residence time in the CW and CCW state increases with the pump current, while the residence time in the bidirectional mode decreases. Tristability between bidirectional and unidirectional modes is observed. In agreement with the phase space picture in Figure 4.6(a), hopping events preferentially occur between the bidirectional and one of the unidirectional modes. A detail of a sequential transition from the CW mode to bidirectional operation, to the

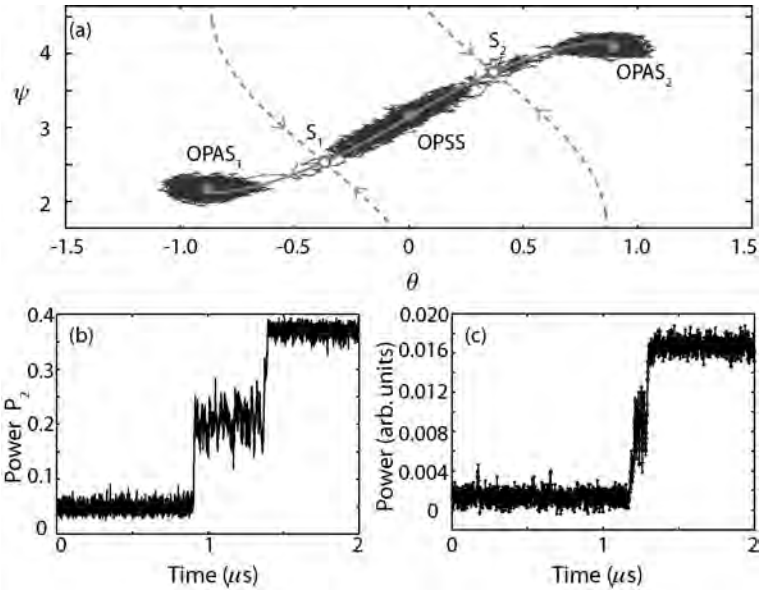

Figure 4.9: Simulations vs. experiments for a sequential transition $OPAS_1 \rightarrow OPSS \rightarrow OPAS_2$ for the phase space described in Figure 4.7(b). (a) projection on the phase space; (b) numerical time series; (c) experimental data. The model parameters for (a)-(b) are $J = 1.05$, $\phi_k = 1.02$, $\alpha = 3.5$. The experimental conditions for (c) were $I_p = 45.31$mA and $I_w = 9.81$mA.

CCW mode for $I_p = 45.21$mA is shown in Figure 4.9(c). The agreement with the numerical simulations of Eqs. (2.31)-(2.32) as shown in Figure 4.9(a)-(b) is clear. The simulated hopping trajectory is projected in the phase space (θ, ψ) in Figure 4.9(a). In the limit of vanishing noise intensity, the topology of the phase space Figure 4.9(a) predicts only transitions between a unidirectional mode and the bidirectional mode. The observation of some direct transitions between unidirectional modes suggests that the noise-induced diffusion length is not negligible when compared to the size of the basin of attraction of the bidirectional mode. When the pump current is increased to $I_p = 46.39$mA as shown in Figure 4.8(c), no bidirectional operation is observed, and direct transitions between CW and CCW modes are possible as predicted by the phase space portrait in Figure 4.7(b). Further increase in the bias current corresponds to an increase in the average residence time in the two unidirectional modes. As such the whole bifurcation sequence as in Figure 4.6(a) has been experimentally reconstructed.
We then fix the waveguide current to $I_w = 12.0$mA and we adjust the voltage on the piezoelectric controller until the symmetry in the system is restored. Once

again we tune the pump current I_p on the ring and we investigate the different dynamical regimes. Typical time traces for the CCW mode are shown in Figure 4.8(d)-(f). Close to threshold the laser operates in the bidirectional regime, for slightly higher values of the bias current, alternate oscillations appear as reported in Figure 4.8(d) for I_p = 40.23mA. This operating regime reveals the phase space portrait shown in Figure 4.7(c). When increasing the bias current, the amplitude of the alternate oscillations increases until the SRL becomes multistable and the alternate oscillations coexist with the two unidirectional modes as shown in Figure 4.8(e) for a bias current I_p = 44.35mA. The inset in Figure 4.8(e) is a zoom on a burst that reveals the periodical oscillations. This operating regime corresponds to the phase space portrait shown in Figure 4.7(d). In this regime both transitions between the unidirectional modes and between the unidirectional modes and the limit cycle are observed, as allowed by the topology of the phase space in Figure 4.7(d). When the current is further increased, the bursts of oscillations disappear and bistability between CW and CCW modes is achieved as shown in Figure 4.8(f) for I_p = 45.94mA. Such regime corresponds to the phase space pictured in Figure4.7(b). Short excursions from CW to CCW operation and vice versa are observed in the time traces when the laser operates in this regime [see inset in Figure 4.8(f)]. They have been previously observed [1] and explained as noise induced diffusion between the folds of the stable manifolds of the saddle point OPSS in Figure 4.7(b). The presence of such excursions in the time trace of Figure 4.8(f) represents a further confirmation of the phase space structure described in Figure 4.7(b).

4.6 Asymptotic analysis of the Fokker-Planck Equation

In the previous Sections, we have studied, both theoretically and experimentally, stochastic transitions between different attractors in the bistable and multistable regimes of operation of the SRL. In the bistable regime, discussed in Sections 4.2-4.3, we have investigated two different kinds of transitions using topological arguments [1]. In particular, the first kind of transitions are the result of a noise-induced activation process, whereas the short excursions are a consequence of the particular shape of the stable manifold of the saddle point in the system in combination with a noise-induced diffusion in the phase space. In this Section and the remainder of this Chapter, we aim to address the first kind of mode-hopping, by formulating it in the form of an activation in a non-equilibrium bistable system.

A non-equilibrium system is a physical system that does not satisfy the detailed balance condition, such that they are far less symmetrical than systems that do satisfy the detailed balance condition. In particular, the forward/backward transitions have different probabilities and the fluctuation - dissipation theorem[6] relating the intensity of noise fluctuations with the damping of energy due to dissipation does not hold anymore [39]. Due to this lack of symmetry, out-of-equilibrium systems are intrinsically more complicated than equilibrium ones. The most promising results in the investigation of non-equilibrium stochastic systems have been achieved in the limit of zero noise intensity. When considering the Langevin equation for a general nonlinear stochastic system

$$\dot{x} = K(x,t) + \sigma(x,t)\xi(t), \tag{4.1}$$

with $K(x,t)$ describing the deterministic dynamics of the system and $\xi(t)$ representing the stochastic process[7], its probability $\rho(x,t)$ has been shown to satisfy the Fokker-Planck Equation (FPE) [40]

$$\frac{\partial \rho(x,t)}{\partial t} + \frac{\partial}{\partial x}(K(x,t)\rho(x,t)) - D\frac{\partial^2}{\partial x^2}(Q(x,t)\rho(x,t)) = 0, \tag{4.2}$$

where the matrix $Q(x,t) = \sigma(x,t)\sigma^T(x,t)$ is known as the diffusion matrix.
It is known from the theory of stochastic systems [41] that activation problems can be characterized by the mean-first-passage-time $\langle \tau_{FPT} \rangle$ across the boundary of the basin of attraction of the initial state. In other words $\langle \tau_{FPT} \rangle$ gives the average time it takes to escape from the basin of attraction of one mode, such that the system can hop to the other mode. The mean-first-passage time can be expressed to logarithmic accuracy by a generalized non-equilibrium potential [8, 42–45]

$$\langle \tau_{FPT} \rangle \propto e^{S/D} \tag{4.3}$$

where S is the non-equilibrium potential and D is the intensity of the stochastic force that drives the fluctuations. It is important to understand the dependence of the quasi-potential S on the parameters of the system (2.1)-(2.3). However, Eqs. (2.1)-(2.3) are too complicated for an analytical or quasi-analytical approach. Nevertheless, one cannot introduce any *ad-hoc* model such as a double-well potential, as this would introduce phenomenological model-parameters which are

[6] In statistical physics, the fluctuation-dissipation theorem is a powerful tool for predicting the non-equilibrium behavior of a system — such as the irreversible dissipation of energy into heat — from its reversible fluctuations in thermal equilibrium. The fluctuation dissipation theorem relies on the assumption that the response of a system in thermodynamic equilibrium to a small applied force is the same as its response to a spontaneous fluctuation. Therefore, there is a direct relation between the fluctuation properties of the thermodynamic system and its linear response properties. Often the linear response takes the form of one or more exponential decays.

[7] The function $\sigma(x,t)$ can introduce a dependence of the noise properties on the position or on the time.

not related to the physically relevant quantities such as k, ϕ_k or α.
However, from the observation that the escape events are rare when compared to the other time scales of the system, and the quasi-conservation of the total power during the hopping, we propose that the hopping problem can be successfully described in the framework of the asymptotically reduced model given by Eqs. (2.31)-(2.32). The slow timescale dynamics is then described by the time evolution of two auxiliary angular variables:

$$\begin{aligned} \theta' &= K_\theta(\theta,\psi) + \xi_\theta \\ &= -2\sin\phi_k \sin\psi + 2\cos\phi_k \cos\psi \sin\theta \\ &\quad + J\sin\theta\cos\theta + \xi_\theta, \qquad (4.4) \\ \psi' &= K_\psi(\theta,\psi) + \xi_\psi \\ &= \alpha J \sin\theta + 2\cos\phi_k \frac{\sin\psi}{\cos\theta} \\ &\quad + 2\sin\phi_k \cos\psi \tan\theta + \xi_\psi. \qquad (4.5) \end{aligned}$$

We make here the assumption of uncorrelated white Gaussian noise terms $\xi_{\theta,\psi}$ for the angular variables too. This assumption is a priori not justified, as multiplicative terms and cross-correlations are expected to appear in the noise. However, the agreement with the results of the full model (see below) and the benefits in simplicity will justify this assumption.
In order to investigate the stochastic properties of the reduced SRL model (4.4)-(4.5), we study the FPE [Eq. (4.2)] for the probability density $\rho(\theta,\psi)$. The FPE is written as follows:

$$\frac{\partial\rho}{\partial t} = -\frac{\partial}{\partial\theta}K_\theta\rho - \frac{\partial}{\partial\psi}K_\psi\rho + D\frac{\partial^2}{\partial\theta^2}\rho + D\frac{\partial^2}{\partial\psi^2}\rho \qquad (4.6)$$

where D is the noise intensity for the reduced system which is the small parameter in our theory[8]. The value of D is the only quantity that requires a fitting in our analysis.
In the limit of vanishing noise intensity $D \to 0$, an asymptotic Wentzel-Kramers-Brillouin (WKB) expansion[9] can be performed for the probability density ρ [18].

[8] We would like to mention that realistically the strength of the diffusion terms in Eq. (4.6) with respect to the θ variable and the ψ variable are not equal. In fact our numerical simulations of the rate-equation model (2.1)-(2.3) with white noise has shown us that the noise diffusion term is larger with respect to the ψ variable. Including this difference in diffusion strength in the presented derivation would lead to p_θ and p_ψ having a different strength as well. The qualitative results remain similar though.

[9] The WKB approximation is a widely used example of a semiclassical calculation in quantum mechanics in which the wavefunction is recast as an exponential function, semiclassically expanded, and then either the amplitude or the phase is taken to be slowly changing. WKB theory is a method for approximating the solution of a differential equation whose highest derivative is multiplied by a small parameter.

We stress here that we consider two separate asymptotic limits in our approach. The first limit (discussed above) is related to time-scales separation and depends on the laser parameters. In what follows, we introduce a second asymptotic limit that depends on the noise intensity and not on the laser parameters.
We consider the following ansatz for ρ:

$$\rho = Ze^{-\frac{S}{D}}, \tag{4.7}$$

with $D \to 0$ and S an auxiliary function. S is the analogue of a potential in a gradient system and is referred to as a *quasi-potential* in non-equilibrium systems such as Eqs. (4.4)-(4.5). It is known from the theory of stochastic systems that, at the leading order $1/D$, the quasi-potential S satisfies a Hamilton-Jacobi equation for a classical action [15, 46]:

$$\frac{\partial S}{\partial t} = -H\left(\theta, \psi, \frac{\partial S}{\partial \theta}, \frac{\partial S}{\partial \psi}\right) \tag{4.8}$$

with the Hamiltonian $H\left(\theta, \psi, \frac{\partial S}{\partial \theta}, \frac{\partial S}{\partial \psi}\right)$ defined as:

$$H = \frac{1}{2}\left(\frac{\partial S}{\partial \psi}\right)^2 + \frac{1}{2}\left(\frac{\partial S}{\partial \theta}\right)^2 + \frac{\partial S}{\partial \theta}K_\theta + \frac{\partial S}{\partial \psi}K_\psi. \tag{4.9}$$

In what follows, we will refer to the function S indifferently as action or nonequilibrium potential. The analogy with the case of a classical Hamiltonian problem is completed by defining the auxiliary momenta:

$$p_\theta = \frac{\partial S}{\partial \theta} \quad p_\psi = \frac{\partial S}{\partial \psi}, \tag{4.10}$$

leading to the Hamiltonian

$$H\left(p_\theta, p_\psi, \theta, \psi\right) = \frac{p_\theta^2}{2} + \frac{p_\psi^2}{2} + K_\theta p_\theta + K_\psi p_\psi. \tag{4.11}$$

With this approach, the initial stochastic system (4.4)-(4.5) can be mapped into a deterministic Hamiltonian system

$$\dot{\theta} = \frac{\partial H}{\partial p_\theta} = K_\theta + p_\theta \tag{4.12}$$

$$\dot{\psi} = \frac{\partial H}{\partial p_\psi} = K_\psi + p_\psi \tag{4.13}$$

$$\dot{p}_\theta = -\frac{\partial H}{\partial \theta} = -\frac{\partial K_\theta}{\partial \theta}p_\theta - \frac{\partial K_\psi}{\partial \theta}p_\psi \tag{4.14}$$

$$\dot{p}_\psi = -\frac{\partial H}{\partial \psi} = -\frac{\partial K_\theta}{\partial \psi}p_\theta - \frac{\partial K_\psi}{\partial \psi}p_\psi \tag{4.15}$$

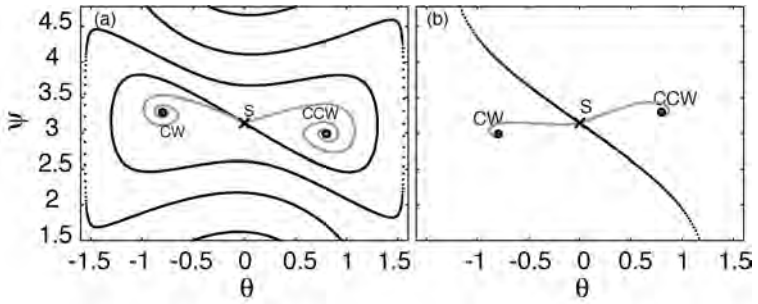

Figure 4.10: MPEP paths from the CW mode to the CCW mode are shown by the grey lines for different values of the backscattering phase: (a) ϕ_k = 1.5; (b) ϕ_k = 1.08. The other parameters are J = 0.734 and α = 3.5. The black lines represent the stable manifold of the saddle S.

The action S evolves along the solutions of (4.12)-(4.15) following the equation[10]

$$\frac{dS}{dt} = \frac{1}{2}p_\psi^2 + \frac{1}{2}p_\theta^2 \tag{4.16}$$

The action S calculated along a certain trajectory can be interpreted as a "cost" for such transition to take place, and ultimately its probability. Consider a transition between an initial point x_i and a final point x_f. A large action indicates a trajectory with low probability whereas a smaller action indicates a more likely trajectory. In the limit of vanishing noise intensity $D \to 0$, the transitions corresponding to the minimum actions become exponentially more likely than any other transition path, and only trajectories with minimum actions become relevant in the calculation of the probability distribution. In other words, only those trajectories corresponding to a global minimum can be observed in a physical experiment in the zero noise-intensity limit [47–49].

4.7 Optimal escape paths

In the previous Section, we reviewed the general theory for stochastic fluctuations in the limit of vanishing noise intensity. In this Section, we formulate the problem for the mode-hopping in SRLs and we discuss the general topological features of the escape trajectories that realize the hopping.
During the regular operation of SRL, the system spends the majority of its time

[10] $\frac{dS}{dt}$ is defined as $\frac{\partial S}{\partial t} + \frac{\partial S}{\partial \theta}\frac{\partial \theta}{\partial t} + \frac{\partial S}{\partial \psi}\frac{\partial \psi}{\partial t}$.

in the close vicinity of one of the stationary states. In order for a mode-hop to take place, the spontaneous emission noise must drag the system outside the basin of attraction of the original state (for instance CW) to the basin of attraction of the counter-propagating mode (for instance CCW). As the basins of attraction of the CW and CCW modes are separated by the stable manifold of the saddle S [see Figure 4.5(d)-(f)], the mode-hop is realized by a trajectory solution of Eqs. (4.12)-(4.15) that connects the stationary state CW with the stable manifold of the saddle.
In general there are infinitely many solutions of Eqs. (4.12)-(4.15) that emanate from the initial state and reach the basin boundary. According to the discussion in Sec. 4.6, in the limit of small noise intensity $D \to 0$, the escape takes place with overwhelming probability along the trajectory that minimizes the action S. This minimum of the action S is called the activation energy and the associated escape path is known in the literature as the *most probable escape path* (MPEP) [15, 19, 48, 50–52].
As the motion along the stable manifold of S is deterministic, and deterministic motion does not increase the action, the minimal action along the stable manifold of the saddle coincides with the saddle itself [15, 19, 48, 50, 51]. Therefore, the MPEP satisfies the following boundary conditions: it emanates from the initial state CW (CCW) at time $t \to -\infty$ and converges to the saddle S at time $t \to \infty$. The transition to the opposite mode is completed deterministically by following the unstable manifold of S.
We have calculated the MPEP for a SRL by minimization of the action functional (4.16) along the solutions of Eqs. (4.12)-(4.15) for different values of the system parameters. Some examples of MPEPs are shown in Figure 4.10 for transitions from the CW state to the CCW state. As expected according to the previous discussion, the MPEP connects the CW state to the saddle S and a deterministic relaxation completes the mode hop to the CCW mode. It is clear from Figure 4.10, that the backscattering phase ϕ_k plays a major role in determining the actual shape of the MPEP. In the next sections, we will discuss the role of ϕ_k and the other parameters of the system in the mode hopping.

4.8 Dependence of the activation energy on the parameters of the system

In order to validate our analysis and to provide insight in the dependence of the mode hopping versus the parameters of the system, we calculate the activation energy for different values of the current and the backscattering phase using both numerical simulation and Hamiltonian theory.

4.8. DEPENDENCE OF THE ACTIVATION ENERGY ON THE PARAMETERS OF THE SYSTEM

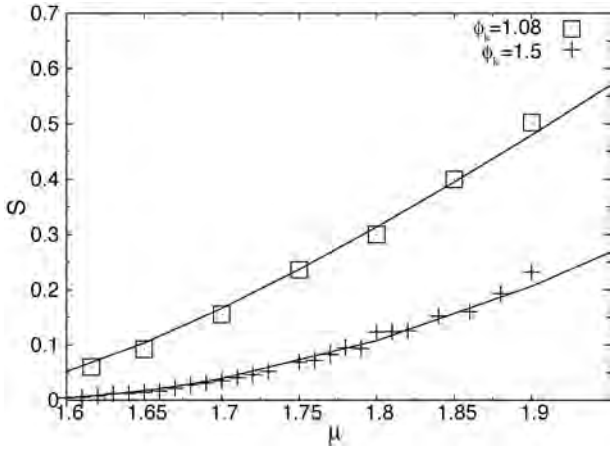

Figure 4.11: Activation energy as a function of the current μ for different values of the backscattering phase. Markers are used to indicate the results of the integration of the full rate equation model (2.1)-(2.3), whereas the solid lines represent the solution of the auxiliary Hamiltonian system (4.12)-(4.15).

The full set of rate equations Eqs. (2.1)-(2.3) is solved using a numerical simulations [53] for different values of the noise intensity D'. The activation energy is calculated by fitting the mean-first-passage-time versus $1/D'$. The dependence of the activation energy versus current μ and phase ϕ_k is shown in Figure 4.11 by markers.

The theoretical activation energy is calculated by solving the boundary value problem associated with Eqs. (4.12)-(4.15) and by minimization of the function S [48]. The parameters are the same as in Eqs. (2.1)-(2.3), excluding the noise intensity D which is fitted. The results of this calculation are shown in Figure 4.11 with lines. The agreement between theoretical and numerical values of the activation energy is good.

In Figure 4.12(a), we show the dependence of the activation energy calculated by solving the boundary value problem as a function of the backscattering phase ϕ_k for different values of the bias current μ. We observe that the activation energy increases with μ, in accordance with the results of Figure 4.11 and the intuitive argument that increasing the bias current stabilizes the laser operation. However, the dependence of S on the backscattering phase is nonmonotonic, indicating that the stability of the directional modes versus random fluctuations decreases exponentially from a maximum at $\phi_k^{max} \approx 0.85$. The loss of stability of the directional modes can be understood by considering the bifurcation scenario

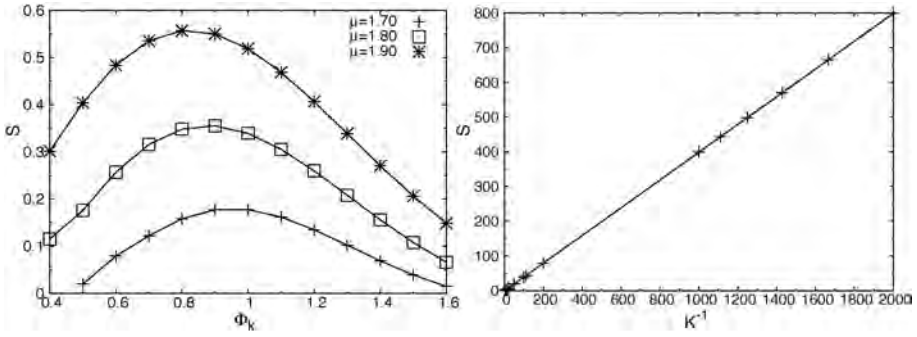

Figure 4.12: (a) Activation energy S as a function of (a) the phase of the backscattering ϕ_k for different values of the bias current μ. (b) Activation energy S as a function of the inverse backscattering $1/K$ obtained as a solution of Eqs. (4.12)-(4.15). The current is set at $\mu = 1.8$ and the phase at $\phi_k = 1.3$.

of a SRL as presented in Chapter 2 [17]. For the physically relevant parameters considered in Figure 4.12(a), stable unidirectional lasing is possible between a pitchfork bifurcation taking place at $\phi_k \approx 0.2$ and a subcritical Hopf bifurcation taking place at $\phi_k \approx 1.6$ (see Figure 2.2). Therefore, in this limit, the decreasing of S for $\phi_k < \phi_k^{max}$ corresponds to a loss of stability of the system when approaching the pitchfork bifurcation line, whereas the decreasing of S for $\phi_k > \phi_k^{max}$ is consistent with a loss of stability of the directional modes when approaching the subcritical Hopf bifurcation.

The asymptotic limit $J \to \infty$ can be treated analytically, which corresponds to either $\mu \to \infty$ or $K \to 0$. In this limit, we can neglect the terms depending on the backscattering phase ϕ_k in Eqs. (4.4)-(4.5) and obtain:

$$\theta' = +J \sin\theta \cos\theta \tag{4.17}$$

$$\cos\theta\psi' = \alpha J \sin\theta \cos\theta \tag{4.18}$$

Therefore, the dynamics of the variable θ is decoupled from the variable ψ which becomes a follower of θ. The activation energy S can be calculated by noticing that $\theta' = -\nabla U$ with $U = J\cos(2\theta)/4$. Therefore $S = J/4$. In this limit, the action is linearly dependent on J and inversely proportional to $|K|$. In Figure 4.12(b) the dependence of the activation energy versus the inverse of the backscattering magnitude for $\mu = 1.8$ and $\phi_k = 1.3$ is shown as the solution of Eqs. (4.12)-(4.15). The linearity is evident.

Finally, we investigate the effect of a change in the linewidth enhancement factor in the laser medium. In Figure 4.13(a), the activation energy is calculated

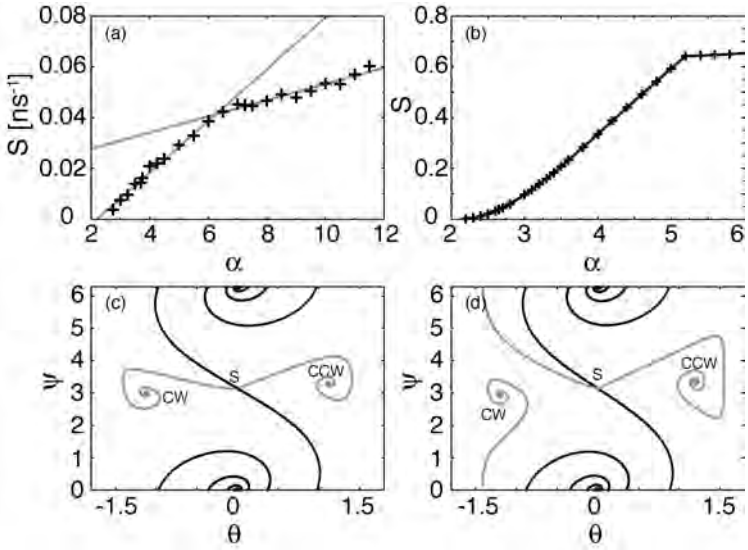

Figure 4.13: Activation energy S as a function of the linewidth enhancement factor α when calculated (a) by fitting the mean-first-passage-times obtained from numerical simulations of Eqs. (2.1)-(2.3) and (b) from the Hamiltonian formalism. Both approaches reveal the "knee". The current is set at $\mu = 1.8$, the backscattering amplitude to $k = 0.44$ and the phase at $\phi_k = 1.2$. (bottom) Qualitatively different MPEP for $\alpha = 5$ (c) and $\alpha = 6$ (d) as calculated with the Hamiltonian system (4.12)-(4.15).

numerically using the full rate equation model Eqs. (2.1)-(2.3). A monotonic increase of the activation energy with α is evident. An unexpected feature of the dependence of S versus α is the abrupt change in the gradient of S. Such a change in scaling can be interpreted by investigating the topology of the MPEP in the reduced model. A typical dependence of S on α calculated using the Hamilton's Equations (4.12)-(4.15) is exemplified in Figure 4.13(b). The same change in scaling as in Figure 4.13(a) is observed. Moreover, this can be explained by studying the different topology of the MPEP for parameters corresponding to the different branches of the $S - \alpha$ curve.

For values of α lower than a critical value α_c, the MPEP connects the initial stationary state CW with the saddle directly [Figure 4.13(c)], whereas, for $\alpha > \alpha_c$ the MPEP surrounds the unstable in-phase bidirectional mode [Figure 4.13(d)]. At the critical value α_c, the MPEP is degenerate and two qualitatively different trajectories reach the saddle with the same probability. We would like to remark

here that simpler double-well models, such as e.g. used for VCSELs [8], cannot predict such a change in the gradient of the activation energy.

4.9 Conclusion

In conclusion, we have investigated the stochastic mode hopping in semiconductor ring lasers, both theoretically and experimentally. A control scheme based on the reflection of power from the cleaved facet of an optical fiber and the active bias of the bus waveguide has been devised in order to control the (otherwise inaccessible) coupling parameter ϕ_k. In this way, we could explore the dynamics of the SRL over the whole parameter space $J - \phi_k$, including previously undisclosed regimes.
In the bistable regime, we have shown that the residence time distribution for the mode hopping in semiconductor ring lasers is non-Arrhenius and cannot be described by a single transition rate. Two separate time scales are observed in the residence time distribution, which can be understood in the framework of the reduced two-dimensional model derived in Chapter 2.
Whereas alternate oscillations, bidirectional and unidirectional operation have previously been reported in semiconductor ring lasers [12], we have observed experimentally the coexistence between alternate oscillations and unidirectional operation, and more generally the coexistence of a limit cycle and two stable nodes in a semiconductor laser system. Moreover, coexistence of three stable nodes has been demonstrated. The experimentally revealed dynamical regimes thus match the phase space topologies of the reduced two-dimensional model.
The stochastic planar system (4.4)-(4.5), was subsequently mapped into a four-dimensional Hamiltonian system (4.12)-(4.15) and the optimal escape paths could be calculated. As expected from the general theory of escape in nonlinear systems [47, 48, 52], the most probable escape path connects the initial stationary lasing operation with a saddle in the phase space. The results of the reduced model were confirmed by the numerical simulations of the full rate equation model (2.1)-(2.3).
In contrast to the adoption of a phenomenological bistable system such as a double-well potential, the use of the asymptotic reduction Eqs. (4.4)-(4.5) does not require the introduction of phenomenological parameters to be matched with Eqs. (2.1)-(2.3). In this way we have investigated the dependence of the activation energy on the principal parameters as shown in Figs. 4.11 – 4.13. In particular, our asymptotic method allowed us to understand the change in scaling of the dependence of S on α which cannot be explained with other phenomenological models such as a double-well potential.
Our approach can be straightforwardly extended to analyze the problem of fluc-

tuations in other bistable optical systems [5–9] or in the multistable regimes of operation of semiconductor ring lasers, presented in Section 4.4 [3]. The analysis and experimental results presented are general and apply to any kind of semiconductor laser with a circular geometry, such as e.g. micro-ring lasers and micro-disk lasers.
In the next two Chapters, we will study the nonlinear dynamical behavior of semiconductor ring lasers when their Z_2-symmetry is broken. We will demonstrate how the bifurcation scenario is qualitatively altered with respect to the Z_2-symmetric case and demonstrate that the ring laser can become excitable. This excitability is further analyzed, both theoretically as experimentally.

References

[1] S. Beri, L. Gelens, M. Mestre, G. Van der Sande, G. Verschaffelt, A. Scirè, G. Mezosi, M. Sorel, and J. Danckaert, "Topological insight into the non-Arrhenius mode-hopping of semiconductor ring lasers," *Phys. Rev. Lett.* **101**, 093903, 2008.

[2] S. Beri, L. Gelens, G. Van der Sande, and J. Danckaert, "An asymptotic approach to the analysis of mode-hopping in semiconductor ring lasers," *Phys. Rev. A* **80**, 013823, 2009.

[3] L. Gelens, S. Beri, G. Van der Sande, G. Mezosi, M. Sorel, J. Danckaert, and G.Verschaffelt, "Exploring multistability in semiconductor ring lasers: Theory and experiment," *Phys. Rev. Lett.* **102**, 193904, 2009.

[4] R. Loudon, *The Quantum Theory of Light*, Oxford University Press, Oxford, 2000.

[5] M. Ohtsu, Y. Teramachi, Y. Otsuka, and A. Osaki, "Dynamics of a two-mode semiconductor laser," *IEEE J. Quantum Electron.* **2239**, 535, 1986.

[6] G. Giacomelli and F. Marin, "Statistics of polarization competition in VCSELs," *Quantum Semiclass. Opt.* **10**, 469, 1998.

[7] M. B. Willemsen, M. P. van Exter, and J. P. Woerdman, "Anatomy of a polarization switch of a vertical-cavity semiconductor laser," *Phys. Rev. Lett.* **84**, 4337, 2000.

[8] B. Nagler, M. Peeters, J. Albert, G. Verschaffelt, K. Panajotov, H. Thienpont, I. Veretennicoff, J. Danckaert, G. G. S. Barbay, , and F. Marin, "Polarization-mode hopping in single-mode vertical-cavity surface-emitting lasers: Theory and experiment," *Phys. Rev. A* **68**, 013813, 2003.

[9] G. Giacomelli, M. Giudici, S. Balle, and J. R. Tredicce, "Experimental evidence of coherence resonance in an optical system," *Phys. Rev. Lett.* **84**, 3298, 2000.

[10] A. Fioretti, L. Guidoni, R. Mannella, and E. Arimondo, "Stochastic resonance in a laser with saturable absorber," *J. Stat. Phys.* **70**, 403–412, 1993.

[11] B. McNamara, K. Wiesenfeld, and R. Roy, "Observation of stochastic resonance in a ring laser," *Phys. Rev. Lett.* **60**, 2626, 1988.

[12] M. Sorel, J. P. R. Laybourn, A. Sciré, S. Balle, G. Giuliani, R. Miglierina, and S. Donati, "Alternate oscillations in semiconductor ring lasers," *Opt. Lett.* **27**, 1992–1994, 2002.

[13] H. Zeghlache, P. Mandel, N. B. Abraham, L. M. Hoffer, G. L. Lippi, and T. Mello, "Bidirectional ring laser - stability analysis and time-dependent solutions," *Phys. Rev. A* **37**, 470, 1988.

[14] G. Van der Sande, L. Gelens, P. Tassin, A. Sciré, and J. Danckaert, "Two-dimensional phase-space analysis and bifurcation study of the dynamical behaviour of a semiconductor ring laser," *J.Phys.B* **41**, 095402, 2008.

[15] D. Ludwig, "Persistence of dynamical systems under random perturbations," *SIAM Rev.* **17**, 605–640, 1975.

[16] P. Lett and L. Mandel, "Investigation of time-dependent correlation-properties of the bidirectional dye ring laser," *J. Opt. Soc. Am. B* **2**, 1615, 1985.

[17] L. Gelens, G. Van der Sande, S. Beri, and J. Danckaert, "Phase-space approach to directional switching in semiconductor ring lasers," *Phys. Rev. E* **79**, 016213, 2009.

[18] M. I. Dykman, P. V. E. McClintock, V. N. Smelyanski, N. D. Stein, and N. G. Stocks, "Optimal paths and the prehistory problem for large fluctuations in noise-driven systems," *Phys. Rev. Lett.* **68**, 2718–2721, 1992.

[19] A. N. Silchenko, S. Beri, D. G. Luchinsky, and P. V. E. McClintock, "Fluctuational transitions through a fractal basin boundary," *Phys. Rev. Lett.* **91**, 174104, 2003.

[20] F. Ravelet, L. Marié, A. Chiffaudel, and F. Daviaud, "Multistability and memory effect in a highly turbulent flow: Experimental evidence for a global bifurcation," *Phys. Rev. Lett.* **93**, 164501, 2004.

[21] E. L. Rempel, W. M. Santana, and A. Chian, "Alfvén multistability: Transient and intermittent dynamics induced by noise," *Phys. Plasmas* **13**, 032308, 2006.

[22] E. M. Ozbudak, M. Thattai, H. Lim, B. Shraiman, and A. van Oudenaarden, "Multistability in the lactose utilization network of Escherichia coli," *Nature* **427**, 737–740, 2004.

[23] F. Foss, A. Longtin, B. Mensour, and J. Milton, "Multistability and delayed recurrent loops," *Phys. Rev. Lett.* **76**, 708–711, 1996.

[24] M. Timme, F. Wolf, and T. Geisel, "Coexistence of regular and irregular dynamics in complex networks of pulse-coupled oscillators," *Phys. Rev. Lett.* **89**, 258701, 2002.

[25] K. Chie, N. Okazaki, Y. Tanimoto, and I. Hanazaki, "Tristability in the bromate-sulfite-hydrogencarbonate pH oscillator," *Chem. Phys. Lett.* **334**, 55–60, 2001.

[26] F. T. Arecchi, R. Meucci, G. Puccioni, and J. Tredicce, "Experimental evidence of subharmonic bifurcations, multistability, and turbulence in a Q-switched gas laser," *Phys. Rev. Lett.* **49**, 1217–1220, 1982.

[27] G.-Q. Xia, S.-C. Chan, and J.-M. Liu, "Multistability in a semiconductor laser with optoelectronic feedback," *Opt. Express* **15**, 572–576, 2007.

[28] G. S. Agarwal, "Existence of multistability in systems with complex order parameters," *Phys. Rev. A* **26**, 888–891, 1982.

[29] M. D. Shrimali, A. Prasad, R. Ramaswamy, and U. Feudel, "The nature of attractor basins in multistable systems," *Int. J. of Bifurcation and Chaos (IJBC)* **18**, 1675–1688, 2008.

[30] S. Kraut and U. Feudel, "Multistability, noise, and attractor hopping: The crucial role of chaotic saddles," *Phys. Rev. E* **66**, 015207(R), 2002.

[31] G. Huerta-Cuellar, A. N. Pisarchik, and Y. O. Barmenkov, "Experimental characterization of hopping dynamics in a multistable fiber laser," *Phys. Rev. E* **78**, 035202(R), 2008.

[32] S. Wieczorek, B. Krauskopf, and D. Lenstra, "A unifying view of bifurcations in a semiconductor laser subject to optical injection," *Opt. Communications* **172**, 279–295, 1999.

[33] I. A. Khovanov, N. Khovanova, E. Grigorieva, D. Luchinsky, and P. McClintock, "Dynamical control: Comparison of map and continuous-flow approaches," *Phys. Rev. Lett.* **96**, 083903, 2006.

[34] I. A. Khovanov, D. Luchinsky, R. Mannella, and P. McClintock, "Fluctuations and the energy-optimal control of chaos," *Phys. Rev. Lett.* **85**, 2100–2103, 2000.

[35] A. De Rossi, C. Conti, and S. Trillo, "Stability, multistability, and wobbling of optical gap solitons," *Phys. Rev. Lett.* **81**, 85–88, 1998.

[36] E. Knobloch and M. R. E. Proctor, "Non-linear periodic convection in double-diffusive system," *J. Fluid. Mech.* **108**, 291–316, 1981.

[37] M. T. Hill, H. J. S. Dorren, T. de Vries, X. J. M. Leijtens, J. H. den Besten, B. Smalbrugge, Y. S. Oei, H. Binsma, G. D. Khoe, and M. K. Smit, "A fast low-power optical memory based on coupled micro-ring lasers," *Nature* **432**, 206–209, 2004.

[38] G. Lippi, S. Barland, N. Dokhane, F. Monsieur, P. Porta, H. Grassi, and L. Hoffer, "Phase space techniques for steering laser transients," *J. Opt. B: Quantum Semiclass. Opt.* **2**, 375–381, 2000.

[39] D. Luchinsky and P. V. E. McClintock, "Irreversibility of classical fluctuations studied in analogue electrical circuits," *Nature* **389**, 463–466, 1997.

[40] H. Risken, *The Fokker-Planck equation: Methods of Solution and Applications*, Volume 18 of Springer series in Synergetics, Springer, Berlin, 1984.

[41] A. D. Wentzel and M. I. Freidlin, *Fluctuations in Dynamic Systems - Effects of Small Random Perturbations*, Nauka, Moscow, 1979.

[42] R. Maier and D. Stein, "Escape problem for irreversible systems," *Phys. Rev. E* **48**, 931–938, 1993.

[43] V. I. Melnikov, "The Kramers problem - 50 years of development," *Phys. Rep.* **209**, 1–71, 1991.

[44] P. Hänggi, P. Talkner, and M. Borkovec, "Reaction-rate theory - 50 years after Kramers," *Rev. Mod. Phys.* **62**, 251–341, 1990.

[45] B. Nagler, M. Peeters, I. Veretennicoff, and J. Danckaert, "Stochastic resonance in vertical-cavity surface-emitting lasers based on a multiple time-scale analysis," *Phys. Rev. E* **67**, 056112, 2003.

[46] R. Graham and T. Tel, "Weak noise limit of Fokker-Planck models and nondifferentiable potentials for dissipative dynamical systems," *Phys. Rev. A* **31**, 1109–1122, 1985.

[47] V. N. Smelyanskiy, M. I. Dykman, and R. S. Maier, "Topological features of large fluctuations to the interior of a limit cycle," *Phys. Rev. E* **55**, 2369–2391, 1997.

[48] S. Beri, R. Mannella, D. G. Luchinsky, A. N. Silchenko, and P. V. McClintock, "Solution of the boundary value problem for optimal escape in continuous stochastic systems and maps," *Phys. Rev. E* **72**, 036131, 2005.

[49] D. G. Luchinsky, P. V. E. McClintock, and M. I. Dykman, "Analogue studies of nonlinear systems," *Rep. Prog. Phys.* **61**, 889–997, 1998.

[50] M. I. Dykman and M. A. Krivoglaz, "Theory of fluctuational transitions between the stable states of a non-linear oscillator," *Sov. Phys. JETP* **50**, 30, 1979.

[51] A. N. Silchenko, S. Beri, D. G. Luchinsky, and P. V. E. McClintock, "Fluctuational transitions across different kinds of fractal basin boundaries," *Phys. Rev. E* **71**, 046203, 2005.

[52] M. I. Dykman, M. M. Millonas, and V. N. Smelyanskiy, "Observable and hidden singular features of large fluctuations in nonequilibrium systems," *Phys. Lett. A* **195**, 53, 1994.

[53] R. Mannella, *A Gentle Introduction to the Integration of Stochastic Differential Equations*, Stochastic Processes in Physics, Chemistry, and Biology, Springer, Berlin, 2000.

Piled Higher and Deeper ***by Jorge Cham*** **www.phdcomics.com**

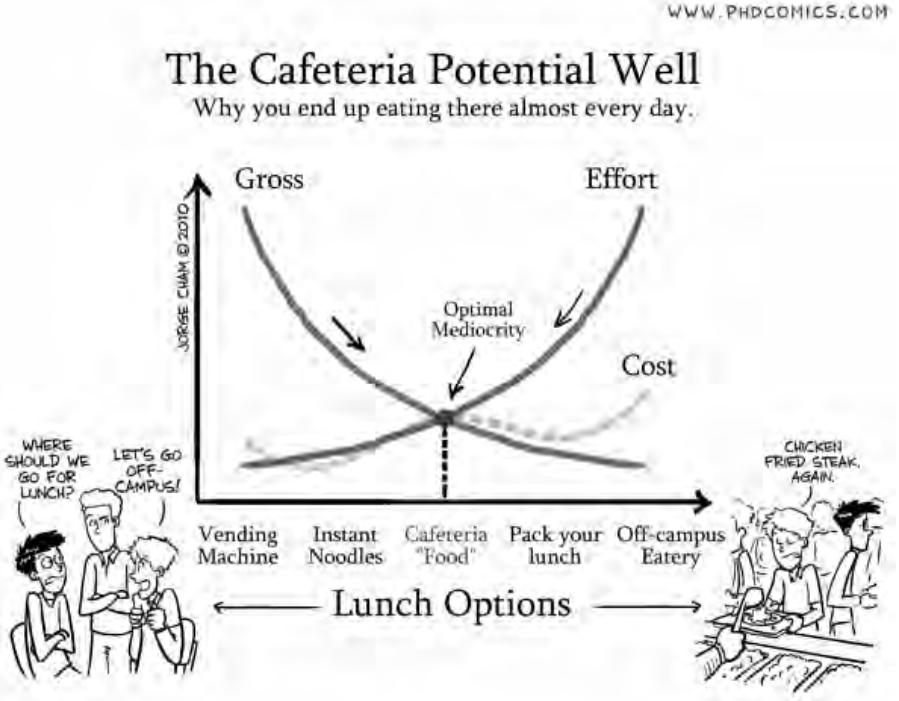

title: "Cafeteria Potential Well" - originally published 1/25/2010

CHAPTER 5

Breaking of the Z_2-symmetry

"I think I've broken something." — Merry in Lord of the Rings

We theoretically study the bifurcation scenario and the evolution of the counter-propagating modes in a semiconductor ring laser when their Z_2-symmetry is broken. Theoretical predictions and insights in the different dynamical regimes of the asymmetric semiconductor ring laser are obtained.[1]

5.1 Introduction

In the previous Chapters, we have repeatedly motivated the technological interest of the SRL by stressing that the bistable unidirectional regime can be used to encode digital information in the emission direction of SRLs [2]. Therefore, we have studied in depth the dynamical behavior of a SRL with a perfectly symmetric cavity and out-coupler, such that a Z_2-symmetry was retained. However, as we have already mentioned in Chapter 1, breaking the cavity symmetry in the laser through preferential scattering into one direction can greatly enhance the unidirectional operation in micro-ring and micro-disk lasers. This is why several studies have focussed on the importance of asymmetries in the design and modeling of semiconductor micro-ring and micro-disk lasers [3–10].
In this Chapter, we will tackle the problem of the SRL with a broken Z_2-symmetry

[1] The work presented in this Chapter has been published in the following journal paper: [1].

similarly as we did for the symmetric problem. Starting from a more general rate-equation model incorporating saturation processes and the asymmetric linear coupling between the SRL modes, we will derive (as in Chapter 2) an asymptotic two-dimensional SRL model. A bifurcation analysis of this asymptotic model will provide us with both a qualitative and quantitative picture of how the position of all bifurcations shift in parameter space. Moreover, this bifurcation study will allow us to understand the locus of different nodes, limit cycles and the specific shape of invariant manifolds of saddle points in the two-dimensional phase space of the SRL. This knowledge will be exploited in the next Chapter, where we discuss excitable properties of the SRL.

5.2 Semiconductor ring laser rate-equation models with asymmetric linear coupling

We consider a SRL operating in a single-longitudinal, single-transverse mode. In the limit of small outcoupling from the ring cavity, the total electric field oscillating in the ring can be written as the sum of two counter-propagating waves (see also Section 1.4.1):

$$E(z,t) = E_{cw}(t)\exp\left[i\left(\omega_0 t - k_0 z\right)\right] + E_{ccw}(t)\exp\left[i\left(\omega_0 t + k_0 z\right)\right] + \text{c.c.}. \tag{5.1}$$

Here k_0 is the longitudinal wavenumber and ω_0 is the optical frequency of the mode. In the slow varying approximation, the amplitudes of the clockwise E_{cw} and counter-clockwise propagating modes E_{ccw} vary on time scales which are slower that ω_0. The rate-equation model is formulated mathematically in terms of two rate equations for the slowly varying amplitudes $E_{CW,CCW}$ and one rate equation for the carrier number N. The equations read:

$$\begin{aligned}
\dot{E}_{cw} &= \kappa(1+i\alpha)\left[g_{cw}N - 1\right]E_{cw} - (k - \Delta k/2)e^{i(\phi_k - \Delta\phi_k/2)}E_{ccw}, && (5.2)\\
\dot{E}_{ccw} &= \kappa(1+i\alpha)\left[g_{ccw}N - 1\right]E_{ccw} - (k + \Delta k/2)e^{i(\phi_k + \Delta\phi_k/2)}E_{cw}, && (5.3)\\
\dot{N} &= \gamma[\mu - N - g_{cw}N|E_{cw}|^2 - g_{ccw}N|E_{ccw}|^2] && (5.4)
\end{aligned}$$

where dot represents differentiation with respect to time t, $g_{cw} = 1 - s|E_{cw}|^2 - c|E_{ccw}|^2$, $g_{ccw} = 1 - s|E_{ccw}|^2 - c|E_{cw}|^2$, κ is the field decay rate, γ is the carrier decay rate, α is the linewidth enhancement factor and μ is the renormalized injection current with $\mu \approx 0$ at transparency and $\mu \approx 1$ at lasing threshold. The two counter-propagating modes are considered to saturate both their own and each other's gain due to e.g. spectral hole burning effects and carrier heating (see also Sect. 1.3.2). Self- and cross-saturation effects are added phenomenologically and

are modeled by s and c. A possible carrier grating formed by the two counter-propagating waves is washed out on a time scale faster than the photon lifetime as we discussed before in Section 1.4.1. Reflection of the counter-propagating modes occurs at the point where light is coupled out of the ring cavity into a coupling waveguide and can also occur at the end facets of the coupling waveguide. These localized reflections result in a linear coupling between the two fields characterized by an amplitude k and a phase shift ϕ_k. Moreover, due to unavoidable imperfections in the SRL introduced during the fabrication process, the SRL will have a certain asymmetry in the linear coupling between both counter-propagating modes. This asymmetry is introduced in Eqs. (5.2)-(5.4) as Δk and $\Delta\phi_k$, representing the difference in backscattering strength and phase, respectively.

In the previous Chapter, the rate-equation model with symmetric backscattering ($\Delta k = \Delta\phi_k = 0$) has proved to provide a very good description of many of the dynamical features that are experimentally observed in SRLs [11–13]. However, several dynamical phenomena observed in experiments require the inclusion of an asymmetry in the linear mode coupling [14]. An example of such behavior, excitability, will be discussed in the next Chapter.

In the case of symmetric backscattering a two-dimensional reduced set of SRL equations has allowed us to gain a much deeper insight in the organizing mechanisms of the different nonlinear dynamical regimes (see Chapter 2 and Ref. [15]). To gain access to the same two-dimensional phase space in the case of asymmetric mode coupling, we propose a similar asymptotic simplification of Eqs. (5.2)-(5.4). On time scales slower than the relaxation oscillations we can still numerically show that the total intensity is conserved:

$$|E_{cw}|^2 + |E_{ccw}|^2 = \mu - 1 > 0. \tag{5.5}$$

Under the same conditions as in Chapter 2 and provided that $\Delta k/\kappa$ is small, the slow time scale dynamics is described by the time evolution of two auxiliary angular variables:

$$\begin{aligned} \theta' &= J\sin\theta\cos\theta + 2(1-\delta)\cos(\phi_k+\psi) - (1-\sin\theta) \\ &\quad [(1-\delta)\cos(\phi_k+\psi) + (1+\delta)\cos(\phi_k-\psi)], \qquad (5.6) \\ \cos\theta\psi' &= \alpha J\sin\theta\cos\theta - (1+\delta)(1-\sin\theta)\sin(\phi_k-\psi) \\ &\quad +(1-\delta)(1+\sin\theta)\sin(\phi_k+\psi). \qquad (5.7) \end{aligned}$$

where $\theta = 2\arctan\sqrt{|E_{CCW}|^2/|E_{CW}|^2} - \pi/2 \in [-\pi/2, \pi/2]$ represents the relative modal intensity and $\psi = \Phi_{CCW} - \Phi_{CW} - \Delta\phi_k/2 \in [0, 2\pi]$ is the phase difference between the counter-propagating modes, with $\Phi_{CW,CCW}$ the phases of the CW and CCW mode, respectively. Prime now denotes derivation to the slow time scale $\tau = kt$. The difference in linear coupling strength has been re-normalized

as $\delta = \Delta k/2k$. Finally, as in Chapter 2, in this reduced model the pump current has been rescaled as

$$J = \kappa(c - s)(\mu - 1)/k. \tag{5.8}$$

As the phase space of Eqs. (5.6)-(5.7) is restricted to two dimensions, it allows for a clear physical picture of the influence of all parameters on the dynamical evolution of the variables in a plane. It is interesting to notice that the asymmetry in the coupling phase $\Delta\phi_k$ only arises as a shift of the auxiliary variable ψ and does not influence the actual dynamics which happens at the level of the two-dimensional system Eqs. (5.6)-(5.7). In a similar way, the saturation coefficients c, s and the average backscattering strength k only rescale the pump current J and also do not influence the underlying dynamical system Eqs. (5.6)-(5.7). Therefore, we will focus on the influence of the relevant dynamical parameters, being the normalized driving current J, the relative asymmetry in backscattering δ and the average coupling phase ϕ_k. The linewidth-enhancement factor α will be kept constant throughout this Chapter.

5.3 Bifurcation analysis

In the case of symmetric linear coupling, for $\delta = 0$, two different types of stationary solutions exist. On the one hand, solutions corresponding to bidirectional emission ($\theta = 0$) exist for all model parameters and are identified by their value of ψ. For $\psi = 0$ and $\psi = \pi$, we can distinguish between the in-phase symmetric-solution (IPSS) and the out-of-phase symmetric solution (OPSS). On the other hand, in-phase and out-of-phase asymmetric solutions (IPAS, OPAS) corresponding to unidirectional emission can emerge from either a pitchfork bifurcation of the symmetric solutions or from a saddle-node bifurcation (see Refs. [15, 16] and Chapter 2).
However, when the symmetry is broken ($\delta \neq 0$), it becomes harder to distinguish between bidirectional and unidirectional operation, since the symmetric solution with $\theta = 0$ no longer exists. All solutions are now in a sense unidirectional (with smaller or larger values of θ), and are given in a parametrized form $\{\theta(\psi), J(\psi)\}$:

$$\theta(\psi) = 2\arctan\left[\left(\frac{-\sin\psi(I) - \cos\psi(II)}{\sin\psi(III) + \cos\psi(IV)}\right)^{\frac{1}{2}}\right] - \frac{\pi}{2}, \tag{5.9}$$

$$\begin{aligned} J(\psi) = {} & \csc\theta(\psi)\sec\theta(\psi)[2(\delta - 1)\cos(\phi_k + \psi) + (1 - \sin\theta) \\ & [(1 - \delta)\cos(\phi_k + \psi) + (1 + \delta)\cos(\phi_k - \psi)]]. \end{aligned} \tag{5.10}$$

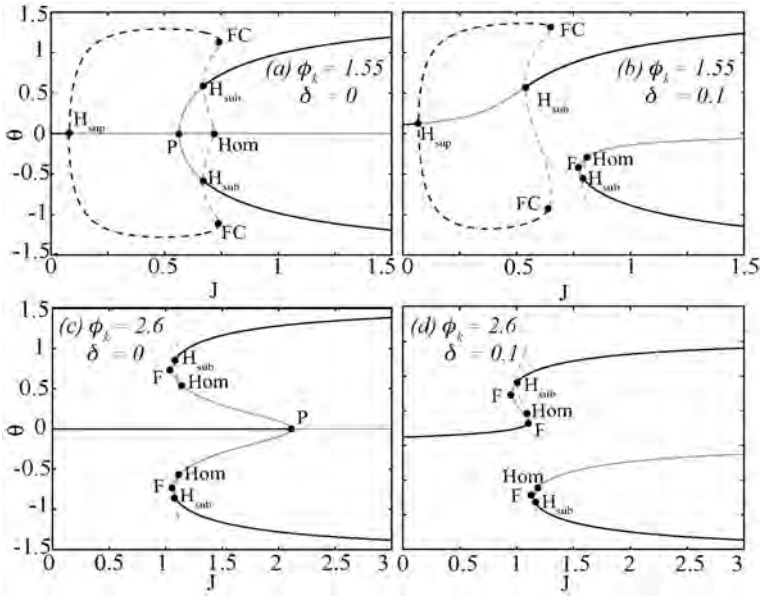

Figure 5.1: Bifurcation diagrams of Eqs. (5.6)-(5.7) depicting the extremes of θ vs. injection current J. The steady state values of θ are denoted by full lines, while the extrema of periodically oscillating θ are indicated with dashed lines. Black (gray) color is used for stable (unstable) fixed points or limit cycles. From (a) to (d), we have ϕ_k = 1.55, 2.6 and δ = 0 and 0.1, respectively. α = 3.5. H_{sub}, H_{sup}, P, F, Hom and FC denote the following bifurcations: subcritical Hopf, supercritical Hopf, pitchfork, Fold, homoclinic and fold of cycles.

with

$$I = (1+\delta)\cos(\phi_k) + \alpha(1+\delta)\sin(\phi_k), \tag{5.11}$$

$$II = \alpha(1+\delta)\cos(\phi_k) + (1+\delta)\sin(\phi_k), \tag{5.12}$$

$$III = (1-\delta)\cos(\phi_k) + \alpha(1-\delta)\sin(\phi_k), \tag{5.13}$$

$$IV = -\alpha(1-\delta)\cos(\phi_k) + (1-\delta)\sin(\phi_k). \tag{5.14}$$

This absence of the purely bidirectional solutions can be observed in Figure 5.1, where bifurcation diagrams of Eqs. (5.6)-(5.7) depicting the extremes of θ vs. injection current J are plotted. The steady state values of θ are denoted by full lines, while the extrema of periodically oscillating θ are indicated with dashed lines. Black (gray) color is used for stable (unstable) fixed points or limit cycles. Figs. 5.1(a) and (c) depict the bifurcation diagrams in the symmetric case (δ = 0)

for two different values of the linear coupling phase ϕ_k = 1.55 and 2.6, respectively.
First, we will briefly revisit the bifurcation diagrams Figs. 5.1(a) and (c) for the symmetric case. At the threshold current, $J \approx 0$, laser action starts. When operating close to the threshold, at low power, the laser operates bidirectionally with CW and CCW operating either in-phase or out-of-phase according to ϕ_k (see Ref. [16] and Chapter 2). For large values of the pump parameter J, the nonlinear gain saturation becomes the dominant coupling mechanism between the counterpropagating modes and two out-of-phase (in-phase) new solutions can be found. In this region, the optical output power is mainly concentrated in one propagation direction, called unidirectional operation. When the device is symmetric two unidirectional solutions exist: one where $|E_{cw}|^2 > |E_{ccw}|^2$ and vice versa. Hence, the device exhibits bistability. For intermediate values of J, the linear and nonlinear coupling are comparable and the dynamics of the system depends on the value of ϕ_k. In Figure 5.1(a) one can find alternating oscillations (H_{sup}) in this intermediate region. The large stable limit cycle corresponding to these oscillations is destroyed in a fold of cycles (FC) with an unstable limit cycle created slightly beforehand (for lower values of J) in a homoclinic bifurcation (Hom). Figure 5.1(c) shows a qualitatively different behavior for intermediate values of J. Two fold (or saddle-node) bifurcations (F) create the unidirectional solutions while the stable bidirectional solution still exists. This creates the possibility of the coexistence of three stable solutions. Only for higher values of the pump current J, the bidirectional solution disappears in a pitchfork bifurcation (P), after which one is left with a bistability between both unidirectional modes. When introducing asymmetry in the linear coupling between the two counterpropagating fields of the SRL (δ = 0.1), one can see that the purely bidirectional solution does not exist anymore and that the pitchfork bifurcation (creating the unidirectional solutions in the symmetric case) is replaced by a fold bifurcation [see Figs. 5.1(b),(d)]. The absence of the pitchfork bifurcation in the asymmetric case is of immediate relevance in the experimental measurements of PI-curves. When the asymmetry is non-negligible, one observes that it is always either the CW or the CCW that is first created in a fold bifurcation. The reason for this becomes evident from Figs. 5.1(b),(d), where one clearly sees that one of the counter-propagating unidirectional modes is created at higher pump currents in the fold bifurcation.
Figure 5.1(c) shows the possibility of multistability for certain values of (J, ϕ_k), where three stable states coexist in the symmetric SRL [16]. This principle of multistability in the symmetric SRL has been experimentally confirmed in Ref. [13] (see Chapter 4). When introducing an asymmetry in the linear mode coupling, one can observe in Figure 5.1(d) that the two fold bifurcations and one pitchfork bifurcation now are replaced by three fold bifurcations. Moreover,

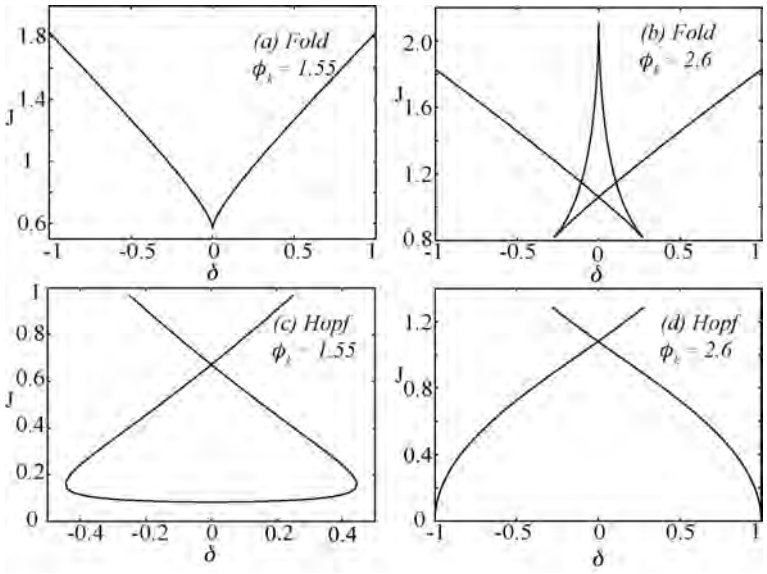

Figure 5.2: Bifurcation diagrams of Eqs. (5.6)-(5.7) depicting the change in the fold and Hopf bifurcation currents J for changing values of the asymmetry in coupling strength δ and for two different values of the coupling phase ϕ_k = 1.55 [(a)-(c)] and 2.6 [(b)-(d)]. α = 3.5.

these different fold bifurcations occur at different values of the pump current J. Depending on the value of the parameter set (J, ϕ_k, δ), the possibility of multistable behavior between more than two stable states remains. The observable sequence of different operational regimes is, however, much richer than in the case of a symmetric SRL, as the different fold bifurcations can occur at different pump currents depending on the coupling phase ϕ_k and the amount of asymmetry δ. This opens up the possibility of e.g. bistable behavior of the bidirectional mode (or at least $\theta \approx 0$) and only one of the unidirectional modes. We have experimentally verified such behavior in Ref. [1].

Bearing this in mind, we are interested in the relative position of the different fold bifurcations as a function of (J, δ). Figure 5.2(a) and (b) depicts the fold bifurcation currents J as a function of the percentage of asymmetry in the coupling strength δ, for two different values of the coupling phase (ϕ_k = 1.55 and 2.6). The locus of the bifurcations has been determined using the continuation software package AUTO [17]. For ϕ_k = 1.55, there was only a pitchfork bifurcation in the symmetric case ($\delta = 0$) and no folds were present. When increasing δ, this picture stays qualitatively the same, but the pitchfork becomes a fold that shifts approx-

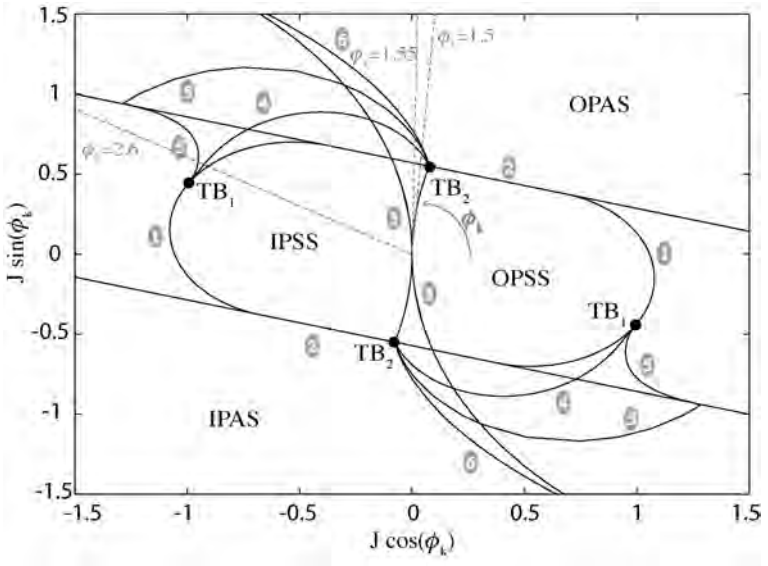

Figure 5.3: Stability diagram for a fixed value $\alpha = 3.5$ and $\delta = 0$ showing the different stable operation regimes for $J > 0$. The different black solid lines indicate the different bifurcation currents, and are depicted in a polar plot (J, ϕ_k). The denotations ①- ⑥ correspond to ① fold bifurcation of the OPSS (IPSS), ② the pitchfork bifurcation of the OPSS (IPSS), ③ supercritical Hopf bifurcation of the OPSS (IPSS), ④ subcritical Hopf bifurcation the OPAS (IPAS), ⑤ double homoclinic bifurcation with gluing and ⑥ a fold of cycles. Multiple Takens-Bogdanov (TB) points are also depicted. The gray dashed lines show the ϕ_k for which bifurcation diagrams are shown in Figs. 5.1-5.2.

imately linearly to higher pump currents J for increasing asymmetry δ. More interesting is the case for $\phi_k = 2.6$, where we have previously seen that there exist two fold bifurcations for $\delta = 0$. For increasing values of the asymmetry δ, the fold that corresponds with the pitchfork in the symmetric case shifts to lower current values until it disappears when coinciding with one of the other fold bifurcations. Only one fold remains for higher values of the asymmetry, which as for $\phi_k = 1.55$ moves to higher pump currents J approximately linearly. It is clear that, in general, one is not only interested in the existence of multiple states, but wishes to know where exactly these solutions are stable in time. Figure 5.2(c) and (d) show the Hopf bifurcation currents J as a function of the percentage of asymmetry in coupling strength δ for the same coupling phase as in Figure 5.2(a) and (b). One can observe that for $\phi_k = 1.55$ increasing the asymmetry δ above

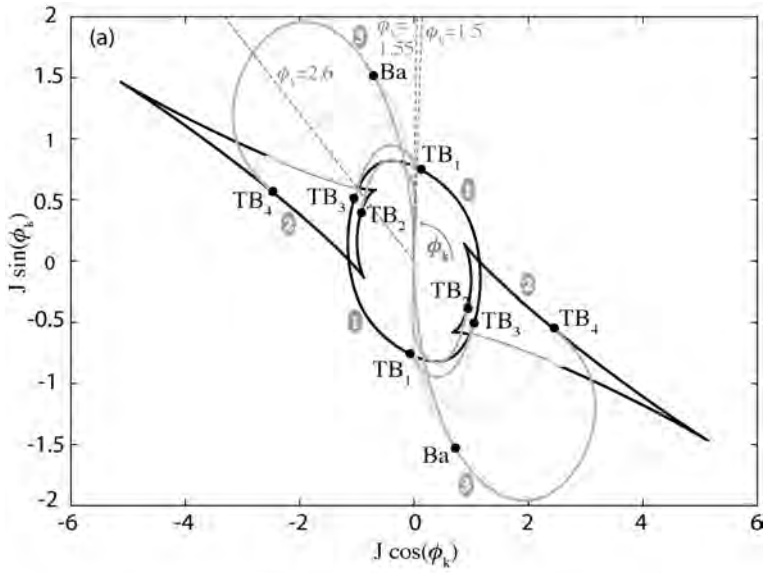

Figure 5.4: Stability diagram for a fixed value $\alpha = 3.5$ and $\delta = 0.1$ showing the different stable operation regimes for $J > 0$. The different solid lines indicate the different bifurcation currents, and are depicted in a polar plot (J, ϕ_k). The denotations ① - ③ correspond to ① a fold bifurcation creating a new branch of solutions with $\theta < 0$, ② a fold bifurcation creating a new branch of solutions with $\theta > 0$ and ③ a supercritical Hopf bifurcation. The fold bifurcations are depicted in black solid lines, all Hopf bifurcations are in dark gray solid lines, while the global bifurcations are shown in light gray solid lines. Different Takens-Bogdanov (TB) and Bautin (Ba) co-dimension two points are also depicted. The gray dashed lines show the ϕ_k for which bifurcation diagrams are shown in Figs. 5.1-5.2.

about 0.45 removes the Hopf bifurcation and thus stabilizes the unidirectionally lasing mode. However, for $\phi_k = 2.6$ increasing the asymmetry δ from 0 to 1 shifts the Hopf bifurcation current to lower and lower values of the pump current J, but nonetheless the Hopf instability is retained over the entire domain. Only at $\delta = 1$ the Hopf bifurcation needs to disappear as the linear coupling coefficient in one field equation becomes zero. Therefore, an increase in the amplitude of that field will not be coupled back to the counter-propagating field such that no oscillations can be sustained. We can conclude that a strong dependence on the phase coupling ϕ_k of the loci of the Hopf bifurcation points exists in SRLs.

In Ref. [16] (see Chapter 2), an elaborate bifurcation analysis of the symmetric SRL had been carried out for a fixed value of $\alpha = 3.5$, showing the different

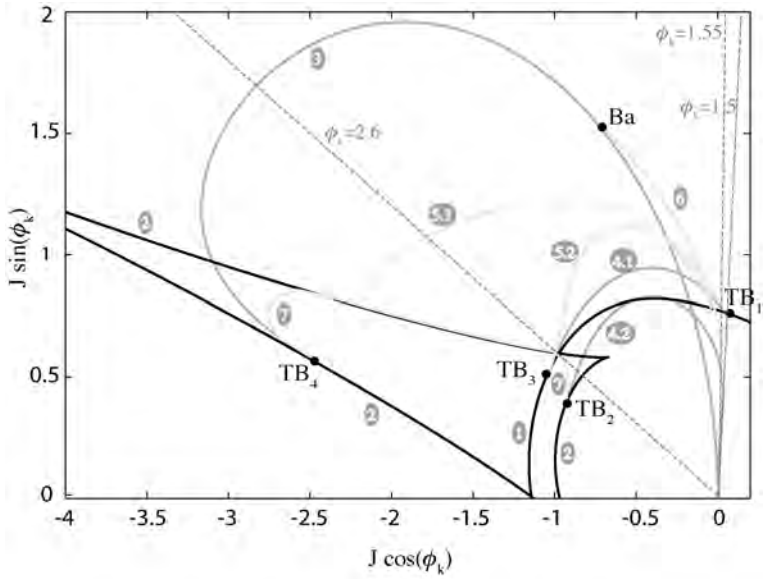

Figure 5.5: A zoom of the stability diagram shown in Figure 5.4, using the same notation and parameters. The bifurcations denoted by ④ - ⑦, where ④ are subcritical Hopf bifurcations, ⑤,⑦ are homoclinic bifurcations, and ⑥ a fold of cycles are shown in more detail.

bifurcation lines in the parameter plane (J, ϕ_k) for $J > 0$. We briefly revisit the bifurcation scenario of the symmetric SRL in order to be able to compare it with the asymmetric case later on. As can be seen from the polar plot in Figure 5.3, the dynamics is organized by two co-dimension two Takens-Bogdanov points. From TB_1, the point where the fold (saddle-node) bifurcation line ① and the subcritical Hopf line ④ meet, emerges a homoclinic bifurcation line ⑦. From TB_2, the point where the supercritical Hopf bifurcation line ③ and the pitchfork bifurcation ② meet, emerges a double homoclinic connection with a gluing bifurcation ⑤ and a fold of cycles ⑥. Finally, also the supercritical Hopf bifurcation and the fold of cycles coincide in a co-dimension 2 point called a Bautin bifurcation point (not shown) [18, 19]. The gray dashed lines denote $\phi_k = 1.55$ and 2.6 for which bifurcation diagrams are shown in Figures 5.1-5.2.
Introducing an asymmetry $\delta = 0.1$, while keeping the same fixed value $\alpha = 3.5$, changes the stability diagram as shown in Figure 5.4 and Figure 5.5. The different fold bifurcations are depicted in black solid lines, all Hopf bifurcations in dark gray solid lines, while the global bifurcations are shown in light gray solid lines. The same notation as in Figure 5.3 is used. The dynamics is still organized

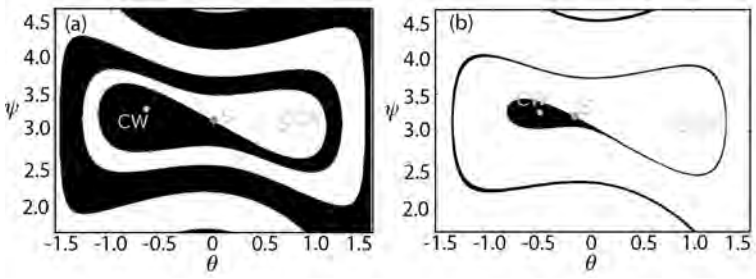

Figure 5.6: Stable manifold separating the two basins of attraction (black and white) of both asymmetric stable states for $J = 0.71$, $\phi_k = 1.5$ and $\Delta\phi_k = 0$. $\delta = 0$ and 0.05 in (a) and (b), respectively.

by TB points, but unlike in the symmetric case, there are now four TB points. The bifurcation diagram is to a large extent similar as the symmetric SRL, with as main difference that the subcritical Hopf bifurcations and the accompanying homoclinic bifurcations no longer occur at the same current value J. This has as result that the number of subcritical Hopf lines ④ and homoclinic bifurcations ⑤ are now doubled, and are organized by an extra TB point with respect to the symmetric case. Moreover, the two pitchfork bifurcation lines ② of the symmetric SRL that were parallel to each other, are now replaced by fold bifurcation lines ② crossing at a finite parameter values. Again, the gray dashed lines denote $\phi_k = 1.55$ and 2.6 for which the bifurcation diagrams are shown in Figs. 5.1-5.2. For a more generic and in-depth study of the unfolding of the different bifurcations from a Takens-Bogdanov bifurcation point in a system with broken Z_2-symmetry, we refer to Refs. [19, 20].

5.4 Phase space portraits

In Refs. [12, 16] and Chapter 2, we have shown that the phase space portrait of a symmetric SRL can have a particular shape, which is reflected in the dynamical behavior of the SRL (see Chapters 3-4). More specifically, for values of (J, ϕ_k) close to, but past, the homoclinic bifurcation ⑤, the stable manifold of the saddle point spirals around S and the basins of attraction of CW and CCW fold around each other. For a symmetric SRL operating in a unidirectional regime this is exemplified in Figure 5.6(a). Four stationary solutions exist for Eqs. (5.6)-(5.7): an unstable in-phase bidirectional state in $(0, 0)$ (not shown); two symmetric stable states CW and CCW at $\psi \approx \pi$, both corresponding to unidirectional operation; and a saddle point S in $(0, \pi)$ which is the unstable out-of-phase bidirectional

solution. The folded shape of the stable manifold of S that separates the basins of attraction of CW and CCW has lead to interesting dynamical behavior, such as a particular kind of noise-driven mode-hopping between the CW and CCW mode (see Chapter 4) [12] and backfire dynamics when including optical injection [16, 21] (see Chapter 3).
We have shown that these folding basins of attraction persist in the (J, ϕ_k, α) parameter space [16] (see Chapter 2), provided that one stays close enough to the homoclinic bifurcation and the fold of cycles. Whereas the phase space portraits in Figure 5.6 are drawn for $\phi_k = 1.5$, similar results can be obtained for other values of ϕ_k as long as the basins of attraction of the CW and CCW mode intertwine. This is the case for both $\phi_k = 1.5$ and 1.55 of which a cut is shown in the stability diagram of Figure 5.4 and Figure 5.5.
When breaking the Z_2-symmetry of the laser by including an asymmetry in the linear mode coupling, the basin of attraction of either the CW or the CCW mode is greatly enlarged. This is shown in Figure 5.6(b), where we have taken $\delta = 0.05$. The black and white regions represent the basins of attraction of both stable unidirectional states, which are separated by the stable manifold of the saddle point. Due to the large asymmetry in the basins of attraction of both counter-propagating modes of the SRL, the CW with the much smaller basin of attraction has become a *metastable* state. Unavoidable spontaneous noise fluctuations will drive the laser out of the basin of attraction of the CW towards the CCW mode. Therefore, with the asymmetry δ large enough, we expect in practice to see the laser always operating in the CCW mode, as small fluctuations will drive the system outside of the basin of attraction of the CW state. However, based on the structure of the phase space as shown in Figure 5.6(b), we conjecture that the same noisy fluctuations can lead to the excitation of pulses in the system. This process, well-known since a long time in e.g. neural networks [22], is called excitability and will be studied in depth in the next Chapter.

5.5 Conclusion

We have studied the bifurcation structure of an asymptotically derived two-variable reduced model for the dynamical behavior of a semiconductor ring laser when its Z_2 symmetry is broken. We have shown how this two-dimensional model for an asymmetric ring laser can be used to interpret and predict regions of monostable, bistable and multistable behavior in the laser. As in Chapter 2, the basins of attraction of the attractors in the bistable regime of the ring laser have been studied in the two-dimensional phase space. In the following Chapter, these results will be used to gain theoretical understanding of excitable behavior in the ring laser. Then we will also compare with experiments.

References

[1] L. Gelens, S. Beri, G. Van der Sande, G. Verschaffelt, and J. Danckaert, "Multistable and excitable behavior in semiconductor ring lasers with broken Z_2-symmetry," *Eur. Phys. J. D* , doi::10.1140/epjd/e2010–00042–7, 2010.

[2] M. T. Hill, H. Dorren, T. de Vries, X. Leijtens, J. den Besten, B. Smalbrugge, Y. Oei, H. Binsma, G. Khoe, and M. Smit, "A fast low-power optical memory based on coupled micro-ring lasers," *Nature* **432**, 206–209, 2004.

[3] J. J. Liang, S. Lau, M. Leary, and J. Ballantyne, "Unidirectional operation of waveguide diode ring lasers," *Appl. Phys. Lett.* **70**, 1192–1194, 1997.

[4] H. Cao and M. Osinski, "Large s-section-ring-cavity diode lasers: directional switching, electrical diagnostics, and mode beating spectra," *Photon. Technol. Lett.* **17**, 282, 2005.

[5] J. Y. Lee, X. S. Luo, and A. W. Poon, "Reciprocal transmissions and asymmetric modal distributions in waveguide-coupled spiral-shaped microdisk resonators," *Opt. Express* **15**, 14650–14666, 2007.

[6] C. M. Kim, J. Cho, J. Lee, S. Rim, S. H. Lee, K. R. Oh, and J. H. Kim, "Continuous wave operation of a spiral-shaped microcavity laser," *Appl. Phys. Lett.* **92**, 131110, 2008.

[7] J. Wiersig, S. W. Kim, and M. Hentschel, "Asymmetric scattering and nonorthogonal mode patterns in optical microspirals," *Phys. Rev. A* **78**, 053809, 2008.

[8] L. Shang, L. Y. Liu, and L. Xu, "Single-frequency coupled asymmetric microcavity laser," *Opt. Lett.* **33**, 1150–1152, 2008.

[9] M. Hentschel and T. Y. Kwon, "Designing and understanding directional emission from spiral microlasers," *Opt. Lett.* **34**, 163–165, 2009.

[10] M. Strain, G. Mezosi, J. Javaloyes, M. Sorel, A. Perez-Serrano, A. Sciré, S. Balle, G. Verschaffelt, and J. Danckaert, "Semiconductor snail lasers," *App. Phys. Lett.* **96**, 121105, 2010.

[11] M. Sorel, P. Laybourn, A. Sciré, S. Balle, G. Giuliani, R. Miglierina, and S. Donati, "Alternate oscillations in semiconductor ring lasers," *Opt. Lett.* **27**, 1992–1994, 2002.

[12] S. Beri, L. Gelens, M. Mestre, G. Van der Sande, G. Verschaffelt, A. Sciré, G. Mezosi, M. S. M, and J. Danckaert, "Topological insight into the non-Arrhenius mode hopping of semiconductor ring lasers," *Phys. Rev. Lett.* **101**, 093903, 2008.

[13] L. Gelens, S. Beri, G. Van der Sande, G. Mezosi, M. Sorel, J. Danckaert, and G. Verschaffelt, "Exploring multistability in semiconductor ring lasers: Theory and experiment," *Phys. Rev. Lett.* **102**, 193904, 2009.

[14] S. Beri, L. Mashall, L. Gelens, G. Van der Sande, G. Mezosi, M. Sorel, J. Danckaert, and G. Verschaffelt, "Excitability in optical systems close to Z_2-symmetry," *Phys. Lett. A* **374**, 739–743, 2010.

[15] G. Van der Sande, L. Gelens, P. Tassin, A. Sciré, and J. Danckaert, "Two-dimensional phase-space analysis and bifurcation study of the dynamical behavior of a semiconductor ring laser," *J.Phys.B* **41**, 095402, 2008.

[16] L. Gelens, G. Van der Sande, S. Beri, and J. Danckaert, "Phase-space approach to directional switching in semiconductor ring lasers," *Phys. Rev. E* **79**, 016213, 2009.

[17] E. Doedel *et al.*, "Auto 97," *http://indy.cs.concordia.ca/auto/main.html* , 1997.

[18] Y. Kuznetsov, *Elements of Applied Bifurcation Theory*, Springer, 3rd edition, New York, 2004.

[19] J. Guckenheimer and P. Holmes, *Nonlinear Oscillations, Dynamical Systems, and Bifurcations of Vector Fields*, Springer-Verlag, New York, 2002.

[20] G. Dangelmayr and J. Guckenheimer, "On a four parameter family of planar vector fields," *Arch. Ration. Mech. An.* **97**, 321–351, 1987.

[21] L. Gelens, S. Beri, G. Van der Sande, J. Danckaert, N. Calabretta, H. Dorren, R. Nötzel, E. Bente, and M. Smit, "Optical injection in semiconductor ring lasers: backfire dynamics," *Opt. Expr.* **16**, 16968–16974, 2008.

[22] E. M. Izhikevich, "Neural excitability, spiking and bursting," *Int.J.Bifurcat.Chaos* **10**, 1171–1266, 2000.

Piled Higher and Deeper ***by Jorge Cham*** **www.phdcomics.com**

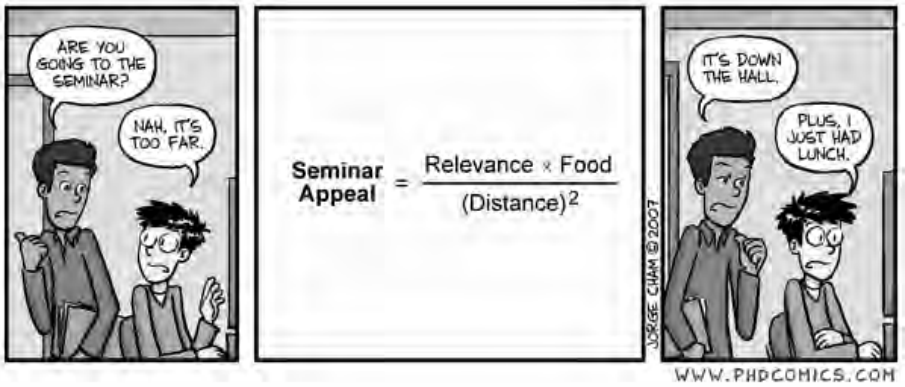

title: "Seminar Appeal" - originally published 11/21/2007

CHAPTER 6

Excitability

"That doesn't make sense to me. But, then again, you are very small..." — Treebeard in Lord of the Rings

We reveal a mechanism of excitability in semiconductor ring lasers. This mechanism is general for systems close to Z_2-symmetry. The global shapes of the invariant manifolds of a saddle in the vicinity of a homoclinic loop determine the origin of excitability and the features of the excited pulses. The characteristics of these excited pulses are studied both deterministically and in the presence of noise. We confirm our findings experimentally.[1]

6.1 Introduction

Excitability in systems outside equilibrium is a very fertile and interdisciplinary research topic. It has been observed in various fields including Chemistry, Physics, Biology or neural networks [3–9]. In particular, excitability attracts a lot of attention in the field of optics [10–17] due to its application as a way to generate well-defined optical pulses. In the last decade, lasers with saturable absorber [10, 11], optically injected lasers [12, 17], lasers with optical feedback [16] or VCSELs with opto-electronic feedback [18] have all been proposed as optical excitable units.
A general feature of excitable systems is their highly nonlinear response to external perturbations. When unperturbed, the system remains quiescent and

[1]The work presented in this Chapter has been published in the following journal papers: [1, 2].

resides in a resting state. Small perturbations only lead to a small-amplitude linear response. However, if the perturbation is sufficiently large, the system is transferred from the resting state to an excited state (the firing state). After this strong response, the system returns to its initial resting state through a refractory cycle. This large excursion of the system's variables in phase space corresponds to the emission of a large amplitude pulse. During the refractory cycle it is impossible to generate a second pulse as the system does not respond to any external perturbation.
In this Chapter, we aim to disclose the excitable properties of the wide class of nonlinear dynamical systems with weakly broken Z_2-symmetry [19, 20]. For the majority of optical systems, excitability takes place around a homoclinic bifurcation of a *stable* limit cycle [10–13, 17]. The presence of the stable limit cycle can easily be observed in these systems as it leads to Q-Switching oscillations. However, it is known that only *unstable* limit cycles undergo homoclinic bifurcations in SRLs [21], which are intrinsically more challenging to address as they are not associated to observable dynamical regimes. We will analyze the origin of the excitability based on the bifurcation study and the topology of the invariant manifolds of SRL with broken Z_2-symmetry as presented in the previous Chapter. In such a way, we can predict the onset of excitability near the homoclinic bifurcation of an *unstable* limit cycle as well as the properties of single and multiple excited pulses. We determine both the deterministic and stochastic properties of these excited pulses, and verify our findings experimentally.

6.2 Origin of excitability in semiconductor ring lasers

In Figure 6.1(b) we revisit the phase space picture of a SRL with broken Z_2 symmetry as modeled by Eqs. (5.6)-(5.7) and also shown in Figure 5.6(b). Two counter-propagating unidirectional stable attractors are present in the SRL — the CW and the CCW mode — and are depicted here in the two-dimensional (θ, ψ) phase space as in the previous Chapters. The gray and white regions indicate the basins of attraction of the CW and the CCW mode. They are separated by the stable manifolds of a saddle state indicated by S. The asymmetry between both modes in Eqs. (5.6)-(5.7) becomes clear as the basin of attraction of the CW state is much smaller than the one of the CCW state.
Assuming the unperturbed SRL resides in the CCW state, the SRL can be perturbed to cross the stable manifold, by e.g. optical injection, and will then respond by making a large excursion in phase space before relaxing again to the CCW state [see Figure 6.1(b)]. In other words, a pulse is generated which will turn around the CW state before returning to the CCW lasing mode by following the unstable manifold of the saddle S.

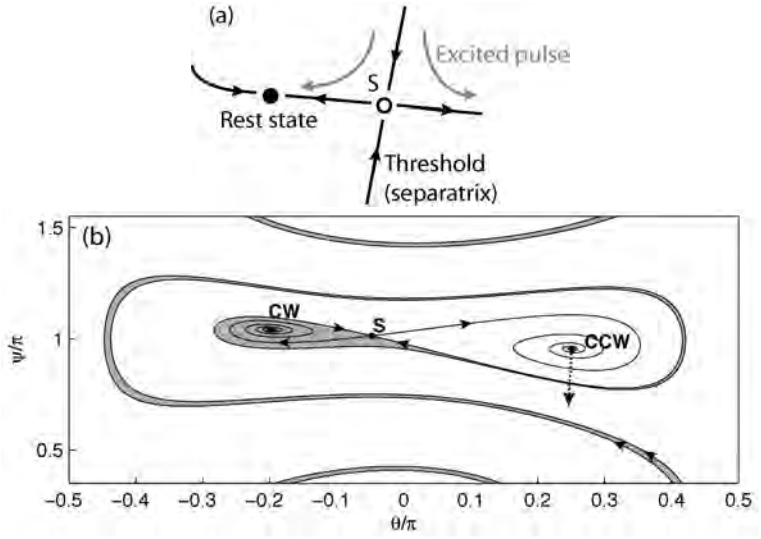

Figure 6.1: (a) Sketch of excitability behavior near a saddle-node bifurcation. (b) The phase space topology of an asymmetric SRL. CW, CCW and S are respectively two quasiunidirectional states and a saddle state of which the stable and unstable manifolds are displayed. The basin of attraction of the CW (CCW) quasiunidirectional state is colored gray (white).

In the majority of excitable systems encountered in optics, the generation of an optical pulse is initiated stochastically by the crossing of one branch of the stable manifold of a saddle and is completed deterministically by following a branch of the unstable manifold of the same saddle back to the initial quiescent state [10–12, 15, 17] [see Figure 6.1(a)]. However, one notices from Figure 6.1(b) that in the SRL model with weakly broken symmetry a second stable fixed point CW can still be present in the system. The unstable manifold of the saddle S connects to CW and does not lead to an excited pulse. Excitability therefore initiates by stochastically crossing *both* branches of the stable manifold and continues deterministically in the basin of attraction of CCW initially *without* following the unstable manifold of *S*. Only at the end of the pulse the system relaxes to the CCW state by following the unstable manifold of S.
We point out that this excitable behavior disappears when the current J is either too small or too large. When J is too large, the system returns to a bistable situation such that in the presence of noise there will be a competition between mode-hopping events between both stable states and excitable excursions (see Chapter 4). For J too small, the system will exhibit alternating oscillations [21].

Finally, for the asymmetry δ large enough, one of the two stationary states collides with the saddle and disappears in a saddle node bifurcation [see Figures 5.1(b) and 5.2(a)]. In the corresponding regime the laser remains excitable; however, the excitability threshold is no longer associated with an invariant manifold of the system and becomes a quasi-threshold (or separatrix) in the phase space. A similar scenario appears for instance in FitzHugh-Nagumo and Hodgkin-Huxley models for neural excitability [8].
Before characterizing the stochastic properties of the excited pulses in the SRL, we will demonstrate deterministically the presence of excitability in the SRL by optically injecting pulses to drive the SRL beyond the excitability threshold, thus inducing an excitable excursion.

6.3 Deterministic analysis

The stable saddle manifold can be crossed by either altering the phase difference ψ or the relative power distribution θ between the counter-propagating modes. This can, e.g., be done by optically injecting a pulse into the SRL. We analyze the response of the SRL for two limiting cases: *long* and *short* pulses. For long pulses the SRL will have the time to relax to a new state from which it will be "released" once the pulse is finished, while for short pulses the SRL will briefly be kicked out of equilibrium.
We simulate the general rate-equation set (5.2)-(5.4) to model the CW and CCW electric fields and the carrier density of the SRL with an asymmetric linear coupling between both modes. Extra terms $F_{1,2}(t) = (1/\tau_{in})E_i \exp(i\Delta t)$ are added to Eqs. (5.2)-(5.4) to model the optical injection into the CW and CCW mode (see also Eqs. (3.1)-(3.2) for a symmetric SRL). τ_{in} is the flight time in the ring cavity (see Table 1.1), $|E_i|^2$ the injected power and $\Delta = \omega_i - \omega_0$ the detuning between the frequency of the injected light and the longitudinal mode laser frequency of the SRL. We always prepare the system in the stable CCW state and inject pulses with a rectangular shape in time. The results of the numerical time evolution simulations of the rate equations (5.2)-(5.4) are interpreted by projecting the results in the two-dimensional phase space (θ,ψ) corresponding to Eqs. (5.6)-(5.7).

6.3.1 Long trigger pulses

If the pulse width is long enough, the SRL will evolve to one of the stable attractors of the optically injected SRL. For our parameter values, this is the case if the pulse width is larger than the intrinsic time scale of alternate oscillations (AO)

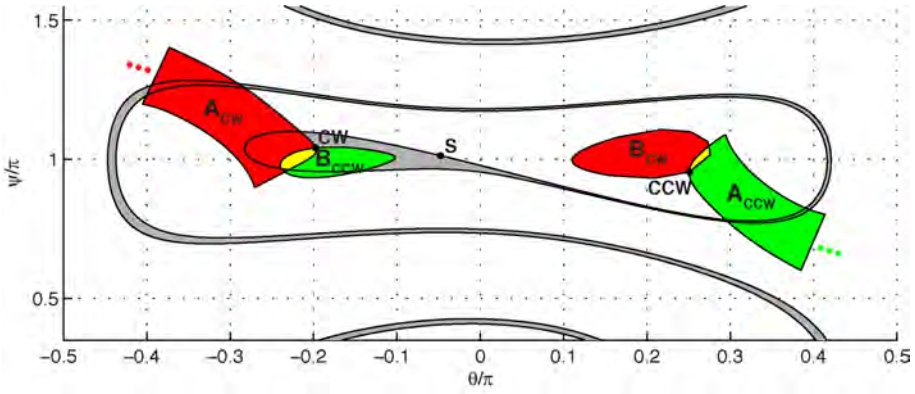

Figure 6.2: Simulation of Eqs. (5.2)-(5.4). Location of the injection-locked states for different injection amplitudes and values of the detuning. Red (green) areas indicate counter-propagating (copropagating) optical injection. $\mu = 1.65$ and $\delta = 0.045$. Other parameters are as given in Table 1.1.

in the SRL. It is clear that as the system relaxes to a steady-state of the injected SRL system, this can no longer be viewed as a small perturbation of the original SRL without injection in which we want to investigate excitability. However, the analysis of the projected position of the injection-locked solutions in the phase space of the SRL without injection and the fact whether upon releasing the injection a pulse is perceived provides us with a convincing confirmation of the excitability mechanism presented in Section 6.2.

AO are an operating regime of the SRL in which the intensities of both modes oscillate in anti-phase yielding a large clockwise excursion in the (θ, ψ) phase space, covering a very large portion of the phase space (see e.g. Chapter 2). Hence the period of the alternate oscillations gives us a quantitative measure for the transit time needed to cross the phase space. The AO operating regime is located at lower bias currents than the one we use, but is still relatively close to our operating regime. If we choose the bias current too high, the folded structure of the manifolds which enables the excitability will disappear. The vicinity to the AO operating regime implies that transit times will still be very similar. Hence, the time needed for the SRL to settle down to a new stable structure somewhere in phase space can well be approximated by the period of AO of about 10 ns.

The knowledge of the phase space structure of the optically injected SRL now allows us to predict its response. As shown in Ref. [22], where the dynamical regimes of an optically injected (symmetric) SRL are investigated, several stable structures may coexist in this phase space. Note that only steady states

(injection-locked states) will provide an accurate prediction of the system's location in phase space; as opposed to stable periodic attractors which may cover a considerable portion of the phase space. If the steady state is located somewhere across the stable manifold, it will induce an excitation after removing the injection[2]. Due to the asymmetry in the backscattering, the SRL is no longer symmetric and neither are the locations of the injection-locked states (opposite to the analysis presented in Section 3.2). Their location now depends on the mode in which we inject: CW or CCW. Since the SRL favors CCW lasing in our case, these can respectively be labeled as counter-propagating and copropagating injection. The location of the injection-locked solutions for a broad range of injection amplitudes and values of the detuning are shown in Figure 6.2. The red regions indicate the loci of injection-locked solutions for counter-propagating optical injection. Two different regions A_{CW} and B_{CW} can be distinguished when injecting in the CW mode. Both regions correspond to the existence of two resonance tongues in the optically injected SRL, related to the two unidirectional solutions CW and CCW in the non-injected system. For low injection powers the two separate injection-locked solutions A_{CW} and B_{CW} can co-exist. However, for higher injection powers the B_{CW} becomes unstable because of the increased effective gain of the CW mode when optically injecting it. In contrast, when injecting light co-propagating with the CCW mode, similar green regions indicating the injection-locked states A_{CCW} and B_{CCW} exist. The stable B_{CCW} region is smaller than B_{CW} due to the asymmetry of the SRL. A more elaborate discussion of the dynamical behavior of optical-injected SRLs is given by us in Ref. [22].
Simulations of Eqs. (5.2)-(5.4) have confirmed that the injection-locked solutions that have crossed both branches of the stable manifold indeed lead to a deterministic pulse upon releasing the injected field (not shown here). The other injection-locked solutions immediately relax to the stable state without the firing of a pulse prior to this relaxation. This result gives us confidence that the excitability scheme based on the reduced phase space (θ, ψ) explained in the previous Section is indeed valid. We now try to verify whether perturbing the SRL by injecting only short trigger pulses can be used to cross the excitability threshold to induce an optical pulse.

6.3.2 Short trigger pulses

Prior to the injection of a short pulse, the SRL will reside in the resting state, which we choose to be the CCW state with the largest basin of attraction. When

[2]Assuming that the system relaxes quickly towards the two-dimensional phase-plane (θ,ψ) after removing the optical injection such that the time evolution of the SRL can be correctly modeled by Eqs. (5.6)-(5.7)

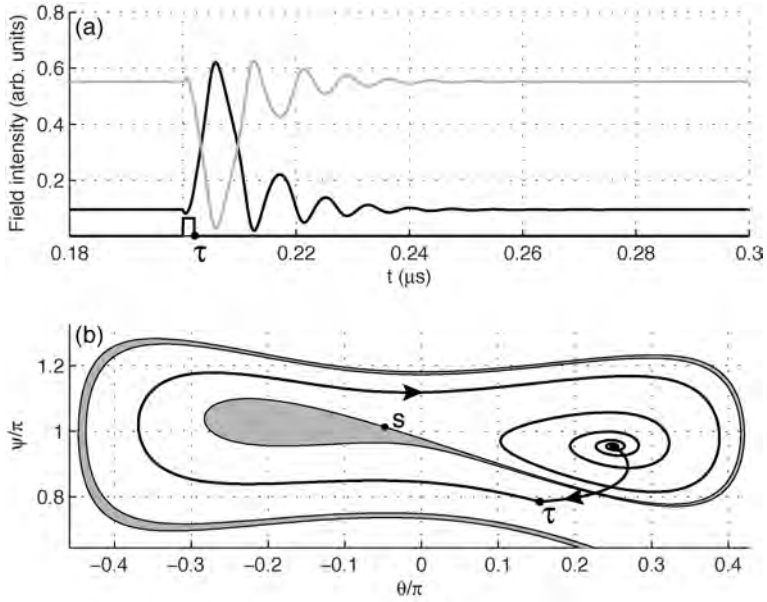

Figure 6.3: Simulation of Eqs. (5.2)-(5.4) when optically injecting a 2 ns wide square pulse. (a) Time trace of the modal intensities. The CW (CCW) modal intensity is depicted in black (gray). The injected pulse is depicted in black. τ indicates the time at which the injected pulse ends. (b) Two-dimensional phase space trajectory corresponding to the time trace. The point τ also corresponds to moment when the injected pulse ends. S indicates the location of the saddle. The basin of attraction of the CW state is depicted in gray. $\mu = 1.65$, $\delta = 0.045$ and $E_i = 0.9\,10^{-4}$ (Phase difference = $2.5\pi/2$, zero detuning - resonant injection). Other parameters are as given in Table 1.1.

injecting a short optical pulse the system can be pushed across the two folds of the stable manifold of the saddle point and thus again find itself in the basin of attraction of the CCW state. It will then follow a large deterministic excursion in phase space before relaxing again to the stable CCW state. This behavior is demonstrated in Figure 6.3 where a 2 ns wide square pulse is injected in the CW mode to trigger an excitable excursion.

The direction in phase space in which the SRL is kicked out of its stable state is mainly determined by the phase difference between the injected field and the SRL field. Depending on the value of the phase difference the fields will either constructively or destructively interfere, kicking the SRL out in opposite directions in phase space. The initial direction of the trajectory in the (θ, ψ)

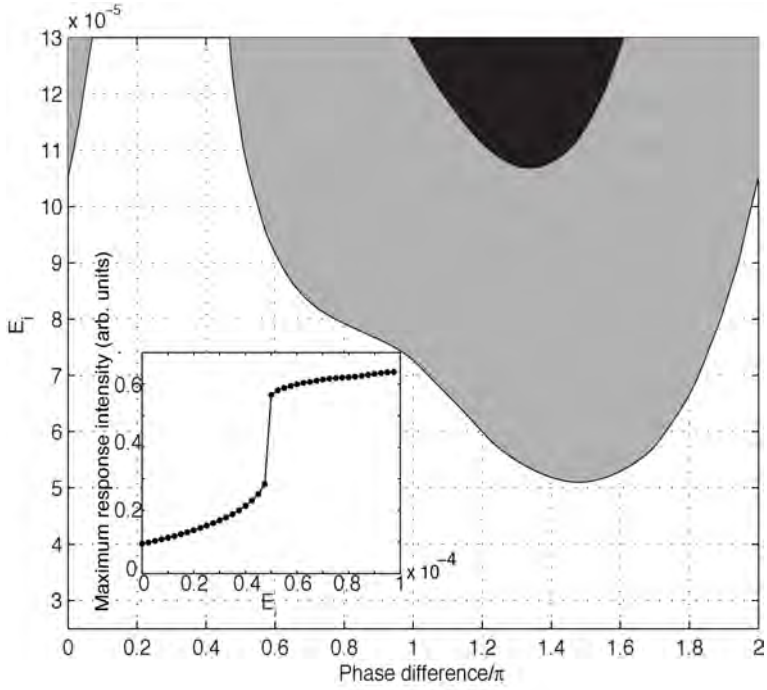

Figure 6.4: Simulation of Eqs. (5.2)-(5.4). Influence of the phase difference between the injected field and the SRL field on the excitability of the SRL. A rectangular pulse with a fixed width of 2 ns is injected in the CW direction with varying phase difference and amplitude E_i. $\mu = 1.65$ and $\delta = 0.045$. Other parameters are as given in Table 1.1. Gray indicates excitation of a single pulse while black indicates excitation of two consecutive pulses. Inset: Magnitude of the response peak vs. amplitude of the optical excitation pulse for a fixed phase difference of $3\pi/2$.

phase space is hence largely determined by this phase difference, which is an uncontrollable quantity in a practical setup and will thus play an important role in whether or not the SRL will be excited to fire a pulse. An unfavorable phase difference might lead to a failure to cross the stable manifold and thus a failure to excite the SRL.

The influence of the phase difference on the firing of the SRL is shown in Figure 6.4 for resonant optical injection of a rectangular pulse with a fixed width of 2 ns. For low injection powers, the SRL only fires a pulse when the phase difference is close to $-\pi/2$. For higher injection powers, the phase condition is less stringent but nevertheless does not allow firing when the phase difference is close to $\pi/4$.

The presence of a distinct excitability threshold can be more clearly observed in the Figure 6.4 inset. The importance of the phase difference between the fields in exciting a pulse decreases when the length of the pulses increases or when the frequencies are largely detuned.
This cumbersome phase dependency is an aspect that will arise in every optical excitable system, when the excitation is done by an optically injected pulse. The experimental results of Wünsche *et al.* in Ref. [15], covering an optically excitable multisection laser, indeed show a distinct jitter in the spikes although nominally identical pulses were injected. These failures to excite pulses in the system may also be caused by the same phase difference as here in the SRL.

6.4 Stochastic analysis

Just as the mode-hopping events in Chapter 4 were induced stochastically, the generation of optical excited pulses can be initiated similarly by crossing two branches of the stable manifold of the saddle point S. In the next Section, where we discuss our experimental characterization of excitability in the SRL using the set-up mentioned in Section 4.2, the excitable excursions will be induced by the spontaneous emission noise present in the system.
We first characterize the variation in the shape of noise-excited pulses. After crossing the excitability threshold they follow first the flow of the system and finally relax back to the initial quiescent CCW state by following the branch of the unstable manifold of the saddle S. We will demonstrate that although this excursion in phase space is largely deterministic the noisy conditions cause a spread in width and amplitude of the pulses. Moreover a more complicated interaction with the metastable CW state can largely influence the shape of the pulses. Secondly, we briefly discuss the exponential distribution of the inter-spike-interval (ISI) diagram of the pulses, confirming the excitability to be a noise-activated process.

6.4.1 Pulse characterization

Figure 6.5 shows results of simulations of the full rate-equation model (5.2)-(5.4)[3]. As in Chapter 4, spontaneous emission noise has been introduced in the field equations of Eqs. (5.2)-(5.4) by zero-mean complex Langevin forces ξ described by the correlation terms $\langle \xi_i(t+\tau)\xi_j^*(t)\rangle = 2DN\delta_{ij}\delta(\tau)$, where i, j ={CW, CCW}, N is the carrier density and D is the noise intensity. For simplicity, carrier noise

[3] An explanation of the numerical integration schemes that we use can be found in Appendix B.

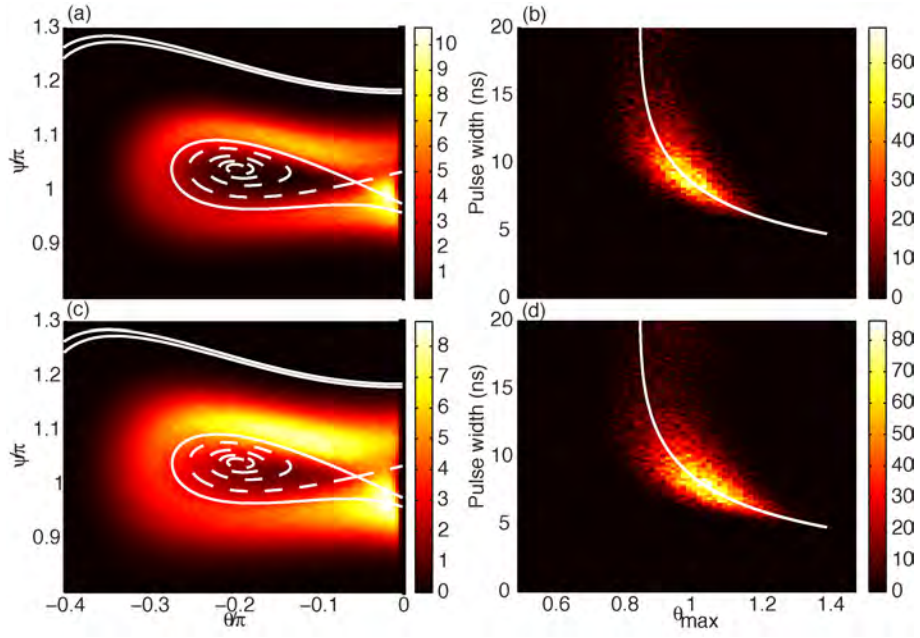

Figure 6.5: Results of simulations of Eqs. (5.2)-(5.4) with noise. (a)-(b): $D = 1.5 \times 10^{-4}$ ns^{-1}, $t_{obs} = 100$ ms, (c)-(d): $D = 2.5 \times 10^{-4}$ ns^{-1}, $t_{obs} = 10$ ms. (a) and (c): Pulse width vs pulse height. White curve indicates the prediction from the deterministic reduced model. (b) and (d): Histogram of the trajectories in asymptotically reduced two-dimensional phase space. The full (dashed) white lines indicate the stable (unstable) manifolds of the saddle. The number of events has been rescaled by a factor 10^4. $\mu = 1.65$ and $\delta = 0.05$. Other parameters are as given in Table 1.1.

has been disregarded. During the time t_{obs}, all noise-activated pulses across the boundary $\theta = 0$ are collected. After each excursion the system is put back in the CCW lasing state and rare excursions that reside longer than 20 ns around the metastable CW state are discarded. Figure 6.5(a) and (c) show histograms of the collected trajectories projected onto the asymptotically reduced two-dimensional phase space (θ, ψ), and this for two different values of the noise strength D. The full (dashed) white lines indicate the stable (unstable) manifolds of the saddle S. The histogram shows clearly that most of the noise-activated trajectories avoid the saddle point and cross the two stable manifolds "earlier". Afterwards, the excursions show a certain distribution in (θ, ψ)-space and somewhat cluster after having turned around the CW state (notice the higher number of events at

higher values of ψ). The distribution of the pulses in (θ, ψ) for different noise strengths seems qualitatively comparable. Such a distribution of the excited excursions (and thus of their amplitudes as well) can also be present in other excitable models such as the FitzHugh-Nagumo system [8].
We gain more information by analyzing the pulse width and height. The boundaries defining the width of the pulse in the time domain are defined by the moments at which the power in both counter-propagating modes is equal ($\theta = 0$). The pulse height is given by the maximum value of θ. The histograms constructed in this way are plotted in Figure 6.5(b) and (d). It is clear that there exists a close correlation between the width and the height of the different pulses: higher (larger θ) pulses move faster in phase space and are thus narrower, while lower pulses are slower and consequently also wider. This relation holds for the two different noise strengths, although it is clear that for lower noise strengths [Figure 6.5(b)] the pulses tend to be less high in amplitude and thus wider than in the case of higher noise strengths [Figure 6.5(d)]. The fact that the point cloud opens up for decreasing pulse heights is related to the nature of these pulses. These relatively long pulses tend to wander around the metastable CW state or the saddle point. Near the saddle point the deterministic trajectory greatly slows down. Hence, in this case, the transit times of the pulses are mainly determined by the noise, giving rise to a larger spread.
In fact, this correlation between the width and height of the excited pulses as observed by simulating the general rate-equation model (5.2)-(5.4) can be perfectly understood by the topology of the associated two-dimensional phase space (θ, ψ). The flow in the phase space imposes a clear relationship between the height of the pulse and the pulse width. We take $\theta = 0$ (the moment at which the power in both counter-propagating modes is equal) as the boundaries of our pulse in the time domain and choose different values of ψ as initial condition. Numerical simulations of the reduced model (5.6)-(5.7) have allowed us to construct a curve relating the width and height shown by the white line in Figure 6.5(b) and (d). The deterministic curve calculated from the reduced model perfectly fits the histogram created from the stochastic simulations of the more general rate-equation model (5.2)-(5.4). The effect of increasing noise strength amounts to shifting the point cloud *along* the curve towards lower widths and higher pulse maxima. Decreasing the noise strength has the opposite effect.
A more tangible picture is given by showing the distribution of the pulse heights and widths not in the two-dimensional space, but only in considering the width distribution or the height distribution. These histograms are shown in Figure 6.6. The pulse height distribution can be properly fitted by a Gaussian distribution $A \exp[-(\theta_{max} - B)^2/C^2]$, indicating that the height of the pulse is mainly determined by the magnitude of the perturbation and less by the topology of the flow. The average pulse height also increases with increasing noise intensity,

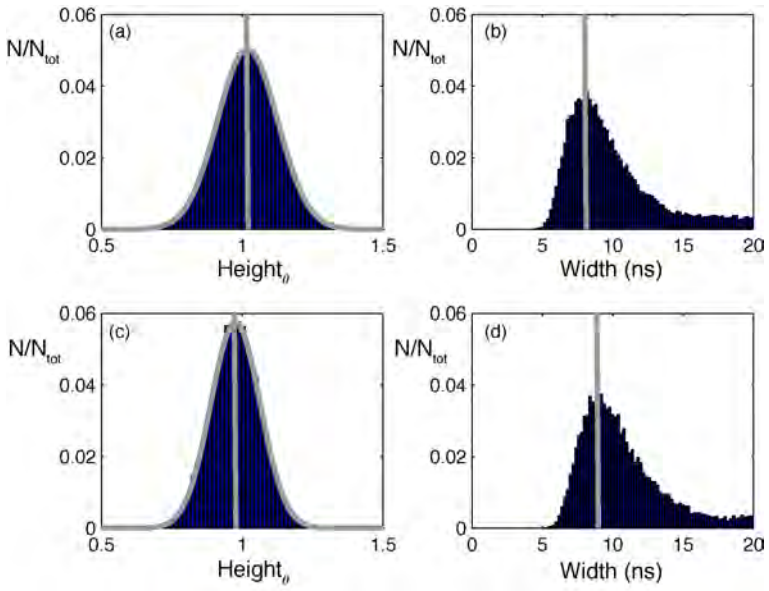

Figure 6.6: Results of simulations of Eqs. (5.2)-(5.4) with noise. The histograms N/N_{tot} are shown in function of the pulse heights (a),(c) and in function of the pulse widths (b),(d). $D = 2.5\times10^{-4}$ for (a)-(b) and $D = 1.5\times10^{-4}$ for (c)-(d). The histogram of the pulse heights can be fitted by a Gaussian: $A\exp(-((x-B)/C)^2)$. (a) 23748 events, $A = 0.0503, B = 1.019, C = 0.1508$. (c) 15052 events, $A = 0.0575, B = 0.9762, C = 0.1237$. The vertical gray lines show the maxima of the histograms: ≈ 7.99 ns in (b) and ≈ 9.20 ns in (d). $\mu = 1.65$ and $\delta = 0.05$. Other parameters are as given in Table 1.1.

initiating excursions further away from the stable saddle manifold. On the other hand, the pulse width distribution is asymmetric. Again, some of the pulses tend to erratically wander around the CW state or the saddle giving rise to the tail in the pulse width distribution. The average pulse width decreases with increasing noise intensity indicating that the flow near the stable manifold is slower. This also confirms the pulse height-width trade-off trend of Figure 6.5.

Finally, in Figure 6.7 we show typical pulse shape as the pulse width varies. Figure 6.7(a)-(e) show a random collection of pulses with widths in the following intervals: 5-6 ns, 8-9 ns, 11-12 ns, 14-15 ns, 17-18 ns, respectively. Their corresponding trajectories in the (θ, ψ) phase space is shown in gray. The faster, narrower pulses start out at a relatively large distance from the stable manifold, and afterwards remain distant from the stable manifold during the whole pulse

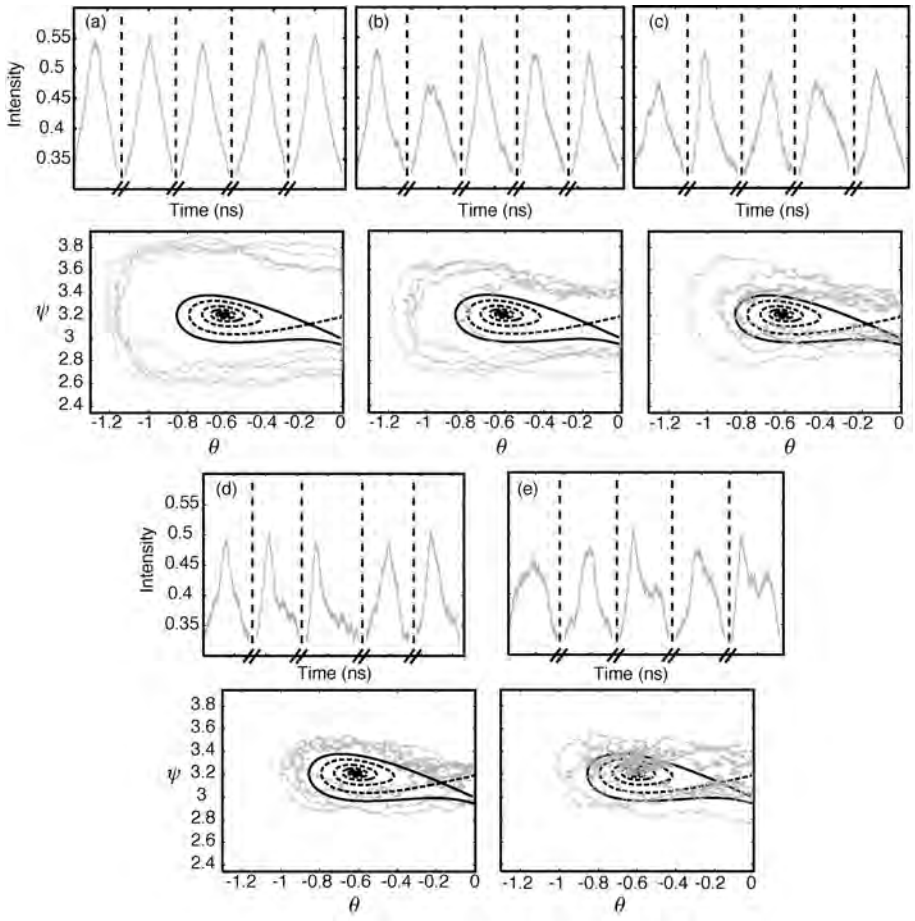

Figure 6.7: Simulation of Eqs. (5.2)-(5.4) with noise. Typical pulse shapes corresponding to different pulse widths are shown. Single pulses are collected from the time traces in panels (a)-(e) with below each panel (a)-(e) the corresponding trajectories in the (θ, ψ) phase space in gray. Stable (full) and unstable (dashed) manifolds are drawn in black. From (a) to (e) pulses are shown with widths in the following intervals: 5-6 ns, 8-9 ns, 11-12 ns, 14-15 ns, 17-18 ns. $\mu = 1.65$, $\delta = 0.05$ and $D = 2.5 \times 10^{-4}$ ns^{-1}. Other parameters are as given in Table 1.1.

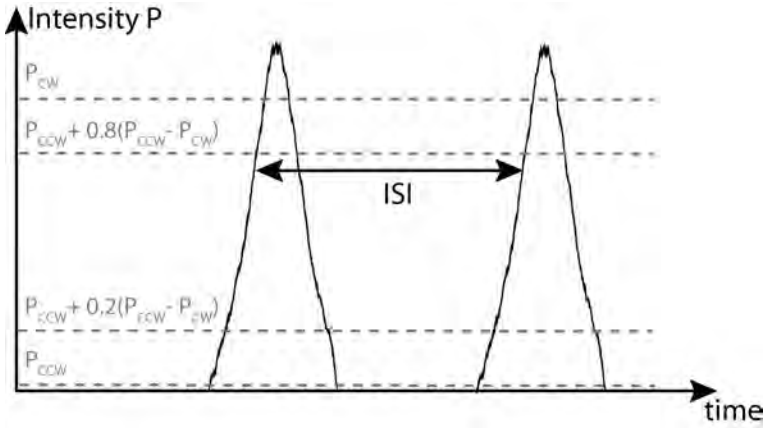

Figure 6.8: Schematic explanation of the used numerical detection criterium for the inter-spike-interval (ISI) between consecutive pulses. P represents the intensity in the CW mode.

trajectory, determining its shape. This is clearly visible in the pulses in Figure 6.7(a)-(b). Oppositely, pulses that start out closer to the stable manifold slow down and are less high. For the latter type of excursions, if the pulse trajectory comes too close to the stable manifold it can get tangled up in the metastable CW state or slowed down near the saddle, explaining the formation of possible plateaus in the pulse. In the case one gets trapped in the CW state, the pulse would show a plateau at the pulse maximum, while if the pulse slows down near the saddle, it would reveal a plateau at the edge of the pulse. The collection of exemplary pulse shapes with increasing width in Figure 6.7(a)-(e) illustrates these phenomena well. A slowing down of the pulse at the falling edge (higher values of ψ) is best visible in panels (b) and (c). In Figure 6.7(d), many of the pulses come very close to the saddle point, resulting in an even more pronounced slowing down, especially at the trailing edge of the pulse. Several rare pulse events where the system briefly gets stuck in the CW state are depicted in panel (e).

6.4.2 Inter-spike-interval diagram

In order to determine the inter-spike-interval (ISI) between consecutive pulses we have simulated Eqs. (5.2)-(5.4) during a time t = 1ms. In general the system resides in the CCW state. Defining the intensities of the CW and CCW state by

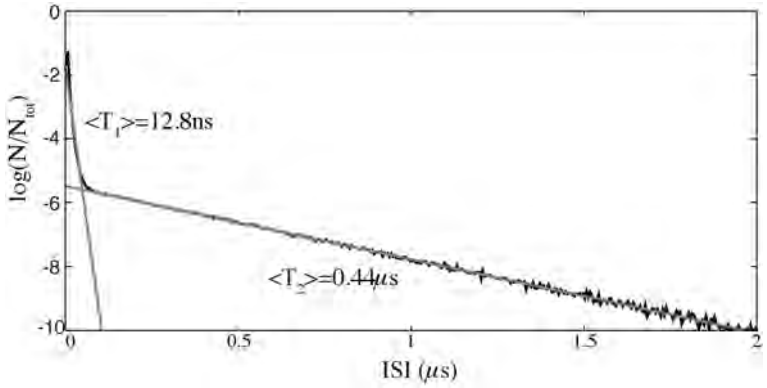

Figure 6.9: Simulation of Eqs. (5.2)-(5.4) with noise showing the inter-spike-interval diagram. Log(N/N_{tot}) is plotted in function of the inter-spike-interval in μs. The best linear fit is shown by the lines in gray. $\mu = 1.65$, $\delta = 0.05$ and $D = 2.5 \times 10^{-4}$ ns^{-1}. Other parameters are as given in Table 1.1.

$P_{CW,CCW}$ as shown in Figure 6.8, we register an excited pulse from the moment the intensity in the CW mode $P > P_{CCW} + 0.8(P_{CW} - P_{CCW})$. We define the end of the pulse as the moment when the intensity $P < P_{CCW} + 0.2(P_{CW} - P_{CCW})$. The ISI time between two such pulses is defined as in Figure 6.8.

The distribution of the ISI between all excited pulses is shown in Figure 6.9. We have plotted the logarithm of the normalized number of events log(N/N_{tot}) in function of the inter-spike-interval in μs, with N the total number of events in each bin and $N_{tot} = 1.22\ 10^6$ the total amount of excited pulses. It becomes evident from Figure 6.9 that the short ISIs and long ISIs are distributed in a different way and together represent a strongly non-Arrhenius type of behavior. Separately, each region of the ISI diagram can be fitted by an exponential curve [$\propto \exp(-t/\langle T_{1,2}\rangle)$], where the average ISI $\langle T_{1,2}\rangle$ is the fitting parameter. The fast time scale corresponds to an average ISI $\langle T_1\rangle$ of 12.8 ns, while the slow time scale events have an average ISI $\langle T_2\rangle$ of 0.44 μs. The short ISI times are a signature of multiple consecutive excited pulses, while the slow ISI time scale $\langle T_2\rangle$ corresponds to the generation of the pulses in an Arrhenius type noise-activation process across the excitability threshold. The presence of these time scales was also found in our study of stochastic mode-hopping in the bistable regime in Chapter 4. Both a mode-hop in the bistable regime and any excitation beyond the excitability threshold are described by a noise-activated escape, corresponding to the slow Arrhenius time-scale. The fast non-Arrhenius character of the ISI,

similar as for the residence time distribution for the mode-hopping, finds its origin in a noise-induced diffusion through both branches of the stable manifold, thus initiating another excursion in phase space before relaxing to the CCW state.

6.5 Experiments

The experiments have been performed on the same InP-based multi-quantum-well SRL with a racetrack geometry as in Chapter 4. The experimental set-up we have used is the one shown in Figure 4.1. A detailed description of the set-up can be found in Chapter 4. An important feature is the fact that an electrical contact has been applied to the bus waveguide that couples the light out of the ring, which can be independently pumped. The purpose of the contact is twofold: it allows to counteract absorption and to amplify on-chip the signal emitted by the ring. More interestingly, the presence of a contact allows us to continuously break the symmetry of the device in a controlled way by changing in an asymmetric way the relative strength δ and the phase $\Delta\phi_k$ of the coupling between the CW and CCW mode. Using the cleaved facet of the fiber as mirror, we are able to reflect power from one mode (e.g. CW) back into the waveguide and finally to the counter-propagating mode in the ring. The amount of power that is coupled to the CCW mode can then be controlled by tuning the waveguide current I_w, whereas its phase can be tuned by positioning the fiber facet with a piezoelectric controller. We analyze the output power of the CW mode using a fast photodiode connected to an oscilloscope with a sampling rate of 4 ns. This sampling rate is slow enough for the purpose of recording long time series for statistical purposes, and it is fast enough to sample accurately the individual excitable pulses.

6.5.1 Anatomy of the excited pulses

Due to the intrinsic symmetry of SRLs, the device is expected to operate with equal probability in either the CW or the CCW state. However, by breaking the symmetry using the piezo-controlled optical fiber and the bias-current on the bus-waveguide, the operation in one of the states (e.g. here CCW) can be favored. A time series of the power emitted in the CW direction is shown in Figure 6.10(a) for a bias-current on the ring of I_p = 45.38mA and for a waveguide current of I_w = 14.0mA. It is clear from Figure 6.10(a) that the ring operates most of the time in the CCW mode. An example of one of the single excitable pulses from this time series is shown in Figure 6.11(a). The average width of these pulses is 33.9 ± 4ns. The ISI are distributed exponentially (see inset in

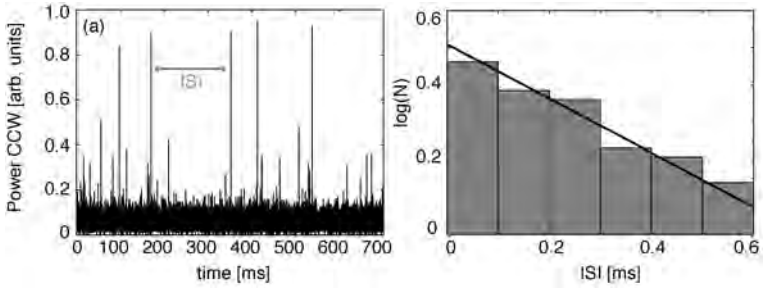

Figure 6.10: (a) Experimental time trace displaying excitability for I_p = 45.38mA and for a waveguide current of I_w = 14.0mA. (b) Distribution of the inter-spike intervals for the same I_p and I_w.

I_p [mA]	ISI [μs]	τ_1 [ns]	τ_{pp} [ns]	τ_2 [ns]
44.07	23.3	30	53.0	25.0
44.62	95.20	26.7	51.0	26.6
45.07	110.7	32.5	49.5	25.5
45.38	154.6	33.9	X	28.0

Table 6.1: Measured peak properties for different values of the bias current I_p on the ring. The current on the waveguide for I_p = 45.07mA is I_w = 14.45mA; for the other bias currents I_w = 14.0mA. The uncertainty is ±0.01mA for the bias current and ±4ns for the other quantities. For I_p = 45.38mA no double peaks were observed.

Figure 6.10(b)) with an average value of 154μs. We can therefore deduce that the pulses have the characteristic signatures of excitability, being generated in noise-activation process across a threshold and having thereafter a deterministic evolution. We remark here that no residence in the *CW* state has been observed[4]. The dependence of the ISI and pulse width τ_1 on I_p is shown in Tab. 6.1; the ISI increases with I_p, consistent with the picture of a noise activation process, whereas the pulse width remains almost constant.

Among the pulses in the time series, double-pulse events are observed such as the one shown in Figure 6.11(b). This kind of events consists of two well defined consecutive pulses separated by a drop of power to the ground state. The peak to peak interval τ_{pp} for different values of the bias current is shown in Tab. 6.1. Other pulse-shapes such as the one in Figure 6.11(c) have also been observed.

[4]We would like to remark that the ISI diagram as shown in Figure 6.10(b) is constructed by collecting the ISI between each excited pulse, where we have counted multi-pulses as one event. Therefore, the non-Arrhenius behavior as shown in Figure 6.9 is not visible here.

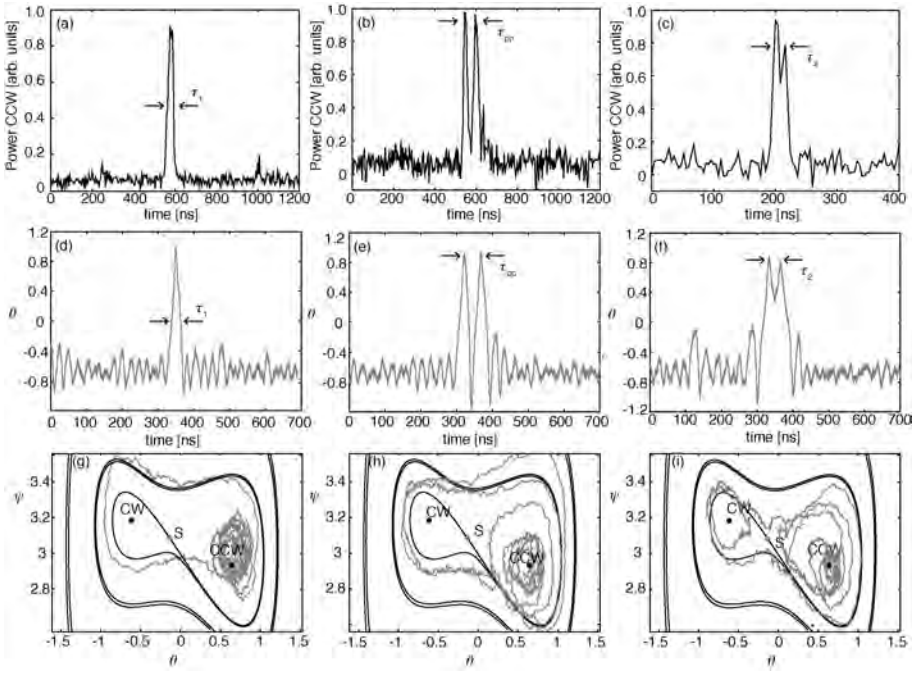

Figure 6.11: Panels (a)-(c) show experimentally measured excited pulses: (a) a single excited pulse for I_p = 45.38mA with τ_1 the pulse width; (b) a double pulse for I_p = 44.62mA with τ_{pp} the inter-peak interval; (c) a pulse with a short excursion in the metastable CW state for I_p = 44.62mA with τ_2 the distance between the two maxima. Panels (d)-(i) show the results of numerical solutions of Eqs. (5.6)-(5.7) with noise revealing excited pulses in time domain (d)-(f) and their projection on the phase space (g)-(i): (d) a single excited pulse; (e) a double pulse; (f) a pulse with two maxima associated with the "metastability" of the CW state. The parameters are the following: δ = 0.045, ϕ_k = 1.5, α = 3.5 and J = 0.691.

They are characterized by two well-defined maxima separated by a shallow dip, and are a signature of the metastability of the CW mode. The interval τ_2 between the consecutive maxima is shown in Table 6.1.

The above experimental results can be compared in a more quantitative way with numerical simulations by choosing the $k = 0.1715\ \text{ns}^{-1}$ as the dimensionless time in Eqs. (5.6)-(5.7) is scaled with the physical backscattering strength k. Figure 6.11(d)-(i) shows results from numerical simulations of Eqs. (5.6)-(5.7) with noise. The numerical time series show the same experimentally observed excited pulses as shown in Figure 6.11(a)-(c). The duration τ_1 of the single excited

pulse is a deterministic time scale corresponding to a revolution of the system in the phase space [see Figure 6.11(g)-(h)]. The peak-width has been calculated by averaging the Full-Width-Half-Maximum of a sample of 771 peaks yielding $\tau_1 = 27.54$ns corresponding well with the experimental time scale in Table 6.1.
The double pulses shown in Figure 6.11(b) are also found numerically, see Figure 6.11(e) and (h). Two well defined pulses are emitted by the SRL with an average peak-to-peak interval $\tau_{pp} = 49.22$ns (averaged on a sample of 286 double pulses). In such double pulses, the emission of the first pulse is due to a noise induced activation. During the pulse, the system evolves deterministically towards the *CCW* state. When the Z_2-symmetry is weakly broken and J is close to the homoclinic bifurcation J_{hom}, the deterministic evolution of the pulse brings the system in the vicinity of the stable manifold of S. A second excursion in the phase space, without residence in the *CCW* mode is therefore possible as shown in Figure 6.11(h). The peak-to-peak interval for such double pulses is determined by the duration of the deterministic rotation around the saddle in the phase space which is approximately twice the pulse-width. This topological insight is confirmed by the almost $2:1$ relation between $\tau_{pp} = 49.22$ ns and the pulse-width $\tau_1 = 27.54$ns (see also Table 6.1).
Finally, excitable events occur that are characterized by two maxima separated by a minimum that does not reach the ground state such as the one shown in Figure 6.11(c). A numerical time trace of such an event is depicted in Figure 6.11(f) and (i). The presence of such pulses is a result of the metastability of the CW-mode. If the system enters the basin of attraction of CW, it starts a rotation around CW which results in the oscillation of power. Due to the closeness to the homoclinic bifurcation, during the rotation the system remains close to the stable manifold of S. The noise eventually drives the SRL back into the basin of attraction of the CCW mode as shown in Figure 6.11(i). The interval between the two peaks corresponds to a rotation around the CW node and can be estimated as being approximately 1/2 of the period of a full rotation around the phase space. This is confirmed by the experimental data given in Table 6.1.

6.5.2 Width-height correlation of single pulses

In Figure 6.12 we show an analysis of the width and height of experimentally measured excited pulses for varying values of the bias current I_p on the ring. The pulses have been sampled with an accuracy of ±1ns. For all bias currents used there is a clear correlation between the width and height of the pulses as we have analyzed in more detail in Section 6.4 (see Figure 6.5). The experiments confirm that pulses with a higher peak power are narrower, while pulses with a

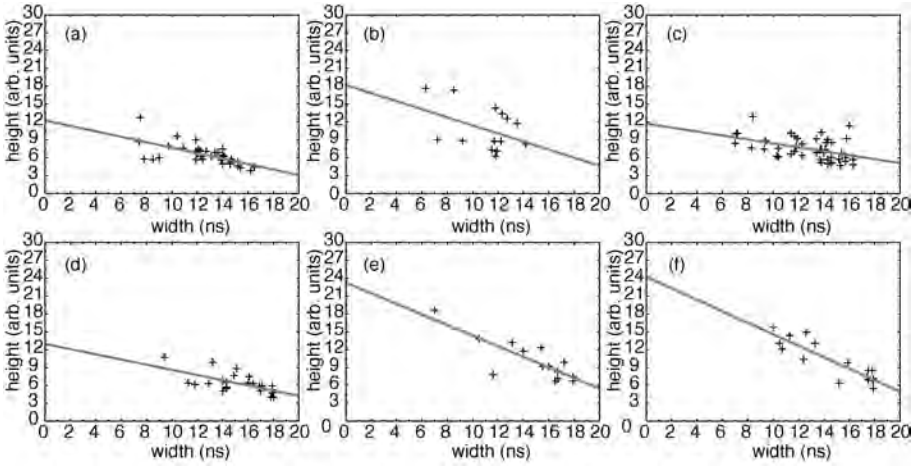

Figure 6.12: Measured width and height of the excited pulses for different values of the bias current I_p on the ring. The current on the waveguide is I_w = 14.0mA. The pulses have been sampled with an accuracy of ±1ns. From (a) to (f) the following bias current I_p have been used: (a) I_p = 42.29mA, (b) I_p = 42.38mA, (c) I_p = 42.82mA, (d) I_p = 43.54mA, (e) I_p = 44.1mA, (f) I_p = 44.49mA.

lower peak power are wider. This correlation becomes more pronounced as the bias current on the ring increases.

6.6 Conclusion

In conclusion, we have investigated excitability for generic planar systems close to Z_2-symmetry and disclosed how the shape of the invariant manifolds lead to optical pulses, either excited deterministically by e.g. an optically injected pulse or either excited through spontaneous emission noise. An optical excitable unit based on this concept has been implemented using a multi quantum-well SRL with slightly asymmetric mode-coupling. Such a unit can in principle be integrated on a chip and does not require external optical injection or feedback from an external cavity. We have used topological analysis to predict the features of three different types of excited pulses, as well as quantitative relations between the relevant time-scales. The presence of an excitability threshold has been demonstrated deterministically by optically injecting pulses to induce excitable excursions. As pulses are excited by unavoidable spontaneous emission noise in

the laser, we have performed a detailed investigation of the pulse characteristics in the presence of noise. The predictions of the theory have been confirmed by the experiments.

References

[1] S. Beri, L. Mashall, L. Gelens, G. Van der Sande, G. Mezosi, M. Sorel, J. Danckaert, and G. Verschaffelt, "Excitability in optical systems close to Z_2-symmetry," *Phys. Lett. A* **374**, 739–743, 2010.

[2] L. Gelens, S. Beri, G. Van der Sande, G. Verschaffelt, and J. Danckaert, "Multistable and excitable behavior in semiconductor ring lasers with broken Z_2-symmetry," *Eur. Phys. J. D* , doi::10.1140/epjd/e2010–00042–7, 2010.

[3] A. L. Hodgkin and A. F. Huxley, "A quantitative description of membrane current and its application to conduction and excitation in nerve," *J. Physiol.* **117**, 500, 1952.

[4] R. Kapral and K. Showalter, *Chemical Waves and Patterns*, Kluwer Academic Publishers,, Dordrecht, 2005.

[5] R. Bertram, M. J. Butte, T. Kiemel, and A. Sherman, "Topological and phenomenological classification of bursting oscillations," *B. Math. Biol.* **57**, 413–439, 1995.

[6] W. Maass, "Networks of spiking neurons: The third generation of neural network models," *Neural Networks* **10**, 1659–1671, 1997.

[7] A. S. Pikovsky and J. Kurths, "Coherence resonance in a noise-driven excitable system," *Phys. Rev. Lett.* **78**, 775, 1997.

[8] E. M. Izhikevich, "Neural excitability, spiking and bursting," *Int.J.Bifurcat.Chaos* **10**, 1171–1266, 2000.

[9] B. Lindner, J. Garcia-Ojalvo, A. Neiman, and L. Schimansky-Geier, "Effects of noise in excitable systems," *Phys. Rep.* **392**, 321, 2004.

[10] M. A. Larotonda, A. Hnilo, J. M. Mendez, and A. Yacomotti, "Experimental investigation on excitability in a laser with a saturable absorber," *Phys. Rev. A* **65**, 033812, 2002.

[11] J. L. A. Dubbeldam, B. Krauskopf, and D. Lenstra, "Excitability and coherence resonance in lasers with saturable absorber," *Phys. Rev. E* **60**, 6580, 1999.

[12] S. Wieczorek, B. Krauskopf, and D. Lenstra, "Multipulse excitability in a semiconductor laser with optical injection," *Phys. Rev. Lett.* **88**, 063901, 2002.

[13] D. Gomila, M. A. Matías, and P. Colet, "Excitability mediated by localized structures in a dissipative nonlinear optical cavity," *Phys. Rev. Lett.* **94**, 063905, 2005.

[14] F. Marino and S. Balle, "Excitable optical waves in semiconductor microcavities," *Phys. Rev. Lett.* **94**, 094101, 2005.

[15] H. J. Wünsche, O. Brox, M. Radziunas, and F. Henneberger, "Excitability of a semiconductor laser by a two-mode homoclinic bifurcation," *Phys. Rev. Lett.* **88**, 023901, 2002.

[16] G. Giacomelli, M. Giudici, S. Balle, and J. R. Tredicce, "Experimental evidence of coherence resonance in an optical system," *Phys. Rev. Lett.* **84**, 3298–3301, 2000.

[17] D. Goulding, S. P. Hegarty, O. Rasskazov, S. Melnik, M. Hartnett, G. Greene, J. G. McInerney, D. Rachinskii, and G. Huyet, "Excitability in a quantum dot semiconductor laser with optical injection," *Phys. Rev. Lett.* **98**, 153903, 2007.

[18] A. R. S. Romariz and K. H. Wagner, "Tunable vertical-cavity surface-emitting laser with feedback to implement a pulsed neural model. 1. principles and experimental demonstration," *Appl. Optics* **46**, 4736–4745, 2007.

[19] K. A. Wiesenfeld and E. Knobloch, "Effect of noise on the dynamics of a nonlinear oscillator," *Phys. Rev. A* **26**, 2946–2953, 1982.

[20] Y. Kuznetsov, *Elements of Applied Bifurcation Theory*, Springer, 3rd edition, New York, 2004.

[21] L. Gelens, G. Van der Sande, S. Beri, and J. Danckaert, "Phase-space approach to directional switching in semiconductor ring lasers," *Phys. Rev. E* **79**, 016213, 2009.

[22] W. Coomans, S. Beri, G. V. der Sande, L. Gelens, and J. Danckaert, "Optical injection in semiconductor ring lasers," *Phys. Rev. A* **81**, 033802, 2010.

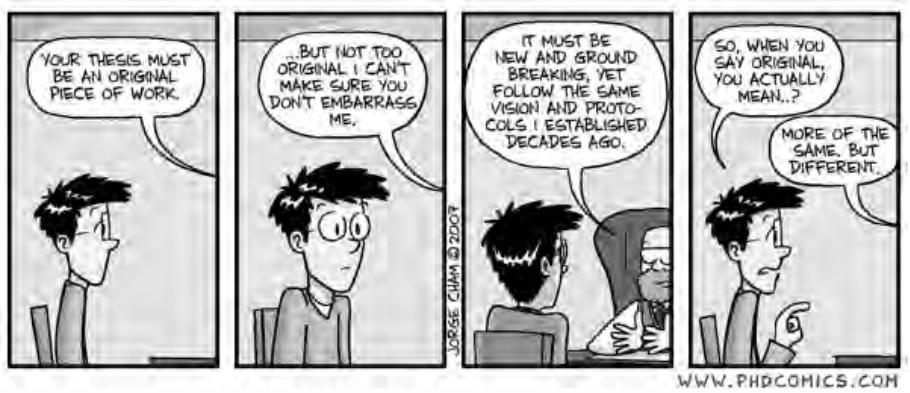

title: "More of the same" - originally published 10/3/2007

CHAPTER 7

Conclusions to Part I

We have presented an analysis and discussion of several aspects of the dynamical behavior of a semiconductor ring laser (SRL) operating in a single longitudinal and transverse mode. The results obtained can also readily be used to understand the dynamics of two interacting whispering gallery modes observed in semiconductor micro-disk lasers. Such semiconductor micro-ring and micro-disk lasers are a class of semiconductor lasers with a circular laser cavity. Such a study of the nonlinear dynamics of SRLs and micro-disk lasers comes at the right time as both lasers are presently recognized to be promising candidates for all-optical signal processing integrated on chip. More in particular, due to the possibility of bistable operation, SRLs and disk lasers can serve as optical memories by encoding digital information in the emission direction, allowing for fast switching speeds at low power [M. T. Hill *et al.*, Nature **432**, 206 (2004); L. Liu *et al.*, Nature Photon. **4**, 182 (2010)].
The study of the possible dynamical regimes in the SRL presented here is not only useful from an application point-of-view. SRLs are characterized by central reflection invariance, also called Z_2-invariance, which is encountered in a wide number of bistable systems such as in the field of biology, aerodynamics, fluid mechanics, optics and mechanics. Therefore, both the theoretical and experimental results obtained for SRLs can prove to be interesting for researchers working in these different fields.
In **Chapter 2**, we have used asymptotic methods to derive a two-variable model for the dynamical behavior of a SRL. One variable is defined by the relative intensity distribution between the two counter-propating modes present in a SRL, the clockwise mode and the counter-clockwise mode. The second variable

describes the phase difference between both of these modes. The model derived accounts for both a linear mode coupling through backscattering processes and a nonlinear mode coupling through gain saturation effects. The derivation of this simplified SRL model has allowed us to perform a systematic and largely analytical bifurcation study of all the steady-state solutions and time-periodic solutions in the system. This bifurcation analysis has provided us with an accurate prediction of the different possible operating regimes in the SRL. Moreover, we have revealed a non-trivial folded shape of the basins of attraction of the bistable unidirectional solutions in the system.

In **Chapter 3**, we have used this particular intertwining shape of the basins of attraction to propose three novel schemes to switch the operation of the ring from clockwise to counter-clockwise or vice versa. The first of such schemes shows that the operation direction of a semiconductor ring laser can be controlled by injecting a signal from only one port. We have predicted the counter-intuitive phenomenon of inducing a switch by injecting a signal which is co-propagating with the field in the ring. Such a scheme could provide practical advantages as only one master laser is needed for the switching back and forth. The second scheme consists of a well-chosen modulation in the bias current, which drags the system outside the basin of attraction of the initial state and releases it when inside the basin of attraction of the final state. Finally a third scheme has been proposed which consists of modulating the backscattering phase. The topological prediction of the three switching schemes, which present an alternative to the injection of a counter-propagating pulse to switch the laser, have been confirmed numerically.

Chapter 4 presented a theoretical and experimental investigation of the stochastic mode-hopping between the two counter-propagating lasing modes of a SRL. Experiments pointed out that the residence time distribution of both modes cannot be described by a simple one parameter Arrhenius exponential law and revealed the presence of two different mode-hop scenarios with distinct time scales. These non-Arrhenius hopping features in the SRL have been explained using the particular topology of the two-dimensional phase-space of the SRL in the bistable regime. We have also demonstrated how to steer the operation of the SRL, not only to monostable and bistable operation regions, but also multistable dynamical regimes have been uncovered. Stochastic mode-hops between multiple stable states in the SRL have been observed experimentally as predicted and understood by the two-dimensional SRL model. Finally, in the limit of small noise intensity, an auxiliary Hamiltonian system has been defined and the optimal escape paths have been calculated as well. The dependence of the activation energy on the principal laser parameters has been investigated as well.

In **Chapter 5** and **Chapter 6**, we have studied the nonlinear dynamical behavior of SRLs when their Z_2 symmetry is broken. A detailed bifurcation analysis has

shown that the SRL can become excitable. The global shapes of the invariant manifolds of a saddle in the vicinity of a homoclinic loop have been demonstrated to determine the origin of this excitability. The presence of an excitability threshold has been demonstrated deterministically by optically injecting pulses to induce excitable excursions. As in general pulses are excited by unavoidable spontaneous emission noise in the laser, we have performed a detailed investigation of the pulse characteristics in the presence of noise. A good match between theory and experiments on an asymmetric SRL has been obtained.

In summary, the good correspondence between the experiments performed both on a symmetric and asymmetric SRL and the theoretical predictions from the two-dimensional reduced SRL model confirms the relevance and strength of this model. Both the theoretical and the experimental work have benefitted from cross-fertilization. An initial observation of two distinct time-scales in the mode-hopping behavior of the bistable SRL motivated us to carry out a more detailed study of the reduced SRL model. This in-depth study of the bifurcations in the reduced system and especially a careful inspection of the two-dimensional attractor landscape of the SRL greatly increased our understanding. Novel dynamical regimes predicted by the two-dimensional model, such as the different kinds of tristable behavior, were observed in experiments only after and thanks to the theory. Based on the phase-space structure of the SRL, novel switching schemes between the unidirectional modes in the SRL could be conceived, which we hope will be verified experimentally in the future. Finally, the topological insight into the operation of the symmetric SRL was also expanded to the asymmetric SRL. The theoretical and experimental pursuit of excitability in the asymmetric SRL and the characterization of the excited pulses went hand in hand, and once again confirmed the strength of the two-dimensional asymptotic model.

To further test the applicability of the reduced model, we will confront theoretical predictions such as chaos under optical injection or current modulation and coherence resonance with experiments on a single SRL. A more ambitious goal that we would like to pursue in the near future is to study the dynamics of several SRLs coupled in different network topologies. Using theory of complex dynamics and numerical simulations, we would like to focus on the emerging behavior from network motifs that are e.g. dominantly present in neuronal networks. An experimental implementation and measurement of coupled excitable SRLs can perhaps establish a first all-optical implementation of neuronal network motifs. Such networks could be integrated on a chip and combine the advantages of SRLs and the inherent parallelism and computational power of neuronal networks.

"And now for something completely different." — Monty Python

Part II

Dissipative Solitons

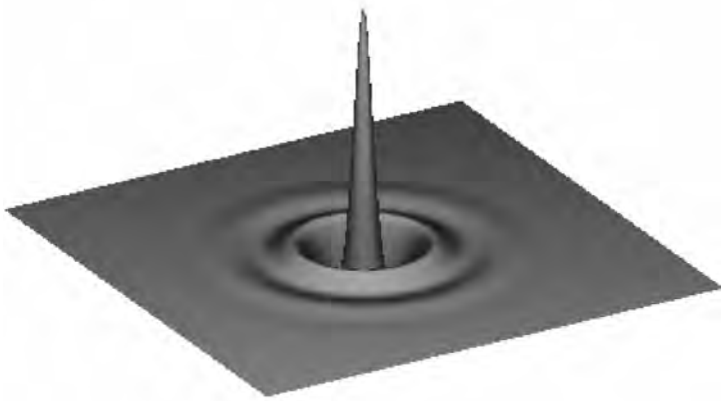

An example of a two-dimensional cavity soliton in the Lugiato-Lefever equation (Courtesy of Damià Gomila).

CHAPTER 8

Introduction

Living cells, ecosystems, stock markets, the weather and society are all examples of complex systems – large aggregations of many smaller interacting parts. These parts may be e.g. species, stocks and investors, air particles or individuals. There is one particular property that secludes a complex system from one that is merely complicated: *emergence*. Emergence is the appearance of behavior that cannot be anticipated from the behavior of one of the constituents of the system alone. In complex systems this behavior appears through self-organization, i.e. there is no external entity engineering the appearance of emergent features, but these appear spontaneously.

In this part of the thesis, we focus on emergent structures in *spatially-extended systems*. We will restrict our attention to systems that are internally dissipative and externally driven; also referred to as systems out of thermodynamical equilibrium. Emergent structures are patterns that appear spontaneously due to the interaction of each part with its immediate surroundings in space. Such patterns will not arise if the various parts are simply coexisting; the presence and nature of the spatial interaction of these parts is central. Well-known examples of spontaneous pattern formation include Rayleigh-Bénard convection in a layer of viscous fluid heated from below, Faraday surface waves on a surface of a vertically shaken liquid or granular layer, and reaction-diffusion dynamics, proposed for example to organize many processes in developmental biology [1–3].

It is interesting to note that similar patterns are seen in wildly different natural contexts, such as e.g. the stripes of a zebra [see Figure 8.1(a)] and the ripple patterns in a sand dune [see Figure 8.1(b)]. It turns out to be common for a given pattern to show up in several different systems, and many aspects of the

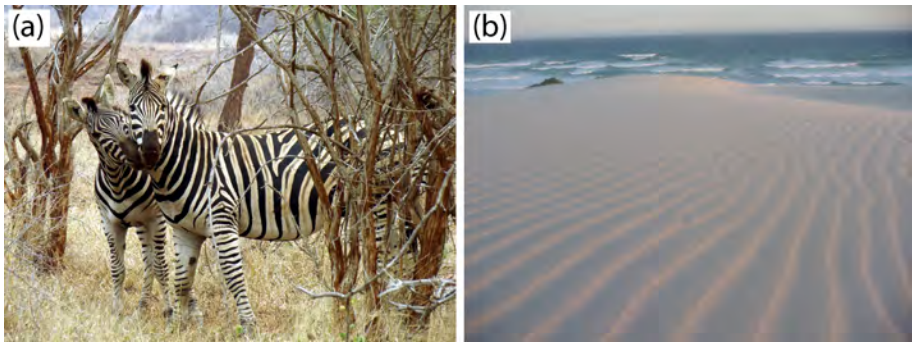

Figure 8.1: Examples of emergent spatial structures in nature. (a) Stripes on the coat of zebras [4]. (b) Ripple patterns in a sand dune created by wind or water [5].

patterns are not dependent on the finer details of the system. In fact, it has been shown that many of the characteristics of patterns can be understood from the underlying symmetry [3]. Combining methods of nonlinear dynamics and bifurcation theory led to the derivation of e.g. *amplitude equations*, that describe the dynamical behavior close to bifurcation points, or *phase equations*, modeling the slow distortions of patterns even far from the instability threshold [1–3]. Such generic model equations have been essential in the development of a universal description of pattern formation and their dynamics.
The above mentioned techniques have been proven particularly powerful to describe and understand structures with a spatial periodicity. More difficult is providing a deeper insight into the formation of *spatially localized structures*, which are emergent structures where one state is "embedded" in a background consisting of a different state. Such spatially localized structures in non-equilibrium systems are also often referred to as *dissipative solitons*. In this thesis, we will study these dissipative solitons in several generalizations of important universal model equations. In the coming Section, we provide the reader with a more detailed description and examples of dissipative solitons.

8.1 From integrable to dissipative solitons

A soliton is a localized solution of a partial differential equation (PDE) describing the evolution of an (spatially) extended nonlinear system. Solitons are strictly speaking particular solutions of systems which possess the property of *integra-*

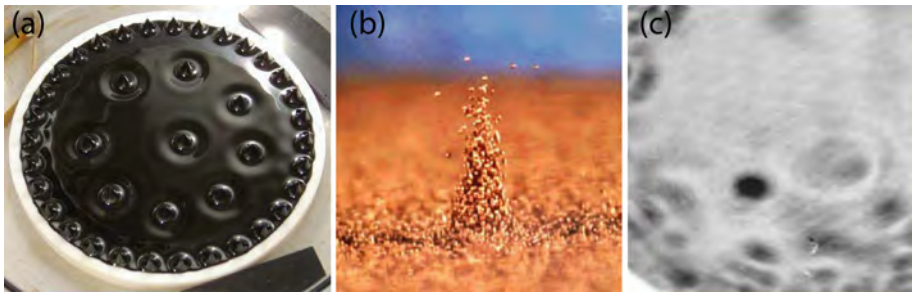

Figure 8.2: Examples of DSs in different experimental set-ups. (a) Isolated peaks on the surface of a ferrofluid driven by a homogeneous magnetic field [10]. (b) An oscillon in a vibrated layer of sand [11]. (c) A cavity soliton in a Vertical Cavity Surface Emitting Laser (VCSEL) [12].

bility. Among other special properties, such solitons remain unchanged during interactions, apart from a phase shift. Although in a part of the mathematical community, the word *soliton* is only used in the context of integrable systems, others have used the word *soliton* more loosely also for solitary waves. As real-world systems far from equilibrium are in general dissipative and non-integrable, their model equations do not admit the integrable solitons, but only solitary waves, which we will refer to in the remainder of this thesis as *dissipative solitons* (DSs) [6–9]. The main feature of these systems is that they include energy exchange with external sources.

These dissipative solitons, or *(spatially) localized structures* (LSs), are common and have been shown to arise in a wide variety of pattern forming systems, such as e.g. chemical reactions [13–15], neural systems [16, 17], granular media [11, 18], binary-fluid convection [19, 20], vegetation patterns [21, 22] and nonlinear optics [12, 23–29]. A (homogeneous) external forcing is often used to sustain the localized and extended patterns in these systems.

Figure 8.2 shows experimental observations of dissipative solitons in three different systems. Figure 8.2(a) depicts a ferrofluid, a liquid suspension containing magnetic particles. When placing such a dish of ferrofluid in a spatially homogeneous, time-independent, vertical magnetic field one stationary, isolated peak of liquid or clusters of several of such peaks can be formed on the surface [10]. Figure 8.2(b) shows a localized oscillation in a layer of sand, called *oscillon*, which alternately takes the shape of peaks and craters as the sand is vibrated vertically [11]. Finally, Figure 8.2(c) shows bright localized light spots at the output of a vertical cavity surface emitting laser (VCSEL) [12]. Such bright light spots in nonlinear optical cavities are also referred to as *cavity solitons*.

The occurrence of DSs in such diverse systems points to the presence of an underlying generic principle. It is generally accepted that the existence of DSs is directly related to the presence of bistability between two states in the system. The localized structure resembles a slug of one of these two states embedded in a background of the other state. A DS is then interpreted as a pair of bound fronts between both states. These two fronts typically interact with each other through the interior of the DS. A further classification of DS can be made on the basis of whether the bistability occurs between homogeneous or structured (patterned) solutions. This way we can distinguish different types of DSs:

- DSs in the presence of modulational instabilities:
  In systems where a homogeneous stable solution is destabilized in a modulational (or Turing) instability, patterns can be created subcritically. In this case, the homogeneous steady state coexists with the patterned state. In many cases, a slug of pattern (one or more peaks) embedded in the homogeneous background can be stable, creating DSs. Moreover, in some cases a portion of one pattern embedded in another pattern can be stable as well [30, 31].

- DSs in the presence of bistability between two homogeneous solutions:
  Bistable systems leading to the coexistence of two equivalent homogeneous solutions represent a second large group of systems that possibly allow for DSs. The different regions occupied by different homogeneous states are also called domains, and the fronts between the different domains are called domain walls. The formation and stability properties of this kind of DSs is thus intimately related to the general problem of front propagation or domain wall motion.

8.2 Generic models for dissipative solitons

In this Section, we will shortly present three important model equations admitting DS solutions that will be used in subsequent Chapters: the Lugiato-Lefever equation, the Swift-Hohenberg equation and the Ginzburg-Landau equation. While the Lugiato-Lefever equation has been derived specifically for the mean electric field in a nonlinear optical cavity, the Swift-Hohenberg equation and the Ginzburg-Landau equation are generic amplitude equations that describe the universal behavior near a bifurcation point.

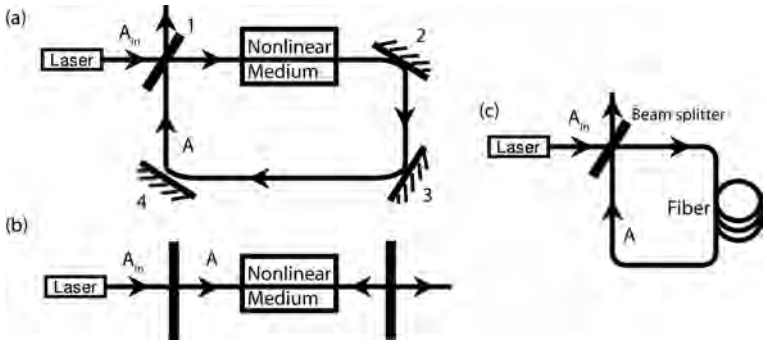

Figure 8.3: Different set-ups where the field A is described by the LLE. (a) A ring cavity partially filled with a nonlinear medium. Mirror 1 partially transmits the input beam A_{in}, while mirrors 2-4 are completely reflecting. (b) A Fabry-Perot resonator filled with a nonlinear medium. (c) A nonlinear all-fiber cavity.

8.2.1 The Lugiato-Lefever equation

Driving a nonlinear optical resonator with a homogeneous beam of light allows for a localized bright light spot embedded in a background of a homogeneous light distribution to exist at the output of the resonator [12] [see Figure 8.2(c)]. These bright light spots have also been named *cavity solitons* and are a result of the interplay between diffraction — the spreading of a light beam as it propagates — and nonlinearity. An important step forward in the study of cavity solitons and transverse structures in general, was the seminal paper of Lugiato and Lefever [32]. They introduced a mean-field cavity model, in which alternation of propagation around the cavity with coherent addition of the input field is replaced by a single partial differential equation with a driving term. The Lugiato-Lefever equation (LLE) is applicable in different types of cavities as shown in Figure 8.3. Figure 8.3(a),(b) shows schematically a ring cavity partially filled with a nonlinear medium and a Fabry-Perot resonator containing the nonlinear medium. The LLE model can also be used in the context of fiber cavities if diffraction is interchanged for a dispersion contribution, where dispersion leads to the spreading of an optical pulse as it propagates [see Figure 8.3(c)] [33–35].[1]

The LLE can be derived from the nonlinear Schrödinger equation (NLSE). The

[1]When considering the LLE as a model for the slowly varying envelope of light within a fiber cavity in the presence of dispersion, the spatial coordinate in the LLE for a spatially extended cavity with diffraction is replaced by a time coordinate. This time then corresponds to a time coordinate in the frame moving with the group velocity.

NLSE assumes an *infinite* medium, which clearly does not exist in reality. The propagation of temporal solitons in an optical fiber for thousands of kilometers comes close, but when working with spatial solitons one typically has no more than a few centimeters of material — which hardly qualifies as infinite. It is thus natural to put mirrors at each side of the medium to enlarge the travelled distance of the spatial solitons. This has the advantage that the intensity of the light is built up and the larger intensity greatly enhances the nonlinear effect. The presence of the mirrors makes the system lossy, but this can be compensated for by introducing a driving beam that feeds the cavity. This leads to a perturbed NLSE:

$$i\frac{\partial A}{\partial t} + \frac{\partial^2 A}{\partial x^2} + \eta|A|^2 A = i\epsilon(-A - i\theta A + A_{in}) \,, \tag{8.1}$$

where the right-hand side are perturbations of the NLSE. The first term on the right-hand side is a linear loss ($\epsilon > 0$), and the last one is the driving field A_{in} needed to sustain the field A against that loss. As the NLSE admits sech-like soliton solutions [36, 37], one can expect that for small perturbations ϵ Eq. (8.1) might also admit soliton solutions for a well-chosen driving term A_{in} — which is indeed the case. If one rescales Eq. (8.1), this yields the LLE, which was first introduced to describe pattern formation [32]:

$$\frac{\partial A}{\partial t} = A_{in} - (1 + i\theta)A + i\alpha\nabla_\perp^2 A + i\eta\,|A|^2\,A \,, \tag{8.2}$$

with $A(x, y, t)$ the scaled slowly varying amplitude of the field, A_{in} the input field used as a reference frequency, θ the cavity detuning, $\eta = \pm 1$ determining whether the nonlinearity is of the focusing (+) or defocusing (-) type, and $\nabla_\perp^2$ the transverse laplacian. Time is scaled to the cavity response time. The LLE model is valid for high finesse cavities, and assumes that only one longitudinal mode is excited.

The stationary homogeneous solutions A_0 of LLE [Eq. (8.2)] are easily found by taking the time- and spatial derivatives zero:

$$|A_0|^2[1 + (\theta - |A_0|^2)^2] = |A_{in}|^2 \tag{8.3}$$

For $\theta < \sqrt{3}$ this equation only has one homogeneous solution, which is the monostable regime. The homogeneous solution loses its stability at $|A_0|^2 = 1$ at which point a patterned solution is created either supercritically ($\theta < 41/30$) or subcritically ($\theta > 41/30$). For $\theta > \sqrt{3}$, there exist two homogeneous solutions for a range of input intensities $|A_{in}|^2$. This is the bistable regime[2]. The different

[2] In this bistable regime, one can again recognize two other regimes, one in which the modulational instability occurs at $|A_0|^2 = 1$, and one where the instability shifts to higher values of $|A_0|^2$, thus having $|A_0|^2 > 1$ at the instability (with critical wavenumber $k = 0$). These two different kinds of bistable regions occur at $\sqrt{3} < \theta < 2$ and $\theta > 2$, respectively.

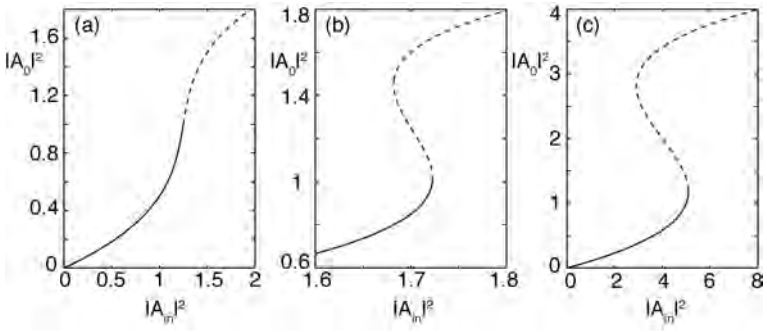

Figure 8.4: Intensity of the homogeneous solution $|A_0|^2$ as a function of the input intensity $|A_{in}|^2$ for a self-focusing Kerr cavity. (a) $\theta = 1.5 < \sqrt{3}$. (b) $\sqrt{3} < \theta = 1.85 < 2$. (c) $\theta = 3 > 2$. Solid (dashed) lines indicate stable (unstable) solutions.

monostable and bistable regions are shown in Figure 8.4. It is not hard to show the existence of these two regimes analytically. Consider the input $|A_{in}|^2$ to be a function of the stationary state $|A_0|^2$, and put the derivative $\partial|A_{in}|^2 / \partial|A_0|^2$ equal to zero,

$$\frac{\partial|A_{in}|^2}{\partial|A_0|^2} = 1 + (\theta - |A_0|^2)^2 - 2(\theta - |A_0|^2)|A_0|^2 = 0\,, \tag{8.4}$$

which gives the turning points $|A_t|^2$,

$$|A_{t\pm}|^2 = \frac{2\theta}{3} \pm \frac{1}{3}\sqrt{\theta^2 - 3}\,. \tag{8.5}$$

It is clear that for $\theta^2 < 3$ there are no turning points, while for $\theta^2 > 3$ there are two, $|A_{t\pm}|^2$. At $|A_{t-}|^2$ the solution switches up from the lower branch to the higher branch, at $|A_{t+}|^2$ it switches down again.
In the remainder of this thesis we will mainly focus on the monostable regime $41/30 < \theta < \sqrt{3}$ where for $|A_0|^2 < 1$ one stable homogeneous solution exists, and can coexist with a stable pattern created subcritically in the modulational instability at $|A_0|^2 = 1$.

8.2.2 The Swift-Hohenberg equation

The real Swift-Hohenberg equation (RSHE) has proved to be an invaluable model equation for systems undergoing a bifurcation to time-independent structured

states with a finite wavenumber at onset [38]. The equation was originally suggested as a model of infinite Prandtl number convection [39] but finds application in its simplest form in the theory of buckling [40], phase transitions [41] and nonlinear optics [42, 43]. The equation is particularly useful for understanding DSs that are commonly found in systems exhibiting bistability between two states, one of which is homogeneous in space (the trivial state) and the other heterogeneous or structured [38]. In this case the equation takes the following form, in one spatial dimension,

$$\frac{\partial A}{\partial t} = rA - (\frac{\partial^2}{\partial x^2} + k_0^2)^2 A + f(A)\,, \tag{8.6}$$

where $A(x,t)$ is a real order parameter and $f(A)$ denotes nonlinear terms. Most useful are the two cases, $f = f_{23} \equiv b_2 A^2 - A^3$ [44] and $f = f_{35} \equiv b_3 A^3 - A^5$ [45]. When $b_2 > \sqrt{27/38}k_0^2$ (resp. $b_3 > 0$) the primary bifurcation from the trivial state $A = 0$ takes place at $r = 0$ and yields a *subcritical* branch of spatially periodic states with wavenumber k_0. This characteristic length scale k_0 can be scaled out of the equation by applying the transformation

$$k_0^4 t \to t,\, r/k_0^4 \to r,\, k_0 x \to x,\, f(\cdot)/k_0^4 \to f(\cdot). \tag{8.7}$$

As it is convenient in the following Chapters to see the dependence of the dynamical behavior on the length scale k_0, we will leave k_0 explicitly in Eq. (8.6). Furthermore, it is interesting to note that the RSHE has a variational structure with a Lyapunov function (free energy) F_{SH} given by

$$F_{SH} = \frac{1}{2L}\int_0^L [-r|A|^2 + \frac{1}{2}|A|^4 + |(\frac{\partial^2}{\partial x^2} + k_0^2)A|^2]dx, \tag{8.8}$$

such that

$$\frac{dF_{SH}}{dt} = -\frac{1}{L}\int_0^L |A_t|^2 dx \tag{8.9}$$

and the free energy F_{SH} continuously decreases with time until a stationary state is reached corresponding to a local minimum of F_{SH}.
There are many systems, however, that are described by the Swift-Hohenberg equation for a complex order parameter:

$$\frac{\partial A}{\partial t} = rA - (1 + i\beta)(\frac{\partial^2}{\partial x^2} + k_0^2)^2 A - (1 + ib)f(A), \tag{8.10}$$

where A is a complex field and we take $f(A) = |A|^2 A$ as the nonlinear term in this thesis. The equation is fully parametrized by the real coefficients r, β and b. Eq. (8.10) models pattern formation arising from an oscillatory instability with

a finite wavenumber at onset [46, 47]. As a result the complex Swift-Hohenberg equation (CSHE) frequently arises in nonlinear optics. For example, Lega *et al.* [48, 49] have shown that the general set of Maxwell-Bloch equations for Class A and C lasers can be adequately described by the CSHE; see also [50]. The CSHE also describes nondegenerate optical parametric oscillators (OPOs) [51–53], photorefractive oscillators [54], semiconductor lasers [55] and passively mode-locked lasers [56]. In general, the resulting Swift-Hohenberg equation for a complex field in these systems also has complex coefficients which breaks the variational structure of the SHE and allows for more complex dynamics. Whereas DSs in the RSHE have been studied in great depth [38, 44, 45, 57, 58], much less is known about DSs in the CSHE.

8.2.3 The Ginzburg-Landau equation

As mentioned at the beginning of this Section, *Ginzburg-Landau*-type equations (like Swift-Hohenberg-type equations) are *amplitude equations* that serve as universal model equations near a bifurcation point [1, 59]. The name of this type of equations is derived from the formal similarity with the Ginzburg-Landau theory of superconductivity [60], although the latter did not deal with dynamics. However, apart from providing a theory for superconductivity, a large number of pattern forming phenomena can be analyzed by using these amplitude equations, which describe slow modulations in space and time of a simple basic pattern that can be determined from the linear analysis of the equations of the physical system. The form of the amplitude equation depends only on the nature of the linear instability, but not on other details of the system. The most important distinction is whether the basic pattern is stationary, leading to the real amplitude equation, or intrinsically time dependent, in which case an equation with complex coefficients describes a complex amplitude. There are several forms of these Ginzburg-Landau equations, a 1D prototype with real coefficients of which is

$$\frac{\partial A}{\partial t} = \mu A + \frac{\partial^2 A}{\partial x^2} - A^3, \tag{8.11}$$

with A being a real field and μ the gain parameter. The diffusion and the nonlinear term have been scaled to one without loss of generality. We will refer to Eq. (8.11) as the real Ginzburg-Landau equation (RGLE) [1, 59], which can serve as a prototypical model of a spatially extended system with two equivalent steady state solutions $\pm\sqrt{\mu}$. Eq. (8.11) arises naturally near any stationary supercritical bifurcation when the system is translationally invariant and spatially reversible ($x \to -x$), such as e.g. in Rayleigh-Bénard convection and Taylor-Couette flow [61].

If the instability leads to traveling waves, i.e. if the pattern which emerges is time-dependent, the resulting amplitude equation generalizes to the complex Ginzburg-Landau equation (CGLE):

$$\frac{\partial A}{\partial t} = \mu A + (1 + \mathrm{i}\alpha)\frac{\partial^2 A}{\partial x^2} - (1 + \mathrm{i}\beta)|A|^2 A, \tag{8.12}$$

where μ measures the distance from the oscillatory instability threshold, α and β represent the linear and nonlinear dispersion. For $\alpha, \beta \to 0$, the RGLE is recovered. The CGLE equation arises e.g. in Rayleigh-Bénard convection, hydrothermal waves, and various optical systems, such as lasers, parametric amplifiers, Fabry-Perot cavities filled with nonlinear material, and optical transmission lines [1, 59, 61].
Although the RGLE and the CGLE look rather similar, the behavior of their solutions is very different. Like the RSHE, the RGLE (8.11) can be written in a variational form:

$$\frac{\partial A}{\partial t} = -\frac{\partial F_{GL}}{\partial A^*} \tag{8.13}$$

with the free energy F_{GL}

$$F_{GL} = \int [-\mu|A|^2 + \frac{1}{2}|A|^4 + |\frac{\partial^2 A}{\partial x^2}|^2]dx, \tag{8.14}$$

from which it follows that $dF_{GL}/dt \leq 0$. A lot of understanding can be gained in this case by analyzing the energy landscape and knowing that the system evolves towards local minima of the free energy function F_{GL}. In the case $\alpha, \beta \neq 0$ the CGLE (8.12) can no longer be derived from a Lyapunov function and it displays a much richer variety of dynamical behavior than its real counterpart (8.11) (just like is the case when comparing the RSHE (8.6) and the CSHE (8.10)).
Finally, we also mention the parametrically forced Complex Ginzburg Landau Equation (PCGLE) as a type of Ginzburg-Landau equation:

$$\frac{\partial A}{\partial t} = (1 + \mathrm{i}\alpha)\frac{\partial^2 A}{\partial x^2} + (\mu + \mathrm{i}\nu)A - (1 + \mathrm{i}\beta)|A|^2 A + pA^* \tag{8.15}$$

where μ measures the distance from the oscillatory instability threshold, ν is the detuning between the driving and the natural frequencies, $p > 0$ is the forcing amplitude, α and β represent the linear and nonlinear dispersion. The PCGLE is a generic amplitude equation for oscillatory systems parametrically forced at twice the natural frequency [62]. Like the RGLE (but opposite to the CGLE) Eq. (8.15) has two equivalent steady state solutions, a property which we will use in later Chapters. The PCGLE has been used to describe a light sensitive form of the Belousov-Zhabotinsky reaction [63], and finds applications in the optical vectorial Kerr resonator [64, 65] and the degenerate Optical Parametric Oscillator (OPO) [65, 66].

8.3 Overview of Part II

- In **Chapter 9**, we investigate the snaking behavior of one-dimensional bright and dark solitons in a nonlinear optical cavity with diffraction and/or dispersion compensation. Opposite to previous studies, higher order spatial/temporal effects are taken into account. A stability analysis of a LLE with fourth-order spatial derivatives is carried out. Furthermore, the snaking bifurcation structure of both bright and dark solitons in the presence of a subcritical modulational instability towards patterns is studied.

- In **Chapter 10**, we explore the size and dynamical instabilities of dissipative solitons in a nonlinear optical cavity, called cavity solitons, modeled by the LLE model with higher order spatial derivatives. These higher order terms need to be included in the region of diffraction compensation. For small values of the diffraction coefficient, we show that higher order spatial derivatives can impose a new limit on the width of cavity solitons, going beyond the traditional diffraction limit. Furthermore, we elaborate on the different possible mechanisms that can destabilize the cavity solitons, leading to stable oscillations, expanding patterns, or making the solitons disappear. Multiple routes towards excitability are shown to be present in the system and we demonstrate that different regions admitting stationary, oscillating or excitable solitons unfold from two Takens-Bogdanov codimension-2 points.

- In **Chapter 11**, we study the CSHE with real coefficients admitting phase-winding states in which the real and imaginary parts of the order parameter oscillate periodically but with a constant phase difference between them. Such solutions can be unstable to a longwave instability. We demonstrate that depending on parameters the evolution of this instability may or may not conserve phase. In the former case the system undergoes slow coarsening described by a Cahn-Hilliard equation; while in the latter it undergoes repeated phase-slips leading either to a stable phase-winding state or to a faceted state consisting of an array of frozen defects connecting phase-winding states with equal and opposite phase. The transitions between these regimes are studied and their location in parameter space is determined.

- In **Chapter 12**, we expand the study of the CSHE presented in Chapter 11 by allowing the coefficients to be complex, breaking the variational structure of the model equation. A convective Cahn-Hilliard type equation is derived to describe the evolution of long-wavelength instabilities in the

system and a great complexity in dynamical behavior is uncovered in the CSHE.

- In **Chapter 13**, we demonstrate that nonlocal coupling strongly influences the dynamics of fronts connecting two equivalent states. In two Ginzburg-Landau prototype models, the RGLE and the PCGLE, we observe a large amplification in the interaction strength between two opposite fronts increasing front velocities several orders of magnitude. By analyzing the spatial dynamics we prove that way beyond quantitative effects, nonlocal terms can also change the overall qualitative picture by inducing oscillations in the front profile. This leads to a mechanism for the formation of localized structures not present for local interactions. Finally, nonlocal coupling can induce a steep broadening of localized structures, eventually annihilating them.

- Finally, in **Chapter 14**, we shortly revisit the obtained results in Part II of this thesis.

References

[1] M. Cross and P. Hohenberg, "Pattern-formation outside of equilibrium," *Rev. Mod. Phys.* **65**, 851–1112, 1993.

[2] J. Murray, *Mathematical Biology*, Springer, New York, 1989.

[3] R. Hoyle, *Pattern Formation: an introduction to methods*, Cambridge University Press, 2006.

[4] "`http://upload.wikimedia.org/wikipedia/commons/e/e1/Zebras_in_love-JD.jpg`,"

[5] "`http://en.wikipedia.org/wiki/File:Sand_dune_ripples.jpg`,"

[6] S. Trillo and W. Toruellas, *Spatial Solitons*, vol. 82 of *Springer Series in Optical Sciences*, Springer-Verlag, Berlin, 2001.

[7] Y. S. Kivshar and G. P. Agrawal, *Optical Solitons: From Fibers to Photonic Crystals*, Academic Press, San Diego, 2003.

[8] N. N. Rosanov, *Spatial Hysteresis and Optical Patterns*, Springer series in synergetics, Springer, Berlin, 2002.

[9] T. Ackemann and W. J. Firth, "Dissipative solitons in pattern-forming nonlinear optical systems: Cavity solitons and feedback solitons," in *Lecture Notes in Physics, Berlin Springer Verlag*, **661**, 55–100, 2005.

[10] R. Richter and I. V. Barashenkov, "Two-dimensional solitons on the surface of magnetic fluids," *Phys. Rev. Lett.* **94**, 184503, 2005.

[11] P. B. Umbanhowar, F. Melo, and H. L. Swinney, "Localized excitations in a vertically vibrated granular layer," *Nature* **382**, 793–796, 1996.

[12] S. Barland, J. R. Tredicce, M. Brambilla, L. A. Lugiato, S. Balle, M. Giudici, T. Maggipinto, L. Spinelli, G. Tissoni, T. Knödl, M. Miller, and R. Jäger, "Cavity solitons as pixels in semiconductor microcavities," *Nature* **419**, 699–702, 2002.

[13] J. E. Pearson, "Complex patterns in a simple system," *Science* **261**, 189–192, 1993.

[14] K. J. Lee, W. D. McCormick, Q. Ouyang, and H. L. Swinney, "Pattern formation by interacting chemical fronts," *Science* **261**, 192–194, 1993.

[15] V. K. Vanag and I. R. Epstein, "Localized patterns in reaction-diffusion systems," *Chaos* **17**, 037110, 2007.

[16] C. R. Laing, W. C. Troy, B. Gutkin, and G. B. Ermentrout, "Multiple bumps in a neuronal model of working memory," *SIAM J. Appl. Math.* **63**, 62–97, 2002.

[17] S. Coombes, "Waves, bumps, and patterns in neural field theories," *Biological Cybernetics* **93**(2), 91–108, 2005.

[18] O. Lioubashevski, Y. Hamiel, A. Agnon, Z. Reches, and J. Fineberg, "Oscillons and propagating solitary waves in a vertically vibrated colloidal suspension," *Phys. Rev. Lett.* **83**, 3190–3193, 1999.

[19] J. J. Niemela, G. Ahlers, and D. S. Cannell, "Localized traveling-wave states in binary-fluid convection," *Phys. Rev. Lett.* **64**, 1395, 1990.

[20] O. Batiste and E. Knobloch, "Simulations of localized states of stationary convection in He-3-He-4 mixtures," *Phys. Rev. Lett.* **95**, 244501, 2005.

[21] E. Meron, E. Gilad, J. von Hardenberg, M. Shachak, and Y. Zarmi, "Vegetation patterns along a rainfall gradient," *Chaos, Solitons and Fractals* **19**, 367–376, 2004.

[22] O. Lejeune, M. Tlidi, and P. Couteron, "Localized vegetation patches: A self-organized response to resource scarcity," *Phys. Rev. E* **66**, 010901, 2002.

[23] A. J. Scroggie, W. J. Firth, G. S. McDonald, M. Tlidi, R. Lefever, and L. A. Lugiato, "pattern-formation in a passive kerr cavity," *Chaos, Solitons and Fractals* **4**, 1323, 1994.

[24] V. B. Taranenko, K. Staliunas, and C. O. Weiss, "Spatial soliton laser: Localized structures in a laser with a saturable absorber in a self-imaging resonator," *Phys. Rev. A* **56**, 1582–1591, 1997.

[25] M. Pesch, E. Große Westhoff, T. Ackemann, and W. Lange, "Observation of a discrete family of dissipative solitons in a nonlinear optical system," *Phys. Rev. Lett.* **95**, 143906, 2005.

[26] M. Tlidi, P. Mandel, and R. Lefever, "Localized structures and localized patterns in optical bistability," *Phys. Rev. Lett.* **73**, 640–643, 1994.

[27] U. Bortolozzo, L. Pastur, P. L. Ramazza, M. Tlidi, and G. Kozyreff, "Bistability between different localized structures in nonlinear optics," *Phys. Rev. Lett.* **93**, 253901, 2004.

[28] X. Hachair, S. Barland, L. Furfaro, M. Giudici, S. Balle, J. R. Tredicce, M. Brambilla, T. Maggipinto, I. M. Perrini, G. Tissoni, and L. Lugiato, "Cavity solitons in broad-area vertical-cavity surface-emitting lasers below threshold," *Phys. Rev. A* **69**, 043817, 2004.

[29] P. Genevet, S. Barland, M. Giudici, and J. Tredicce, "Cavity soliton laser based on mutually coupled semiconductor microresonators," *Phys. Rev. Lett.* **101**, 123905, 2008.

[30] U. Bortolozzo, M. G. Clerc, C. Falcon, S. Residori, and R. Rojas, "Localized states in bistable pattern-forming systems," *Phys. Rev. Lett.* **96**, 214501, 2006.

[31] G. Lippi, H. Grassi, T. Ackemann, A. Aumann, B. Schapers, J. Seipenbusch, and J. Tredicce, "Bistability and transients in CO2 laser patterns," *J. Opt. B - Quantum. S. O.* **1**, 161, 1999.

[32] L. A. Lugiato and R. Lefever, "Spatial dissipative structures in passive optical systems," *Phys. Rev. Lett.* **58**, 2209–2211, 1987.

[33] M. Tlidi, A. Mussot, E. Louvergneaux, G. Kozyreff, A. G. Vladimirov, and M. Taki, "Control and removal of modulational instabilities in low-dispersion photonic crystal fiber cavities," *Opt. Lett.* **32**, 662, 2007.

[34] G. Kozyreff, M. Tlidi, A. Mussot, E. Louvergneaux, M. Taki, and A. G. Vladimirov, "Localized beating between dynamically generated frequencies," *Phys. Rev. Lett.* **102**, 043905, 2009.

[35] M. Tlidi and L. Gelens, "High-order dispersion stabilizes dark dissipative solitons in all-fiber cavities," *Opt. Lett.* **35**, 306, 2010.

[36] R. Chiao, E. Garmire, and C. Townes, "Self-trapping of optical beams," *Phys. Rev. Lett.* **13**, 479–482, 1964.

[37] V. Zakharov and A. Shabat, "Exact theory of two-dimensional self-focusing and one-dimenstional self-modulation of waves in nonlinear media," *Sov. Phys. JETP* **34**, 1972.

[38] A. R. Champneys, "Homoclinic orbits in reversible systems and their applications in mechanics, fluids and optics," *Physica D* **112**, 158–186, 1998.

[39] J. Swift and P. Hohenberg, "Hydrodynamic fluctuations at convective instability," *Phys. Rev. A* **15**, 319–328, 1977.

[40] G. W. Hunt, M. A. Peletier, A. R. Champneys, P. D. Woods, M. A. Wadee, C. J. Budd, and G. J. Lord, "Cellular buckling in long structures," *Nonlinear Dynamics* **21**, 3–29, 2000.

[41] P. L. Geissler and D. R. Reichman, "Nature of slow dynamics in a minimal model of frustration-limited domains," *Phys. Rev. E* **69**, 021501, 2004.

[42] M. Tlidi, P. Mandel, and R. Lefever, "Localized structures and localized patterns in optical bistability," *Phys. Rev. Lett.* **73**, 640, 1994.

[43] G. Kozyreff and M. Tlidi, "Nonvariational real Swift-Hohenberg equation for biological, chemical, and optical systems," *Chaos* **17**, 037103, 2007.

[44] J. Burke and E. Knobloch, "Localized states in the generalized Swift-Hohenberg equation," *Phys. Rev. E* **73**, 056211, 2006.

[45] J. Burke and E. Knobloch, "Snakes and ladders: Localized states in the Swift-Hohenberg equation," *Phys. Lett. A* **360**, 681–688, 2007.

[46] B. A. Malomed, "Nonlinear waves in nonequilibrium systems of the oscillatory type. 1.," *Z. Phys. B* **55**, 241–248, 1984.

[47] M. Bestehorn and H. Haken, "Traveling waves and pulses in a 2-dimensional large-aspect-ratio system," *Phys. Rev. A* **42**, 7195–7203, 1990.

[48] J. Lega, J. V. Moloney, and A. C. Newell, "Swift-Hohenberg equation for lasers," *Phys. Rev. Lett.* **73**, 2978–2981, 1994.

[49] J. Lega, J. V. Moloney, and A. C. Newell, "Universal description of laser dynamics near treshold," *Physica D* **83**, 478–498, 1995.

[50] K. Staliunas, "Laser Ginzburg-Landau equation and laser hydrodynamics," *Phys. Rev. A* **48**, 1573–1581, 1993.

[51] S. Longhi and A. Geraci, "Swift-Hohenberg equation for optical parametric oscillators," *Phys. Rev. A* **54**, 4581–4584, 1996.

[52] V. J. Sánchez-Morcillo, E. Roldán, G. J. de Valcárcel, and K. Staliunas, "Generalized complex Swift-Hohenberg equation for optical parametric oscillators," *Phys. Rev. A* **56**, 3237–3244, 1997.

[53] K. Staliunas, G. Slekys, and C. O. Weiss, "Nonlinear pattern formation in active optical systems: shocks, domains of tilted waves, and cross-roll patterns," *Phys. Rev. Lett.* **79**, 2658–2661, 1997.

[54] K. Staliunas, M. F. H. Tarroja, G. Slekys, C. O. Weiss, and L. Dambly, "Analogy between photorefractive oscillators and class-A lasers," *Phys. Rev. A* **51**, 4140–4151, 1995.

[55] J.-F. Mercier and J. V. Moloney, "Derivation of semiconductor laser mean-field and Swift-Hohenberg equations," *Phys. Rev. E* **66**, 036221, 2002.

[56] J. M. Soto-Crespo and N. Akhmediev, "Composite solitons and two-pulse generation in passively mode-locked lasers modeled by the complex quintic Swift-Hohenberg equation," *Phys. Rev. E* **66**, 066610, 2002.

[57] P. D. Woods and A. R. Champneys, "Heteroclinic tangles and homoclinic snaking in the unfolding of a degenerate reversible Hamiltonian-Hopf bifurcation," *Physica D* **129**, 147, 1999.

[58] J. Knobloch and T. Wagenknecht, "Homoclinic snaking near a heteroclinic cycle in reversible systems," *Physica D* **203**, 82–93, 2005.

[59] I. S. Aranson and L. Kramer, "The world of the complex Ginzburg-Landau equation," *Rev. Mod. Phys.* **74**, 99–143, 2002.

[60] V. Ginzburg and L. Landau *Zh. Eksp. Teor. Fiz.* **20**, 1064, 1950.

[61] W. van Saarloos, "Front propagation into unstable states," *Phys. Rep.* **386**, 29–222, 2003.

[62] P. Coullet, J. Lega, B. Houchmanzadeh, and J. Lajzerowicz, "Breaking chirality in nonequilibrium systems," *Phys. Rev. Lett.* **65**, 1352–1355, 1990.

[63] V. Petrov, Q. Ouyang, and H. L. Swinney, "Resonant pattern formation in a chemical system," *Nature* **388**, 655–657, 1997.

[64] D. Gomila, P. Colet, G.-L. Oppo, and M. San Miguel, "Stable droplets and growth laws close to the modulational instability of a domain wall," *Phys. Rev. Lett.* **87**, 194101, 2001.

[65] D. Gomila, P. Colet, M. San Miguel, A. J. Scroggie, and G.-L. Oppo, "Stable droplets and dark-ring cavity solitons in nonlinear optical devices," *IEEE J. Quantum. Electron.* **39**, 238–244, 2003.

[66] K. Staliunas, "Transverse pattern-formation in optical parametric oscillators," *J. Mod. Opt.* **42**, 1261, 1995.

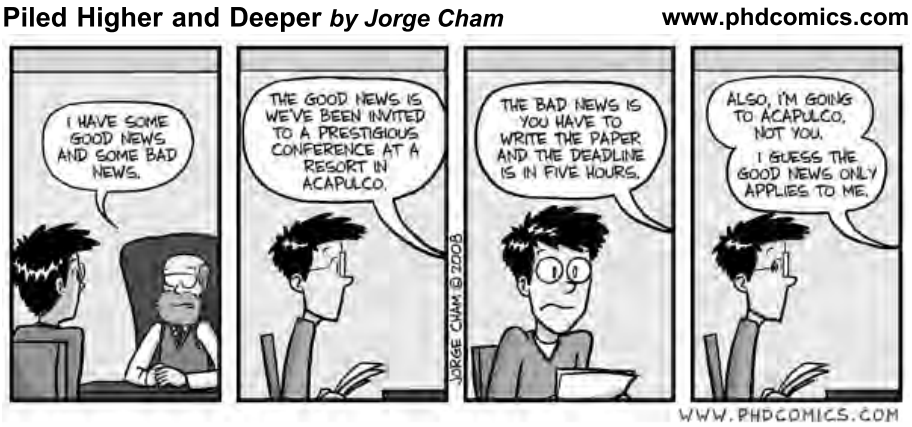

title: "Good news" - originally published 3/31/2008

CHAPTER 9

One dimensional snaking of bright and dark cavity solitons

"And god said to the snake "ye shall crawl on your belly for the rest of your days". Not really a punishment for a snake." — Ricky Gervais in Animals.

In this Chapter, we study the snaking behavior of one-dimensional bright and dark dissipative solitons in a nonlinear optical cavity with diffraction/dispersion compensation, taking into account higher order spatial/temporal effects. A stability analysis of a Lugiato-Lefever equation with fourth-order spatial derivatives is carried out. Next, the bifurcation structure of both bright and dark solitons in the presence of modulational instabilities is studied. [1]

9.1 Introduction

In the introduction of the second part of this thesis, we have discussed two types of spatially Localized Structures (LSs): LSs in the presence of modulational instabilities and LSs in the presence of bistability between two homogeneous solutions. In the next two Chapters, we will focus on the first type, LSs that can form in subcritical pattern forming bifurcations, where the homogeneous steady state coexists with a heterogeneous or patterned solution arising from the

[1] The work presented in this Chapter has been published in the following journal papers: [1, 2].

instability (usually referred to as a Turing instability or as modulation instability in the optics literature). In some cases, a part of these stable patterns (one or more isolated peaks) embedded in the homogeneous stable solution can be stable as well, forming a LS. In optics, this has been demonstrated in many different configurations [3–5], and in particular in self-focusing Kerr cavities [6], where these LSs have been called Kerr cavity solitons.

The existence of this kind of LSs in nonlinear optics was first reported in a Swift-Hohenberg equation describing, in the weak dispersion limit, nascent optical bistability with transverse effects [3]. This equation was valid (i) close to the critical point associated to the onset of bistability and (ii) in the limit of large (long wavelength) pattern forming systems. More generally, the Swift-Hohenberg equation has proved to be an invaluable model equation for systems undergoing a bifurcation to time-independent structured states with a finite wave number at onset [7]. As shown in Figure 9.1 and also discussed in Section 8.2.2, depending on the nonlinear terms and the parameters, a subcritical branch of spatially periodic states (P) can be created at a modulational instability point ($r = 0$) in the Swift-Hohenberg equation. This branch is unstable but acquires stability at finite amplitude at a saddle-node bifurcation. In addition, it is known that on the real line there are two branches of spatially LSs that bifurcate from the homogeneous solution simultaneously with the periodic states, and do so likewise subcritically. These states are therefore also initially unstable. When followed numerically these states become better and better localized and once their amplitude and width become comparable to the amplitude and wavelength of the competing periodic state these states begin to grow in spatial extent by adding rolls symmetrically at either side. In a bifurcation diagram this growth is associated with back and forth oscillations across a *pinning* interval. This behavior is known as *homoclinic snaking* [7–11], and is associated with repeated gain and loss of stability of the associated LS.

Homoclinic snaking can be understood both on a qualitative level and on a mathematical level. Qualitatively this behavior is related to the movement and pinning of fronts. A LS is formed when fronts at either side of that LS "pin" to the heterogeneous structure between them [12]. In general, either the pattern or the homogeneous solution will dominate, such that the front connecting both will move until the entire space is filled with the dominant state. However, there can exist a *Maxwell* point M in parameter space, shown in Figure 9.1, at which the dominant role switches from the pattern to the homogeneous state (or vice versa). At this point the *free energy*, as defined by the Lyapunov function in Eq. (8.8), of both solutions is equal. The *pinning* interval in which the LSs exist has in fact spread out into a locking range with finite width around the Maxwell point. Mathematically, the snaking behavior is a consequence of transverse intersection of the two-dimensional unstable manifold of the homogeneous state

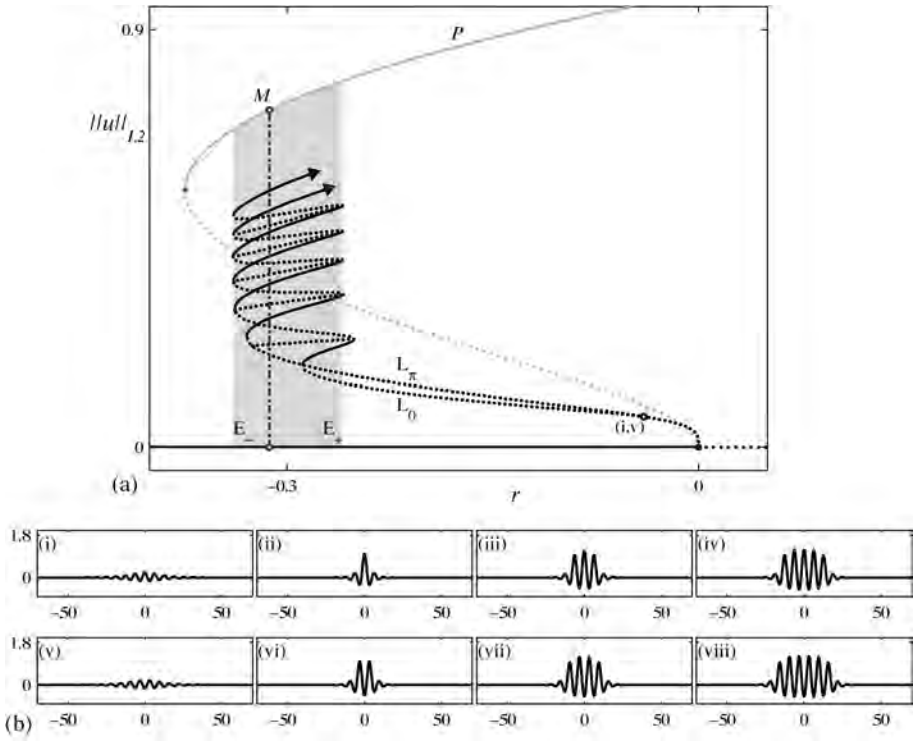

Figure 9.1: (a) Bifurcation diagram showing the snakes-and-ladders structure of LSs in the subcritical real Swift-Hohenberg equation. The L_2-norm of the solutions $u(x)$ is plotted. Away from the origin the snaking branches L_0 and L_π are contained within the pinning region (shaded) between E_- and E_+. Both snaking branches snake up until they eventually connect to the periodic patterned branch P. Solid (dotted) lines indicate stable (unstable) states. (b) shows examples of the localized profiles when snaking up the branch. (reprinted with permission from Ref. [16])

and the three-dimensional center-stable manifold of the spatially periodic state [7, 8, 13, 14], together with reversibility under $x \to -x$. These results are reviewed in [15].

This phenomenon of homoclinic snaking of LSs has been widely studied in the real Swift-Hohenberg equation [7–11, 13, 14]. This equation can be used as a prototypical model for many systems. Nevertheless, there still exists a wealth of other systems for which the real Swift-Hohenberg equation cannot be used as

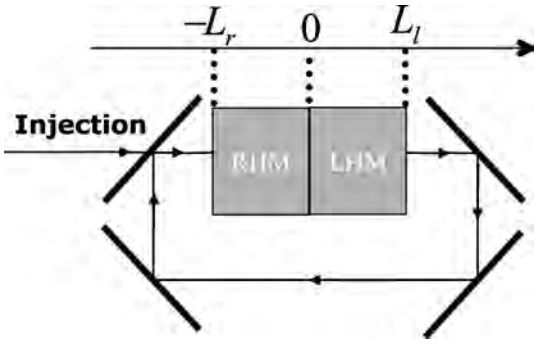

Figure 9.2: Schematic setup of a ring cavity filled with right-handed and left-handed materials. The cavity is driven by a coherent external injected beam.

it is variational and only models a real field. In this Chapter, we will study the snaking of LSs in non-variational models for a complex field. In particular, we will consider a generalized version of the LLE model (Lugiato-Lefever equation [17]) that has been derived to model the light in a microresonator driven by a coherent optical beam taking into account higher order spatial effects [1, 18]. The formation of LSs in such microresonators can be attributed to the balance between nonlinearities due to light-matter interaction, transport processes (diffusion and/or diffraction), and dissipation [19–22]. The LSs take the shape of bright or dark light spots at the output of the cavity. Such LSs, also referred to as cavity solitons, have been proposed for information encoding and processing [20, 21, 23].

Thanks to recent advances in the fabrication of metamaterials and photonic crystal fibers (PCFs), it is now possible to conceive a nonlinear system which allows for diffraction and/or dispersion management. On the one hand, the progression of the fabrication of left-handed metamaterials (LHM) towards optical frequencies [24, 25], and the proposition of nonlinear LHM [26, 27] allow control of diffraction. In Refs. [28, 29] the possibility of altering the strength of diffraction is considered by inserting a layer of LHM, in addition to a layer of right-handed material (RHM) [see Figure 9.2], in the cavity of an optical microresonator, and they show how to reduce the diffraction coefficient to (in principle) arbitrarily small values. In this case, higher order spatial effects can no longer be neglected. On the other hand, photonic crystal fibers (PCFs) allow for a high control along the dispersion curve [30], such that wavelengths at which the dispersion is almost zero can be engineered. Near such a zero dispersion wavelength, high order dispersion effects in a fiber cavity [see Figure 8.3(c)] have to be taken into

account as well. In this Chapter, the existence of snaking of Kerr cavity solitons (LSs in an optical cavity with Kerr type nonlinearity) will be verified and the influence of a higher order bilaplacian term on these LSs is investigated.

9.2 Model

We consider a microresonator driven by a coherent optical beam. In each roundtrip, the light passes through two adjacent nonlinear Kerr media: a RHM and a LHM (see Figure 9.2). It has been shown in Ref. [28] that the evolution of the electric field in this microresonator is governed by the well-known LLE [17], with the diffraction coefficient $\mathcal{D}$ given by

$$\mathcal{D} = \frac{\lambda \mathcal{F}}{2\pi^2}\left(\frac{l_R}{n_R} - \frac{l_\mathrm{L}}{|n_\mathrm{L}|}\right). \tag{9.1}$$

n_R, n_L, l_R and l_L are the indices of refraction and the lengths of the RHM and the LHM, respectively. λ is the wavelength of the light in the cavity and $\mathcal{F}$ the finesse of the resonator. By changing l_R and l_L, $\mathcal{D}$ can be engineered to ever smaller, positive diffraction coefficients. From the LLE, one can estimate the diameter of localized solutions to be

$$\Lambda_0 = 2\pi\sqrt{\frac{\mathcal{D}}{2-\theta}}, \tag{9.2}$$

with θ the cavity detuning. Therefore, LS will become infinitely small when $\mathcal{D}$ tends to zero. In that case, however, higher order effects will start to dominate the spatial dynamics. Indeed, from the derivation of the LLE, one can show that a nonlocal response comes into play when diffraction becomes negligible. The effect of such higher order spatial contributions remains largely unexplored. Under the same approximations under which the LLE is valid, i.e., slowly varying envelope approximation, weak nonlinearity and a nearly resonant cavity, it is shown that the nonlocality comes in as follows [31]:

$$\frac{\partial A}{\partial t} = -(1+\mathrm{i}\theta)A + A_\mathrm{in} + \mathrm{i}\,|A|^2 A + \mathrm{i}\mathcal{D}\nabla_\perp^2 A + \mathrm{i}\iint \delta(\mathbf{r}_\perp - \mathbf{u})A(\mathbf{u})\mathrm{d}\mathbf{u}. \tag{9.3}$$

The kernel function δ, describing the nonlocal response of the linear LHM, effectively couples the electric field at different positions. The details of the derivation of Eq. (9.3) can be found in Ref. [31]. When the nonlocality is weak, the last term of Eq. (9.3) can be expanded in a series of spatial derivatives of A, and, taking into account the rotational invariance of the system, it is found that

$$\iint \delta(\mathbf{r}_\perp - \mathbf{u})A(\mathbf{u})\mathrm{d}\mathbf{u} \simeq \delta_0 A + \delta_1\nabla_\perp^2 A + \delta_2\nabla_\perp^4 A. \tag{9.4}$$

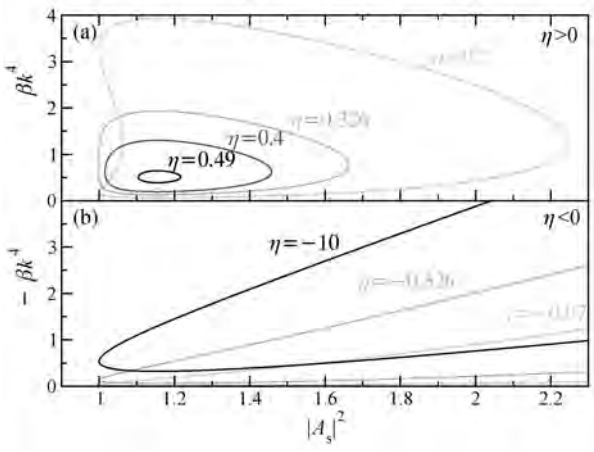

Figure 9.3: Influence of the nonlocality to diffraction ratio η on the marginal stability curves as given by Eq. (9.6). The wavevectors inside the curves destabilize the homogeneous steady state solution of Eq. (9.5). $\theta = 1.23$. (a) Positive η. (b) Negative η. [1]

The first two terms in Eq. (9.4) only change the value of the detuning and diffraction coefficients, respectively. In what follows, we absorb their contribution into the parameters θ and α, keeping the same notation. We finally arrive at

$$\frac{\partial A}{\partial t} = -(1 + \mathrm{i}\theta)A + A_{\mathrm{in}} + \mathrm{i}\,|A|^2 A + \mathrm{i}\alpha\nabla_\perp^2 A + \mathrm{i}\beta\nabla_\perp^4 A. \tag{9.5}$$

9.3 Linear stability analysis

Eq. (9.5) is similar to the LLE, and has the same homogeneous steady state (HSS) solutions A_s. In this work, we want to study the LS arising from the modulational instability of the homogeneous solution. If $\beta = 0$ and for $41/30 < \theta < \sqrt{3}$, the system admits one homogeneous solution that creates a subcritical patterned branch at $|A_s|^2 = 1$.[2] Therefore, close to that modulational instability point ($|A_s|^2 = 1$), there exists a region of coexistence of the patterned branch and

[2] In one spatial dimension with $\beta = 0$, the condition $\theta_{sub} = 41/30$ determines the threshold between a supercritical and a subcritical bifurcation towards patterned solutions. In the remainder of this Chapter, we will continue to work in the regime corresponding to $\theta_{sub} < \theta < \sqrt{3}$. The threshold θ_{sub}, however, will shift when including $\beta \neq 0$.

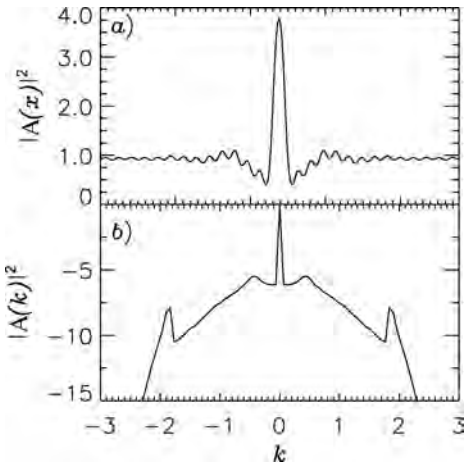

Figure 9.4: (a) A transverse cut of a cavity soliton for $\beta = 0.07$, $|A_s|^2 = 0.93$ and $\theta = 1.23$ over a domain width of $L = 48$. In (b) the fourier transform of (a) is shown, from which it is clear that there are two characteristic wavevectors.

the stable homogeneous solution. In this Section, we focus on this monostable regime and investigate the linear stability of the homogeneous solution in the presence of the higher order diffraction term ($\beta \neq 0$).
We have performed a stability analysis by linearizing Eq. (9.5) around the steady state solution, and seeking for the deviation in the form $A = A_s + \delta A \ \exp(\mathrm{i}\,\mathbf{k}\cdot\mathbf{r} + \lambda t)$, with $\mathbf{k} = (k_x, k_y)$ and $\mathbf{r} = (x, y)$. The marginal stability ($\lambda = 0$) is given by

$$\alpha k^2 - \beta k^4 = 2|A_s|^2 - \theta \pm \sqrt{|A_s|^4 - 1}. \tag{9.6}$$

The modulational instability (MI) depends strongly on the parameter η, defined as the nonlocality to diffraction ratio $\eta = \beta/\alpha^2$. In Figure 9.3, the marginal stability curves are shown for several values of η.[3]

For $\eta > 0$ [see Figure 9.3(a)], these curves have the form of a cardioid, which contains the unstable wavevectors. A first MI arises with two critical wave numbers at an intensity of $|A_s|^2 = 1$. This corresponds to the threshold associated

[3]By rescaling the field A and space, one can impose $\alpha = 1$ and write Eq. (9.5) in function of η . Take $x' = x/\sqrt{\alpha}$. Eq. (9.5) changes to

$$\frac{\partial A}{\partial t} = -(1 + \mathrm{i}\theta)A + A_{\mathrm{in}} + \mathrm{i}\,|A|^2 A + \mathrm{i}\nabla_\perp^2 A + \mathrm{i}\eta\nabla_\perp^4 A,$$

with $\eta = \beta/\alpha^2$.

with the pattern forming instability even in the absence of higher order diffraction ($\beta = 0$). However, when considering the bilaplacian term $\beta \neq 0$, this bifurcation becomes degenerate. At $|A_s|^2 = 1$, there exist two unstable wave numbers k_m that appear simultaneously and spontaneously in this system:

$$k_m^2 = \frac{\alpha \pm \sqrt{\alpha^2 + 4\beta(\theta - 2)}}{2\beta}. \tag{9.7}$$

This can lead to the formation of complex patterns with two wavevector components [1, 32]. In Figure 9.4, a typical profile of a stationary LS and its Fourier spectrum is shown for a background of $|A_s|^2 = 0.93$. It is clear that there indeed exist oscillations with two characteristic wave vectors. It has also been shown that, close to this degenerate MI point, the beating can be localized [33]. As η increases above $\eta_{cr} = 1/4(2-\theta)$, the cardioid form evolves into an elliptical shape with equal critical wave numbers at both sides: $\beta k_m^4 = 1/4\eta$. In both cases, at higher background intensities stability of the HSS is recovered. When increasing η even more such that $\eta > 1/4\left(\sqrt{3} - \theta\right)$, the unstable region contained in the marginal stability curve disappears, effectively stabilizing all the HSS. For $\eta < 0$ [see Figure 9.3(b)], the MI occurs again for intensities $|A_s|^2 > 1$, but here the HSS are not stabilized for high input fields.
In the following Sections, we focus on the effect of the fourth-order spatial derivative in Eq. (9.5) on the snaking bifurcation structure of both bright and dark 1D LSs. The bright LSs originate at the first MI point at $|A_s|^2 = 1$. Dark LSs are dips in a stable homogeneous background intensity, and thus can only exist for $\eta > 0$ such that the homogeneous solution is stabilized at higher intensities.

9.4 Snaking of 1D bright cavity solitons

In the introduction, we briefly reviewed a bifurcation structure for 1D LSs that is commonplace, called *homoclinic snaking*. Homoclinic snaking of 1D LSs has been widely studied in several model equations, such as e.g. the Swift-Hohenberg equation [7–11, 13, 14]. Figure 9.1 demonstrates the "classical" *snakes-and-ladders* structure of LSs in the subcritical real Swift-Hohenberg equation [16]. In Ref. [34], it was shown that the same homoclinic snaking structure is present for 1D bright cavity solitons in a nonlinear optical cavity as described by the LLE [Eq. (9.5) where $\beta = 0$]. Furthermore, in that work it was demonstrated that extra complexity, including the existence of additional LSs and complexes, arises due to homoclinic and heteroclinic intersections of the stable and unstable manifolds of the high and low-amplitude periodic solutions [34].
In this Section, we extend the analysis of 1D cavity solitons near zero diffraction

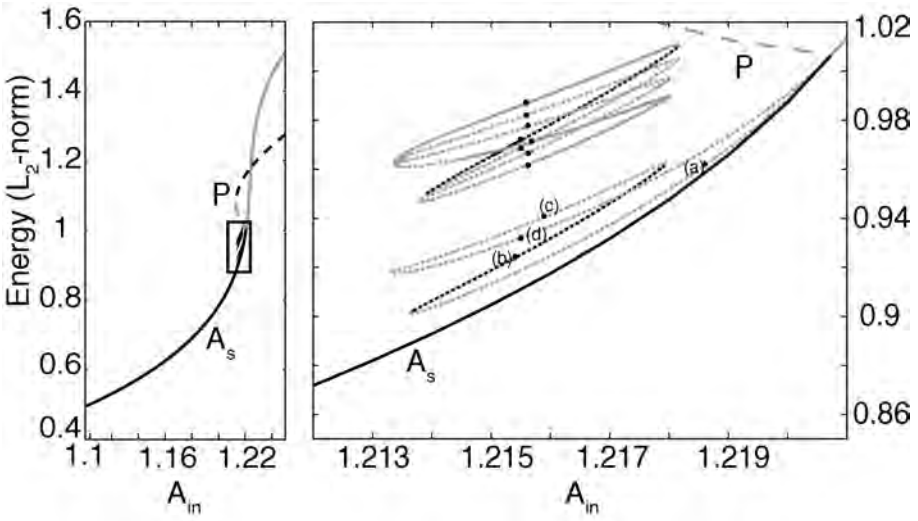

Figure 9.5: Bifurcation diagram demonstrating the snaking of the bright LSs. The parameters are chosen to be: $\theta = 1.7$, $\alpha = 0.5$, $\beta = 0.2$ ($\eta = 0.8$) and the width of the cavity $L = 89.6$. The bright LS branches are structured in isolas, plotted in a dotted line, where the color coding black/grey represents stable/unstable solitons. The homogeneous solutions A_s are depicted by a solid line and periodic pattern branches P by a dashed curve. For these curves the colors black/grey also depict stable/unstable structures. Figure 9.6 provides a zoom of the upper isola.

by considering high order diffraction (or equivalently dispersion in fiber cavities). We consider here the case where $\eta < \eta_{cr}$, such that in principle patterns with two different wave numbers (or possible mixed mode patterns) can be formed. In particular, we study the changes in the snaking structure of 1D bright cavity solitons when adding a fourth order spatial derivative in the Lugiato-Lever equation [Eq. (9.5) with $\beta \neq 0$].

In Figure 9.5, the bifurcation diagram of bright LSs is depicted for $\theta = 1.7$, $\alpha = 0.5$, $\beta = 0.2$ and $L = 89.6$. The detuning θ is chosen to operate in the monostable regime ($\theta < \sqrt{3}$). Moreover, for these values, $\eta = 0.8$ is smaller than $\eta_{cr} = 0.83$. Therefore at the MI point around $|A_s|^2 = 1$, the homogeneous solution destabilizes for periodic modulations with two unstable wave numbers, being $k_m^2 = 1$ and 1.5 [see Eq. (9.7)]. In Figure 9.5, the bright cavity soliton branches are plotted in a dotted line, where the color coding black/grey represents stable/unstable solitons. The homogeneous solutions A_s are depicted by a solid line

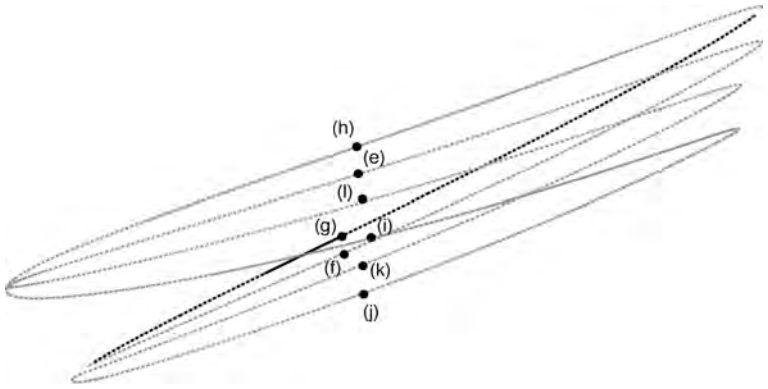

Figure 9.6: A zoom is shown from the isola containing the stable 5-peak LSs in Figure 9.5. The bright LS branches are plotted in a dotted line, where the color coding black/grey represents stable/unstable solitons.

and periodic pattern branches P by a dashed curve. For these curves the colors black/grey also depict stable/unstable structures. For all the solution branches in this bifurcation diagram, the *energy* is plotted as a function of the input field amplitude, where the energy is defined as $(1/L)\int dx\,|A|^2$ (L_2-norm), and L is the domain width. Periodic boundary conditions are used and the domain width L is chosen large enough such that the width of the LSs is much smaller then the domain itself. The solutions are found by time integration with appropriate initial conditions and are then continued in parameter space using a Newton method.[4]

The bifurcation picture is qualitatively very different from the "classical" snaking structure shown in Figure 9.1 [11, 16], where one continuous branch of LSs snakes up with back and forth oscillations across the *pinning* interval. Here, in Figure 9.5, a similar *pinning* interval is present, but the LSs are no longer located on one continuous snaking branch, but instead they live on isolas. Two such isolas are shown in Figure 9.5, namely one associated to the stable one-peak LS and one to the stable five-peak LS. A more detailed picture of the isola containing the stable five-peak LS is given in Figure 9.6. The isolas corresponding to two, three, four, six . . . peaks are omitted here in order not to obscure the figure.

[4]The equation is discretized, from which a set of coupled nonlinear equations is obtained. Since the equation is linear in the spatial derivatives, the diffraction term can be computed in the spatial Fourier space. This approach is very accurate and automatically generates the Jacobian operator, whose eigenvalues determine the stability of the solutions. Note that this method finds both stable and unstable stationary solutions. An appropriate initial condition is found by numerically simulating the equation in time using the integration scheme explained in Appendix B.

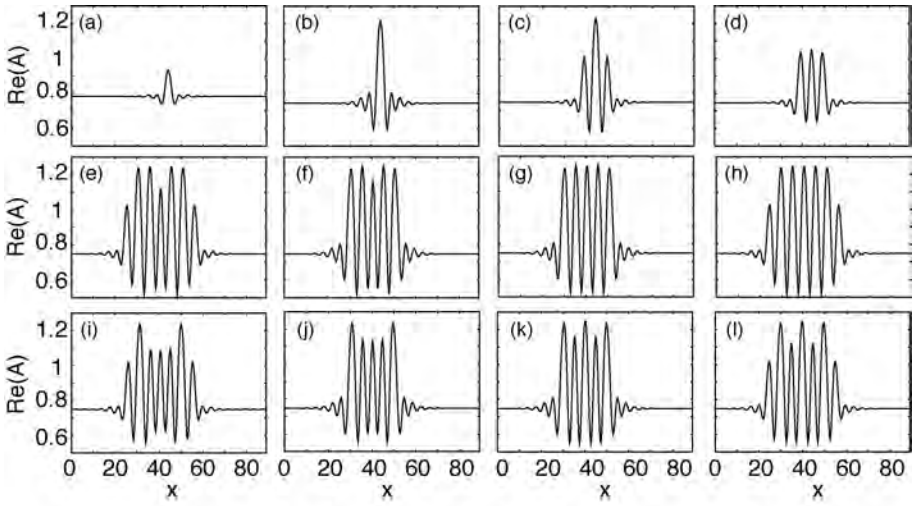

Figure 9.7: Examples of the localized profiles of the bright LSs obtained for input amplitudes A_{in} as shown by the black dots in Figure 9.5. The parameters are as in Figure 9.5.

The black dots labeled (a)-(l) in Figures 9.5 and 9.6 give the positions on the bifurcation diagram of which profiles of the corresponding LSs can be found in Figure 9.7. Panels (a)-(d) in Figure 9.7 provide the profiles of the bright one-peak cavity solitons living on the first isola. The one-peak LSs bifurcate subcritically from the homogeneous solution simultaneously with the periodic states. These states are therefore initially unstable and still small in amplitude [see Figure 9.7(a)]. When followed numerically these states become better and better localized and once their amplitude and width become comparable to the amplitude and wavelength of the competing periodic state the LSs stabilize [see Figure 9.7(b)]. When continuing the branch further around the bend, two extra peaks are added symmetrically at each side. However, instead of connecting to a branch of stable LSs with 3 peaks, the LSs on the branch with profiles (c) and (d) are unstable and terminate again at the MI point of the homogeneous solutions.

Profiles of the LSs on the different branches of the isola associated to the stable 5-peak LSs can be found in Figure 9.7(e)-(l). This isola, shown in more detail in Figure 9.6, contains eight different connected branches of which only one 5-peak LS branch is stable. A profile of such a stable LS is given in Figure 9.7(g). When numerically continuing this stable structure, at each turn in parameter space the

profile of the LS changes qualitatively [see Figure 9.7(e)-(l)]. It goes through many different kinds of LSs where one or more of the 5 peaks exhibit a drop in amplitude. All these different solutions are, however, unstable.
The LLE (9.5) without higher order diffraction ($\beta = 0$) does not show this break-up of the snaking structure in isolas. The breaking up of the homoclinic snaking structure into stacks of isolas has been reported in the literature, but mainly in the context of the 1D real Swift-Hohenberg equation. In Ref. [10], it was shown that dark LSs embedded in a non-zero background can be organized in stacks of figure-eight isolas. In the current case of the LLE (9.5) with bilaplacian term, however, one can notice that the isolas can be much more involved than a figure-eight shaped isola. In the same system, it was demonstrated that LSs corresponding to n-homoclinic orbits, with n >1, do not exist on a snaking curve, but also rather live on an isola [14, 35]. These isolas of n-homoclinic orbits still roughly follow the snaking curve of the one-homoclinic orbits, but their curves do not connect to each other. This scenario is not applicable in our case either as we only consider 1-homoclinic orbits. Yet another mechanism in the Swift-Hohenberg equation that leads to the organization of LSs in stacks of isolas was reported in Ref. [36]. Breaking of the spatial reversibility of the system leads to the destruction of the homoclinic snaking as it is a direct consequence of such spatial reversibility. In this case, however, the LSs also drift. As Eq. (9.5) is still spatially reversible, this mechanism cannot be used to explain the creation of stacks of isolas here.
In the context of the LLE (9.5) with $\beta = 0$, Gomila *et al.* have shown in Ref. [37] that using an external periodic forcing in space leads to the merging of the isolas corresponding to n-homoclinic orbits with the snaking curve of the 1-homoclinic orbits which are structured in a homoclinic snaking branch. In fact, it seems that this scenario is closely related to our observations here. Whereas in Ref. [37] an *external* forcing was applied to the LLE, we have in a way created an *internal* periodic forcing due to the creation of two distinct wave numbers k_{m1} and k_{m2} at the MI. Whether the peaks with two different amplitudes inside a single LS in Figure 9.7 correspond as well to two different widths (related to k_{m1} and k_{m2}) remains to be verified in future work.

9.5 Snaking of 1D dark cavity solitons

In this Section, we focus on the second MI point of the system that allows the homogeneous steady state to restabilize (see Section 9.3). We show that fourth order diffraction (or dispersion in the case of PCFs) allows the nonlinear optical cavity to exhibit dark cavity solitons, whereas this was impossible without the fourth order diffraction (dispersion) term. These structures consist of dips in

a uniform background of the intensity profile. The number of dips and their temporal distribution is solely determined by the initial conditions. In Section 9.5.1, we show that, for the same parameters as in the previous Section, dark cavity solitons are organized in the "classical" homoclinic snaking bifurcation structure, in contrast to the stacks of isolas in the case of bright cavity solitons. Afterwards, in Section 9.5.2, we consider a slightly altered LLE equation (9.5) that has been derived recently in the context of diffraction compensation in cavities with left-handed materials [31]. In this model, we study the snaking behavior of dark LSs in the bistable regime ($\theta > \sqrt{3}$).

9.5.1 Dark cavity solitons in the monostable regime

In the monostable regime ($\theta < \sqrt{3}$), one can generate stable dark solitons that consist of dips in the amplitude of light that can be either isolated or randomly distributed. An example of these solitons is plotted in Figure 9.8(b)-(f). Just like their bright counterparts, dark cavity solitons are characterized by oscillatory tails that decay at large x as shown in Figure 9.8(b)-(f). All these structures are obtained for the same values of the parameters. Therefore, they exhibit multi-stability behavior in a finite range of parameters, the pinning region. Since the minima of these structures are close to one another, we plot again the *energy* of the LSs as a function of the input field amplitude in a bifurcation diagram in Figure 9.9 [where the energy is defined as in the previous Section]. The LSs branches are plotted in a dotted line, where the color coding black/grey represents stable/unstable LS. For completeness, the homogeneous solutions A_s are depicted by a solid line and periodic pattern branches P by a dashed curve. For these curves the colors black/grey also depict stable/unstable structures.

The bifurcation diagram consists of two snaking curves; one describes dark LSs with $2p$ dips, the other corresponds to $2p + 1$ dips (with p a positive integer). Here we only plot the branch corresponding to an odd number of dips. As the energy decreases, at each turning point where the slope becomes infinite, a pair of dips appears. Extra pairs of dips are added each turn until the LS fill the entire domain and the branches exit the snaking region and connect to a periodic pattern branch. Unlike the more complicated snaking structure of the bright cavity solitons, the dark LS are organized in the well-known homoclinic snaking structure [11].

While the snaking structure of Figure 9.9 is very similar to the widely studied homoclinic snaking structure in an infinite domain, as reviewed in Ref. [11], several features that are not accounted for are due to the finite domain size. In particular, it is clear from Figure 9.9 that the dark LSs are not created at the MI

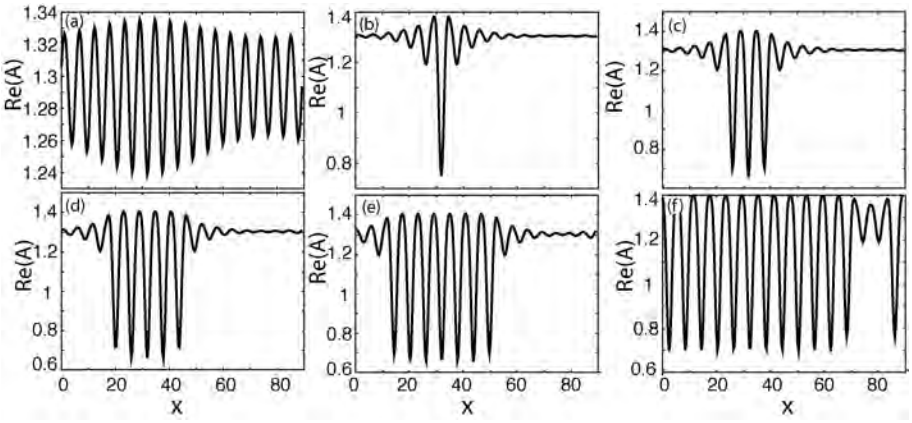

Figure 9.8: Examples of the localized profiles of the dark LSs obtained for input amplitudes A_{in} as shown by the black dots in Figure 9.9. The parameters are the same as in Figure 9.5.

point of the homogeneous solution. Instead, they form as a result of a secondary bifurcation of a spatially periodic pattern, here a periodic pattern with wave number $k_{16} = 2\pi 16/L$. The states produced in this bifurcation are initially only weakly localized [see Figure 9.8(a)], but evolve into strongly LSs by the time the branch enters the pinning region. This effect of the finite period is also present at the other end of the snaking branches, where the dark LSs almost fill the whole domain [see Figure 9.8(f)], forcing the snaking to terminate. The branch now exits the snaking region and terminates on a branch of spatially periodic states whose wave number depends on the domain size. This wave number has been shown to be typically close to the smallest wave number associated with the LSs in the pinning region [38]. Here this periodic branch at which the LSs terminate has as wave number $k_{15} = 2\pi 15/L$. As one can expect decreasing the cavity width L, the two periodic branches split more and the single LS is created further up the pattern branch [point (a) in Figure 9.9]. Oppositely, when increasing L, the origin of the single LS branch moves more to the MI of the homogeneous steady state and both periodic pattern branches tend to merge together. Moreover, we have verified the existence of the LSs in a wider range of system parameters, demonstrating the robust existence of these structures.

Changes of the snaking structure due to the presence of a finite domain width are important as in experiments or numerical simulations the available domain is never infinite. For more information on the effects of a finite domain and of

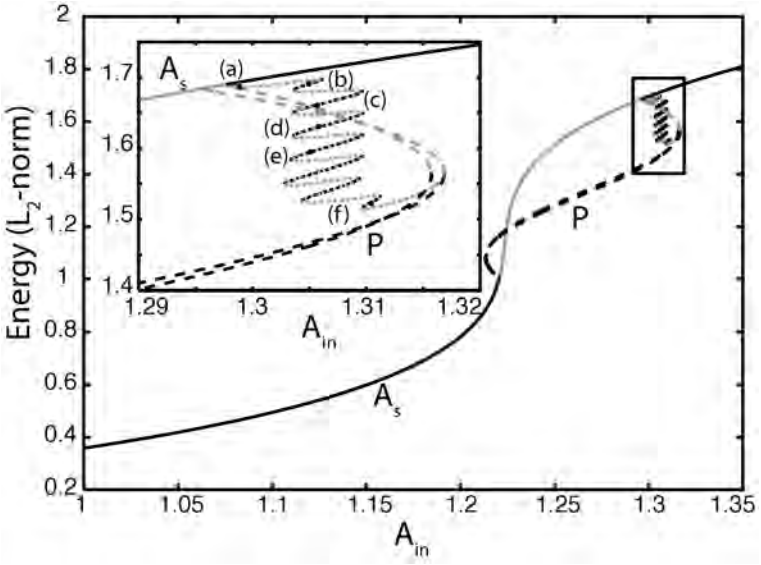

Figure 9.9: Bifurcation diagram demonstrating the snaking of dark LSs. The parameters are the same as in Figure 9.5. The branches of dark LSs are plotted in a dotted line, where the color coding black/grey represents stable/unstable solitons. The homogeneous solutions A_s are depicted by a solid line and periodic pattern branches P by a dashed curve. For these curves the colors black/grey also depict stable/unstable structures.

arbitrary boundary conditions on both the birth and disappearance of spatially LSs, we refer to Refs. [38–41].
In the next Section, we discuss preliminary results on the snaking behavior of dark LSs in the presence of a bistability between the homogeneous states in the system.

9.5.2 Dark cavity solitons in the bistable regime

When operating around the zero-diffraction regime and by taking into account the nonlocal properties of light propagation in an optical cavity filled with a left-handed material and a right-handed material (see Figure 9.2), it has been shown in Ref. [31] that the spatiotemporal evolution of the intracavity field can

be described by the following dimensionless partial differential equation

$$\frac{\partial A}{\partial t} = A_{in} - (1 + i\theta)A + i\Gamma |A|^2 A + i\alpha\nabla_\perp^2 A + \left(i\beta - \frac{\alpha^2}{2}\right)\nabla_\perp^4 A \tag{9.8}$$

where A is the slowly varying envelope of light within the ring cavity, A_{in} is the amplitude of the injected field, θ is the normalized cavity detuning parameter, and Γ is the normalized nonlinear Kerr coefficient. The Laplace operator acting on the transverse plane $r_\perp = (x, y)$ is $\nabla_\perp^2 = \partial_{xx}^2 + \partial_{yy}^2$. The effective diffraction coefficient is denoted by α and β accounts for the effective coefficient of spatial dispersion. The time has been scaled as in Ref. [31]. We would like to remark that this model equation is the same as the Eq. (9.5) discussed in Chapters 9-10, apart from the term $\frac{\alpha^2}{2}\nabla_\perp^4 A$ on the right-hand side. For decreasing diffraction strength $\alpha \to 0$, this term can be neglected such that Eq. (9.8) and Eq. (9.5) become the same.

A theoretical study of the model Eq. (9.8) without this diffusion term, $\alpha^2\nabla_\perp^4 A$, reveals that high order diffraction can give rise to a degenerate MI where two separate unstable wavelengths simultaneously appear, as discussed in Section 9.3 [1, 18]. Close to the first MI threshold, we have shown that bright LSs are structured in a nontrivial snaking structure, i.e. they lie on stacks of isolas. This can possibly be attributed to the presence of two unstable wavenumbers at the MI point. Furthermore, for the same parameter set, the dark LSs are stabilized due to the higher order diffraction term and are organized in the homoclinic snaking structure (see Section 9.5.2). In this Section, we show that the presence of a higher order term of the form $\left(i\beta - \frac{\alpha^2}{2}\right)\nabla_\perp^4 A$ also stabilizes both 1D and 2D dark LSs.

The homogeneous steady states solutions (HSS) A_s of Eq. (9.8) are still given by $A_{in}^2 = [1 + (\theta - \Gamma I_s)^2]I_s$. As before for Eq. (9.5), the transmitted intensity $I_s = |A_s|^2$ as a function of the input intensity $I_i = A_{in}^2$ is monostable for $\theta < \sqrt{3}$ and the bistable behavior arises for $\theta > \sqrt{3}$. The HSS are not affected by the high order diffraction and dispersion terms. However, these effects play an important role in the linear stability analysis with respect to finite wavelength perturbations of the form $\exp(\lambda t + i\mathbf{q}.\mathbf{r}_\perp)$ with $\mathbf{q} = (q_x, q_y)$. The MI occurs when $\lambda = 0$. This leads to the marginal stability curve:

$$\begin{aligned} &\left(\beta^2 + \frac{\alpha^4}{4}\right)q^8 + 2\alpha\beta q^6 + 2[\beta(2\Gamma I_s - \theta) + \alpha^2]q^4 \\ - \quad &2\alpha(\theta - 2\Gamma I_s)q^2 + 1 - \theta^2 - \Gamma I_s(4\theta - \Gamma I_s) = 0. \end{aligned} \tag{9.9}$$

The threshold associated with the MI as well as the wavelength of the periodic structure emerging from that threshold can be obtained when $\partial I_s/\partial q^2 = 0$. The

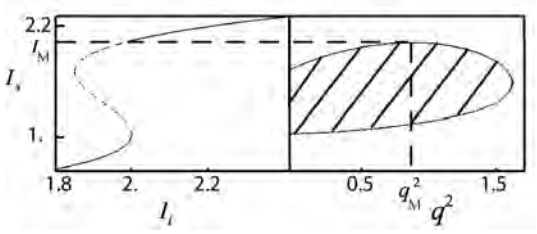

Figure 9.10: (a) The bistable input-output characteristics. The dashed cuve indicate unstable solutions and solid lines indicate instable ones. (b) The marginal instabily curve $I_s = |A_s|^2$ as a function of wavenumber q. The hatched area correpond to unstable region with respect to the Modulational instability. Parameters are $\theta = 2$, $\beta = 0.2$, $\Gamma = 1$ and $\alpha = 0.5$.

results of the linear stability analysis are summarized in Figure 9.10. When decreasing the input field intensity I_i, the upper homogeneous steady state becomes unstable at $I_M = |A_M|^2$. At this bifurcation point, the most unstable wavelength is $2\pi/q_M$ as shown in Figure 9.10. When further decreasing I_i, the lower branch of the bistable input-output characteristics is reached which is stable again.

As in the previous Section, we focus on the situation where the MI appears subcritically. This way there exists a finite domain for $I > I_M$ where the periodic structure coexists with the upper state, which are both linearly stable. In contrast to earlier subsections, we consider here $\theta > \sqrt{3}$ such that the input-output characteristics of the HSS in Eq. (9.8) have a bistable region. In this range of parameters, we generate numerically a single or multiple dips in the intensity profile. Examples of such dark LSs are shown in Figure 9.11, where only panels (b), (g) and (i) of Figure 9.11 present profiles of stable dark LS.

In order to analyze dark LSs in more detail in 1D, we draw a snaking bifurcation diagram in Figure 9.12, plotting the "energy" as a function of the input field amplitude (where the energy is defined as in the earlier subsections). Stable (unstable) solutions are colored in black (gray). These solutions are found by using appropriate initial conditions and are then continued in parameter space using a Newton method. Periodic boundary conditions are again used.

To simplify the analysis, we present only dark LSs with 1, 3 and 5 dips in the intensity profiles of the intracavity field. Although the snaking curve in Figure 9.12 is very similar to the homoclinic snaking as e.g. shown in Figure 9.13, one can notice that on the left-hand side of the snaking curve the process of growth is more complicated. In order to nucleate an extra pair of dark LSs the system evolves through a more intricate transient with dips showing a double-peaked minima. This is clarified by the intermediate profiles in Figure 9.11(c)-(f), which show in more detail the evolution from a stable single dark LS [see Figure 9.11(b)]

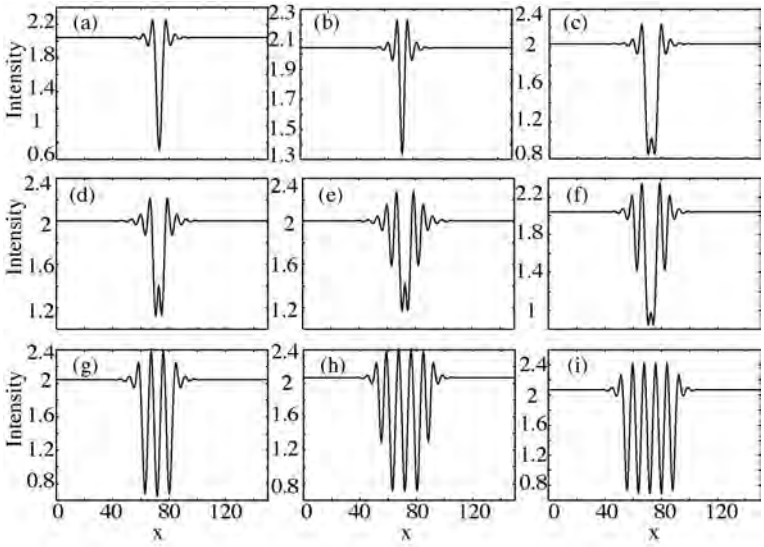

Figure 9.11: Examples of 1D dark LSs obtained for input field amplitudes as indicated in Figure 9.12. Others parameters are the same as in Figure 9.10.

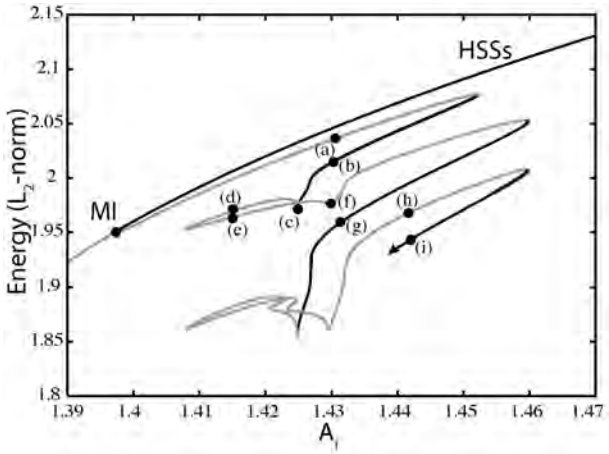

Figure 9.12: Snaking bifurcation diagram of the stable (black) and unstable (gray) 1D dark localized structures. Parameters are the same as in Fig. 9.10 and the profiles at points (a)-(i) are shown in Figure 9.11.

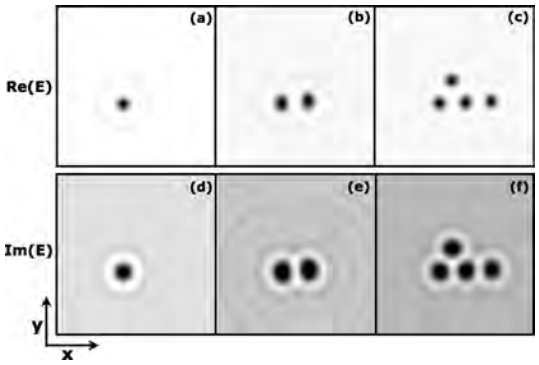

Figure 9.13: Examples of 2D multiple dark localized structures obtained for the same parameters as in Figure 9.10 with $A_{in} = 1.437$. Minima are colored in black and the grid is 256×256. The domain size of the system in both transverse directions is $L_x = L_y = 89.6$.

to a stable dark LS consisting of three dips [see Figure 9.11(g)]. The added complexity in the snaking branches on the left-hand side of the snaking curve can either be attributed to the higher value of θ that leads to the existence of a region of bistability between the lower and upper homogeneous solutions close to the snaking curves, or either to the presence of the extra term $\alpha^2\nabla_\perp^4 A$ in Eq. (9.8). This question remains to be addressed in future work.
In a 2D setting, the number of dark LSs can be much higher than in 1D. We focus on the situation where 2D dark LSs are close to one another. They exert mutual forces due to their overlapping oscillatory tails. As the number of dark LSs increases, the transverse profile of the output electric field exhibits clustering behavior as shown in Figure 9.13. As in the 1D case, the number of 2D dips and their spatial distribution depends only on the initial condition used. Examples of 2D dark LSs are plotted in Figure 9.13. Figure 9.13(a)-(c) correspond to the real part, and Figure 9.13(d)-(f) to the imaginary part of the intracavity field. All these dark LS profiles are obtained for the same values of parameter. The system exhibits a high degree of multistability. Also in 2D the boundary conditions used in the numerical simulations are periodic.

9.6 Conclusion

Due to recent advances in the fabrication of metamaterials and photonic crystal fibers, it is now possible to conceive nonlinear systems that allow for diffraction

and/or dispersion management. In the case of low diffraction and/or dispersion, higher order spatial/temporal effects have to be taken into account as well. We have shown that such a higher order spatial term can effectively stabilize the system in certain conditions. We have investigated the existence and nature of snaking of both bright and dark Kerr cavity solitons and the influence of the higher order bilaplacian term has been evaluated. We have demonstrated a stabilization of dark cavity solitons, which is attributed to fourth order diffraction/dispersion effects. In the monostable regime, the dark cavity solitons have been shown to be organized in a homoclinic snaking structure, while the bright cavity solitons are organized in complicated stacks of isolas. In the bistable regime, the dark solitons are also organized in a snaking structure, which is more complicated than the homoclinic snaking.
In the next Chapter, we investigate the influence of the higher order diffraction term on the size and dynamical instabilities of two-dimensional bright cavity solitons. We study the different possible mechanisms that can destabilize the cavity solitons, leading to stable oscillations, expanding patterns, or disappearance of the solitons.

References

[1] L. Gelens, G. Van der Sande, P. Tassin, M. Tlidi, P. Kockaert, D. Gomila, I. Veretennicoff, and J. Danckaert, "Impact of nonlocal interactions in dissipative systems: towards minimal-sized localized structures," *Phys. Rev. A* **75**(6), 063812, 2007.

[2] M. Tlidi and L. Gelens, "High-order dispersion stabilizes dark dissipative solitons in all-fiber cavities," *Opt. Lett.* **35**, 306–308, 2010.

[3] M. Tlidi, P. Mandel, and R. Lefever, "localized structures and localized patterns in optical bistability," *Phys. Rev. Lett.* **73**, 640, 1994.

[4] K. Staliunas and V. J. Sanchez-Morcillo, "Localized structures in degenerate optical parametric oscillators," *Opt. Comm.* **139**, 306, 1997.

[5] B. Schäpers, M. Feldmann, T. Ackemann, and W. Lange, "Interaction of localized structures in an optical pattern-forming system," *Phys. Rev. Lett.* **85**, 748, 2000.

[6] A. J. Scroggie, W. J. Firth, G. S. McDonald, M. Tlidi, R. Lefever, and L. A. Lugiato, "Pattern-formation in a passive kerr cavity," *Chaos, Solitons and Fractals* **4**, 1323–1354, 1994.

[7] A. R. Champneys, "Homoclinic orbits in reversible systems and their applications in mechanics, fluids and optics," *Physica D* **112**, 158–186, 1998.

[8] P. D. Woods and A. R. Champneys, "Heteroclinic tangles and homoclinic snaking in the unfolding of a degenerate reversible Hamiltonian-Hopf bifurcation," *Physica D* **129**, 147, 1999.

[9] J. Knobloch and T. Wagenknecht, "Homoclinic snaking near a heteroclinic cycle in reversible systems," *Physica D* **203**, 82–93, 2005.

[10] J. Burke and E. Knobloch, "Localized states in the generalized Swift-Hohenberg equation," *Phys. Rev. E* **73**, 056211, 2006.

[11] J. Burke and E. Knobloch, "Snakes and ladders: Localized states in the Swift-Hohenberg equation," *Phys. Lett. A* **360**, 681–688, 2007.

[12] Y. Pomeau, "Front motion, metastability and subcritical bifurcations in hydrodynamics," *Physica D* **23**, 3–11, 1986.

[13] P. Coullet, C. Riera, and C. Tresser, "Stable static localized structures in one dimension," *Phys. Rev. Lett.* **84**, 3069–3072, 2000.

[14] M. Beck, J. Knobloch, D. Lloyd, B. Sandstede, and T. Wagenknecht, "Snakes, ladders, and isolas of localized patterns," *SIAM J. Math. Anal.* **41**, 936, 2009.

[15] J. Burke and E. Knobloch, "Homoclinic snaking: Structure and stability," *Chaos* **17**, 037102, 2007.

[16] J. Burke, *Localized States in Driven Dissipative Systems*, PhD dissertation at the University of California, Berkeley, 2008.

[17] L. A. Lugiato and R. Lefever, "Spatial dissipative structures in passive optical systems," *Phys. Rev. Lett.* **58**, 2209–2211, 1987.

[18] L. Gelens, D. Gomila, G. Van der Sande, J. Danckaert, P. Colet, and M. A. Matías, "Dynamical instabilities of dissipative solitons in nonlinear optical cavities with nonlocal materials," *Phys. Rev. A* **77**, 033841, 2008.

[19] V. B. Taranenko, K. Staliunas, and C. O. Weiss, "Spatial soliton laser: Localized structures in a laser with a saturable absorber in a self-imaging resonator," *Phys. Rev. A* **56**, 1582–1591, 1997.

[20] S. Barland, J. R. Tredicce, M. Brambilla, L. A. Lugiato, S. Balle, M. Giudici, T. Maggipinto, L. Spinelli, G. Tissoni, T. Knödl, M. Miller, and R. Jäger, "Cavity solitons as pixels in semiconductor microcavities," *Nature* **419**, 699–702, 2002.

[21] M. Brambilla, L. A. Lugiato, F. Prati, L. Spinelli, and W. J. Firth, "Spatial soliton pixels in semiconductor devices," *Phys. Rev. Lett.* **79**, 2042–2045, 1997.

[22] M. Tlidi, P. Mandel, and R. Lefever, "Localized structures and localized patterns in optical bistability," *Phys. Rev. Lett.* **73**, 640–643, 1994.

[23] X. Hachair, S. Barland, L. Furfaro, M. Giudici, S. Balle, J. R. Tredicce, M. Brambilla, T. Maggipinto, I. M. Perrini, G. Tissoni, and L. Lugiato, "Cavity solitons in broad-area vertical-cavity surface-emitting lasers below threshold," *Phys. Rev. A* **69**, 043817, 2004.

[24] D. R. Smith, J. B. Pendry, and M. C. K. Wiltshire, "Metamaterials and negative refractive index," *Science* **305**(5685), 788–792, 2004.

[25] V. M. Shalaev, "Optical negative-index metamaterials," *Nature Photon.* **1**, 41–48, 2007.

[26] A. A. Zharov, I. V. Shadrivov, and Y. S. Kivshar, "Nonlinear properties of left-handed metamaterials," *Phys. Rev. Lett.* **91**, 037401, 2003.

[27] M. Lapine, M. Gorkunov, and H. Ringhofer, "Nonlinearity of a metamaterial arising from diode insertions into resonant conductive elements," *Phys. Rev. E* **67**, 065601, 2003.

[28] P. Kockaert, P. Tassin, G. Van der Sande, I. Veretennicoff, and M. Tlidi, "Negative diffraction pattern dynamics in nonlinear cavities with left-handed materials," *Phys. Rev. A* **74**(3), 033822, 2006.

[29] P. Tassin, L. Gelens, J. Danckaert, I. Veretennicoff, G. Van der Sande, P. Kockaert, and M. Tlidi, "Dissipative structures in left-handed material cavity optics," *Chaos* **17**, 037116, 2007.

[30] N. Y. Joly, F. G. Omenetto, A. Efimov, A. J. Taylor, J. C. Knight, and P. S. J. Russell, "Competition between spectral splitting and raman frequency shift in negative-dispersion slope photonic crystal fiber," *Opt. Commun.* **248**, 281, 2005.

[31] P. Kockaert, P. Tassin, I. Veretennicoff, G. Van der Sande, and M. Tlidi, "Beyond the zero-diffraction regime in optical cavities with a left-handed material," *J. Opt. Soc. Am. B* **26**, B148–B155, 2009.

[32] M. Tlidi, A. Mussot, E. Louvergneaux, G. Kozyreff, A. G. Vladimirov, and M. Taki, "Control and removal of modulational instabilities in low-dispersion photonic crystal fiber cavities," *Opt. Lett.* **32**, 662, 2007.

[33] G. Kozyreff, M. Tlidi, A. Mussot, E. Louvergneaux, M. Taki, and A. G. Vladimirov, "Localized beating between dynamically generated frequencies," *Phys. Rev. Lett.* **102**, 043905, 2009.

[34] D. Gomila, A. J. Scroggie, and W. J. Firth, "Bifurcation structure of dissipative solitons," *Physica D* **227**, 70, 2007.

[35] J. Knobloch and T. Wagenknecht, "Snaking of multiple homoclinic orbits in reversible systems," *SIAM J. App. Dyn. Syst.* **7**, 1397, 2008.

[36] J. Burke, S. Houghton, and E. Knobloch, "Swift-Hohenberg equation with broken reflection symmetry," *Phys. Rev. E* **80**, 036202, 2009.

[37] D. Gomila and G.-L. Oppo, "Subcritical patterns and dissipative solitons due to intracavity photonic crystals," *Phys. Rev. A* **76**, 043823, 2007.

[38] A. Bergeon, J. Burke, E. Knobloch, and I. Mercader, "Eckhaus instability and homoclinic snaking," *Phys. Rev. E* **78**, 046201, 2008.

[39] G. Kozyreff, P. Assemat, and S. J. Chapman, "Influence of boundaries on localized patterns," *Phys. Rev. Lett.* **103**, 164501, 2009.

[40] I. Mercader, O. Batiste, A. Alonso, and E. Knobloch, "Convectons in periodic and bounded domains," *Fluid Dyn. Res.* **42**, 0225505, 2010.

[41] S. Houghton and E. Knobloch, "Homoclinic snaking in bounded domains," *Phys. Rev. E* **80**, 026210, 2009.

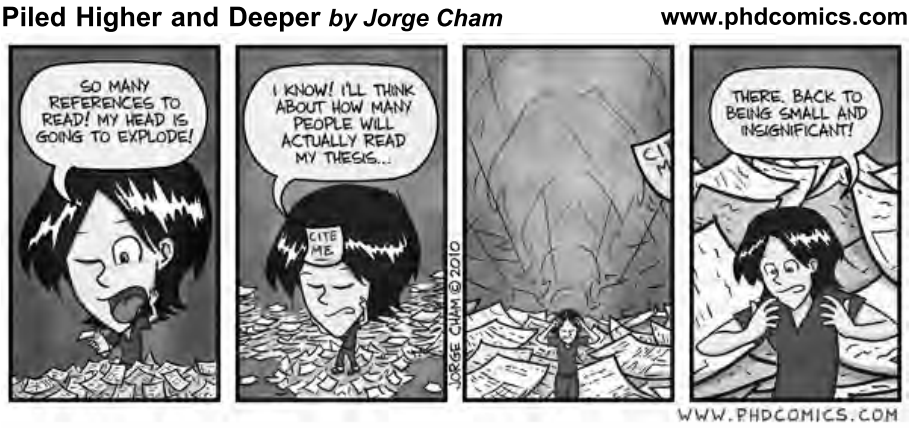

title: "Cecilia in Thesisland, Pt. 3: To be sure, this is generally what happens when you think" - originally published 2/3/2010

CHAPTER 10

Dynamical instabilities of two dimensional bright cavity solitons

"If you were to ask me to name three geniuses, I probably wouldn't say Einstein, Newton... (struggles for word). I'd go Milligan, Cleese, Everett. " — David Brent in the Office.

In this Chapter, we explore the size and dynamical instabilities of radially symmetric two-dimensional cavity solitons in a generalization of the Lugiato-Lefever model that includes a higher order spatial derivative. Such a model can describe an optical micro-resonator that allows for diffraction compensation. It is shown that higher order spatial derivatives can impose a new limit on the width of cavity solitons, going beyond the traditional diffraction limit. Furthermore, we elaborate on the different possible mechanisms that can destabilize the cavity solitons, leading to stable oscillations, expanding patterns, or making the solitons disappear. Multiple routes towards excitability are shown to be present in the system and we demonstrate that different regions admitting stationary, oscillating or excitable solitons unfold from two Takens-Bogdanov codimension-2 points. [1]

[1]The work presented in this Chapter has been published in the following journal papers: [1, 2].

10.1 Introduction

In the previous Chapter, we have introduced a generalization of the well-known Lugiato-Lefever model [3] that takes into account higher order spatial effects by inclusion of fourth-order spatial derivatives. This more general equation (10.1) has been derived in Refs. [1, 4]:

$$\frac{\partial A}{\partial t} = -(1 + \mathrm{i}\theta)A + A_{\mathrm{in}} + \mathrm{i}\,|A|^2 A + \mathrm{i}\alpha\nabla_\perp^2 A + \mathrm{i}\beta\nabla_\perp^4 A. \tag{10.1}$$

Localized structures (LSs) are relatively well understood in one transverse dimension [5], whereas an analytical analysis in two transverse dimensions is still largely unexplored and most of the results are obtained by numerical simulations. In this Chapter, as in the previous Chapter, we will focus on controllable LSs in optical cavities, also referred to as cavity solitons. However, instead of focussing on the snaking bifurcation structure of 1D cavity solitons, we will now study the influence of the bilaplacian term in Eq. (10.1) on the width and dynamical instabilities of 2D cavity solitons.

Their formation can be attributed to the balance between nonlinearities due to light-matter interaction, transport processes (diffusion and/or diffraction), and dissipation [6–9]. These bright spots have been proposed for information encoding and processing [7, 8, 10]. Decreasing the size of LSs would be advantageous for these applications, while also being of fundamental interest. In optical devices, the spatial dimension of LSs is generally restricted by diffraction, imposing the diameter to be of the order of $\sqrt{\mathcal{D}}$, where $\mathcal{D} = l\mathcal{F}/(\pi k)$ is the diffraction coefficient, with k the wavenumber of the beam, and l and $\mathcal{F}$ the length and the finesse of the resonator. E.g. in Ref. [7], LSs at a wavelength of 0.5μm have a transverse size that reaches the diffraction limit of 10μm.

The use of transverse index modulation has been proposed to overcome the diffraction limit of mid-band LSs in a certain class of resonators [11]. These LSs have a large intrinsic transverse velocity that prevents its use for many practical applications. Recently, a different strategy was motivated by the advances of the fabrication of left-handed materials (LHM) towards the optical spectrum [12, 13], and the introduction of nonlinear LHM [14, 15]. In Refs. [16, 17], Kockaert *et al.* study the possibility of altering the strength of diffraction by inserting a layer of LHM, in addition to a layer of right-handed material (RHM), in the cavity of an optical microresonator, and they show how to reduce the diffraction coefficient to arbitrarily small values. As the soliton width scales with the square root of the diffraction coefficient, this method potentially allows for sub-diffraction-limited LSs. Unlike with the use of photonic crystals, this technique works in principle for all types of LSs and microresonators. Although the diffraction limit can be encompassed in this way, one can reasonably expect that the sub-wavelength

structure of LHM will impose a new size limit on LSs. Here, we will show that the higher order spatial derivative terms — which can now no longer be neglected— will significantly change the properties of LSs when diffraction is tuned down, and a new size limit of LSs will be revealed.
Secondly, we elaborate on the different possible mechanisms that can destabilize the LSs. While in many instances the localized structures are stable, there are situations in which they develop different kinds of instabilities. Some instabilities lead to the formation of an extended pattern and therefore the localized character of the LSs is destroyed. More interesting are the instabilities that, while preserving its localized character, induce the LSs to start moving, breathing or oscillating [18–21]. Since LSs can be considered as an entity on their own, these instabilities may lead to dynamical regimes that appear not to be present in the dynamical behavior of the extended system. In this context it has recently been reported that LSs arising in a prototype model for optical cavities filled with a nonlinear Kerr media may show excitable behavior, while locally the system is not excitable [22, 23]. Thus, excitability can be an emergent property arising from the spatial dependence, which allows for the formation of LSs. In that situation excitability is mediated by a saddle-loop bifurcation and the whole scenario is organized by a Takens-Bogdanov (TB) codimension-2 point. In parameter space the TB point is located in the asymptotic limit in which the model becomes equivalent to the Nonlinear Schrödinger Equation (NLSE).
Since this excitability scenario is an emergent property of the spatial dependence of the system, it is particularly important to characterize how this scenario may change when the nature of spatial coupling is varied. In the Lugiato-Lefever model [3] considered in Refs. [22, 23] the spatial coupling arises from optical diffraction in the paraxial approximation and is therefore accounted for by a Laplacian term. Here, we consider an extension of the model, which extends the range of spatial interaction [1, 2]. It will be argued that the additional spatial interaction term is able to shift the bifurcation lines such that now two Takens-Bogdanov points move from infinity to finite parameter values, acting as organizing centers of a richer dynamical behavior.

10.2 Bifurcation diagrams and width of the localized structures

In Section 9.3, we have presented a linear stability analysis of Eq. (10.1). For positive values of $\eta = \beta/\alpha^2 > 1/4(2-\theta)$, we have shown that the MI instability, both the MI at low and high background intensities, occurs with equal critical wave numbers $\beta k_m^4 = 1/4\eta$. From this wave number, we can estimate the typical

width of LSs to be of the order of

$$\Lambda_+ = 2\pi\sqrt[4]{4\beta\eta}. \tag{10.2}$$

In the limit of small diffraction, Eq. (10.2) predicts that the width of LSs increases when α decreases, while Eq. (9.2) indicates a decreasing width. Therefore, there must exist a value of the diffraction strength α for which the LS is of minimal width. In this Section, we will use a numerical method to determine this optimum. However, we want to point out that this minimal size LS can be unstable. Our calculations will also provide insight in this matter. For $\eta < 0$, at the MI point, we can derive the following estimate for the LS width :

$$\Lambda_- = \frac{2\pi\sqrt[4]{4\beta\eta}}{\sqrt{1+\sqrt{1-4(2-\theta)\eta}}}. \tag{10.3}$$

Consequently, when $\eta < 0$, the LS width will still decrease with the diffraction strength α, but due to the nonlocality the width will saturate at $\Lambda_{\text{lim}} = 2\pi\sqrt[4]{-\beta/(2-\theta)}$. Again, the possibility that the LS become unstable before reaching this limit exists, emphasizing the need to numerically check the stability of these structures.

Since two-dimensional cavity solitons are radially symmetric they correspond to stationary solutions of the radial form of Eq. (10.1) with boundary conditions $\partial_r A(r=0) = 0$ and $\partial_r A(r\to\infty) = 0$. We solve this equation numerically using a Newton method [1, 23].[2]

An example of a typical 2D cavity soliton solution is shown in Fig. 10.1. Such a CS solution can then be continued in parameter space using the Newton method. Several bifurcation diagrams calculated in this way are shown for different values of η in Fig. 10.1. In the absence of nonlocality ($\eta = 0$), as previously studied in Refs. [20, 22], a branch of LSs emerges subcritically from the HSS at $|A_s|^2 = 1$. The negative slope part of this branch corresponds to unstable LSs; the positive slope higher branch is stable for low values of $|A_s|^2$. At higher background intensities the intensity peaks become higher and narrower, attributed to the more prominent self-focusing effect, and at a certain point they become again unstable with respect to azimuthal perturbations. For $\eta > 0$ [Fig. 10.1(a)], we observe that the branches extend to smaller $|A_s|^2$ with increasing η, while the domain of

[2]The radial form of this equation is discretized, from which a set of coupled nonlinear equations is obtained. Since the equation is linear in the spatial derivatives, the diffraction term can be computed in the spatial Fourier space. Zero derivatives at the boundaries are imposed. This approach is very accurate and automatically generates the Jacobian operator, whose eigenvalues determine the stability of the solutions. Note that this method finds both stable and unstable stationary solutions. An appropriate initial condition is found by numerically simulating the equation in time using the integration scheme explained in Appendix B.

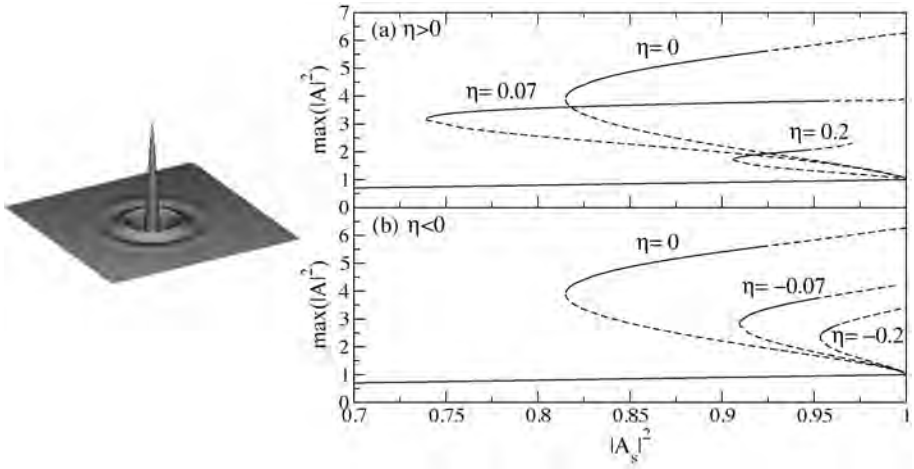

Figure 10.1: Left: Example of a 2D cavity soliton ($|A|$ is plotted in the 2D space). Right: Maximal intensity of the cavity soliton vs. the background intensity for different values of η. Solid lines indicate stable structures, whereas dashed lines correspond to unstable solutions. $\theta = 1.23$. (a) Positive η. (b) Negative η.

stability is enlarged. This trend is reversed from a certain η on, and the stability range decreases. Also note that due to the higher order diffraction due to e.g. nonlocality, which physically tends to spread out the intensity to neighboring points, the peak intensity of cavity solitons drops. For $\eta < 0$ [Fig. 10.1(b)], the branches move monotonically to higher background intensity and to lower peak intensity with stronger η. Again note that the stability range is reduced considerably. A more detailed study of the regions of stability in function of the different parameters is given in the next Section.

To find the minimal LS size as discussed above, we have investigated the scaling of the renormalized full width at half maximum ($\xi = d_{\mathrm{FWHM}}/\sqrt[4]{|\beta|}$) of the LS with η in Figure 10.2. Note that this renormalization enables us to obtain a general result only depending on the detuning θ. For each value of η, we indicate the width ξ of the upper branch LS at the change of stability, when stable LSs exist, while plotting the ξ at the saddle-node bifurcation when the entire upper branch is unstable. For $\eta > 0$ [Figure 10.2(a)], one can distinguish two regions of stable LSs, one in which the width decreases with decreasing diffraction strength, and the other with the inverse effect. One can identify the minimal width ξ_{min} and its corresponding optimal η_{opt} in the leftmost region. For $\eta < 0$ [Figure 10.2(b)], the width decreases monotonically with decreasing diffraction strength, until

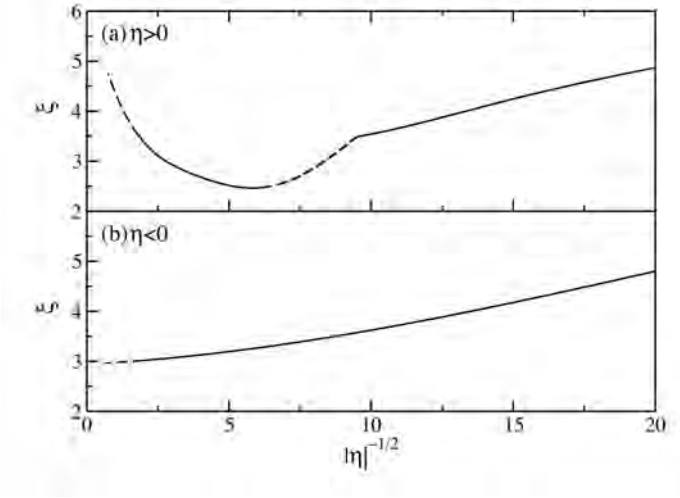

Figure 10.2: Renormalized full width at half maximum ξ vs. diffraction strength ($|\eta|^{-1/2}$). The width ξ is shown of the higher branch LSs at the change of stability or of the LSs at the saddle-node bifurcation when no stable LSs exist Stable LSs are indicated by solid lines, whereas the unstable LSs are in dotted lines. $\theta = 1.23$. (a) Positive η. (b) Negative η.

stability of the LSs is lost. At this point, the minimal width ξ_{min} is obtained. Our numerical calculations thus qualitatively confirm the prediction by the linear stability analysis given above. We have also repeated this procedure for several values of the detuning, which gives us the optimal parameter set that produces minimal size LS given a certain β [1]. In the next sections, we will elaborately discuss all the different kinds of instabilities that can occur in this system.

10.3 Phase diagrams

In this section, we show the different possibilities of dynamical behavior of LSs in parameter space (see Figure 10.3). LSs can undergo two kinds of instabilities, radial instabilities which preserve the localized character of the structure and azimuthal instabilities which lead to the formation of extended patterns. The last ones appear only for large values of the background intensity ($I_s = |A_s|^2$ close

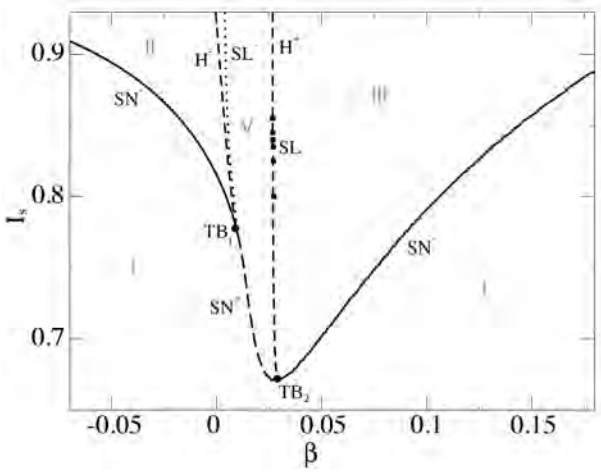

Figure 10.3: Phase diagram of LSs in the Kerr cavity for $\theta = 1.23$. LSs do not exist in Region I, below the saddle node line (SN). LSs are stable between the saddle-node bifurcation (solid line - SN) and the Hopf bifurcation (dashed line - H), namely in Regions II, III, VI and VIII (see also Figure 10.4). In Regions IV and VII delimited by a Hopf and a saddle-loop bifurcation (dotted line - SL) there are stable oscillatory LSs while the stationary LSs are unstable. In Region V the static LSs is unstable and the phase space generated after the destruction of the limit cycle at the SL induces a regime of excitable LSs. Region VI corresponds to a regime of conditional excitability with both stable and excitable LSs. Finally in Region VIII one encounters tristability: a stationary and an oscillatory LSs coexist with the homogeneous solution. Where the saddle-node bifurcation line and the Hopf bifurcation line meet is a Takens-Bogdanov (TB) bifurcation.

to 1) [20]. We focus here on the radial instabilities, so phase diagrams (Figs. 10.3 and 10.4) are plotted only up to $I_s = 0.93$, before the azimuthal instabilities take place.

Since the system has three parameters (I_s, θ, β), for the sake of clarity we fix the detuning at $\theta = 1.23$ in this section and analyze a slice of the whole parameter space. Figure 10.3 shows the region of the parameter plane (β, I_s) that contains the most relevant regimes of dynamical behavior of the system. The line that dominates this parameter plane has the shape of a deformed parabola, and is a line of saddle-node (SN) bifurcations in which two LSs are created. Below this line one has Region I where no LSs exist. We recall that in all the parameter range covered by Figure 10.3 the spatially homogeneous solution is always stable. The

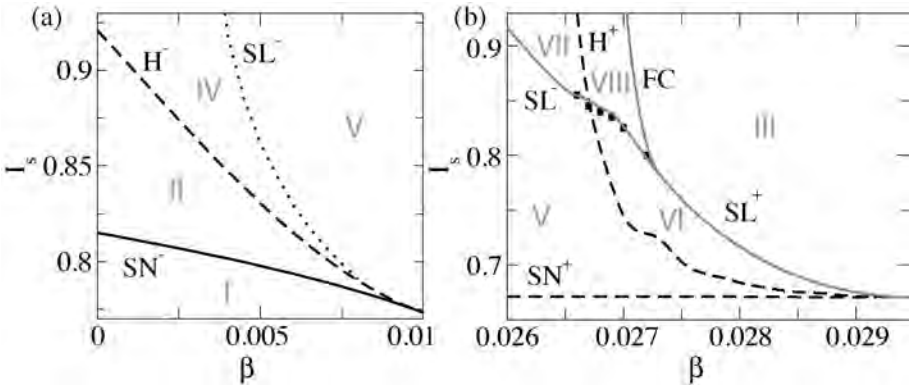

Figure 10.4: Zoom of Figure 10.3 near TB_1 (a) and TB_2 (b). Lines have been determined using the method explained in Section 10.3 with the exception of the SL line in panel (b). In that case the filled squares display the location of the SL obtained from numerical integration of Eq. (10.1), while the grey line through these points is only to guide the eye. $\theta = 1.23$.

different regimes above this line are organized by two codimension-2 Takens-Bogdanov points, TB_1 ($\beta = 0.00987, I_s = 0.7741$) and TB_2 ($\beta = 0.02944, I_s = 0.6707$), discussed in the next two Sections.
Without the bilaplacian term there is only one TB point [22, 23]. In that case, the TB point is found only asymptotically for the limit $\theta \to \infty$. As we will discuss later, that TB point corresponds in fact to the TB_1 point found here. Therefore, the bilaplacian term β has brought this bifurcation to finite parameter values allowing us to fully study the different dynamical regimes around the TB_1 point.

10.4 Dynamical behavior around the TB_1 point

A Takens-Bogdanov (or double-zero) bifurcation is associated to the presence of two (non-diagonalizable) degenerate null eigenvalues [24, 25]. Such a bifurcation occurs when, in a line of SN bifurcations, one of the modes transverse to the center manifold (of the SN bifurcation) passes through zero, implying that this transverse mode switches from stable to unstable or vice versa. If this transverse mode is stable we will denote the SN bifurcation line as SN^-, while we use SN^+ if this mode is unstable. Throughout the remainder of this Chapter, we will use $^-$ for bifurcations for which there is a stable emerging solution and $^+$ if the emerging solutions are unstable. H^- will describe a supercritical Hopf, and H^+ a subcritical one.

Another feature of a TB point is that two new bifurcation lines emerge from it [26]: a Hopf bifurcation line[3] and a saddle-loop (homoclinic) bifurcation line[4]. In order to specify whether the cycle that emerges from the saddle-loop bifurcation is stable or unstable, it is useful to define the saddle-quantity ν. For low-dimensional dynamical systems this quantity is given by $\nu = \lambda_s + \lambda_u$, with $\lambda_u > 0$ and $\lambda_s < 0$ the unstable and stable eigenvalues of the saddle, respectively. The emerging cycle will be stable if $\nu < 0$, and unstable in the opposite case: $\nu > 0$ [26].

At the TB_1 point, the saddle-node bifurcation is *stable* (SN^-), the Hopf is supercritical (H^-), and the saddle-loop creates a stable cycle (SL^-). Along the SN^- line a pair of stationary LSs are created, one stable (upper branch) and the other (middle branch) unstable along a single direction in phase space (thus, a saddle point in dynamical systems parlance). So, Region II is characterized by stable LSs coexisting with the spatially homogeneous solution. A qualitative sketch of the most relevant different kinds of behavior in the system as β is increased can be found in Figure 10.5 (this corresponds to a horizontal line in Figure 10.4 for $I_s \approx 0.8$). In this figure, panel (a) reflects the behavior inside Region II, where the LS is the stable focus, the homogeneous solution is the stable node and the middle branch LS is the saddle.

The upper branch LS solution becomes unstable at the supercritical Hopf bifurcation, H^-, and leads to Region IV, characterized by oscillatory LSs, i.e., autonomous oscillons. Figure 10.5 (b) illustrates the behavior past the Hopf bifurcation: the stable oscillatory LS and the unstable focus in the center can be seen. Approaching the SL^- line a saddle-loop (homoclinic) bifurcation takes place, in which the limit cycle (oscillatory LS) becomes a homoclinic orbit of the saddle (middle branch LS). The SL^- is a global bifurcation, and cannot be detected through a local analysis. Thus, in this study it has been determined through numerical simulations of Eq. (10.1)[5]. Panel (c) in Figure 10.5 illustrates the cycle growing in amplitude and approaching the saddle, while in panel (d) the cycle has become the homoclinic orbit of the saddle. The approach of the stable cycle to the saddle can also be seen quantitatively in panel (a) of Figure 10.6: in this figure bifurcation diagrams corresponding to vertical cuts in parameter space, i.e. with β fixed (cf. Figure 10.3), are presented. Beyond the SL^-, the behavior of the system is excitable (Region V) [22, 23], in particular of type (or class) I [27], as the excitability threshold is the stable manifold of the saddle. An excitable excursion is achieved when localized perturbations beyond this thresh-

[3] The imaginary part of the eigenvalues at the Hopf bifurcation is singularly zero at the TB point, in order to have a double zero.

[4] This is an example of the local origin of a global bifurcation, one of the few situations in which the existence of such a bifurcation can be established analytically.

[5] An explanation of the numerical integration scheme that we use can be found in Appendix B.

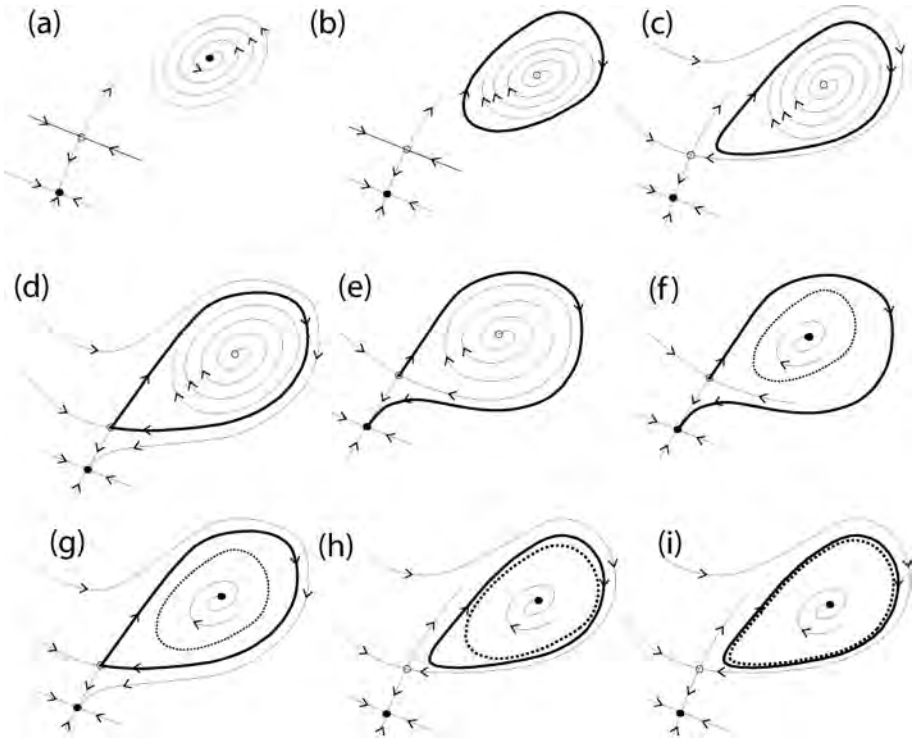

Figure 10.5: Qualitative evolution of the phase space at $I_s \approx 0.8$ and $\theta = 1.23$ for increasing values of β, corresponding to the different dynamical behavior in a horizontal cut of Figure 10.3. From (a) to (i), one goes from stable LS (Region II) to an oscillating LS (Region IV), followed by an excitable LS (Region V), a conditional excitable LS (Region VI), a coexistence of stable LS and oscillatory LS (Region VIII).

old are applied to the spatially homogeneous solution. Fig 10.5 (e) sketches the phase space in the excitable regime past the saddle-loop bifurcation.
Inside Region V, no stable LSs are found, only unstable LSs solutions exist, and the system is excitable for all values of I_s above the SN^+ line. This line which is just the continuation of SN^- past the TB_1 point was not observed in [22, 23] since the TB point without bilaplacian term is located at $\theta \to \infty$. The SN^+ line creates a saddle-unstable node pair (middle and upper branch, respectively). The pair of unstable solutions can be seen in the bifurcation diagram shown in Figure 10.6(b) corresponding to a vertical cut of the parameter plane just to the right of TB_1 point.

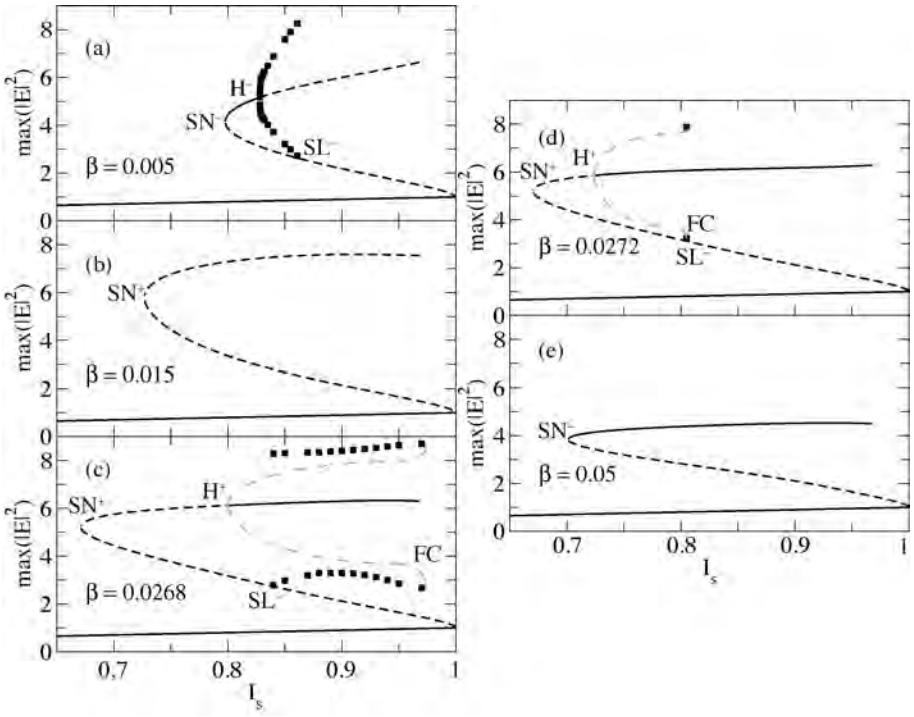

Figure 10.6: Bifurcation diagrams showing the maximum intensity of the LS as function of the background intensity I_s, for: (a) $\beta = 0.005$; (b) $\beta = 0.015$; (c) $\beta = 0.0268$; (d) $\beta = 0.0272$; (e) $\beta = 0.05$. The lowest solid line represents the stable homogeneous solution. The lowest dashed line shows the maximum intensity of the unstable middle branch LS. Above that line, the upper branch LS is shown, where the solid line stands for the stable LS and the dashed line for the unstable LS. In (a), (c) and (d) the system exhibits stable oscillatory behavior (see text). In these cases, the maximum and minimum intensity of the oscillating LS are depicted as filled squares. The grey dashed line, representing the unstable limit cycle, is only a guiding line for the eye. When the limit cycle touches the middle branch LS, a saddle-loop bifurcation occurs. $\theta = 1.23$.

10.5 Dynamical behavior around the TB_2 point

An even richer scenario is found around the TB_2 point. Comparing Figure 10.4(a) and (b), one can see that the TB_2 does not yield the same scenario as around TB_1. In TB_1 the two lines that emerge involve stable objects (H^- and SL^- create and

destroy, respectively, a stable limit cycle), while in TB_2 the Hopf line is subcritical (involving an unstable cycle). Furthermore, in the TB_1 point the two lines, H^- and SL^- are tangent to the line SN^- of stable saddle-node bifurcations while the opposite happens for TB_2 (the lines unfolding are tangent to SN^+) [26].
Crossing the H^+ line coming from Region V, the unstable (upper branch) LS exhibits a subcritical Hopf bifurcation and becomes a stable focus. The cycle that is created is unstable and has only a single unstable direction. In Region VI the system is then bistable (upper branch LS and homogeneous solutions coexist) and the unstable cycle is the basin boundary of the upper branch stable LS as qualitatively illustrated in Figure 10.5(f). Just after the bifurcation this basin of attraction is small (since the initial cycle amplitude is zero) and grows as one moves away from the bifurcation line. This can be seen in the bifurcation diagram displayed in Figure 10.6(c) corresponding to a vertical cut of Figs. 10.3 and 10.4 at $\beta = 0.0268$. The upper branch LS becomes stable around $I_s = 0.8$. The dashed grey line has been drawn with the purpose of guiding the eye only. It represents the unstable cycle that we do not compute. This bifurcation diagram also shows the existence of a stable limit cycle (plotted as squares) corresponding to an oscillatory LS. The stable limit cycle comes from a fold of cycles (FC) bifurcation, discussed in more detail later, which takes place at a larger value of I_s. Decreasing I_s the stable limit cycle disappears at a saddle-loop bifurcation which takes place when the stable limit cycle becomes the homoclinic orbit of the saddle (middle branch soliton). In Figure 10.6(c) Region VI corresponds to the values of I_s limited on the left by the subcritical Hopf (H^+) and the right by the saddle loop (SL^+ and SL^-). Precise values for the SL^- obtained from numerical integration of Eq. (10.1) are plotted as filled squares in Figure 10.4(b) while the grey SL line joining the points have been drawn to guide the eye[6]. As we will discuss in the next section, Region VI corresponds to a regime of conditional excitability.
In Figure 10.6(c), the FC on the one hand and the SL^- on the other limit a new region of *tristability* where a stationary LS, a oscillatory LS and the homogeneous solution coexist. In Figure 10.4(b) the tristable region is labeled as VIII. In Figure 10.5 the panel (g) sketches the phase space at the saddle-loop while the panel (h) illustrates the tristable regime. Increasing β or I_s in parameter space the stable cycle decreases in amplitude while the unstable limit cycle increases until both the stable and unstable cycles are destroyed in the fold bifurcation (Figure 10.5(i)). Figure 10.7 shows the time evolution in the tristable regime obtained starting from an initial condition belonging to the basin of attraction of the limit cycle and from an initial condition within the basin of attraction of the stable LS.
In the phase diagram (Figure 10.4(b)) the SL^- line can also be located to the left

[6] An explanation of the numerical integration scheme that we use can be found in Appendix B.

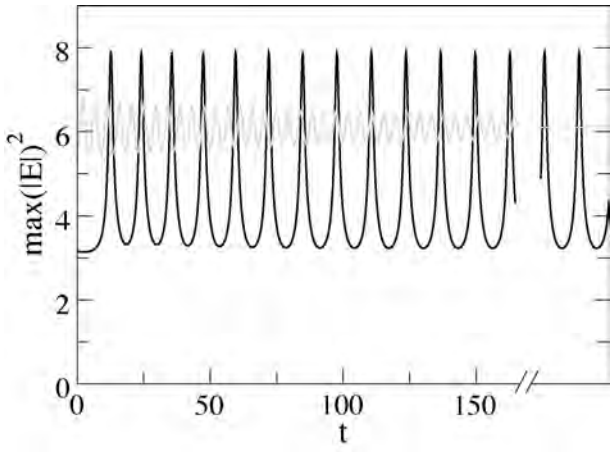

Figure 10.7: Dynamical evolution of the LS in the tristable regime, where the spatially homogeneous fundamental branch (not shown), stable oscillatory LS regime (solid line), and stable focus (gray line) coexists. The maximum intensity of the LS is plotted.

of H^+ (Region VII). The bifurcation diagram in this case would be similar to the one shown in Figure 10.6(c), except for the fact that the SL^- becomes a SL^+ and the H^+ takes place at a larger value of I_s than the SL^-. Therefore VII is a region of bistability where a stable limit cycle corresponding to the oscillatory upper branch LS coexist with the homogeneous solution while the steady state upper branch LS is an unstable focus.

The last region in the phase diagram to be described is Region III, located to the right of the SL^+ and FC lines. The phase space corresponding to this broad region is again the one of Figure 10.5(a). The upper branch stationary LS is a stable point and coexists with the homogeneous solution. Figure 10.6(e) shows a quantitative bifurcation diagram corresponding to a vertical cut of Figure 10.3 for $\beta = 0.05$, to the right of the TB_2. For $I_s < 0.7$ only the homogeneous solution exists (Region I) while above $I_s = 0.7$ one enters in Region III of coexistence of the stable LS with the homogeneous solution.

We now analyze in detail the fold of limit cycles bifurcation. It appears at a secondary codimension-two point referred to as resonant side-switching, where the fold and the saddle-loop bifurcation, that delimit the region of tristability, coalesce [28, 29]. This occurs, roughly, around $\beta = 0.0272$ and $I_s = 0.82$. Figure 10.6(d) depicts a bifurcation diagram close to this codimension-2 point, for which the region of existence of stable limit cycles is quite narrow: the represented square is very close both to the saddle-loop bifurcation and to the fold of

cycles. In the phase diagram shown in Figure 10.4(b) this codimension-2 corresponds to the point where the FC and the SL (SL^- and SL^+) lines meet.
The occurrence of the resonant side-switching bifurcation is related to the eigenvalue spectrum of the saddle, namely, the saddle quantity of the middle branch LS approaches zero, and the cycle emerging from the saddle-loop changes from *stable* to *unstable*. Close to TB_2 point the saddle-loop bifurcation must destroy an unstable cycle (transition from Region VI to III), hence $\nu > 0$, while after the fold has taken place it destroys a stable cycle (transition from Region VIII to VI), so $\nu < 0$. Close to the SL^+ that emerges from the TB_2 point, where the saddle quantity is positive, four localized modes play a role in the dynamical behavior of the system. However, when moving away from the SL^+ line, only two localized modes determining the dynamics remain. So, in conclusion, we can say that the system is essentially two-dimensional for the same reasons as discussed in Ref. [25], except close to the SL^+ line, originating from the TB_2 point.

10.6 Excitability and conditional excitability

When crossing a saddle-loop bifurcation from a region where a stable oscillatory LS exist one enters in a excitable regime. As discussed in Subsection 10.4, this scenario takes place when going from Region IV (where the oscillatory LS is stable) to Region V where LS exhibit excitability. Of course it is also possible to enter in Region V from the other side, namely from the side of the TB_2 point. In fact a similar scenario is found when going from Region VII where the oscillatory LS is stable to Region V. In any case the stable manifold of the saddle (middle branch LS) plays the role of excitability threshold, so the excitable response is triggered only by localized perturbations of the homogeneous solution that bring the system beyond this threshold. Excitability is of Class I [27], characterized by long response times for perturbations that leave the trajectory close to the saddle in phase space.
Close to the TB_2 point there is another region, VI, where one can enter crossing a saddle-loop line. However, the dynamical behavior in Region VI is qualitatively different from Region V since the upper branch LS is an unstable focus in the last one, while it is stable in the former. As discussed before, the upper branch LS has been made stable by the subcritical Hopf bifurcation H^+ that separates Region V from VI. The H^+ bifurcation generates also an unstable limit cycle, which is not present in Region V. Therefore, although the transition from Regions III or VIII to Region VI goes through a saddle-loop bifurcation, the scenario must be qualitatively different from the one discussed above which leads to the *usual* excitability found in Region V. In Region VI, one finds a regime of conditional excitability, in which the LS is simultaneously excitable and bistable. The excitable behavior

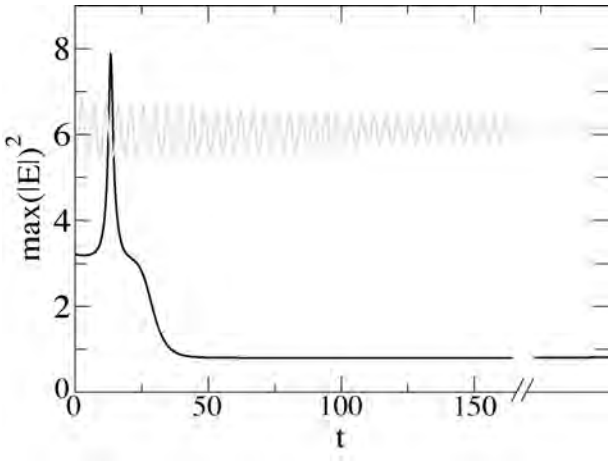

Figure 10.8: The conditional excitability regime is illustrated for $\beta = 0.0272$ and $I_s = 0.8$. The solid line (excitable trajectory) corresponds to time evolution of the maxima of the peak after a localized perturbation of the homogeneous state that brings the system beyond the excitability threshold but outside the basin of attraction of the upper branch LS. The grey line corresponds to a stronger localized perturbation that brings the system inside the boundary of attraction of the upper branch LS.

is also Class I.

To clarify what conditional excitability means, we refer to the phase space sketched in Figure 10.5(f). In this situation, while as usual, perturbations of the homogeneous solution that are not able to cross the excitability threshold (stable manifold of the saddle) lead to normal relaxation, there are two possible different dynamical responses for supra-threshold perturbations. If a localized perturbation of the homogeneous state brings the system inside the basin of attraction of the stable focus, namely inside the unstable cycle, the system jumps from the fundamental solution to this attractor. Therefore after this perturbation the system relaxes to the stable LS in a oscillatory way. The grey line in Figure 10.8 shows the dynamical evolution of the maxima of the peak in this situation. Instead, for localized perturbations of the homogeneous solution which bring the system beyond the stable manifold of the saddle but outside the unstable cycle, the response is excitable. The system exhibits a large response corresponding to a circulation around the unstable limit cycle before returning to the stable homogeneous solution. The black line in Figure 10.8 shows the time evolution of maxima of the peak for a excitable trajectory.

So, in summary, the dynamical response of perturbations is more complex than

simply sub- and supra-threshold, and for the latter type of perturbations two possible regimes are possible. When going from Region VI to Region V at the H^+ line, the upper branch LS becomes unstable and the unstable limit cycle responsible for the conditional excitable response to supra-threshold perturbations disappears, so the conditional excitability becomes a usual one.

10.7 Conclusion

We have studied the nonlinear dynamical behavior of 2D localized structures in a model for an optical cavity filled by a Kerr nonlinear medium and a left-handed metamaterial [1]. The model is a generalization of the Lugiato-Lefever equation [3], and includes higher order spatial effects. Our study confirms the possibility to reduce the size of cavity solitons beyond the diffraction limit by using diffraction compensation techniques. However, we have shown that higher order spatial interactions not only hinder this size reduction, but also alter the stability of cavity solitons in a manifest way, imposing a new limit on their size. We have demonstrated the existence of regions with stationary, oscillating and excitable localized structures. Furthermore, we have shown that the different bifurcation lines originate from two Takens-Bogdanov (TB) codimension-2 points, which is a strong signature for the presence of a homoclinic bifurcation [2]. This homoclinic bifurcation offers a route to the excitable behavior of the 2D localized structures. Finally an extra secondary codimension-2 point (resonant side-switching bifurcation) creates a fold of cycles that leads to two new regimes, one of tristability and one of conditional excitability.

References

[1] L. Gelens, G. Van der Sande, P. Tassin, M. Tlidi, P. Kockaert, D. Gomila, I. Veretennicoff, and J. Danckaert, "Impact of nonlocal interactions in dissipative systems: towards minimal-sized localized structures," *Phys. Rev. A* **75**(6), 063812, 2007.

[2] L. Gelens, D. Gomila, G. Van der Sande, J. Danckaert, P. Colet, and M. A. Matías, "Dynamical instabilities of dissipative solitons in nonlocal optical cavities with nonlocal materials," *Phys. Rev. A* **77**, 033841, 2008.

[3] L. A. Lugiato and R. Lefever, "Spatial dissipative structures in passive optical systems," *Phys. Rev. Lett.* **58**, 2209–2211, 1987.

[4] P. Kockaert, P. Tassin, I. Veretennicoff, G. Van der Sande, and M. Tlidi, "Beyond the zero-diffraction regime in optical cavities with a left-handed material," *J. Opt. Soc. Am. B* **26**, B148–B155, 2009.

[5] P. Coullet, C. Riera, and C. Tresser, "Stable static localized structures in one dimension," *Phys. Rev. Lett.* **84**, 3069–3072, 2000.

[6] V. B. Taranenko, K. Staliunas, and C. O. Weiss, "Spatial soliton laser: Localized structures in a laser with a saturable absorber in a self-imaging resonator," *Phys. Rev. A* **56**, 1582–1591, 1997.

[7] S. Barland, J. R. Tredicce, M. Brambilla, L. A. Lugiato, S. Balle, M. Giudici, T. Maggipinto, L. Spinelli, G. Tissoni, T. Knödl, M. Miller, and R. Jäger, "Cavity solitons as pixels in semiconductor microcavities," *Nature* **419**, 699–702, 2002.

[8] M. Brambilla, L. A. Lugiato, F. Prati, L. Spinelli, and W. J. Firth, "Spatial soliton pixels in semiconductor devices," *Phys. Rev. Lett.* **79**, 2042–2045, 1997.

[9] M. Tlidi, P. Mandel, and R. Lefever, "Localized structures and localized patterns in optical bistability," *Phys. Rev. Lett.* **73**, 640–643, 1994.

[10] X. Hachair, S. Barland, L. Furfaro, M. Giudici, S. Balle, J. R. Tredicce, M. Brambilla, T. Maggipinto, I. M. Perrini, G. Tissoni, and L. Lugiato, "Cavity solitons in broad-area vertical-cavity surface-emitting lasers below threshold," *Phys. Rev. A* **69**, 043817, 2004.

[11] K. Staliunas, "Midband dissipative spatial solitons," *Phys. Rev. Lett.* **91**, 053901, 2003.

[12] D. R. Smith, J. B. Pendry, and M. C. K. Wiltshire, "Metamaterials and negative refractive index," *Science* **305**(5685), 788–792, 2004.

[13] V. M. Shalaev, "Optical negative-index metamaterials," *Nature Photon.* **1**, 41–48, 2007.

[14] A. A. Zharov, I. V. Shadrivov, and Y. S. Kivshar, "Nonlinear properties of left-handed metamaterials," *Phys. Rev. Lett.* **91**, 037401, 2003.

[15] M. Lapine, M. Gorkunov, and H. Ringhofer, "Nonlinearity of a metamaterial arising from diode insertions into resonant conductive elements," *Phys. Rev. E* **67**, 065601, 2003.

[16] P. Kockaert, P. Tassin, G. Van der Sande, I. Veretennicoff, and M. Tlidi, "Negative diffraction pattern dynamics in nonlinear cavities with left-handed materials," *Phys. Rev. A* **74**(3), 033822, 2006.

[17] P. Tassin, L. Gelens, J. Danckaert, I. Veretennicoff, G. Van der Sande, P. Kockaert, and M. Tlidi *Chaos* **17**, 037116, 2007.

[18] W. Firth, A. Lord, and A. Scroggie, "Optical bullet holes," *Phys. Scr.* **T67**, 12, 1996.

[19] S. Longhi, G. Steinmeyer, and J. Wong, "Variational approach to pulse propagation in parametrically amplified optical systems," *J. Opt. Soc. Am. B* **14**, 2167, 1997.

[20] W. J. Firth, G. K. Harkness, A. Lord, J. M. McSloy, D. Gomila, and P. Colet, "Dynamical properties of two-dimensional kerr cavity solitons," *J. Opt. Soc. Am. B* **19**, 747–752, 2002.

[21] V. Vanag and I. Epstein, "Stationary and oscillatory localized patterns, and subcritical bifurcations," *Phys. Rev. Lett.* **92**, 128301, 2004.

[22] D. Gomila, M. A. Matías, and P. Colet, "Excitability mediated by localized structures in a dissipative nonlinear optical cavity," *Phys. Rev. Lett.* **94**, 063905, 2005.

[23] D. Gomila, A. Jacobo, M. A. Matías, and P. Colet, "Phase-space structure of 2D excitable localized structures," *Phys. Rev. E* **75**, 026217, 2007.

[24] F. Takens, "Singularities of vector fields," *Publ. Math. IHES* **43**, 47–100, 1974.

[25] R. I. Bogdanov, "Versal deformations of a singular point on the plane in the case of zero eigenvalues," *Functional Analysis and its Applications* **9**, 144–145, 1974.

[26] Y. Kuznetsov, *Elements of Applied Bifurcation Theory*, Springer, 3rd edition, New York, 2004.

[27] E. M. Izhikevich, "Neural excitability, spiking and bursting," *Int. J. Bifurcation Chaos Appl. Sci. Eng.* **10**, 1171–1266, 2000.

[28] S.-N. Chow, B. Deng, and B. Fiedler, "Homoclinic bifurcation at resonant eigenvalues," *J. Dyn. Diff. Eqs.* **2**, 177–244, 1990.

[29] A. R. Champneys and Y. A. Kuznetsov, "Numerical detection and continuation of codimension-two homoclinic bifurcations," *Int. J. Bif. Chaos* **4**, 785–822, 1994.

CHAPTER 11

Coarsening and faceting dynamics

"My theory by A. Elk, brackets, Miss, brackets. This theory goes as follows and begins now. All brontosauruses are thin at one end, much much thicker in the middle, and the thin again at the far end. That is my theory, it is mine, and it belongs to me, and I own it, and what it is, too." — Miss. Anne Elk in Monty Python.

The complex Swift-Hohenberg equation models pattern formation in lasers, optical parametric oscillators and photorefractive oscillators. With real coefficients this equation admits time-independent phase-winding states in which the real and imaginary parts of the order parameter oscillate periodically but with a constant phase difference between them. We show that these states may be unstable to a longwave instability. Depending on the parameters the evolution of this instability may or may not conserve phase. In the former case the system undergoes slow coarsening described by a Cahn-Hilliard equation; in the latter it undergoes repeated phase-slips leading either to a stable phase-winding state or to a faceted state consisting of an array of frozen defects connecting phase-winding states with equal and opposite phase. The transitions between these regimes are studied and their location in parameter space is determined.[1]

[1]The work presented in this Chapter has been published in the following journal papers: [1, 2].

11.1 Introduction

The complex Swift-Hohenberg equation (CSHE) has a number of applications in nonlinear optics. For example, the CSHE describes, under appropriate conditions, Class A and C lasers [3–5]. The CSHE also describes nondegenerate optical parametric oscillators (OPOs) [6–8], photorefractive oscillators [9], semiconductor lasers [10] and passively mode-locked lasers [11]. More generally, the CSHE models pattern formation arising from an oscillatory instability with a finite wave number at onset [12, 13]. In most of these examples the bifurcation towards non-zero spatially homogeneous solutions in the CSHE arises *supercritically*, implying the presence of spatially structured states for parameter values exceeding the linear stability threshold. In general, the resulting CSHE has complex coefficients and hence time-dependent solutions. In this Chapter, we restrict our attention to an important but special case of the CSHE, namely the case of real coefficients, that admits only stationary solutions. Understanding of this special case is a prerequisite for gaining a deeper insight into the behavior of the supercritical CSHE with complex coefficients, studied in the next Chapter.

11.2 Formulation of the problem

We study the supercritical CSHE with real coefficients,

$$u_t = ru - (\partial_x^2 + k_0^2)^2 u - |u|^2 u, \tag{11.1}$$

where u is a complex field and the subscripts x and t indicate partial derivatives with respect to position and time. The equation is fully parametrized by the real parameter r; in the following we find it convenient to retain the wave number k_0 in the formulation despite the fact that it can be scaled out. We study Eq. (11.1) on a periodic domain with period $L \gg 2\pi/k_0$ as a function of both r and k_0 using a combination of analytical and numerical tools [1]. The equation has variational structure with a Lyapunov function (free energy) F_{SH} given by

$$F_{SH} = \frac{1}{L}\int_0^L [-r|u|^2 + \frac{1}{2}|u|^4 + |(\partial_x^2 + k_0^2)u|^2]dx. \tag{11.2}$$

Thus

$$\frac{dF_{SH}}{dt} = -\frac{2}{L}\int_0^L |u_t|^2 dx \tag{11.3}$$

and F_{SH} decreases with time until a stationary state is reached corresponding to a local minimum of F_{SH}. As throughout this Chapter, we will interpret the results

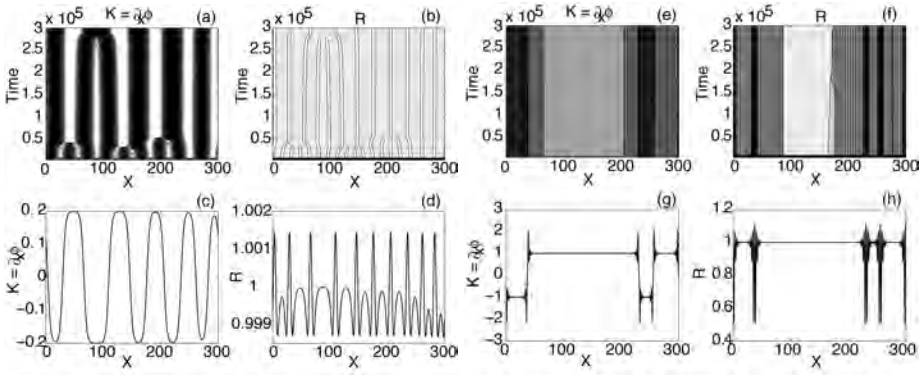

Figure 11.1: Time evolution of the CSHE with $r = 1$, $L = 300$ and $N = 1024$ discretization points, starting from random initial conditions. Coarsening behavior is observed in panels (a)-(d) for $k_0 = 0.2$. Faceting behavior is observed in panels (e)-(h) for $k_0 = 1$. The spatio-temporal evolution of $K = \partial_x \phi$ is shown in panels (a) and (e), with the corresponding profiles at $t = 3\ 10^5$ in (c) and (g). The evolution of the amplitude R is given in panels (b) and (f), with the corresponding profiles at $t = 3\ 10^5$ in (d) and (h).

in terms of either the real and imaginary parts of the order parameter $u(x,t)$, or in terms of amplitude and phase variables, we write Eq. (11.1) also as follows:

$$\begin{aligned} R_t &= (r - k_0^4)R - R^3 - 2k_0^2 R_{xx} + 2k_0^2 R\phi_x^2 + 6R_{xx}\phi_x^2 \\ &\quad +12R_x\phi_x\phi_{xx} - R\phi_x^4 + 3R\phi_{xx}^2 + 4R\phi_x\phi_{xxx} - R_{xxxx}, \end{aligned} \tag{11.4}$$

$$\begin{aligned} R\phi_t &= -4k_0^2 R_x\phi_x - 2k_0^2 R\phi_{xx} + 4R_x\phi_x^3 - 6R_{xx}\phi_{xx} \\ &\quad -4R_x\phi_{xxx} - 4R_{xxx}\phi_x + 6R\phi_x^2\phi_{xx} - R\phi_{xxxx}. \end{aligned} \tag{11.5}$$

where $u(x,t)$ is defined by

$$u(x,t) = u_R(x,t) + iu_I(x,t) \equiv R(x,t)e^{i\phi(x,t)}. \tag{11.6}$$

Figures 11.1(a)-(d) show typical time evolution obtained using direct numerical integration of Eq. (11.1) when $r = 1$ and $k_0 = 0.2$ starting from random initial conditions[2]. Figure 11.1(a) depicts the spatio-temporal evolution of the phase gradient $K \equiv \phi_x$, while the evolution of the amplitude R is depicted in Fig. 11.1(b). The profiles of both the phase gradient K and the amplitude R at the final time step of the numerical simulation are shown in Figs. 11.1(c) and (d). Initially a modulational instability develops after which several kink-antikink pairs or

[2] An explanation of the numerical integration scheme that we use can be found in Appendix B.

"bubbles" are created in the system. These bubbles are unstable and in time smaller bubbles repeatedly merge forming larger and larger structures, a process called *coarsening* [14]. This merging of bubbles continues until only one bubble remains in the system. Quite different behavior is observed when k_0 is larger, as indicated in Figs. 11.1(e)-(h) for $k_0 = 1$, again starting from random initial conditions. For this set of parameters no coarsening dynamics is observed. Instead the different bubbles present in the system are stationary and take the form of stable *facets* with wavenumbers $K = \pm k_0$ connected by sharp interfaces with oscillatory internal structure. The existence of these structures was noted already by Raitt and Riecke [15, 16] in the context of the fourth order Ginzburg-Landau equation; in the following we refer to them as spatially localized states (LS)..

In this Chapter, we provide a detailed analysis of both the coarsening dynamics and the faceting dynamics in the CSHE. Insight into the transition between both regimes is provided as well. We first describe the basic properties of this equation, following recent work by us on the subcritical case [1]. In Section 11.4, we introduce the notion of *phase-winding states* and study their stability properties. Phase-winding states are solutions of the CSHE in which the real and imaginary parts of the order parameter oscillate (in space) with a constant, but nonzero, phase difference. The phase of each jumps by the same integer multiple of 2π across the domain. In Section 11.5, we study the evolution of the longwave instability of phase-winding states as identified in Section 11.4 and show that under appropriate conditions it follows Cahn-Hilliard dynamics, leading to slow coarsening in wave number space. In Section 11.6, we show that in other regimes the longwave instability generates phase-slips, resulting either in stable phase-winding states with a different wave number or localized states that take the form of defects connecting phase-winding states with equal and opposite phase lag. We refer to states of this type as faceted, and show that bound states of such defects can be stable over a wide range of parameter values. Finally, in Section 11.7, we examine the transition between the coarsening and faceting regimes. Direct numerical simulations of the CSHE complement the theory throughout.

11.3 The spatially homogeneous solutions

Spatially homogeneous solutions, hereafter referred to as “flat”, take the form $u = R_0(t)e^{i\phi_0(t)}$. Thus

$$R_{0t} = (r - k_0^4)R_0 - R_0^3, \tag{11.7}$$

$$\phi_{0t} = 0, \tag{11.8}$$

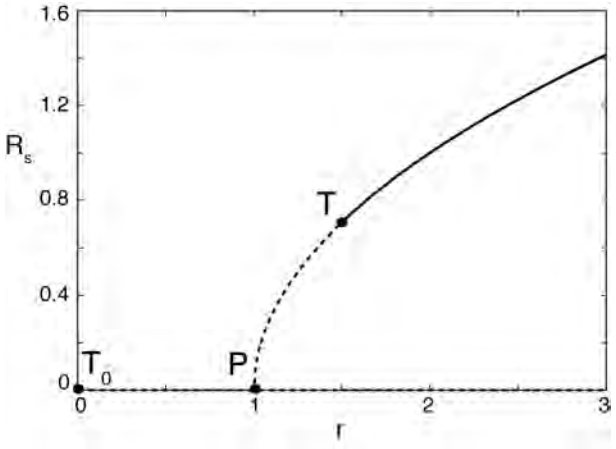

Figure 11.2: Stationary homogeneous solutions R_s for $k_0 = 1$. These states are always unstable to phase modes, although the amplitude mode becomes stable beyond the Turing bifurcation T of the non-zero state (solid line).

with stationary solutions given by

$$R_0^2 = R_s^2 \equiv 0, r - k_0^4, \tag{11.9}$$
$$\phi_0 = \phi_s, \tag{11.10}$$

where ϕ_s is a constant ($R_s \neq 0$). The amplitude R_s of these homogeneous states is shown in Figure 11.2.

11.3.1 Temporal stability

To determine the stability of these states we let $u(x,t) = (R_s + \delta(x,t)) \exp i\phi_s$, where δ is a complex infinitesimal perturbation satisfying

$$\delta_t = r\delta - (\partial_x^2 + k_0^2)^2\delta - R_s^2(2\delta + \bar{\delta}). \tag{11.11}$$

Writing $\delta \equiv \delta_R + i\delta_I$ we obtain

$$\delta_{Rt} = r\delta_R - (\partial_x^2 + k_0^2)^2\delta_R - 3R_s^2\delta_R, \tag{11.12}$$
$$\delta_{It} = r\delta_I - (\partial_x^2 + k_0^2)^2\delta_I - R_s^2\delta_I. \tag{11.13}$$

Thus with $(\delta_R, \delta_I) \propto \exp(ikx + \sigma t)$ we find the pair of growth rates

$$\sigma_R = -2R_s^2 + (2k_0^2 - k^2)k^2, \tag{11.14}$$

$$\sigma_I = (2k_0^2 - k^2)k^2, \tag{11.15}$$

describing the stability of the flat states $R_s \neq 0$ with respect to amplitude and phase perturbations, respectively.

Temporal stability of the trivial state:
The state $u = 0$ is destabilized by periodic modulations with wave number $k = k_0$ at $r = 0$ (point T_0) in a Turing bifucation (also called modulational instability in the optics literature). A band of unstable wave numbers develops around $k = k_0$ for $r > 0$ and spreads to $k = 0$ when r reaches $r = k_0^4$ (point P) corresponding to a reversible pitchfork bifurcation to nonzero flat states.

Temporal stability of the nonzero flat states:
As can be seen from Eqs. (11.14)-(11.15), the nonzero flat states are always unstable to phase perturbations with wave number k in the range $0 < k^2 < 2k_0^2$; translation invariance implies that the phase growth rate of these perturbations vanishes when $k = 0$. Thus the states beyond the Turing point T ($r > 3k_0^4/2$) are amplitude-stable but phase-unstable, and for small wave numbers ($k \ll k_0$) the growth rate of the instability is positive but small. This observation will be important in what follows.
Figure 11.2 summarizes these results. Solid/dashed lines denote solutions that are stable/unstable with respect to the amplitude mode.

11.3.2 Spatial stability

In order to understand the presence of LS homoclinic or heteroclinic to the flat states we also need to know their stability properties in *space*. For this purpose we write $R(x) = (R_s + \delta(x)) \exp i\phi_s$, where $\delta \equiv \delta_R + i\delta_I \propto e^{\lambda x}$. The spatial eigenvalues λ satisfy the equations

$$\lambda^4 + 2\lambda^2 k_0^2 + 2R_s^2 = 0, \tag{11.16}$$

$$\lambda^2(\lambda^2 + 2k_0^2) = 0. \tag{11.17}$$

The former gives the spatial eigenvalues corresponding to amplitude perturbations; these are as in the real Swift-Hohenberg equation. The latter equation gives the spatial eigenvalues corresponding to phase perturbations. Evidently there is always a pair of zero spatial eigenvalues, a consequence of the invariance of the CSHE under phase shifts, together with spatial reversibility. In addition,

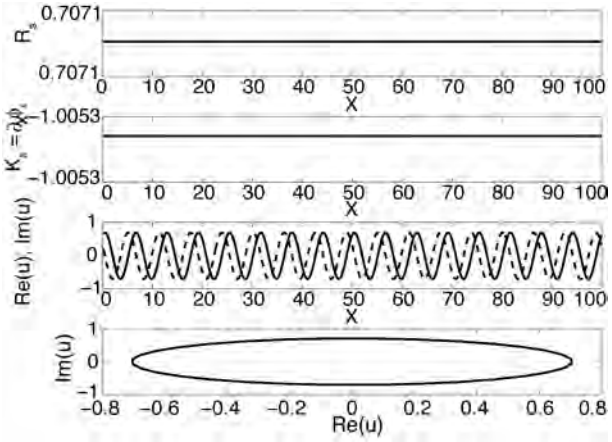

Figure 11.3: RW: A phase-winding state in terms of its amplitude R_s and the modulation wave number $K_s \equiv \partial_x \phi_s$ (top two panels), the real (solid) and imaginary (dashed) parts of the field u (third panel), and the field u in the complex plane (bottom panel). Parameters: $r = 0.5$, $k_0 = 1$, $L = 100$, $N = 512$.

there is a pair of purely imaginary eigenvalues. Neither of these depends on the state or the value of r.

11.4 The phase-winding states

In the numerical simulations we encounter states in which the phase is no longer constant in space: over large parts of the domain the phase may vary *linearly* with the spatial coordinate x. Stable states of this type, referred to as *phase-winding* states, were observed in Ref. [17] and studied in the context of the subcritical CSHE by us in Ref. [1]. These states take the form $u = R_s \exp i\phi_s$, $R_s \neq 0$, where

$$R_s^2 = r - (K_s^2 - k_0^2)^2, \tag{11.18}$$

$$\phi_s = K_s x, \tag{11.19}$$

and K_s is a real constant. In the following we refer to the quantity $K_s \equiv \partial_x \phi_s$ as the wave number of the solution. These states are characterized by the free energy

$$F_{SH,RW} = -\frac{1}{2}[r - (K_s^2 - k_0^2)^2], \tag{11.20}$$

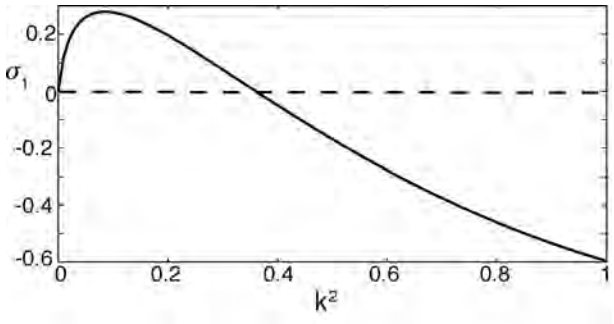

Figure 11.4: Temporal growth rate σ_1 of the phase-winding solution for $k_0 = 1$, $r = 0.7$ and $K_s = 1.3$ as given by Eq. (11.21); σ_2 is not shown since it is always more stable.

as obtained from Eq. (11.2). Thus states with $K_s = k_0$ minimize the free energy at each fixed r.

Figure 11.3 shows an example of a stable phase-winding state when $r = 0.5$ and $k_0 = 1$, obtained using time integration of Eq. (11.1) with periodic boundary conditions at $x = 0, L$ and $N = 512$ mesh points. Observe that this state is not symmetric under spatial reflection; generically states of this type are expected to drift but here these states are necessarily stationary. This is a consequence of the variational nature of Eq. (11.1) when the coefficients are real. In view of the constant phase difference (in space) between the real and imaginary parts of the order parameter u [Figure 11.3(c)] we refer to phase-winding states of this type as *rotating waves* (RW): in the (u_R, u_I) plane the RW correspond to closed orbits around the origin [Figure 11.3(d)]. In contrast, we refer to the spatially periodic states in which u_R and u_I oscillate in phase as *standing waves* (SW). In the complex u plane the SW correspond to oscillations along straight lines through the origin.

The solution shown in Figure 11.3 shows that time evolution of Eq. (11.1) may result in stable states with a wave number that differs from k_0. In view of the imposed periodic boundary conditions the net phase jump $\Delta\phi$ across a domain of length L associated with a solution must be $2\pi n$, where n is an integer. When this phase jump is uniformly distributed it produces a constant phase gradient specified by $K_n \equiv 2\pi n/L$. In the event that $K_n = k_0$ the corresponding phase-winding solution bifurcates at $r = 0$, i.e., simultaneously with the SW branch. However, although these two periodic states have, in this case, the same wave number k_0 they are distinct.

11.4.1 Temporal stability

Writing $R = R_s + \delta_R e^{ikx+\sigma t}$ and $\phi = \phi_s + \delta_\phi e^{ikx+\sigma t}$, where R_s and ϕ_s are given by Eqs. (11.18)-(11.19), one finds that the temporal growth rate σ satisfies the quadratic equation

$$\begin{aligned}&\sigma^2 + \sigma[2k^4 + 11K_s^2k^2 - 3k_0^2k^2 + 2R_s^2] \\ &-k^2[2k_0^2 - k^2 - 6K_s^2][k^4 - 2k^2(k_0^2 - 3K_s^2) + 2R_s^2] \\ &-16k^2K_s^2[k_0^2 - k^2 - K_s^2]^2 = 0. \end{aligned} \tag{11.21}$$

When $K_s = 0$ this equation reduces to Eqs. (11.14)-(11.15). In the following we refer to the two roots of this equation as $\sigma_{1,2}$; Figure 11.4(a) shows the larger root σ_1 as a function of k^2 when $K_s = 1.3$. It becomes clear that the phase-winding states are unstable to longwave perturbations. The solution is stable for large wave number perturbations.

11.4.2 Spatial stability

Writing $R = R_s + \delta_R e^{\lambda x}$ and $\phi = \phi_s + \delta_\phi e^{\lambda x}$, where R_s and ϕ_s are given by Eqs. (11.18)-(11.19), one finds that the spatial eigenvalues λ satisfy

$$\begin{aligned}&\lambda^2[(\lambda^4 + 2(k_0^2 - 3K_s^2)\lambda^2 + 2R_s^2][\lambda^2 + 2k_0^2 - 6K_s^2] \\ &+16\lambda^2K_s^2[\lambda^2 + k_0^2 - K_s^2]^2 = 0. \end{aligned} \tag{11.22}$$

This equation reduces to Eqs. (11.16)-(11.17) when $K_s = 0$. When $K_s \neq 0$ the pair of zero eigenvalues remains but the remaining sixth order characteristic equation no longer factors.

11.5 Coarsening dynamics: the Cahn-Hilliard equation

In this section, we study the evolution of the longwave instability of both the flat and the phase-winding states. The analysis is motivated by the temporal stability results which indicate the presence of a slowly growing long wavelength phase mode [Eqs. (11.15) and (11.21)]. We show that the evolution of this mode is described by a Cahn-Hilliard-type equation for the perturbation wave number. In the region of validity of this equation, there is no locking of oscillatory tails and coarsening of the growing perturbations is predicted. This prediction compares

well with direct numerical simulations of the CSHE described in Section 11.5.4. Extensions of the theory to other regimes do predict locking of adjacent structures and hence evolution to a frozen asymptotic state (Section 11.6).

11.5.1 Derivation of the Cahn-Hilliard equation

We consider the evolution of long wavelength phase modulation of the flat state $R_0^2 = R_s^2 \equiv r - k_0^4$, $\phi_0 = \phi_s$, where ϕ_s is a constant. We first rewrite Eqs. (11.4)-(11.5) as coupled equations for the amplitude $R(x,t)$ and modulation wave number $K(x,t) \equiv \partial_x \phi(x,t)$:

$$\begin{aligned} R_t &= rR - R^3 - 2k_0^2 R_{xx} - (k_0^2 - K^2)^2 R + 6K^2 R_{xx} \\ &\quad +12KK_x R_x + 3K_x^2 R + 4KK_{xx} R - R_{xxxx} \qquad (11.23) \\ K_t &= -2\Big(2k_0^2 \frac{R_x}{R} K + 2\frac{R_{xxx}}{R} K + 3\frac{R_{xx}}{R} K_x + 2\frac{R_x}{R} K_{xx} \\ &\quad -2\frac{R_x}{R} K^3\Big)_x - 2k_0^2 K_{xx} - K_{xxxx} + 2(K^3)_{xx}. \qquad (11.24) \end{aligned}$$

Writing $R = R_s(1+u)$ and $K = v$, where $u = O(\epsilon^2)$, $v = O(\epsilon)$ and $\epsilon \ll 1$ is a small parameter measuring the wave number of the perturbation, one obtains the following equation for u:

$$\begin{aligned} u_t &= -2R_s^2 u - 3R_s^2 u^2 + 2k_0^2 v^2 + 2k_0^2 uv^2 \\ &\quad +3v_x^2 + 4vv_{xx} - v^4 - 2k_0^2 u_{xx} + \text{higher order terms} \qquad (11.25) \end{aligned}$$

We now write $u = \alpha v^2 + w$, where $\alpha = O(1)$ and w is of order $O(\epsilon^4)$, and take $\partial_t \equiv O(\epsilon^4)$, obtaining $\alpha = k_0^2/R_s^2$ and

$$w = \frac{1}{2R_s^4}[-(R_s^2 + k_0^4)v^4 + (3R_s^2 - 4k_0^4)v_x^2 + 4(R_s^2 - k_0^4)vv_{xx}]. \qquad (11.26)$$

Equation (11.24) now yields the result

$$v_t = -[2k_0^2 v + v_{xx} + \kappa_0 v^3]_{xx}, \qquad (11.27)$$

where $\kappa_0 \equiv (8k_0^4/3R_s^2) - 2$, correct to $O(\epsilon^5)$. This is the Cahn-Hilliard equation [14]. In the CSHE context this equation first appears in the work of Malomed *et al.* [18].

The Cahn-Hilliard equation was originally derived to describe the dynamics of phase separation in systems with a conserved quantity in the context of binary alloys [14]. However, the model equation arises in many other areas of

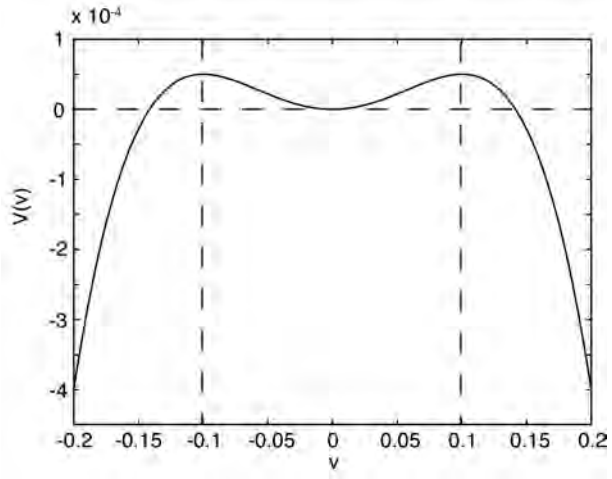

Figure 11.5: Potential $V(v)$ as a function of v for $k_0 = 0.1$ and $\kappa_0 = -2$.

physics as well [19], including spinodal decomposition in thin films [20], pattern formation on surfaces, dislocations of microstructures, crack propagation and electromigration, where it is used to describe progressive coarsening [19]. The equation also describes wavelength selection in fixed flux thermal convection [21]. In the present context the form of the equation is a consequence of phase conservation across the domain, together with the symmetry of Eqs. (11.23)-(11.24) with respect the spatial reflection: $x \to -x$, $R \to R$, $K \to -K$.
Equation (11.27) describes the evolution of the longwave instability triggered by the negative diffusion coefficient $\gamma = -2k_0^2$. The equation applies for solutions with zero mean, so that $\Delta\phi = 0$ across the domain, as required of any perturbation of a constant phase state.

11.5.2 Stationary solutions of the Cahn-Hilliard equation

The Cahn-Hilliard equation, Eq. (11.27), has the Lyapunov functional

$$F_{CH}[v] = \int dx[\frac{1}{2}v_x^2 - V(v)], \tag{11.28}$$

where (see Figure 11.5)

$$V(v) \equiv k_0^2 v^2 + \frac{1}{4}\kappa_0 v^4, \tag{11.29}$$

defined such that

$$v_t = \partial_{xx}[\delta F_{CH}(v)/\delta v(x)]. \tag{11.30}$$

Thus

$$\frac{dF_{CH}}{dt} = -\int_0^L [v_{xx} + V'(v)]^2\, dx \tag{11.31}$$

and $F_{CH}[v]$ decreases until it reaches a stationary state of Eq. (11.27). These stationary states satisfy

$$v_{xx} + 2k_0^2 v + \kappa_0 v^3 + \lambda_1 + \lambda_2 x = 0, \tag{11.32}$$

where λ_1, λ_2 are integration constants. Symmetry with respect to reflection in v requires that $\lambda_1 = 0$, while the requirement that $v = 0$ is a solution implies that $\lambda_2 = 0$. Thus

$$\frac{1}{2}v_x^2 + V(v) = E; \tag{11.33}$$

we refer to the integration constant E as the energy.
Since V has two identical maxima ($\kappa_0 \approx -2$), there is a pair of symmetry-related spatially homogeneous steady states given by

$$v_s \approx \pm k_0 \tag{11.34}$$

with energy $E_s = -k_0^4/\kappa_0 > 0$. When $0 < E < E_s$, there is a family of spatially periodic nonlinear solutions of zero mean whose period and amplitude depend on E. These solutions are, however, known to be unstable [22, 23]. As $E \to E_s$ from below these solutions degenerate into a pair of heteroclinic states connecting a pair of symmetry-related equilibria. These states are called kinks if the phase increases across the associated defect, and antikinks if it decreases. A kink-antikink pair is the long time zero-area attractor of the equation [22–24]. Thus a system consisting of several kink-antikink pairs or "bubbles" is unstable and in time exhibits coarsening dynamics, in which smaller bubbles repeatedly merge together forming larger and larger structures. This process is driven by the mutual interaction between the kink and antikink pairs and is present whenever the spatial eigenvalues of $v_s \approx \pm k_0$ are real, i.e., provided there is no pinning. At large times the width of the broadest bubble increases exponentially slowly as a result of the exponentially small interaction between kinks and antikinks when these are widely separated [25, 26].

11.5.3 Derivation of the Cahn-Hilliard equation for phase-winding states

In this section we consider the growth of unstable perturbations of phase-winding states given by $R = R_s$, $K = K_s$, where $R_s^2 = r - (k_0^2 - K_s^2)^2$ and $K_s \neq 0$ is a

constant. As before we write $R = R_s(1+u)$, $K = K_s(1+v)$ but this time take both u and v to be $O(\epsilon)$. At the same time we suppose that spatial derivatives are $O(\epsilon)$ and time derivatives of at least $O(\epsilon^3)$. Substitution into Eqs. (11.23) and (11.24) yields coupled equations for u and v. As before we can solve for u in terms of v:

$$u = \beta_1 v + \beta_2 v^2 + \beta_3 v^3 + \beta_4 v_{xx} + O(\epsilon^4), \tag{11.35}$$

where

$$\beta_1 = \frac{2K_s^2(k_0^2 - K_s^2)}{R_s^2} \tag{11.36}$$

$$\beta_2 = \frac{K_s^2(k_0^2 - 3K_s^2)}{R_s^2} - \frac{5}{2}\beta_1^2 \tag{11.37}$$

$$\beta_3 = -\beta_1(\beta_1^2 + 3\beta_2) \tag{11.38}$$

$$+\frac{K_s^2}{R_s^2}[(k_0^2 - K_s^2)(\beta_1 + 2\beta_2) - 2(\beta_1 + 1)K_s^2] \tag{11.39}$$

$$\beta_4 = \frac{-(k_0^2 - 3K_s^2)\beta_1 + 2K_s^2}{R_s^2}. \tag{11.40}$$

It follows that v satisfies the equation [27]

$$v_t = [\gamma v - \delta v_{xx} - \frac{1}{2}\kappa_1 v^2 - \frac{1}{3}\kappa_2 v^3]_{xx}, \tag{11.41}$$

where the coefficients are given by

$$\gamma = -2k_0^2(1 + 2\beta_1) + 2K_s^2(3 + 2\beta_1) \tag{11.42}$$

$$\delta = 1 + 4\beta_1 + 4(k_0^2 - K_s^2)\beta_4 \tag{11.43}$$

$$\kappa_1 = 4[k_0^2(\beta_1 - \beta_1^2 + 2\beta_2) - K_s^2(3 + 3\beta_1 - \beta_1^2 + 2\beta_2)] \tag{11.44}$$

$$\kappa_2 = -4k_0^2(2\beta_1^2 - \beta_1^3 - 2\beta_2 + 3\beta_1\beta_2 - 6\beta_3) \tag{11.45}$$

$$-2K_s^2(3 + 6\beta_1 - 6\beta_1^2 + 2\beta_1^3 + 12\beta_2 - 6\beta_1\beta_2 + 6\beta_3).$$

Note that since Eq. (11.1) is variational, the phase dynamics is also variational. Equation (11.41) resembles the Cahn-Hilliard equation (11.27) except for the presence of an asymmetrical potential V. When $\gamma = O(\epsilon^2)$, $\epsilon \ll 1$, the dynamics is described by

$$v_t = (\gamma v - \delta v_{xx} - \frac{1}{2}\kappa_1 v^2)_{xx}, \tag{11.46}$$

provided $v = O(\epsilon^2)$. Such an equation is thus valid for small wave number changes near the stability boundary $\gamma = 0$ (Figure 11.6). A similar equation

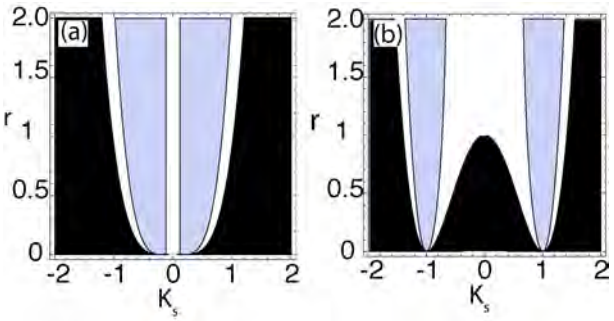

Figure 11.6: The condition $R_s > 0$ with the Eckhaus-stable region ($\gamma > 0$) in gray and the Eckhaus-unstable region ($\gamma < 0$) in white in the (K_s, r) plane. No solutions R_s are present in the black region. (a) $k_0 = 0.2$. (b) $k_0 = 1$.

arises in the classical theory of the Eckhaus instability based on the complex Ginzburg-Landau equation with real coefficients [28, 29], where $\gamma < 0$ in the Eckhaus-unstable regime (white regions in Figure 11.6 near $K_s = \pm k_0$) and the nonlinear term drives v, and hence u, to such large amplitudes that R reaches zero and a defect forms. In this case phase is no longer conserved: the conservation law $\int_0^L v\, dx = 0$ implied by Eqs. (11.24) and (11.46) requires that $R > 0$ throughout the evolution of R and K. Equations of the form (11.46) arise in other systems with variational dynamics, including the rupture of thin liquid films [30] and compressible fixed heat flux convection [31], and require that both γ and v are taken so small that the stabilizing fourth derivative term is competitive. In all these applications the resulting dynamics leads to the formation of a singularity.

In this present case we find that if the effective value of ϵ, as defined by the magnitude of γ, is not too small, the quartic term in the potential does enter into the dynamics and may, under appropriate conditions, prevent the formation of defects. In these circumstances the Cahn-Hilliard equation (11.41) describes the behavior of the CSHE for all time, and one again observes coarsening. In the CSHE this is the case for small wave numbers K_s, i.e., near band center. In contrast, the Ginzburg-Landau approximation applies near $K_s = \pm k_0$, and here the band center is Eckhaus-stable (Figure 11.6 and [15]). However, away from the band center in the CSHE, i.e., for K_s sufficiently far from zero, one does observe defect formation instead of coarsening, much as in the Eckhaus-unstable regime in the Ginzburg-Landau equation. We discuss this behavior next.

11.5.4 Numerical verification of coarsening dynamics

In this section we confirm that the CSHE equation does indeed follow the coarsening dynamics predicted from the Cahn-Hilliard equations with $K_s = 0$ and $K_s \neq 0$ provided that K_s is appropriately small.
In Figs. 11.7 and 11.9 we show the results of simulations starting from a phase-winding state with a net phase jump $\Delta\phi = 2\pi n$ across the domain, where n is an integer. Such a state has wave number $K_s = K_n \equiv 2\pi n/L$. In the region of validity of Eq. (11.41) this phase jump should be conserved by the evolution, i.e. the area $A \equiv \int_0^L K(x,t)\,dx = 2\pi n$ throughout the evolution. When $\gamma < 0$ (white regions in Figure 11.6) the phase-winding state is modulationally unstable. Figure 11.7 shows the spatiotemporal evolution of the real and imaginary parts of the complex field u and of the wave number K when $k_0 = 0.2$ (Figure 11.6(a)) and $r = 2$, $K_s = 2\pi/100 = 0.063$ ($n = 1$). The simulations confirm the conservation of the area A and demonstrate that the phase-winding state develops a modulational instability after which the system coarsens in time until only one bubble remains. From area conservation the width d_- of the $K < 0$ part of the bubble is given by

$$d_- = \frac{LK_+}{K_+ - K_-} - \frac{2\pi n}{K_+ - K_-}, \tag{11.47}$$

where n is an integer determined by the initial condition (here $n = 1$) and $K_\pm$ are the wave numbers connected by the pair of heteroclinic connections that form as $t \to \infty$. We find that $K_\pm = K_s(1 + v_\pm)$, where $v_\pm$ correspond to the two maxima of the potential $V_2(v) \equiv \lambda_1 v - \frac{1}{2}\gamma v^2 + \frac{1}{6}\kappa_1 v^3 + \frac{1}{12}\kappa_2 v^4$ associated with Eq. (11.41). Of course, such a connection is only possible when the two maxima are identical, a requirement that selects the quantity λ_1. With this choice of λ_1 the potential V_2 remains asymmetrical but resembles Figure 11.5. The numerical simulations indicate, in addition, that the resulting values of $v_\pm$ are such that $K_\pm \approx \pm k_0$, i.e., the evolution of the system replaces the phase-winding state with wave number K_s with the preferred wave number k_0. Thus the asymmetrical potential is a consequence of the fact that $K_s \neq k_0$.

To understand the numerical results in more detail we rewrite Eq. (11.41) in terms of the wave number $K = K_s(1 + v)$ obtaining

$$K_t = [(\gamma + \kappa_1 - \kappa_2)K - \delta K_{xx} + \frac{\rho}{K_s}K^2 - \frac{\kappa_2}{3K_s^2}K^3]_{xx}. \tag{11.48}$$

Figure 11.8(a) shows the quantity $\rho \equiv \kappa_2 - \frac{1}{2}\kappa_1$ that measures the importance of the quadratic term in Eq. (11.48) as a function of k_0. Thus for small to moderate values of k_0 the quadratic term is indeed small, and coarsening is expected. Figure 11.8(b) shows, moreover, that in this regime the selected wave numbers

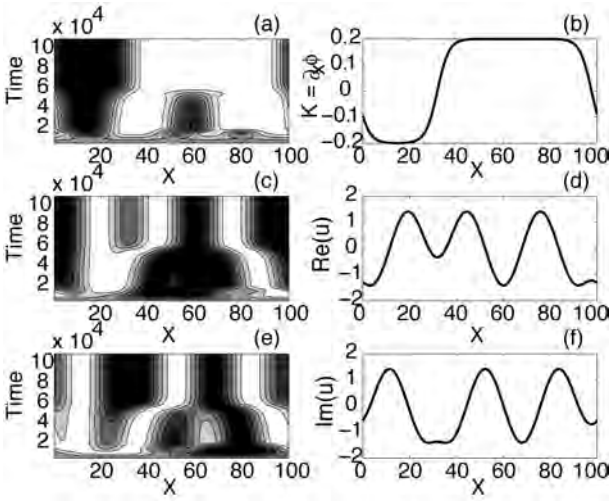

Figure 11.7: Time evolution of the CSHE with $k_0 = 0.2$ and $r = 2$ starting from an unstable phase-winding state with initial wave number $K_n = 2\pi n/L$, where $L = 100$ and $n = 1$. For these parameter values coarsening behavior is observed in panels (a)-(f). The spatio-temporal evolution of $K = \partial_x \phi$ is shown in panel (a), with the corresponding profiles at $t = 10^4$ in (b). The evolution of the real part and imaginary part of the field is plotted in panels (c) and (e), with the corresponding profiles at $t = 10^4$ in (d) and (f).

satisfy

$$K_{\pm} = \pm K_s \sqrt{3(\gamma + \kappa_1 - \kappa_2)/\kappa_2} \approx \pm k_0. \tag{11.49}$$

For larger values of K_s, or equivalently of γ, the quadratic term in the potential is no longer negligible, and the evolution begins to resemble behavior familiar from earlier studies of the nonlinear evolution of the Eckhaus instability [28, 29]. In this regime defects form and phase is no longer conserved. A typical example of this type of evolution is shown in Figure 11.9. We again take $k_0 = 0.2$ and $r = 2$, but now consider a phase-winding state with $K_n = 2\pi(18/100) \approx 1.131$ ($n = 18$). As shown in Figure 11.6(a) for these parameters $\gamma < 0$ indicating that this phase-winding state is also modulationally unstable. However, coarsening does not take place and one observes instead successive formation of defects. The associated change in phase is tracked in Figure 11.9(c); the final state that results is a phase-winding state with a stable wave number K_n, $n = 5$. Thus the modulational instability acts to shift the wave number of the state from an unstable wave number to one that is stable (shaded region in Figure 11.6(a)).

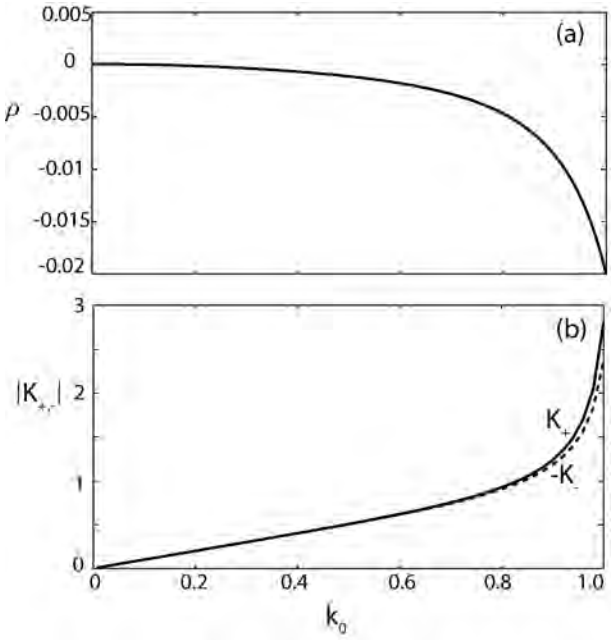

Figure 11.8: (a) The quantity $\rho \equiv \kappa_2 - \frac{1}{2}\kappa_1$ and (b) the location $K_\pm$ of the maxima of the resulting potential V_2 when these are equal, both as functions of k_0. Parameters: $r = 2$ and $K_s = 0.1$.

11.5.5 Transition from coarsening to Eckhaus dynamics

In an attempt to locate the transition from coarsening behavior to evolution via phase slips we have performed a series of numerical computations spanning the unstable regions ($\gamma < 0$) in Figure 11.6. We describe here the results for $k_0 = 0.2$, $r = 2$ on a domain of length $L = 300$ with $N = 1024$ mesh points. In each case we initialize the calculation with an unstable phase-winding state, specified by n, and allow numerical error to trigger the instability. As a result we do not control the initial condition and so find the most "likely" outcome of the instability. We emphasize that multiple outcomes are in general possible, depending on initial conditions, and that even small changes in the resolution (for example) lead to different results. This is because the Eckhaus instability in effect amplifies small amplitude noise which develops into a distribution of phase slips that depends on the noise details. Thus in the Eckhaus-unstable regime the outcome of the instability requires a probabilistic description.

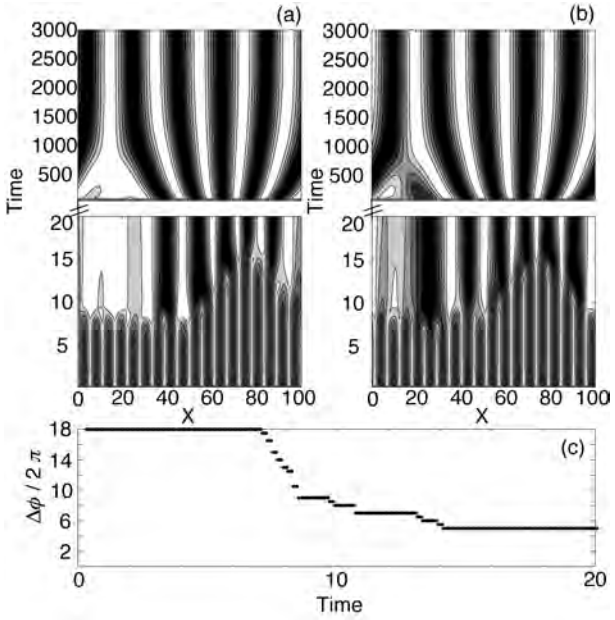

Figure 11.9: Time evolution of the CSHE with $k_0 = 0.2$ and $r = 2$ starting from an unstable phase-winding state with initial wave number $K_n = 2\pi n/L$, where $L = 100$ and $n = 18$. Panels show the spatio-temporal evolution of (a) Re(u) and (b) Im(u), while (c) shows the evolution of the total phase jump over the domain.

$n = K_s L/2\pi$	1	2	3	4	5						
behavior	C	C	C	C	C						
n_{final}	1	2	3	4	5						
$n = K_s L/2\pi$	47	48	49	50	51	52	53	54	55	56	57
behavior	E	E	E	E	E	E	E	E	EC	EC	EC
n_{final}	44	31	26	24	17	16	15	7	5	0	-2

Table 11.1: Outcome of the modulational instability of phase-winding states when $k_0 = 0.2$, $r = 2$, $L = 300$, $N = 1024$. The top row specifies the wave number of the unstable initial state while n_{final} specifies the phase jump across the domain in the final state. The letters C (coarsening) and E (Eckhaus) indicate the evolution type; EC indicates evolution via phase slips followed by coarsening.

The results are summarized in Table I. The top row specifies the wave number K_n of the unstable initial state while the third row lists $n_{final} \equiv \Delta\phi_{final}/2\pi$ that measures the total phase jump across the domain in the final state of the simulation. The letter C indicates evolution via coarsening. Since this process is phase-conserving, $n_{final} = n_{initial}$. This type of behavior dominates throughout the unstable band near $K_s = 0$. In the remaining unstable regions in Figure 11.6 the evolution is via phase slips and we label this type of evolution with the letter E. The final states reached consist of new phase-winding states with a wave number in the Eckhaus-stable regime. The table reveals that near the inner boundary of these regions the Eckhaus instability generates only a small number of defects, $n_{initial} - n_{final}$. However, this number increases approximately linearly with $n_{initial}$, until the total phase jump across the domain is almost zero. The corresponding wave numbers, as measured by n_{final} are once again in the unstable regime near $K_s = 0$ and one therefore anticipates a second phase of the evolution resembling coarsening. We indicate this type of behavior using the symbol EC.
Figure 11.10 shows an example typical of the EC regime. Numerous phase slips take place that reduce the effective n from its initial value $n_{initial} = 55$ to $n_{final} = 5$. At this point the solution is still far from a phase-winding state with a linear phase gradient but from this point on no additional phase slips take place and evolution via coarsening takes over, as expected from a Cahn-Hilliard equation initialized with a large number of "bubbles". The final state of the system is therefore a single stable bubble whose area is determined by the net phase jump across the domain at the end of the Eckhaus phase.

11.6 Faceting of phase-winding states

11.6.1 Origin of frozen facets

In this section we describe the corresponding results for the case $k_0 = 1$ (Figure 11.6(b)). Figures 11.11 and 11.12 show the time evolution of the CSHE for $r = 2$ starting with unstable phase-winding states with wave numbers $K_n \equiv 2\pi n/L$ with $L = 100$ and $n = 2, 22$, respectively. As anticipated the solutions evolve by generating defects, thereby changing their wave number into a stable one. However, the manner with which this is accomplished depends on both parameters and initial conditions. In Figure 11.11, corresponding to $n = 2$, the system evolves into a state with wave numbers $K = \pm k_0$ connected by (a pair of) heteroclinic connections or *fronts*. Owing to the complex spatial eigenvalues λ of these states the fronts lock to each other via their overlapping oscillatory tails [15, 32] forming a bound state of two fronts, i.e., bound states of a kink

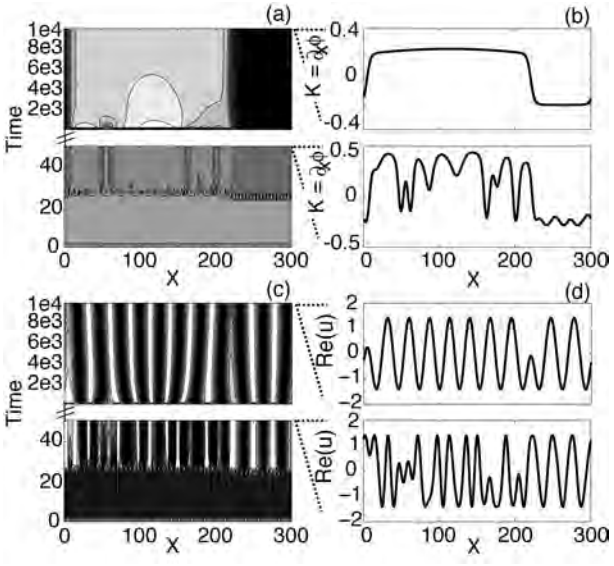

Figure 11.10: Time evolution of the CSHE with $k_0 = 0.2$ and $r = 2$ starting from an unstable phase-winding state with initial wave number $K_n = 2\pi n/L$, where $L = 300$ and $n = 55$. Panels show the spatio-temporal evolution of (a) $K = \partial_x\phi$ and (c) Re(u), with the corresponding profiles at $t = 50$ and $t = 10^4$ shown in (b) and (d).

and an antikink, and this structure is reflected in the amplitude R as well. The formation of such a bound state suppresses further evolution of the system and no coarsening is observed, even when multiple bound states are present. In contrast, Figure 11.12, corresponding to $n = 22$, reveals behavior that conforms to standard Eckhaus evolution, resulting in the formation of a stable phase-winding state with $n = 19$. Here the phase gradient remains homogeneous in space and no facets form.

11.6.2 Bifurcation structure of the frozen facets

In this section, we examine the properties of faceted states of the type shown in Figure 11.11. These states are the typical final states obtained in numerical simulations starting either from an unstable RW as initial condition or starting with random noise. These structures are spatially localized in *both* amplitude *and* phase, and can be symmetric or asymmetric under reflection in x. States of this type exhibit pronounced localization in amplitude together with almost

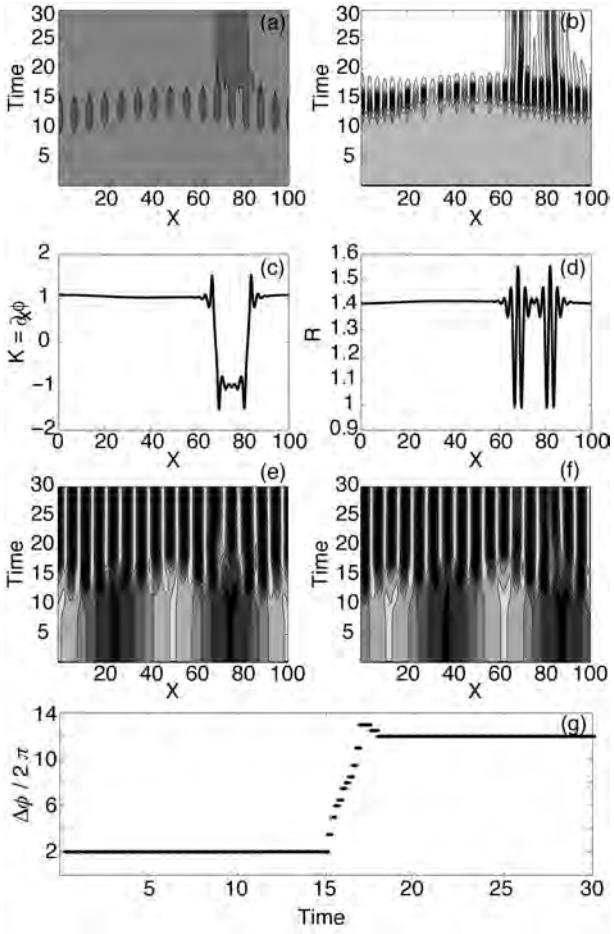

Figure 11.11: Time evolution of the CSHE with $k_0 = 1$ and $r = 2$ starting from an unstable phase-winding state with initial wave number $K_n = 2\pi n/L$, where $L = 100$ and $n = 2$. Panels show the spatio-temporal evolution of (a) K and (b) R, while panels (c)-(d) show the solution profiles at the last time step of (a)-(b). Panels (e)-(f) show the evolution of Re(u) and Im(u), respectively, while (g) shows the evolution of the total phase jump over the domain.

linear phase variation, typically with slopes $\pm k_0$ on either side of the resulting localized structure (LS). The resulting phase variation thus resembles a faceted surface, with the relatively abrupt changes in the phase gradient associated with

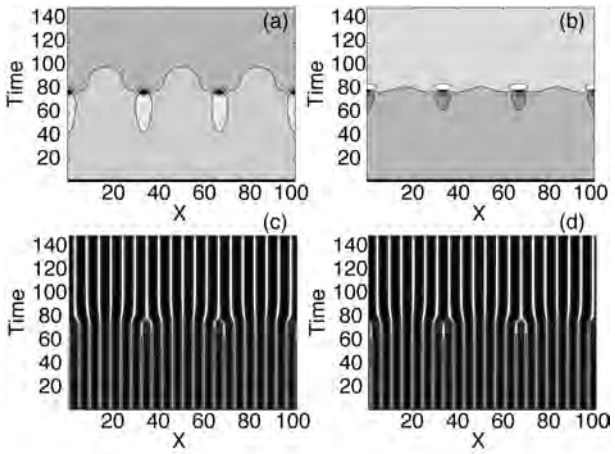

Figure 11.12: Time evolution of the CSHE with $k_0 = 1$ and $r = 2$ starting from an unstable phase-winding state with initial wave number $K_n = 2\pi n/L$, where $L = 100$ and $n = 22$. Panels show the spatio-temporal evolution of (a) K and (b) R, (c) Re(u) and (d) Im(u). The final state has a uniform amplitude and wave number corresponding to $n = 19$.

the amplitude defect. In general, the widths of the amplitude and wave number defects are comparable. In the presence of periodic boundary conditions LS of this type necessarily come in pairs. In view of the variational structure of Eq. (11.1) asymmetric LS remain stationary and hence can easily be continued in parameter space using standard continuation techniques.

Figure 11.13 shows the bifurcation structure of the different types of LS using the L_2 norm (hereafter, the energy) as a function of the control parameter r when $k_0 = 1$. Stable (unstable) solutions are shown in solid (dashed) lines. The branch of in-phase oscillations with wave number k_0, labeled as SW (Standing Waves), bifurcates from $u = 0$ at $r = 0$. An example of an SW [profile (2)] can be seen in Figure 11.14. As r increases beyond $r = 0$, the SW branch bifurcates at point A resulting in a branch of Modulated Rotating Waves (MW), consisting of an equidistant pair of identical defects of opposite chirality. Once again, the phase outside of these defects varies almost linearly, with alternating gradients $\pm k_0$ and no overall phase jump $\Delta\phi = 0$. In this type of solution the amplitude defects are symmetric under reflection since each defect lies exactly midway between its neighbors on either side. Near A the phase gradient is markedly nonuniform in space [see Figure 11.15, profile (3)]. However, with increasing r the nonuniformity in both amplitude and the phase gradient gradually decreases, and the solution resembles more and more a front connecting equal and opposite

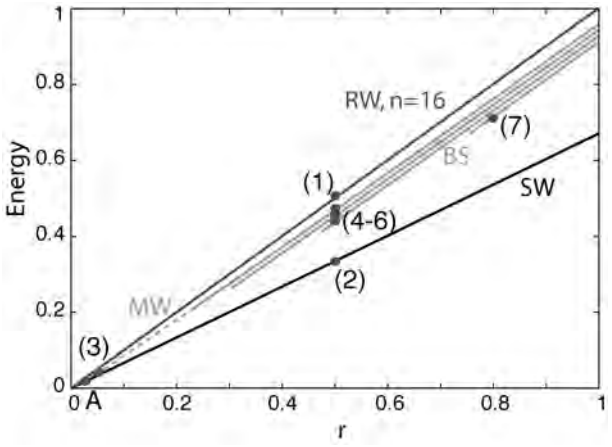

Figure 11.13: Bifurcation diagram showing the classical periodic states (SW, black), together with the new phase-winding (RW, black) and faceted states (MW/BS, gray). The integers indicate locations used for solution profiles in subsequent figures. Solid (dashed) lines depict stable (unstable) solutions. As the stable branches of BS and MW have very similar energies as the MW the former have been displaced slightly downward. Parameters: $k_0 = 1$, $L = 100$, $N = 512$.

wave numbers $\pm k_0$ [see Figure 11.15, profile (4)]. In space these bifurcations correspond to the spatial analogue of the direction-reversing Hopf bifurcation from a group orbit of periodic states discussed in [33].

For comparison, Figure 11.13 also shows a branch of phase-winding states (RW) from Eqs. (11.18)-(11.19), with phase gradient $K_n \equiv 2\pi n/L$ with $n = 16$. In general, numerical simulation produces several LS that are localized in both amplitude and phase (MW, BS in Figure 11.13) but in some cases one obtains a constant amplitude phase-winding state. Figure 11.3 [profile (1)] shows one such state obtained by numerical simulation. The phase gradient on this branch is constant and hence equal to $K_n = 2\pi n/L$ (here $n = 16$).

Figure 11.13 reveals, in addition, the presence of additional but disconnected solution branches (only the stable part of these branches is shown). The solutions on these branches also consist of states with a pair of defects but the defects are no longer equally spaced [Figure 11.16, profiles (5)-(7)]. We refer to solutions of this type as bound states (BS). The BS form via locking between the oscillatory tails of individual LS forming, at each r, a discrete family of BS with different separations. Each of these states lies on a distinct solution branch with like

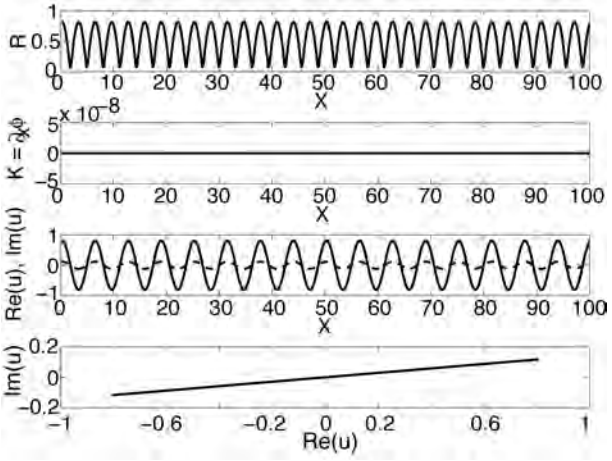

Figure 11.14: SW: Solution profile at location (2) in Figure 11.13. Top two panels: amplitude R and modulation wave number $K \equiv \partial_x \phi$. Third panel: real (solid) and imaginary (dashed) parts of the field u. Bottom panel: the field u in the complex plane. Parameters: $r = 0.5$, $k_0 = 1$, $L = 100$ and $N = 512$.

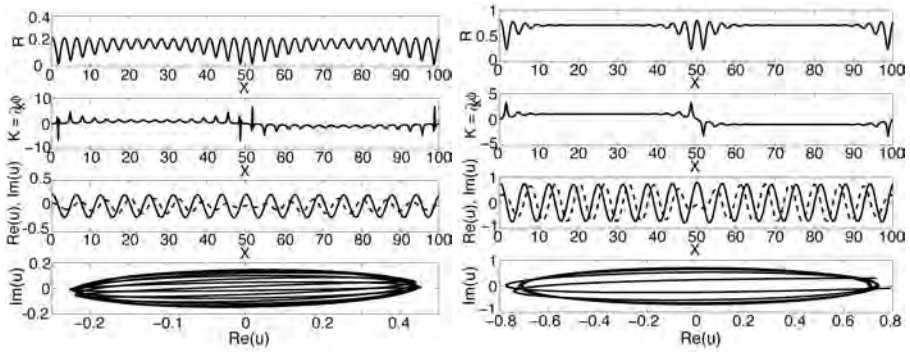

Figure 11.15: MW: Solution profiles at locations (3)-(4) in Figure 11.13, $r = 0.04, 0.5$, respectively. Top two panels: amplitude R and modulation wave number $K \equiv \partial_x \phi$. Third panel: real (solid) and imaginary (dashed) parts of the field u. Bottom panel: the field u in the complex plane. Parameters: $k_0 = 1$, $L = 100$ and $N = 512$.

behavior [15]. Similar bifurcation structure is also present in the subcritical case [1].

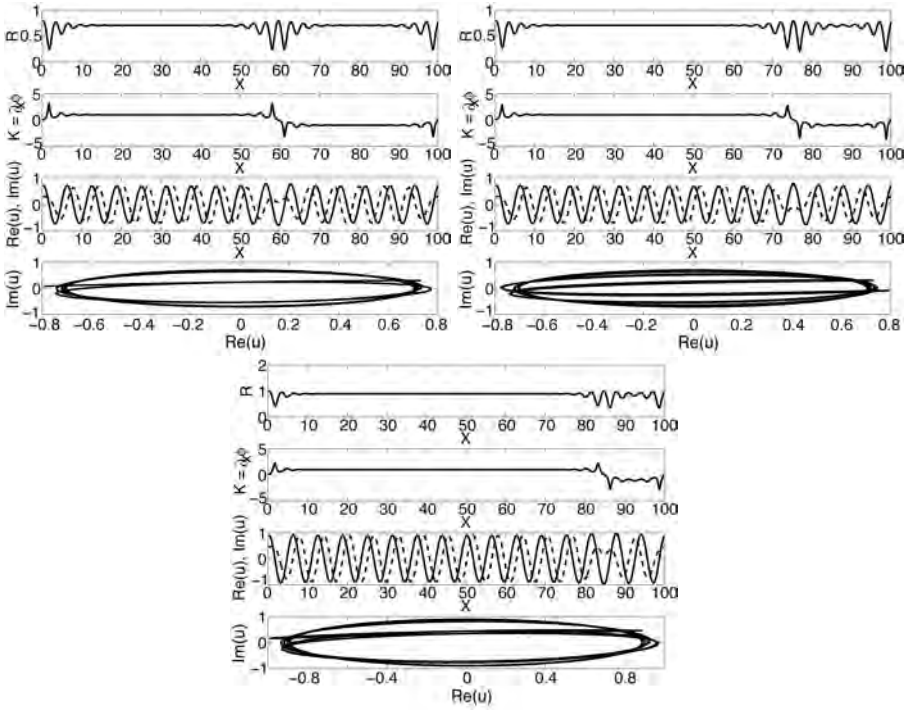

Figure 11.16: BS: Solution profiles at locations (5)-(7) in Figure 11.13, $r = 0.5, 0.5, 0.8$, respectively. Top two panels: amplitude R and modulation wave number $K \equiv \partial_x \phi$. Third panel: real (solid) and imaginary (dashed) parts of the field u. Bottom panel: the field u in the complex plane. Parameters: $k_0 = 1$, $L = 100$ and $N = 512$.

11.7 Transitions between coarsening, frozen faceted structures and Eckhaus dynamics

11.7.1 Transition from coarsening to frozen faceted structures

As discussed in the previous two sections, the behavior of faceted structures in the CSHE depends on the characteristic length scale $2\pi/k_0$. When k_0 is small the facets coarsen indefinitely as described by a Cahn-Hilliard equation, while for larger values of k_0 the coarsening ceases leading to a frozen faceted structure. In this case the fronts connecting equal and opposite phase gradients k_0 form bound states permitting the coexistence of multiple stable bubbles. In this section we

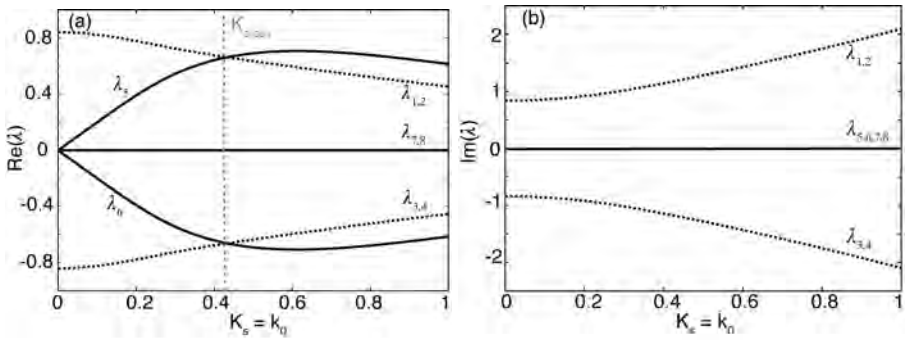

Figure 11.17: The (a) real and (b) imaginary parts of the spatial eigenvalues of the phase-winding state as a function of the phase gradient K_s, $0 \leq K_s \leq 1$, and K_s set equal to k_0 as observed in all numerical simulations resulting in localized states. Thus the plot also represents the variation of the real and imaginary parts of the relevant spatial eigenvalues as a function of the basic wave number k_0 with $r = 1$.

examine the transition between these two regimes.

In order to predict the value of k_0 at which the transition from coarsening to faceting behavior takes place we examine the spatial eigenvalues of the phase-winding state with $K_s = k_0$ as described by Eq. (11.22). Since the decay of spatial perturbations around this state is controlled by the slowest eigenvalue, i.e., the eigenvalue with the smallest nonzero real part, coarsening will take place whenever this eigenvalue is purely real and oscillatory tails are absent. On the other hand, whenever this particular eigenvalue has a nonzero imaginary part oscillatory tails will be present allowing adjacent kink and antikinks to lock to one another [32]. In this case one expects to observe faceting. It follows, therefore, that the transition between coarsening and faceting dynamics is given by the point in parameter space where the eigenvalue with the smallest real part acquires a non-zero imaginary part.

In Figure 11.17 we show the real and imaginary parts of the spatial eigenvalues of a phase-winding state with wave number K_s in the special case in which $K_s = k_0$. This choice is motivated by our numerical simulations which show that the phase gradients involved in the formation of a localized structure are always $\pm k_0$. For the parameters $r = 1$ and $K_s = k_0 \in [0, 1]$ the eight eigenvalues [as obtained from Eq. (11.22)] are organized as follows: there is a quartet of complex eigenvalues ($\lambda_{1,2,3,4} = \pm\lambda_r \pm \lambda_i$), two purely real eigenvalues ($\lambda_5 = -\lambda_6$) and a double zero eigenvalue ($\lambda_{7,8} = 0$). As already mentioned zero eigenvalues are a consequence of the invariance of the CSHE under phase shifts, together with spatial reversibility. From Figure 11.17 it is clear that there is a cross-over

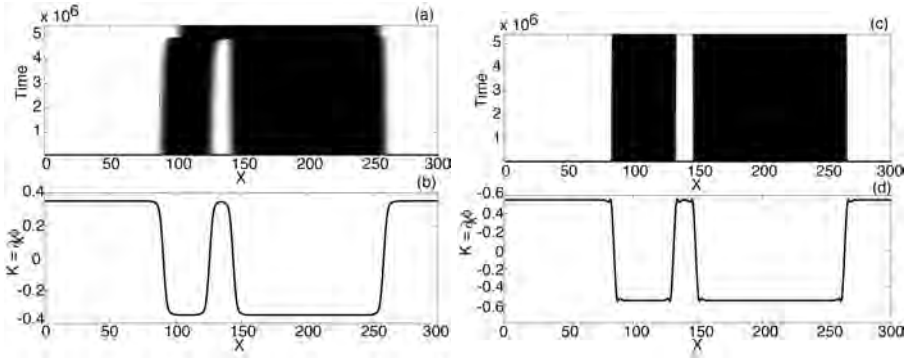

Figure 11.18: Spatio-temporal simulation of the CSHE from an initial condition consisting of two bubbles of different widths. Parameters: $r = 1$, $L = 300$, $N = 1024$ and $k_0 = 0.35, 0.55$ in panels (a)/(b) and (c)/(d), respectively. Panels (a) and (c) show the space-time contour plot of $K \equiv \partial_x \phi$. High/low K is color-coded by white/black. Panels (b) and (d) show profiles taken from panels (a) and (c) close to onset.

between the magnitude of the real parts of the complex quartet and the purely real eigenvalues. This cross-over occurs at $K_{cross} \approx 0.43$ and splits the graph in two regions: a coarsening region for $K_s = k_0 < K_{cross}$ and a faceting region where the LS can pin to the oscillatory tails of the fronts ($K_s = k_0 > K_{cross}$). This prediction of the structure of the spatial eigenvalues is verified in Figure 11.18, where we show two temporal simulations of the CSHE, one for $K_s = k_0 = 0.35 < K_{cross}$ [Figure 11.18(a)] and one for $K_s = k_0 = 0.55 > K_{cross}$ [Figure 11.18(c)]. In both cases we use the same initial condition consisting of two bubbles, one of which is much smaller in width than the other, and identical values of r and L. The results reveal an unambiguous qualitative change in the dynamical behavior of the system, from coarsening to faceting. Moreover, the front profiles of the bubbles [Figure 11.18(b)-(d)], confirm the absence/presence of oscillatory tails when coarsening/faceting takes place.

11.7.2 Transition from frozen faceted states to Eckhaus dynamics

In Figure 11.18 the evolution was started from an initial state with two bubbles to examine the transition form continued coarsening to locking. However, when $k_0 = 1.0, r = 2$ and the simulations are initialized with an unstable phase-winding state the evolution always leads to phase slips. Depending on the wave number

$n = K_s L/2\pi$	1	2	3	4	5	6	7	8	9	10	
behavior	EF	EF	EF	EF	EF	EF	E	EF	EF	E	
n_{final}	24	8	0	11	14	9	50	16	44	53	
n_{facets}	2	4	3	3	4	5	0	4	1	0	
$n = K_s L/2\pi$	11	12	13	14	15	16	17	18	19	20	
behavior	E	E	E	E	E	E	E	E	E	E	
n_{final}	52	52	51	52	51	52	52	50	51	51	
n_{facets}	0	0	0	0	0	0	0	0	0	0	
$n = K_s L/2\pi$	21	22	23	24	25	26	27	28	29	30	31
behavior	E	E	E	E	E	E	E	E	E	E	E
n_{final}	52	47	48	47	46	46	45	44	44	41	37
n_{facets}	0	0	0	0	0	0	0	0	0	0	0
$n = K_s L/2\pi$	66	67	68	69	70	71	72	73	74		
behavior	E	E	E	E	E	E	EF	E	EF		
n_{final}	57	53	51	49	59	45	42	49	13		
n_{facets}	0	0	0	0	0	0	1	0	3		

Table 11.2: Outcome of the modulational instability of phase-winding states when $k_0 = 1.0$, $r = 2$, $L = 300$, $N = 1024$ (or $N = 2048$ for $n \geq 66$). The top row specifies the wave number of the unstable initial state while n_{final} specifies the phase jump across the domain in the final state. The letters E (Eckhaus) and EF (Eckhaus-faceting) indicate the evolution type.

K_n of the unstable state the phase slips may lead to a frozen faceted structure (EF) or to a stable phase-winding state with wave number in the Eckhaus-stable region in Figure 11.6 (E). Table II lists the results for $k_0 = 1.0$, $r = 2$, $L = 300$ and $N = 1024$ and different initial wave numbers K_n ($N = 2048$ is used for the initial $n \geq 66$). In addition to the initial and final values of n and the labels EF and E distinguishing the different types of behavior the table also lists the number n_{facets} of frozen facets in the final state. We mention that for these parameter values γ reaches maximum (maximum stability) when $K_s = 1.18$, corresponding to $n = 56.5$. On the other hand the K_n minimizing the Swift-Hohenberg energy F_{SH} corresponds to $n = 48$. Thus the evolution of the instability only rarely selects the lowest energy phase-winding state and the other states listed in the table corespond to thermodynamically metastable states. The frozen faceted states have even larger energies F_{SH} but these are also linearly stable, and hence also correspond to local minima of the energy landscape.

11.8 Conclusion

We have described a new class of time-independent states in the supercritial complex Swift-Hohenberg equation with real coefficients which we have called *phase-winding states*. These complex-valued solutions oscillate periodically in space, like the periodic states of the real Swift-Hohenberg equation, but with a well-defined phase difference between the real and imaginary parts. Such states are the spatial analogue of states known as rotating waves in the time domain. The solutions fall into different families characterized by the overall phase jump across the domain, which must be a nonzero integer multiple of 2π. These states are easily found in numerical simulations and then followed in parameter space using numerical continuation.

Defects of this type have been studied in the context of pattern-forming systems with a near-degenerate neutral curve. When the neutral curve admits two nearby minima the patterns that result may consist of domains consisting of wave trains with two distinct wavenumbers connected by fronts. As shown in Refs. [15, 16] an envelope description of such domain structures leads to a fourth order Ginzburg-Landau equation, an equation that can be written in the CSHE form (11.1). Our work extends existing work [15, 16] on such domain structures in two directions. (a) It shows that such states can be readily followed in parameter space using numerical continuation and their bifurcation properties determined, and (b) it explains how their presence relates on the one hand to phase slips generated by the Eckhaus instability in some wavenumber regimes and on the other to the coarsening dynamics observed in others.

Specifically, we have seen that these defect structures are associated with the presence of fronts connecting equal and opposite phase gradients. The fronts that are observed for order-one wave number k_0 have oscillatory tails allowing Pomeau locking between kinks and antikinks, stabilizing the localized states. In this region the phase variation resembles a faceted surface with abrupt changes in the phase gradient. On the other hand, when the characteristic wave number k_0 is small, stable facets and defects are no longer present. Instead numerical simulations reveal coarsening dynamics of the fronts. A theoretical analysis of the stability of the zero phase gradient state with respect to long wavelength perturbations showed that the observed coarsening is described by the Cahn-Hilliard equation for the perturbation phase gradient, thereby confirming the coarsening results obtained from simulations of the complex Swift-Hohenberg equation. For larger values of k_0 the cubic term in the effective potential becomes dominant and simulations reveal the formation of defects that shift the wave number of the phase-winding state towards increased stability, behavior that is familiar from existing studies of the Eckhaus instability. We have quantified the parameter regimes where this type of evolution leads to stable phase-winding

states and where the final state consists of two or more time-independent defects. Each defect connects phase-winding states with wave number $\pm k_0$ and pairs of defect form bound states locked to a fixed separation determined by the oscillatory tails of the fronts connecting the $\pm k_0$ phase-winding states. In some cases the Eckhaus instability of the phase-winding state with large K_s selects unstable wave numbers near k_0; if the spatial eigenvalues of this state are real the initial Eckhaus phase is followed by slow evolution via coarsening into a single bubble state. In other cases the eigenvalues are complex and the Eckhaus instability leads to a frozen defect state.

Throughout this Chapter we have chosen to vary the basic length scale $2\pi/k_0$ in the complex Swift-Hohenberg equation even though on the real line this length scale can be scaled out of the equation. Such a rescaling changes the bifurcation parameter r to r/k_0^4. Thus small values of k_0 correspond to large values of the scaled bifurcation parameter, potentially explaining why the coarsening behavior described here is not more widely known. On the other hand for $k_0 = 1$ faceting resulting from phase slips is the generic behavior of the system. One-dimensional fronts in the two-dimensional Swift-Hohenberg equation for a real order parameter may also undergo a faceting or zigzag instability [34, 35]. This instability results in a faceted front and is distinct from the faceting in the spatial phase of the pattern described here.

In future work we will confront the predictions obtained here for the supercritical complex Swift-Hohenberg equation with direct numerical simulations of the Maxwell-Bloch equations [17] or the equations modeling nondegenerate optical parametric oscillators [6–8]. An extension of the present study to the complex Swift-Hohenberg equation with complex coefficients is presented in the following Chapter.

References

[1] L. Gelens and E. Knobloch, "Faceting and coarsening dynamics in the complex Swift-Hohenberg equation," *Phys. Rev. E* **80**, 046221, 2009.

[2] L. Gelens and E. Knobloch, "Coarsening and frozen faceted structures in the supercritical complex Swift-Hohenberg equation," *Eur. Phys. J. D* , 2010.

[3] K. Staliunas, "Laser Ginzburg-Landau equation and laser hydrodynamics," *Phys. Rev. A* **48**, 1573–1581, 1993.

[4] J. Lega, J. V. Moloney, and A. C. Newell, "Swift-Hohenberg equation for lasers," *Phys. Rev. Lett.* **73**, 2978–2981, 1994.

[5] J. Lega, J. V. Moloney, and A. C. Newell, "Universal description of laser dynamics near treshold," *Physica D* **83**, 478–498, 1995.

[6] S. Longhi and A. Geraci, "Swift-Hohenberg equation for optical parametric oscillators," *Phys. Rev. A* **54**, 4581–4584, 1996.

[7] V. J. Sánchez-Morcillo, E. Roldán, G. J. de Valcárcel, and K. Staliunas, "Generalized complex Swift-Hohenberg equation for optical parametric oscillators," *Phys. Rev. A* **56**, 3237–3244, 1997.

[8] K. Staliunas, G. Slekys, and C. O. Weiss, "Nonlinear pattern formation in active optical systems: shocks, domains of tilted waves, and cross-roll patterns," *Phys. Rev. Lett.* **79**, 2658–2661, 1997.

[9] K. Staliunas, M. F. H. Tarroja, G. Slekys, C. O. Weiss, and L. Dambly, "Analogy between photorefractive oscillators and class-A lasers," *Phys. Rev. A* **51**, 4140–4151, 1995.

[10] J.-F. Mercier and J. V. Moloney, "Derivation of semiconductor laser mean-field and Swift-Hohenberg equations," *Phys. Rev. E* **66**, 036221, 2002.

[11] J. M. Soto-Crespo and N. Akhmediev, "Composite solitons and two-pulse generation in passively mode-locked lasers modeled by the complex quintic Swift-Hohenberg equation," *Phys. Rev. E* **66**, 066610, 2002.

[12] B. A. Malomed, "Nonlinear waves in nonequilibrium systems of the oscillatory type. 1.," *Z. Phys. B* **55**, 241–248, 1984.

[13] M. Bestehorn and H. Haken, "Traveling waves and pulses in a 2-dimensional large-aspect-ratio system," *Phys. Rev. A* **42**, 7195–7203, 1990.

[14] J. W. Cahn and J. E. Hilliard, "Free energy of a nonuniform system. i. interfacial free energy," *J. Chem. Phys.* **28**, 258–267, 1958.

[15] D. Raitt and H. Riecke, "Domain-structures in 4th-order phase and Ginzburg-Landau equations," *Physica D* **82**, 79–94, 1995.

[16] D. Raitt and H. Riecke, "Parametric forcing of waves with a nonmonotonic dispersion relation: Domain structures in ferrofluids," *Phys. Rev. E* **55**, 5448–5454, 1997.

[17] J. Pedrosa, M. Hoyuelos, and C. Martel, "Numerical validation of the complex Swift-Hohenberg equation for lasers," *Eur. Phys. J. B.* **66**, 525–530, 2008.

[18] B. A. Malomed, A. A. Nepomnyashchy, and M. I. Tribelsky, "Domain boundaries in convection patterns," *Phys. Rev. A* **42**, 7244, 1990.

[19] L. Q. Chen, "Phase-field models for microstructure evolution," *Ann. Rev. Materials Res.* **32**, 113–140, 2002.

[20] J. W. Cahn, "On spinodal decomposition," *Acta Metall.* **9**, 795–801, 1961.

[21] C. J. Chapman and M. R. E. Proctor, "Nonlinear Rayleigh-Bénard convection between poorly conducting boundaries," *J. Fluid Mech.* **101**, 759–782, 1980.

[22] A. Novick-Cohen and L. A. Segel, "Nonlinear aspects of the Cahn-Hilliard equation," *Physica D* **10**, 277–298, 1984.

[23] J. Carr, M. E. Gurtin, and M. Slemrod, "Structured phase transitions on a finite interval," *Arch. Ration. Mech. Anal.* **86**, 317, 1984.

[24] M. Argentina, M. G. Clerc, R. Rojas, and E. Tirapegui, "Coarsening dynamics of the one-dimensional Cahn-Hilliard model," *Phys. Rev. E* **71**, 046210, 2005.

[25] K. Kawasaki and T. Ohta, "Kink dynamics in one-dimensional non-linear systems," *Physica A* **116**, 573–593, 1982.

[26] T. Nagai and K. Kawasaki, "Statistical dynamics of interacting kinks - ii," *Physica A* **134**, 483–521, 1986.

[27] H. Brand and R. J. Deissler, "Confined states in phase dynamics," *Phys. Rev. Lett.* **63**, 508–511, 1989.

[28] M. C. Cross and P. C. Hohenberg, "Pattern-formation outside of equilibrium," *Rev. Mod. Phys.* **65**, 851–1112, 1993.

[29] R. B. Hoyle, *Pattern Formation*, Cambridge University Press, 2006.

[30] U. Thiele and E. Knobloch, "Thin liquid films on a slightly inclined heated plate," *Physica D* **190**, 213, 2004.

[31] M. C. Depassier and E. A. Spiegel, "The large-scale structure of compressible convection," *Astron. J.* **86**, 496, 1981.

[32] Y. Pomeau, "Front motion, metastability and subcritical bifurcations in hydrodynamics," *Physica D* **23**, 3–11, 1986.

[33] A. S. Landsberg and E. Knobloch, "Direction-reversing traveling waves," *Phys. Lett. A* **159**, 17–20, 1991.

[34] C. Chevallard, M. Clerc, P. Coullet, and J.-M. Gilli, "Interface dynamics in liquid crystals," *Eur. Phys. J. E* **1**, 179, 2000.

[35] M. G. Clerc, D. Escaff, and R. Rojas, "Transversal interface dynamics of a front connecting a stripe pattern to a uniform state," *Europhys. Lett.* **83**, 28002, 2008.

CHAPTER 12

Traveling wave dynamics

"Aren't echoes brilliant? They're not a modern invention, you just shout and it comes back exactly the same, you don't have to do 'owt, the mountain does it all for you. Some mountains are volcanoes, and they really are brilliant. Flooding. Fantastic. Great big waves. Brilliant. Lightning. Brilliant. Forest fires, yeah. Tornadoes, they're the best, wow, amazing." — The Fast Show

In this chapter, we expand our investigation of the complex Swift-Hohenberg equation, presented in the previous Chapter, by allowing the coefficients to be complex, breaking the variational structure of the model equation. A convective Cahn-Hilliard type equation is derived to describe the evolution of long-wavelength instabilities in the system and a great complexity in dynamical behavior is uncovered.

12.1 Introduction

In the previous Chapter, we have studied the complex Swift-Hohenberg equation (CSHE) with real coefficients. This study was motivated by the fact that the CSHE models pattern formation arising from an oscillatory instability with a finite wavenumber at onset [1, 2]. More in particular, the CSHE has a number of applications in nonlinear optics, it provides a description for e.g. Class A and C lasers [3–5], nondegenerate optical parametric oscillators (OPOs) [6–8], photorefractive oscillators [9], semiconductor lasers [10] and passively mode-locked lasers [11]. Having acquired a good understanding of the CSHE with

real coefficients, we now have a solid base to expand the previous analysis to the more general case of the CSHE with complex coefficients and hence time-dependent solutions.
We study the existence and dynamics of different kinds of localized states (LSs) in the one-dimensional CSHE:

$$u_t = ru + i\zeta u_{xx} - (1 + i\beta)(\partial_x^2 + k_0^2)^2 u - (1 + ib)|u|^2 u, \tag{12.1}$$

where u is a complex field. The equation is fully parametrized by the real coefficients r, ζ, β and b [1–4].
The stability and interaction of LSs and their transition to spatio-temporal chaos has especially been studied for the complex Ginzburg-Landau equation (CGLE) [12–15]. E.g. propagating, breathing and composite pulses and holes have been found to stably exist.
In this study, we focus on LSs in the CSHE that arise as defects (or also called domain boundaries [16, 17]) connecting a right and left traveling wave (TW). Experimentally, TW patterns have been e.g. observed in binary-fluid thermal convection [18] and in electrohydrodynamic convection in liquid crystals [19]. Such TWs are closely related to the phase-winding states in the CSHE, studied in the previous Chapter. Phase-winding states break the right/left symmetry and will start moving when introducing complex coefficients that break the variational structure of the CSHE. A typical TW pattern consists of domains where waves propagate in different directions. These domains are separated by defects: sources that send out TWs and sinks that absorb them [20]. Non-variational effects lead to qualitative differences between these defects and their equilibrium counterparts (which are the LSs studied in the previous Chapter). As we will show later, the sinks and the sources are not symmetrical. It has been demonstrated that sinks are generally stable, while the sources are more prone to instabilities [17, 20, 21].
Although TW patterns have been shown to exist in the CSHE [17], most often the field u is expressed as a linear combination of a right and left TW, leading to a system of two coupled CGLE equations for each complex amplitude of the right and left TW (which is valid for r is sufficiently small) [17, 20–24]. In two spatial dimensions, similar studies have been done within the framework of amplitude equations of the Newell-Whitehead-Segel type [16]. The TW dynamics in the CSHE remains, however, largely unexplored.

12.2 Traveling wave solutions

In order to find exact solutions of Eq. (12.1), we prefer to write the complex field u in its amplitude and phase form:

$$u(x,t) = u_R(x,t) + iu_I(x,t) = R(x,t)e^{i\phi(x,t)}. \tag{12.2}$$

Writing Eq. (12.1) in an amplitude and phase equation, one gets:

$$\begin{aligned} R_t &= rR - R^3 + \beta[-4\phi_x^3 R_x + 6\phi_{xx}R_{xx} + 4R_x\phi_{xxx} + 4\phi_x R_x k_0^2 + 4\phi_x R_{xxx} \\ &\quad -6R\phi_x^2\phi_{xx} + 2Rk_0^2\phi_{xx} + R\phi_{xxxx}] + [-2k_0^2 R_{xx} + 6\phi_x^2 R_{xx} + 12\phi_x R_x\phi_{xx} \\ &\quad -Rk_0^4 - R\phi_x^4 + 2Rk_0^2\phi_x^2 + 3R\phi_{xx}^2 + 4R\phi_x\phi_{xxx} - R_{xxxx}] - \zeta R\phi_{xx} \end{aligned} \tag{12.3}$$

$$\begin{aligned} R\phi_t &= -bR^3 + \beta[-2k_0^2 R_{xx} + 6\phi_x^2 R_{xx} + 12\phi_x R_x\phi_{xx} - Rk_0^4 - R\phi_x^4 + 2Rk_0^2\phi_x^2 \\ &\quad +3R\phi_{xx}^2 + 4R\phi_x\phi_{xxx} - R_{xxxx}] - [-4\phi_x^3 R_x + 6\phi_{xx}R_{xx} + 4R_x\phi_{xxx} \\ &\quad +4\phi_x R_x k_0^2 + 4\phi_x R_{xxx} - 6R\phi_x^2\phi_{xx} + 2Rk_0^2\phi_{xx} + R\phi_{xxxx}] + \zeta R_{xx} \end{aligned} \tag{12.4}$$

Searching for traveling wave solutions of the form $u = R_0 e^{i(\omega t \pm kx)}$, we find the following TW solutions:

$$R_0 = \sqrt{r - (k_0^2 - k^2)^2} \tag{12.5}$$

$$\omega = bR_0^2 + \beta(k_0^2 - k^2)^2. \tag{12.6}$$

In the next Section, we present a numerical study of the dynamical regimes present in the CSHE[1]. Afterwards, in Section 12.4, we derive a nonlinear phase equation to describe the long-wavelength instabilities of the TW solutions. This nonlinear phase equation allows to understand and predict several of the observed dynamical regimes in the CSHE.

12.3 Numerical exploration

In the previous Chapter, we have seen that depending on the intrinsic length-scale k_0 in the CSHE a large qualitative difference in dynamical behavior can be observed. Small values of k_0 lead to coarsening behavior, while for k_0 larger than a critical value K_{cross} faceting resulting from phase slips was the generic behavior of the CSHE with real coefficients [25, 26]. Based on this observation, we choose

[1] An explanation of the numerical integration scheme that we use can be found in Appendix B.

here to also study the dynamics of the CSHE with complex coefficients in these two limiting cases: $k_0 << K_{cross}$ and $k_0 >> K_{cross}$[2].

12.3.1 Dynamics in the CSHE with a large intrinsic length scale (k_0 small)

$b \neq 0$, $\beta = 0$

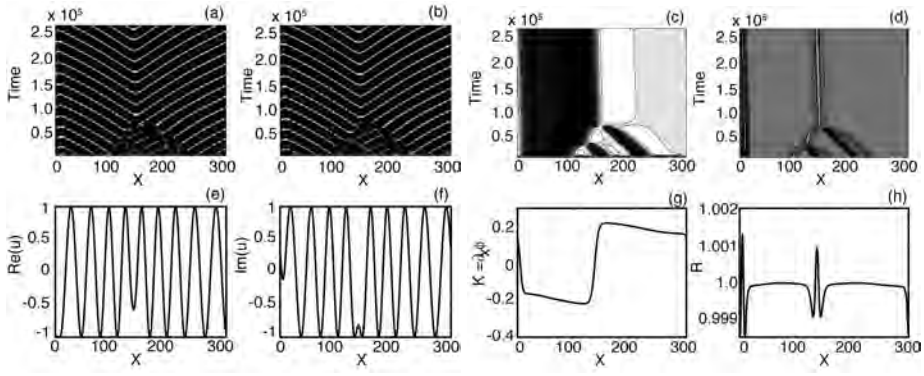

Figure 12.1: Temporal simulation of the CSHE with complex coefficients. (a)-(d) show a space-time plot of the time evolution of the real part of the field u, imaginary part of the field u, derivative of the phase ($K = \phi_x$) and the amplitude (R), respectively. (e)-(h) show the profiles corresponding to the last time step of (a)-(d). White/Black correspond to high/low values of K or R. Parameters: $r = 1$, $b = -0.5$ and $k_0 = 0.2$, $L = 300$, $N = 1024$ (parameters not mentioned are zero).

We start our numerical exploration in the region where k_0 is small such that in the CSHE with real coefficients coarsening behavior is expected. Furthermore, we first assume that the imaginary part of the coefficient with the spatial derivatives β is zero, and scan the dynamical behavior when decreasing the coefficient of the nonlinear term b. In Figure 12.1, a numerical simulation of the time evolution in the CSHE with complex coefficients is shown for $r = 1$, $b = -0.5$ and $k_0 = 0.2$ (and other parameters zero). As an initial condition random noise is taken (as is the case in the remainder of this Chapter). One can see in Figure 12.1 that

[2]We would like to remark that we will not explicitly calculate K_{cross} here. In principle, the critical value K_{cross} where the dominant spatial eigenvalues of the traveling waves go from being complex (creating oscillatory tails) to purely real (creating monotonic tails) can be carried out by studying the spatial dynamics.

there eventually exists one source and one sink solution where the two counter-propagating TWs (real and imaginary part of the field) meet [see Figure 12.1(e) and (f)]. This corresponds to the connection of two opposite phase gradients through a front, where a LS in amplitude is associated to this front [see Figure 12.1(g) and (h)]. The distinction between sources and sinks is made according to whether the nonlinear group velocity of the asymptotic TW points outwards or inwards, respectively [see Figure 12.1(a) and (b)]. A source is an active coherent structure sending out waves to both sides, while a sink is sandwiched between TWs whose group velocity is pointing inwards. It is clear from Figure 12.1 that initially several LSs exist, which subsequently coarsen. Due to this coarsening dynamics, LSs are removed from the system in several collisions until only one sink and source remain which drift slowly, but stably. Similar coarsening behavior is observed for higher values of b. Such coarsening behavior can be described by a Cahn-Hilliard type equation, which will be further discussed in Section 12.4.
The change in dynamical behavior when decreasing b is exemplified in Figure 12.2. When b reaches -1, one observes an initial back-and-forth movement of the phase gradient fronts (and associated LSs), but after this transient behavior the LSs (both source and sink) are stabilized [see Figure 12.2(a) and (b)]. When decreasing b further a regime of spatio-temporal intermittency is found [see Figure 12.2(c) and (d)]. In this regime, defect chaos coexists with stable TWs. Patches of stable TWs are separated by various LSs, some of those LSs are created and destroyed rather fast, while others seem to persist longer displaying similar back-and-forth movement as seen in the transient of Figure 12.2(a) and (b). Such spatio-temporal intermittency has been studied in the context of the CGLE in Refs. [12, 21, 23, 27]. When decreasing b even further, the system exhibits more and more spatiotemporally disordered regimes.

$b \neq 0, \beta \neq 0$

Figures 12.3 - 12.5 show the results of numerical simulations, which have still been done in the long-wavelength regime $k_0 << K_{cross}$ (where fronts are monotic and thus do not have oscillatory tails), but here we take $b = -1$ fixed and vary the coefficient β of the laplacian term. Figure 12.3 shows the typical dynamical behavior that is observed for $\beta < 0$. For all negative values of β coarsening dynamics is found. The long time tendency of the system is to remove LSs through coarsening, until only one source-sink pair is left in the system. Both the source and sink are then stable and either remain stationary or drift in time.

When choosing β positive and in the range $[0, 1]$, spatio-temporal intermittency occurs. We refer again to Figures 12.2(c)-(f) for typical space-time plots of this dynamical behavior. From $\beta \approx 1$, TWs are no longer found in numerical

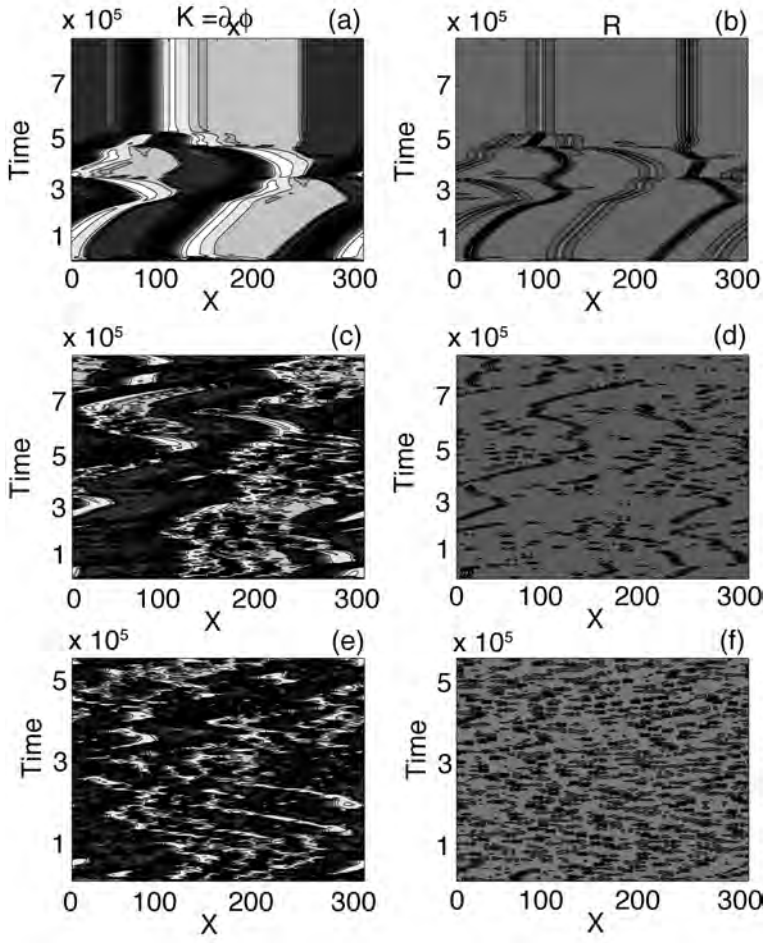

Figure 12.2: Temporal simulation of the CSHE with complex coefficients. Space-time plots are shown of the time evolution of the derivative of the phase ($K = \phi_x$) [(a),(c),(e)] and the amplitude (R) [(b),(d),(r)], for increasing values of $|b|$. White/Black correspond to high/low values of K or R. Parameters: $r = 1$, $b = -1$ (a,b), -1.5 (c,d), -2 (e,f) and $k_0 = 0.2$, $L = 300$, $N = 1024$ (parameters not mentioned are zero).

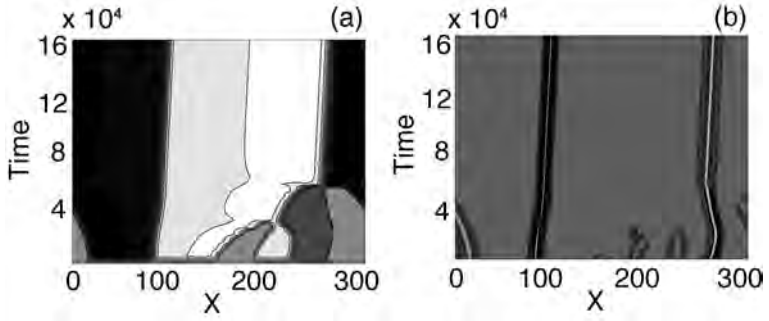

Figure 12.3: Temporal simulation of the CSHE with complex coefficients. Space-time plots are shown of the time evolution of the derivative of the phase ($K = \phi_x$) in (a) and the amplitude (R) in (b). White/Black correspond to high/low values of K or R. Parameters: $r = 1$, $b = -1$, $\beta = -2$ and $k_0 = 0.2$, $L = 300$, $N = 1024$ (parameters not mentioned are zero).

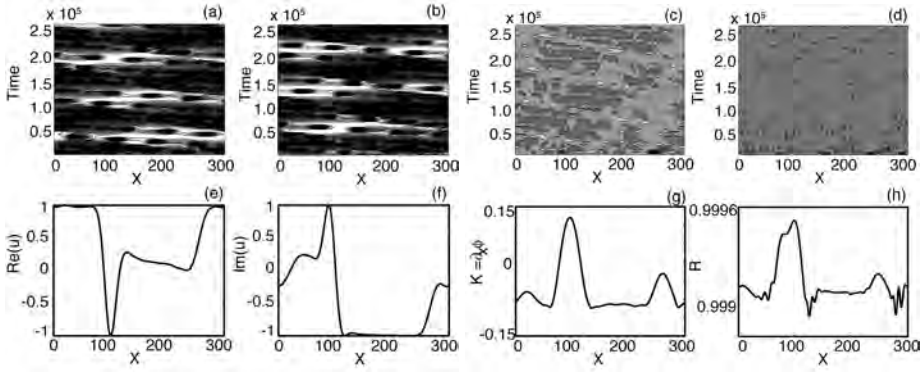

Figure 12.4: Temporal simulation of the CSHE with complex coefficients. (a)-(d) show a space-time plot of the time evolution of the real part of the field u, imaginary part of the field u, derivative of the phase ($K = \phi_x$) and the amplitude (R), respectively. (e)-(h) show the profiles corresponding to the last time step of (a)-(d). White/Black correspond to high/low values of K or R. Parameters: $r = 1$, $b = -1$, $\beta = 1$ and $k_0 = 0.2$, $L = 300$, $N = 1024$ (parameters not mentioned are zero).

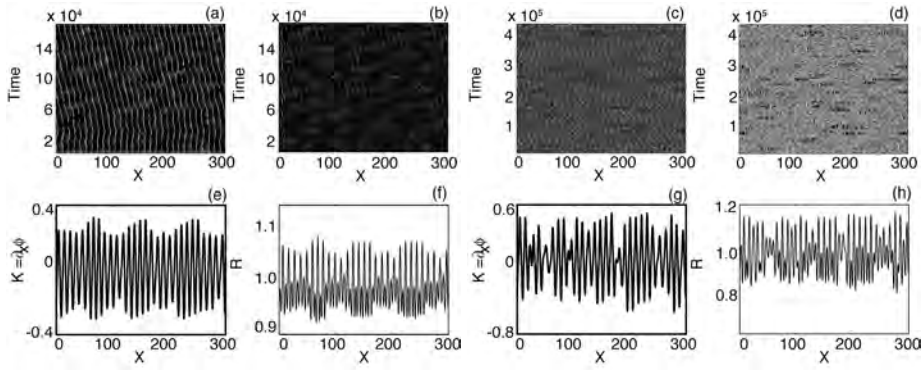

Figure 12.5: Temporal simulation of the CSHE with complex coefficients. Space-time plots of the time evolution of the derivative of the phase ($K = \phi_x$) (a,c) and the amplitude (R) (b,d) are shown. (e)-(h) show the profiles corresponding to the last time step of (a)-(d). White/Black correspond to high/low values of K or R. Parameters: $r = 1$, $b = -1$, $\beta = 2$ (a,b,e,f), 3 (c,d,g,h) and $k_0 = 0.2$, $L = 300$, $N = 1024$ (parameters not mentioned are zero).

simulations. Instead for $\beta = 1$, uniformly moving pulses in real and imaginary part are found to be solutions of the CSHE [see Figure 12.4]. When increasing β further the behavior changes qualitatively. With random initial conditions, the system evolves to a spatially periodic state in the phase gradient $K = \phi_x$ and amplitude R. Such a slowly drifting nonlinear standing wave pattern is shown in Figure 12.5(a) and (b), although one can observe in panels (e) and (f) that the periodic state already shows a certain modulation of its amplitude. This modulation becomes more and more pronounced when increasing β. We can see e.g. in Figure 12.5(c) and (d) that a increase in β leads to an increase of the local wavenumber K and the formation of defects. Such perturbations of the standing wave [panels (a) and (b)] are spontaneously formed, indicating a linear instability. Spatio-temporal chaos of the periodic wave pattern is observed panels (c) and (d). The dynamics evolves on faster time scales and no coherent structures can be observed. Such behavior is also observed in the CGLE [12, 21]. In the case of the CGLE, this spatio-temporal chaos has been described by the Kuramoto-Sivashinsky (KS) equation [27]. We indeed show in Section 12.4 that for these parameters a nonlinear phase equation can be derived, which is of the Kuramoto-Sivashinsky type.

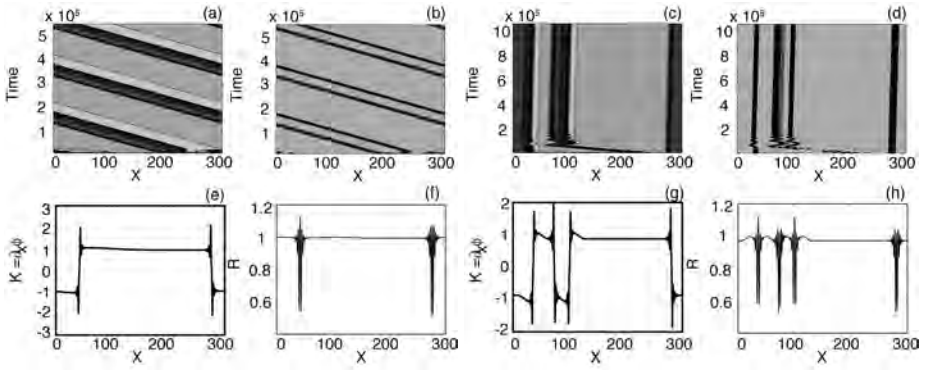

Figure 12.6: Temporal simulation of the CSHE with complex coefficients. Space-time plots of the time evolution of the derivative of the phase ($K = \phi_x$) (a,c) and the amplitude (R) (b,d) are shown. (e)-(h) show the profiles corresponding to the last time step of (a)-(d). White/Black correspond to high/low values of K or R. Parameters: $r = 1$, $b = -0.5$ (a,b,e,f), -1 (c,d,g,h) and $k_0 = 1$, $L = 300$, $N = 1024$ (parameters not mentioned are zero).

12.3.2 Dynamics in the CSHE with a finite intrinsic length scale ($k_0 = O(1)$)

In the previous Chapter (see also Refs. [25, 26]), we have shown that in the CSHE with real coefficients there exists a critical length scale $k_0 = K_{cross}$ after which faceting resulting from phase slips is generally observed. Due to the existence of oscillatory tails in the front profiles of the phase gradient $K = \phi_k$, Eckhaus instabilities of phase-winding states generate phase slips, leading to the formation of LSs (or also called facets). The phase-winding states do not coarsen, but lock to the oscillatory front profile. In this Section, we numerically explore the dynamical behavior that can arise in the CSHE with complex coefficients for $k_0 = 1$ such that oscillatory tails exist. As before, we first consider β to be zero and afterwards allow for both b and β to have non-zero values.

$b \neq 0, \beta = 0$

Taking $\beta = 0$ and varying the nonlinear coefficient b, the results for small negative values of b are shown in Figure 12.6. Starting from random initial conditions, the system relaxes to drifting LSs after a possible transient behavior. Contrary to the case of small k_0, more than one drifting source and sink solution can be

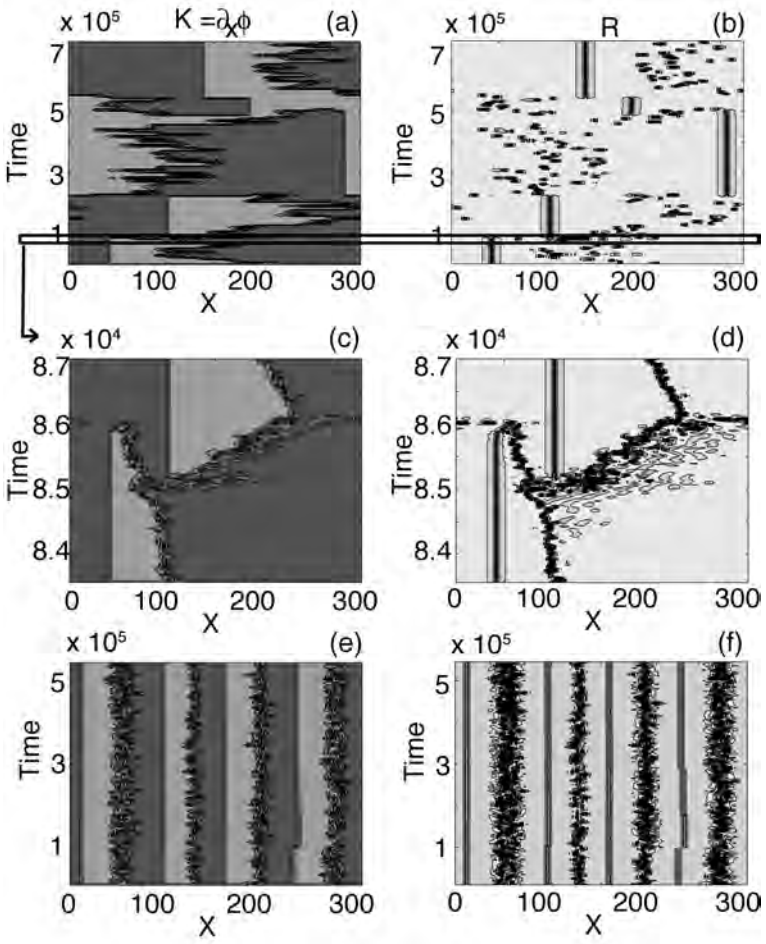

Figure 12.7: Temporal simulation of the CSHE with complex coefficients. Space-time plots are shown of the time evolution of the derivative of the phase ($K = \phi_x$) [(a),(c),(e)] and the amplitude (R) [(b),(d),(r)], for increasing values of b. Panels (c)-(d) represent a zoom of the black box in (a)-(b). White/Black correspond to high/low values of K or R. Parameters: $r = 1$, $b = -3$ (a)-(d) and -5 (e)-(f) and $k_0 = 1$, $L = 300$, $N = 1024$ (parameters not mentioned are zero).

present in the system as no coarsening dynamics occurs in the system.
Figure 12.7 shows spatio-temporal chaotic regimes that are found when decreas-

ing the value of b further. Instead of drifting LSs, one observes a stabilization of a stationary sink solution, while the source behaves very irregularly. Such behavior reminds of the source-induced bimodal chaos that is observed in coupled CGLE [21]. While in the case of coupled CGLE, however, the sink mildly drifts, this is not the case here in the CSHE. The bimodal chaos observed in coupled CGLE has been shown not to occur in a single CGLE. While the sink remains stable and stationary over long periods of time, one can observe in Figure 12.7(a) and (b) that at certain points in time the sink seems to be suddenly destroyed and recreated elsewhere in space ($b = -3$ in this case). Panels (c) and (d) show a blow-up of such an event [indicated by the black box in Figure 12.7(a) and (b)]. It becomes evident from this blow-up that from the chaotic source a new stable sink / chaotic source pair can be born. Once this happens the original sink solution is destabilized and eventually destroyed by one chaotic source. After this process, only one stable sink / chaotic source pair is present in the system, but at a different location as before. This behavior is repeated in time, where the time between consecutive events seems to be distributed chaotically as well. To the best of our knowledge, such behavior has not been observed in other systems. When decreasing b further, multiple stable sink / chaotic source pairs coexist as illustrated in Figure 12.7(e) and (f) for $b = -5$.
Finally, we would like to remark that the same qualitative behavior is observed for positive values of b. For low values of b, single or multiple drifting source-sink pairs are observed. Increasing b eventually leads to the creation of one stable sink / chaotic source pair (e.g. for $b = 3$). For higher values of b, multiple coexisting stable sink / chaotic source pairs are again found (e.g. for $b = 5$).

$b \neq 0$, $\beta \neq 0$

Figure 12.8 demonstrates the dynamics that is observed when taking into account the influence of the imaginary part of the laplacian term β. A full characterization of the spatio-temporal dynamics in the parameter space (b, β) is beyond the scope of this work. We limit ourselves to analyzing the dynamical behavior in a small part of the parameter space. The coefficient b is kept fixed to -1, scanning β from -5 to 5. The following behavior is observed[3]:

- For $\beta < -3.4$, the whole space is filled with coexisting stationary source-sink pairs. For the chosen domain width $L = 300$, either 3 or 4 pairs are present in the system [see e.g. Figure 12.8(a); $\beta = -5$].

[3]We would like to remark to that the boundaries mentioned in this classification of dynamical behavior have been numerically determined with an accuracy of $\Delta\beta = 0.1$.

- In the region $-3.4 < \beta < -2.5$, the same source-sink pairs still coexist, but are no longer stationary and exhibit a slight "breathing" (time-periodic) behavior [see e.g. Figure 12.8(b); $\beta = -3$].

- When increasing β in the region $-2.5 < \beta < 1.2$, the number of source-sink pairs in the system tends to diminish. Furthermore, on top of the "breathing" behavior, the sources and sinks start to drift [see e.g. Figure 12.8(c) and (d); $\beta = -2.5$ and $\beta = 1$]. We remark that around $\beta \approx -0.1$ the drift speed of the structures becomes very slow.

- For $1.2 < \beta < 4$, both source and sink are stabilized again and remain stationary [see e.g. Figure 12.8(e); $\beta = 3$].

- In the region $4 < \beta < 4.2$, a time-periodic "breathing" behavior is observed, where the time-periodic oscillations are much more pronounced than in the previous cases. Moreover, only the source shows time-periodic behavior, while the sink remains stable [see e.g. Figure 12.8(f); $\beta = 4.1$].

- When increasing β such that $4.2 < \beta < 4.8$, the time-periodicity of the source is lost and replaced by chaotic behavior. The sink solution is still stationary [see e.g. Figure 12.8(g); $\beta = 4.5$].

- Finally, for $\beta > 4.8$, the chaotic behavior of the source disappears again, but continues to show time-periodic coherent structures [see e.g. Figure 12.8(h); $\beta = 5$].

In the next Section, we derive a nonlinear phase equation modeling the evolution of long-wavelength perturbations of the homogeneous amplitude solutions. This phase equation will prove useful to gain a deeper understanding of the numerically observed dynamics.

12.4 Derivation of a nonlinear phase equation

In terms of the amplitude R and the phase gradient $K = \partial_x \phi$, Eq. (12.1) takes the form

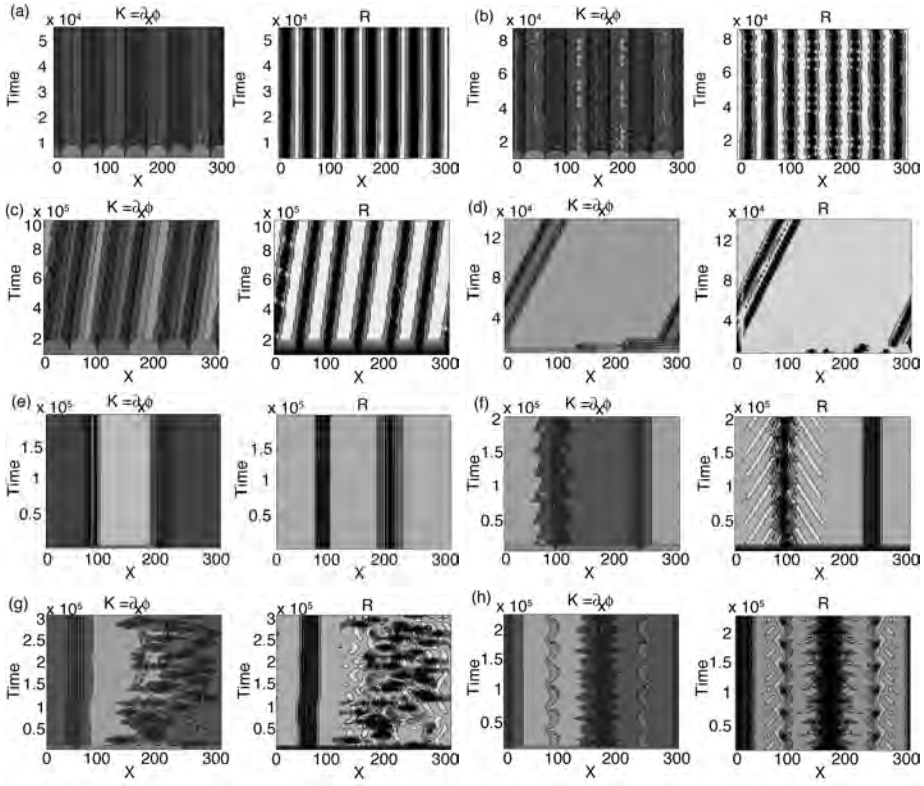

Figure 12.8: Temporal simulation of the CSHE with complex coefficients. Space-time plots of the time evolution of the derivative of the phase ($K = \phi_x$) and the amplitude (R) are shown. White/Black correspond to high/low values of K or R. Parameters: $r = 1$, $b = -1$, $\beta = -5$ (a), -3 (b), -2.5 (c), 1 (d), 3 (e), 4.1 (f), 4.5 (g) and 5 (h), $k_0 = 1$, $L = 300$, $N = 1024$ (parameters not mentioned are zero).

$$
\begin{aligned}
R_t &= rR - R^3 - k_0^4 R + [-2k_0^2 R_{xx} + 6K^2 R_{xx} + 12KR_xK_x - RK^4 + 2RK^2k_0^2 \qquad (12.7)\\
&\quad +3RK_x^2 + 4KK_{xx}R - R_{xxxx}] + \beta[-4K^3R_x + 6K_xR_{xx} + 4R_xK_{xx} + 4KR_xk_0^2\\
&\quad +4KR_{xxx} - 6RK^2K_x + 2Rk_0^2K_x + RK_{xxx}] - \zeta[2R_xK + RK_x]\\
K_t &= -2bRR_x - [4\frac{R_{xxx}}{R}K + 6\frac{R_{xx}}{R}K_x + 4\frac{R_x}{R}K_{xx} + K_{xxx} - 4\frac{R_x}{R}K^3 \qquad (12.8)\\
&\quad -6K^2K_x + 2k_0^2K_x + 4k_0^2K\frac{R_x}{R}]_x + \beta[-2k_0^2\frac{R_{xx}}{R} + 6K^2\frac{R_{xx}}{R} + 12KK_x\frac{R_x}{R}\\
&\quad -K^4 + 2k_0^2K^2 + 3K_x^2 + 4KK_{xx} - \frac{R_{xxxx}}{R}]_x + \zeta[\frac{R_{xx}}{R} - K^2]_x
\end{aligned}
$$

To examine the evolution of perturbations of the homogeneous state ($R^2 = R_0^2 \equiv r - k_0^4$, $\phi = \phi_0$) we write ($R = R_0 + u$, $K = v$) where u and v are of order $O(\epsilon)$. We suppose that spatial derivatives are $O(\epsilon)$ while temporal derivatives are $O(\epsilon^4)$. To leading order, we obtain the following equation:

$$u_t = -2R_0^2 u + 2k_0^2 R_0(\beta v_x + v^2) - \zeta R_0 v_x + \text{higher order terms}, \tag{12.9}$$

and hence $R_0 u \approx (k_0^2\beta - \frac{1}{2}\zeta)v_x + k_0^2 v^2$. Substituting this result in the equation for the phase gradient results in a modified convective Cahn-Hilliard-type equation:

$$\begin{aligned} v_t &= [\gamma v - a v_{xx} - \kappa_0 v^3]_{xx} \\ &\quad + [\frac{D}{2} v^2 + c v_x^2 + d v^4 + e v v_{xx}]_x + \text{higher order terms}. \end{aligned} \tag{12.10}$$

The coefficients in Eq. (12.10) are given by

$$\gamma = -2k_0^2(1 + b\beta) + b\zeta \tag{12.11}$$

$$\kappa_0 = -2(1 - \frac{k_0^4}{R_0^2} + \frac{1}{6}\frac{\gamma k_0^2}{R_0^2}) \tag{12.12}$$

$$D = 4k_0^2(\beta - b) - 2\zeta \tag{12.13}$$

$$a = 1 + \frac{(2k_0^2\beta - \zeta)^2}{2R_0^2} \tag{12.14}$$

$$c = 3\beta - \frac{b}{4R_0^2}(2k_0^2\beta - \zeta)^2 - \frac{2k_0^2}{R_0^2}(2k_0^2\beta - \zeta) \tag{12.15}$$

$$d = -\beta - \frac{b k_0^4}{R_0^2} \tag{12.16}$$

$$e = 4\beta(1 - \frac{2k_0^4}{R_0^2}) + \frac{4k_0^2\zeta}{R_0^2}. \tag{12.17}$$

Depending on the magnitude of the coefficients, the phase equation resembles either the Cahn-Hilliard equation or more the Kuramoto-Sivashinsky equation. While the Cahn-Hilliard equation is a well-known model equation predicting coarsening dynamics [28], as we have also discussed in the previous Chapter, the Kuramoto-Sivashinsky is traditionally used to model turbulence [27].
An interesting limit of the phase gradient equation (12.10) is the one for small values of k_0 (such as e.g. $k_0 = 0.2$ as discussed Section 12.3) and assuming $\zeta = 0$. In this limit, Eq. (12.10) simplifies to

$$v_t = [-2k_0^2(1 + b\beta)v - v_{xx} + 2v^3]_{xx} + [2k_0^2(\beta - b)v^2 + \beta(3v_x^2 - v^4 + 4v v_{xx})]_x. \tag{12.18}$$

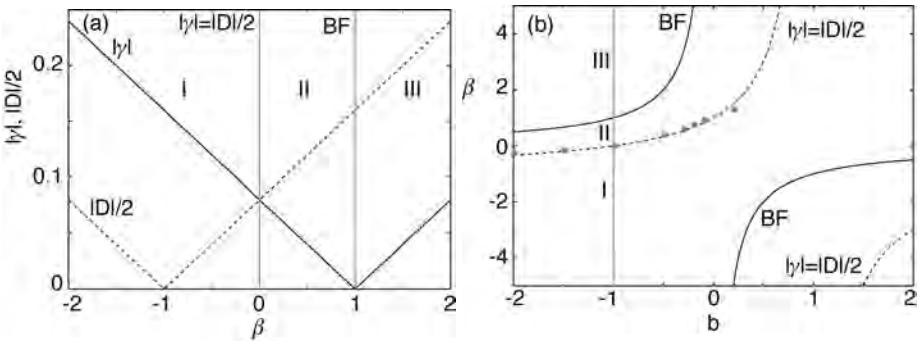

Figure 12.9: (a) shows the magnitude of the coefficients γ and $D/2$ of Eq. 12.18 in function of β for $k_0 = 0.2$, $r = 1$, $b = -1$ and $\zeta = 0$. (b) depicts the locus of the Benjamin-Feir-Eckhaus (BF) instability and the locus of the points where γ and $D/2$ have equal magnitude in the parameter plane (b, β) for $k_0 = 0.2$ and $r = 1$. Transition points from coarsening behavior to spatio-temporal intermittency have been determined numerically with an accuracy $\Delta\beta = 0.1$ and are plotted with grey dots.

This equation helps us to understand the observed behavior in Section 12.3.1, where simulations have been shown for $k_0 = 0.2$, $r = 1$ and $\beta = 0$.
For $\beta = 0$, Eq. (12.18) becomes:

$$v_t = [-2k_0^2 v - v_{xx} + 2v^3]_{xx} + 4k_0^2 b v v_x, \tag{12.19}$$

which is the convective Cahn-Hilliard equation. The transition from coarsening to roughening behavior has been studied in Ref. [29]. For $b \to 0$, Eq. (12.19) reduces further to the Cahn-Hilliard equation, originally derived to describe the dynamics of phase separation in systems with a conserved quantity in the context of binary alloys [28]. However, the model equation arises in many other areas of physics as well (see Section 11.5.1). For small values of b, we indeed numerically confirmed such coarsening dynamics in Section 12.3.1 (see Figure 12.1). For increasing values of b a transition from coarsening dynamics to chaotic spatiotemporal behavior is expected as for $b \to \infty$, Eq. (12.19) reduces to the Kuramoto-Sivashinsky equation [21, 27]. Figure 12.2 confirms this prediction as it shows a transition towards spatio-temporal chaos when increasing the value of b.
When β is no longer zero (see Section 12.3.1), the situation becomes more complicated as Eq. (12.18) can no longer be easily seen as either a Cahn-Hilliard equation or a Kuramoto-Sivashinsky equation because many different terms come into play. However, focusing on the terms of the convective Cahn-Hilliard equation, we can still partly understand the numerically observed behavior. In

Figure 12.9 the magnitude of the leading term γ and the convective term D are studied. The position where the coefficient γ turns zero and changes its sign is shown in (b, β)-space. For negative values of γ, it is clear from Eq. (12.18) that the homogeneous solutions are unstable. The TWs with a finite wavenumber, however, are stable for $\gamma < 0$. The change of sign of γ corresponds to the well-known Benjamin-Feir (BF) instability of TWs (which is the equivalent of the Eckhaus instability for phase-winding states). For $\gamma > 0$ small perturbations are no longer damped out, but now have a positive growth rate, while for $\gamma < 0$ TWs with a finite wavenumber are stable. This BF instability is given by the condition $1 + b\beta = 0$, similarly as for the CGLE. Furthermore, we have also plotted where the magnitude of the terms γ and the convective term $D/2$ are equal. This condition is given by $1 + b + (b - 1)\beta = 0$ and — although being a hand-waving argument — it can be argued that this line provides an estimation of where the transition between Cahn-Hilliard-type dynamics or Kuramoto-Sivashinsky-type dynamics.

Let us now focus on $b = -1$, the chosen value in the numerical simulations of Section 12.3.1. For negative values of β (region I in Figure 12.9), one can see that $\gamma < 0$ and $\left|\gamma\right| > |D/2|$. This way the leading order system corresponds to the convective Cahn-Hilliard equation with a small driving term D. As the convective term is small and the TWs are stable, coarsening dynamics like in the Cahn-Hilliard equation is expected, as also observed in Figure 12.3.

Next, when $\beta \in [0, 1]$ (region II in Figure 12.9), the TWs are still linearly stable ($\gamma < 0$). However, the magnitude of the convective term $D/2$ becomes larger than γ. This way Eq. (12.18) resembles more the Kuramoto-Sivashinsky equation instead of the Cahn-Hiliard equation. Indeed, around this region coarsening dynamics is no longer observed, but instead spatio-temporal intermittency sets in. Such behavior is similar as the one illustrated in Figure 12.2. The spatio-temporal intermittency is defined by the fact that although there exist laminar, absorbing stable TW solutions, there also exists a *turbulent*, active state that consists of localized structures [27]. In order to verify whether our hand-waving argument that the transition to spatio-temporal intermittency is determined by the moment where $\left|\gamma\right| \approx |D/2|$ holds, we have numerically checked the position of this transition in (b, β)-space. The numerically determined transition points have been plotted in Figure 12.9 with the grey dots. One can in fact observe a very good correspondence between the numerics and the line where $\left|\gamma\right| \approx |D/2|$.

Finally, in region III ($\beta > 1$), the convective term $D/2$ is larger in magnitude than γ, such that Eq. (12.18) looks more and more like a Kuramoto-Sivashinsky-type equation. Moreover, the TWs are destabilized ($\gamma > 0$). For β slightly larger than 1, stable standing wave (SW) patterns in the phase gradient K are found (not shown). Increasing β further these SW undergo consecutive spatial period doubling bifurcations, in other words the SW becomes modulated with a certain

second, third, ... wavenumber. As is known for the Kuramoto-Sivashinsky equation, such a period-doubling route leads to chaos [30], as is also the case here (see Figure 12.5). We remark that in the transition from region II (spatiotemporal intermittency) to region III where SW exist, *freezing* occurs [27], which stabilizes the states with a spatially disordered structure. Such a stably drifting disordered solution can be seen in Figure 12.4 ($\beta = 1$).

12.5 Conclusion

In this Chapter, we have numerically explored the dynamical behavior that can arise in the complex Swift-Hohenberg equation with complex coefficients. Moreover, a convective Cahn-Hilliard type equation has been derived to describe the evolution of long-wavelength instabilities in the system and has been used to understand several of the different kinds of dynamical behavior present in the complex Swift-Hohenberg equation.
We want to point out that although many of the observed dynamical regimes can qualitatively be understood by comparing the sign and magnitude of the different terms of the convective Cahn-Hilliard terms, there are undoubtedly certain features of the dynamics in the complex Swift-Hohenberg equation that need inclusion of the novel terms present in Eq. (12.18). Such differences can perhaps be understood by carrying out a systematic study of the influence of all different terms in the full nonlinear phase equation (12.18), and directly comparing numerical simulations of the CSHE with simulations of the phase equation. Furthermore, a derivation of the phase equation for perturbations around the traveling waves with finite wavenumber remains to be carried out and can provide useful information about the Benjamin-Feir instability and other instabilities that the traveling waves undergo.

References

[1] B. A. Malomed, "Nonlinear waves in nonequilibrium systems of the oscillatory type. 1.," *Z. Phys. B* **55**, 241–248, 1984.

[2] M. Bestehorn and H. Haken, "Traveling waves and pulses in a 2-dimensional large-aspect-ratio system," *Phys. Rev. A* **42**, 7195–7203, 1990.

[3] J. Lega, J. V. Moloney, and A. C. Newell, "Swift-Hohenberg equation for lasers," *Phys. Rev. Lett.* **73**, 2978–2981, 1994.

[4] J. Lega, J. V. Moloney, and A. C. Newell, "Universal description of laser dynamics near treshold," *Physica D* **83**, 478–498, 1995.

[5] K. Staliunas, "Laser Ginzburg-Landau equation and laser hydrodynamics," *Phys. Rev. A* **48**, 1573–1581, 1993.

[6] S. Longhi and A. Geraci, "Swift-Hohenberg equation for optical parametric oscillators," *Phys. Rev. A* **54**, 4581–4584, 1996.

[7] V. J. Sánchez-Morcillo, E. Roldán, G. J. de Valcárcel, and K. Staliunas, "Generalized complex Swift-Hohenberg equation for optical parametric oscillators," *Phys. Rev. A* **56**, 3237–3244, 1997.

[8] K. Staliunas, G. Slekys, and C. O. Weiss, "Nonlinear pattern formation in active optical systems: shocks, domains of tilted waves, and cross-roll patterns," *Phys. Rev. Lett.* **79**, 2658–2661, 1997.

[9] K. Staliunas, M. F. H. Tarroja, G. Slekys, C. O. Weiss, and L. Dambly, "Analogy between photorefractive oscillators and class-A lasers," *Phys. Rev. A* **51**, 4140–4151, 1995.

[10] J.-F. Mercier and J. V. Moloney, "Derivation of semiconductor laser mean-field and Swift-Hohenberg equations," *Phys. Rev. E* **66**, 036221, 2002.

[11] J. M. Soto-Crespo and N. Akhmediev, "Composite solitons and two-pulse generation in passively mode-locked lasers modeled by the complex quintic Swift-Hohenberg equation," *Phys. Rev. E* **66**, 066610, 2002.

[12] I. S. Aranson and L. Kramer, "The world of the complex Ginzburg-Landau equation," *Rev. Mod. Phys.* **74**, 99–143, 2002.

[13] M. Cross and P. Hohenberg, "Pattern-formation outside of equilibrium," *Rev. Mod. Phys.* **65**, 851–1112, 1993.

[14] J. Lega, "Traveling hole solutions of the complex Ginzburg-Landau equation: a review," *Physica D* **152–153**, 269–287, 2001.

[15] W. van Saarloos, "Front propagation into unstable states," *Phys. Rep.* **386**, 29–222, 2003.

[16] B. Malomed, A. Nepomnyashchy, and M. I. Tribelsky, "Domain boundaries in convection patterns," *Phys. Rev. A* **42**, 7244–7263, 1990.

[17] H. Sakaguchi and B. Malomed, "Grain boundaries in two-dimensional traveling-wave patterns," *Physica D* **118**, 250–260, 1998.

[18] P. Kolodner, D. Bensimon, and C. Surko, "Weakly nonlinear traveling-wave convection," *Phys. Rev. Lett.* **60**, 1723, 1988.

[19] I. Rehberg, S. Rasenat, and V. Steinberg, "Traveling waves and defect-initiated turbulence in electroconvecting nematics," *Phys. Rev. Lett.* **62**, 756, 1989.

[20] P. Coullet, T. Frisch, and F. Plaza, "Sources and sinks of wave patterns," *Physica D* **62**, 75–79, 1993.

[21] M. V. Hecke, C. Storm, and W. van Saarloos, "Sources, sinks and wavenumber selection in coupled CGL equations and experimental implications for counter-propagating wave systems," *Physica D* **134**, 1–47, 1999.

[22] H. Sakaguchi, "Standing wave patterns for the complex Swift-Hohenberg equation," *Prog. Theor. Phys.* **98**, 577–585, 1997.

[23] A. Amengual, E. Hernández-García, T. Montagne, and M. San Miguel, "Synchronization of spatiotemporal chaos: The regime of coupled spatiotemporal intermittency," *Phys. Rev. Lett.* **78**, 4379–4382, 1997.

[24] H. Sakaguchi, "Herringbone pattern for an anisotropic complex Swift-Hohenberg equation," *Phys. Rev. E* **58**, 8021–8023, 1998.

[25] L. Gelens and E. Knobloch, "Faceting and coarsening dynamics in the complex Swift-Hohenberg equation," *Phys. Rev. E* **80**, 046221, 2009.

[26] L. Gelens and E. Knobloch, "Coarsening and frozen faceted structures in the supercritical complex Swift-Hohenberg equation," submitted for publication.

[27] H. Chaté, "Spatiotemporal intermittency regimes of the one-dimensional complex Ginzburg-Landau equation," *Nonlinearity* **7**, 185–204, 1994.

[28] J. W. Cahn and J. E. Hilliard, "Free energy of a nonuniform system. i. interfacial free energy," *J. Chem. Phys.* **28**, 258–267, 1958.

[29] A. Golovin, A. Nepomnyashchy, S. Davis, and M. Zaks, "Convective Cahn-Hilliard models: from coarsening to roughening," *Phys. Rev. Lett.* **86**, 1550–1553, 2001.

[30] Y. S. Smyrlis and D. T. Papageorgiou, "Predicting chaos for infinite dimensional dynamical systems: The Kuramoto-Sivashinsky equation, a case study," *Proc. Natl. Acad. Sci. USA* **88**, 11129–11132, 1991.

Piled Higher and Deeper ***by Jorge Cham*** **www.phdcomics.com**

CHAPTER 13

Front interaction enhancement induced by nonlocal spatial coupling

*"**Ray McCooney**: I leave yee with a riddle! I'm hard yet soft, I'm coloured yet clear, I am fruity and sweet, I am jelly, what am I?*
***Customer**: Jelly!*
***Ray McCooney**: Muse upon it further, I shall return.*
***Customer**: It's jelly though isn't it?*
***Ray McCooney**: Ye-eees! Yee know too much.....too much. " — Ray McCooney in Little Britain.*

We demonstrate that nonlocal coupling strongly influences the dynamics of fronts connecting two equivalent states. In two prototype models we observe a large amplification in the interaction strength between two opposite fronts increasing front velocities several orders of magnitude. By analyzing the spatial dynamics we prove that beyond quantitative effects, nonlocal terms can also change the overall qualitative picture by inducing oscillations in the front profile. This leads to a mechanism for the formation of localized structures not present for local interactions. Finally, nonlocal coupling can induce a steep broadening of localized structures, eventually annihilating them.[1]

[1]The work presented in this Chapter has been submitted for publication: [1].

13.1 Introduction

Most studies on the emergence of complex behavior in spatially extended systems consider that spatial coupling is either local or alternatively global (all to all coupling) [2, 3]. More recently, systems with nonlocal (or intermediate- to long-range) coupling have received increasing attention, as nonlocal interactions are known to be relevant in diverse fields, ranging from Josephson junction arrays [4] and chemical reactions [5, 6], to several problems in Biology and Ecology [7], such as the neural networks underlying mollusk patterns [8, 9], ocular dominance stripes and hallucination patterns [10], and population dynamics [11]. A nonlocal interaction may emerge from a physical/chemical mechanism that couples points far apart in space, e.g., a long-range interaction [12], or from the adiabatic elimination of a slow variable [13, 14]. Novel phenomena emerging genuinely from nonlocality, such as power-law correlations [13, 15], multiaffine turbulence [5], and chimera states [16, 17] have been reported. Moreover, recent works have reported the effects of nonlocality on the dynamics of fronts, patterns and localized structures (LS), for instance the tilting of snaking bifurcation lines [18] and changes in the size of LS [19, 20], the effects of two-point nonlocality on convective instabilities [21], the nonlocal stabilization of vortex beams [22], or changes in the interaction between solitons [23], and in the velocity of propagating fronts [24].

Whereas in the previous Chapters 9-12, we have studied spatio-temporal dynamics of LSs in model equations having a Laplacian and a bi-Laplacian operator coupling different points in space, we will consider a general nonlocal spatial coupling in this Chapter[2]. Our main goal in this Chapter is to show the crucial relevance of nonlocality on the interaction of fronts connecting two equivalent states in one dimensional systems, as well as on the formation of LS arising from the interaction of two such fronts [25]. Interaction between two monotonic fronts is always attractive, so any domain of one state embedded in the other shrinks and disappears. However, fronts with oscillatory tails can lock at specific distances leading to stable LS. Here we show that oscillatory tails, and therefore stable LS can appear as an effect of repulsive nonlocal interactions. Repulsive (inhibitory) interactions are common, for instance, in neural field theories [9, 10] and genetic networks [26]. Our result is generic and can be qualitatively un-

[2]The nonlocal spatial coupling term acting on the field A can be expanded in a Taylor series of spatial derivatives of A:

$$\int_{-\infty}^{\infty} \theta(x-x')A(x')dx' = \delta_0 A + \delta_1 \frac{\partial}{\partial x}A + \delta_2 \frac{\partial^2}{\partial x^2}A + \delta_3 \frac{\partial^3}{\partial x^3}A + \delta_4 \frac{\partial^4}{\partial x^4}A + \dots \tag{13.1}$$

When approximating the nonlocal term by chopping of the Taylor series, as e.g. in Chapters 9-10, this is strictly speaking referred to as a local contribution.

derstood from the interplay between nonlocality, which couples both sides of the front, and repulsiveness which induces a small depression at the lower side and a small hill at the upper part. Altogether this leads to oscillatory tails as qualitatively obtained from the spatial dynamics.

13.2 The nonlocal real Ginzburg-Landau equation

A prototypical model of a spatially extended system with two equivalent steady states is the real Ginzburg-Landau equation (GLE) [3, 27]. We consider the 1D *nonlocal* real GLE

$$\frac{\partial A(x)}{\partial t} = (\mu - s)A(x) + \frac{\partial^2 A(x)}{\partial x^2} - A^3(x) + sF(x), \tag{13.2}$$

being $A(x)$ a real field and μ the gain parameter. The diffusion and the nonlinear term have been scaled to one without loss of generality. Eq. (13.2) has both a local (diffusive) and a (linear) nonlocal spatial coupling

$$F(x) = \int_{-\infty}^{\infty} \theta_\sigma(x - x')A(x')dx', \tag{13.3}$$

where θ_σ is the spatial nonlocal interaction function (or kernel) and σ indicates the spatial extension of the coupling. For the sake of simplicity, we consider here a Gaussian kernel, $\theta_\sigma(x - x') = (1/\sqrt{2\pi}\sigma)e^{-(x-x')^2/(2\sigma^2)}$, although the results presented in this work do not depend qualitatively on its precise shape, provided it is positively defined. Gaussian kernels appear in contexts such as mollusk pigmentation patterns [28], species competition [29] and Neuroscience [10, 30]. The nonlocal function $F(x)$ includes also a local contribution. This contribution is compensated for by the term $-sA(x)$, such that in the limit $\sigma \to 0$ one recovers the same results as for the local GLE. In the coming Sections, we will first discuss the linear temporal stability of the nonlocal GLE and look at its spatial dynamics. Next, the results from this stability analysis will be used to interpret large changes in the front interaction due to the nonlocal coupling.

13.2.1 Linear stability

The homogeneous steady state solutions (HSSs) A_s of Eq. (13.2) are given by

$$A_s(\mu - A_s^2) = 0. \tag{13.4}$$

Apart from the trivial zero solution $A_s = 0$, two equivalent homogeneous solutions $A_s = \pm\sqrt{\mu}$ are created in a pitchfork bifurcation at $\mu = 0$. One can notice that

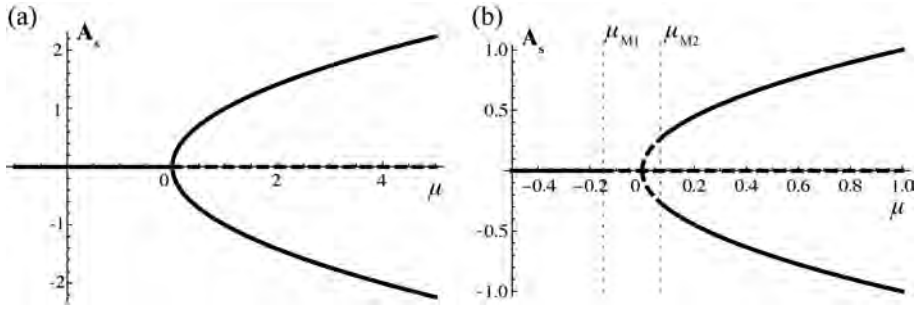

Figure 13.1: Bifurcation diagram of the homogeneous solutions A_s of the nonlocal GLE for (a) $s = 0$ (local case), (b) $s = -1$ (nonlocal case). Other parameters are: $\mu = 3$, $\sigma = 2$. Stable solution are shown in a solid line, unstable ones in a dashed line.

the HSSs are not affected by the nonlocal contribution. However, the nonlocal coupling plays an important role in the linear stability of the HSSs with respect to finite wavelength perturbations of the form $\exp(\tau t + ikx)$. The modulational instability (MI), also referred to as Turing instability, occurs when the growth rate $\tau = 0$, leading to the following marginal stability curve:

$$\tau = (\mu - s) - k^2 - 3A_s^2 + se^{-k^2\sigma^2/2} = 0. \tag{13.5}$$

In the local case ($s = 0$), one can easily verify that at $\mu = 0$ the system goes through a steady state bifurcation, creating the non-zero solutions $A_s = \pm\sqrt{\mu}$ [see Figure 13.1(a)]. For $s \neq 0$, however, Eq. (13.5) is no longer a straight line in the (k^2, τ)-plane as the exponential term comes into play, and leads to MIs where the growth rate becomes positive at finite values of the perturbation wavenumber k. As shown in Figure 13.1(b) a negative nonlocal interaction $s = -1$ introduces MIs at $\mu_{M1} = -0.15$ and $\mu_{M2} = 0.07$ where these were absent in the local case. A negative nonlocal spatial coupling thus has destabilizing effect on the HSSs, while a positive coupling further stabilizes the HSSs. The evolution of these MI points is shown in Figure 13.2. For a fixed value of the spatial extension, the MI point is given as a function of the nonlocal strength s. It is clear that increasing the (negative) nonlocal strength further destabilizes the solution.

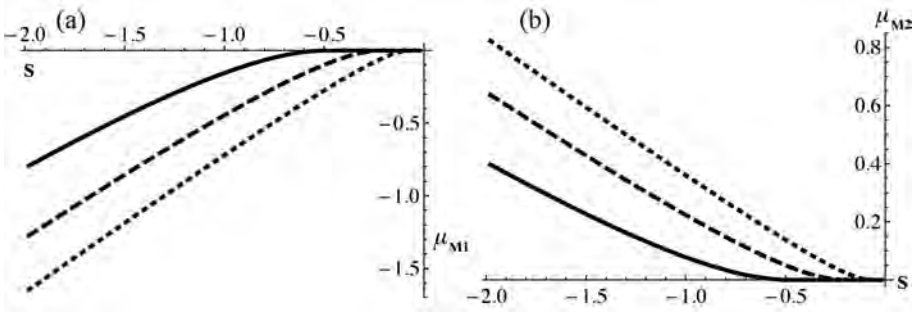

Figure 13.2: The evolution of the modulational instability points of the (a) zero homogeneous solutions and (b) of the non-zero homogeneous solutions as a function of the nonlocal strength $s < 0$. The solid, long-dashed and short-dashed lines correspond to $\sigma = 2, 3, 5$.

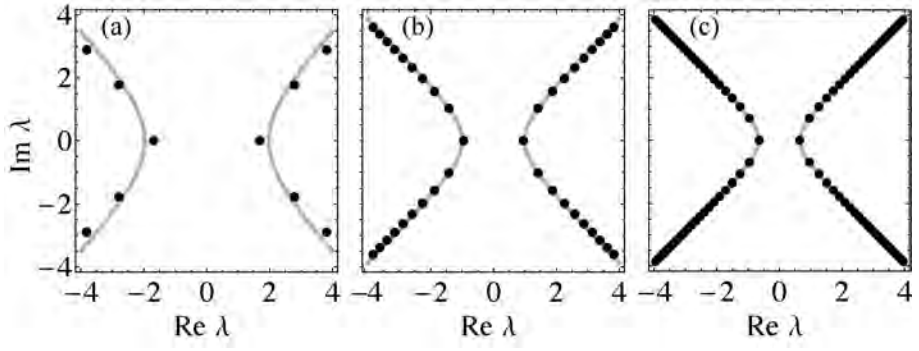

Figure 13.3: The position of the spatial eigenvalues λ of Eq. (13.6) are shown in the complex plane by the black dots. The hyperbola, given by Eq. (13.9), in greyscale represents an approximation for the position of the spatial eigenvalues. $\mu = 3$ and $s = 1$. (a) $\sigma = 1$, (b) $\sigma = 2$, (c) $\sigma = 3$.

13.2.2 Spatial dynamics

Apart from the temporal stability of the HSSs, characterizing the *spatial dynamics*[3] is another prerequisite to studying LSs in a system. Considering a spatial perturbation to the non-zero homogeneous solution of the form $A = \sqrt{\mu} + \epsilon \exp(\lambda x)$,

[3]One neglects the time derivative and takes the spatial coordinate to be the time-like evolution variable; this framework is therefore often referred to as "spatial dynamics".

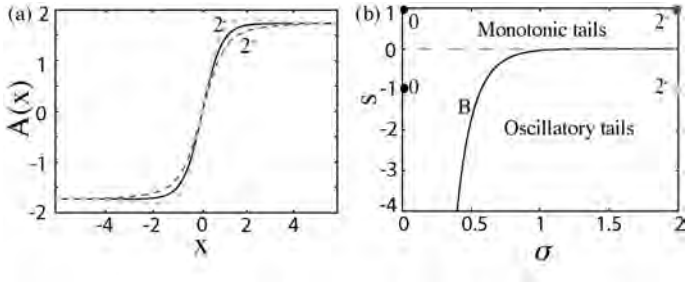

Figure 13.4: Nonlocal GLE, Eq. (13.2) with $\mu = 3$: (a) Front profiles for $s = 0$ (black line) and $s = \pm 1$ with $\sigma = 2$, labeled in the figure as $\sigma^{\mathrm{sgn}(s)}$. (b) The curve B is the boundary in the (σ, s) space between the presence of oscillatory or monotonic tails of a front.

one finds

$$-2\mu - s + \lambda^2 + se^{\lambda^2\sigma^2/2} = 0. \tag{13.6}$$

When including the nonlocal coupling term, the characteristic equation for λ has an infinite number of solutions, as a consequence of the exponential term. This is illustrated in Figure 13.3 where (a part of) the eigenvalues are shown by the dots for different values of the spatial interaction $\sigma = 1, 2, 3$ (with $\mu = 3$ and $s = 1$). The number of eigenvalues within a fixed distance to the origin heavily increases with increasing σ.
The eigenvalues come in pairs $\pm\lambda$ and appear to lie on a hyperbolic-like curve. As the exponential term will rapidly dominate the quadratic term in λ in Eq. (13.6), we try neglecting the quadratic term, an approximation that will become increasingly better for larger values of σ:

$$se^{\lambda^2\sigma^2/2} = \frac{2\mu + s}{s}. \tag{13.7}$$

This expression can be solved explicitly for λ^2, taking into account the periodicity of the complex exponential function:

$$\lambda^2 = \frac{2}{\sigma^2}(log(\frac{2\mu + s}{s}) + 2k\pi i), \tag{13.8}$$

with $k \in \mathbb{Z}$. Writing $\lambda = x + iy$, substituting this in the above equation and splitting the expression into real and imaginary parts then yields the following

system:

$$\begin{aligned} x^2 - y^2 &= \frac{2}{\sigma^2} log(\frac{2\mu}{s}), \\ xy &= \frac{2k\pi}{\sigma^2}. \end{aligned} \tag{13.9}$$

The first equation represents a hyperbola with eccentricity $\sqrt{2}$ in the complex plane. The second equation can then be seen as a sort of selection criterium, which has to be satisfied by a point on the hyperbola to be a spatial eigenvalue of the system. In Figure 13.3, the numerically calculated eigenvalues of Eq. (13.6) are shown, together with the hyperbola as given by Eq. (13.9). When $\sigma \geq 2$ it is clear that the above equation of the hyperbola provides a good approximation of the location of the spatial eigenvalues.
The shape of the front is determined by the eigenvalue λ_1 with real part closest to zero, as in the spatial dynamics all the other directions are damped faster when approaching the fixed point (homogeneous solution). Therefore, we now focus on these dominant eigenvalues. By determining where λ_1 goes from being purely real to complex, one can find the boundary B separating fronts having monotonic and oscillatory tails. As shown in Figure 13.4(b), for kernel widths σ at least as large as the front width, the front profile always shows oscillatory tails for $s < 0$ and as a consequence LSs can in principle exist. Examples of front profiles with either monotonic or oscillatory tails are shown in Figure 13.4(a). For smaller kernel widths an increasingly large nonlocal strength is needed for LSs to be formed (see line B in Figure 13.4).

13.2.3 Front interaction

Armed with the knowledge of both the temporal and the spatial stability of the HSSs in the nonlocal GLE, we can now tackle the question of how two fronts connecting equivalent states interact in the presence of a nonlocal spatial coupling. The profile of GLE fronts without nonlocality is known analytically [31], and the interaction with an opposite front located at a distance d much smaller than the front width can be calculated perturbatively, yielding the following result for the relative velocity $v(d)$ [31],

$$v(d) = \dot{d} = c\, e^{-\gamma d}\,, \tag{13.10}$$

with $c = -24\sqrt{2\mu}$ and $\gamma = \sqrt{2\mu}$. The nonlocal effects in front dynamics can be quantified by looking at the deviations from the interaction given by Eq. (13.10), stemming solely from a local interaction coupling. Therefore we have studied the front velocity $v(d)$ for different kernel widths σ keeping all other parameters

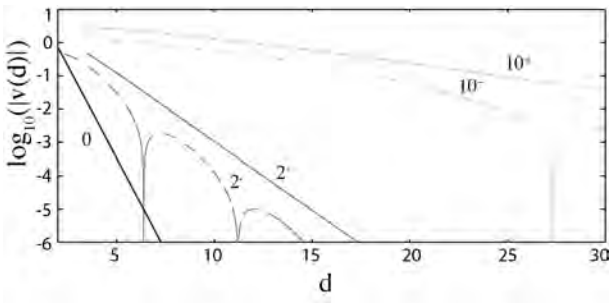

Figure 13.5: Front velocity as a function of d. $\mu = 3, |s| = 1$, and σ is taken to be 0 , 2 and 10, depicted in the figure as $\sigma^{\mathrm{sgn}(s)}$.

fixed and taking the system size much larger than σ. The results are plotted in Figure 13.5[4]. The *local* case, Eq. (13.10), is the straight line labeled with 0 (as $\sigma = 0$). In the nonlocal case ($\sigma \neq 0$), a large qualitative difference in behavior is observed depending on the sign of s.

As shown in Figure 13.5, for an attractive (activatory) interaction ($s > 0$), the logarithm of the velocity decreases linearly with the distance, such that the exponential dependence of the velocity with the distance given by Eq. (13.10) still holds with an effective γ whose value is strongly reduced by the nonlocality. As a consequence the range of spatial interaction, $1/\gamma$, increases with the kernel width σ. Even for moderate values of σ, fronts move several orders of magnitude faster than for the local GLE. Figure 13.6 shows the change of the value of the effective exponent γ as a function of σ. Moreover, the inset shows that γ, to a very good extent, follows a linear dependence with the inverse of the kernel width σ, provided that σ is at least as large as the front width. Therefore, we can conclude that rescaling γ to γ/σ the effective interaction between two fronts follows a universal exponential law (except for a small dependence on the strength of interaction s). It is interesting to notice, however, that the width of the front, defined by the half width at half the maximum (HWHM) does not show this scaling with $1/\sigma$ cf. Figure 13.4(a). Thus, the effect of the nonlocality does not amount to a mere rescaling of the spatial coordinate. This can be understood by noticing that while the general shape of the front is mainly dominated by the local, diffusive, coupling, in turn the nonlocal coupling modifies substantially the exponential tails, which are responsible of the long-range interaction that influences the front velocity.

For $s < 0$, i.e., for a repulsive (inhibitory) interaction, the exponential law, Eq.

[4] An explanation of the numerical integration scheme that we use can be found in Appendix B.

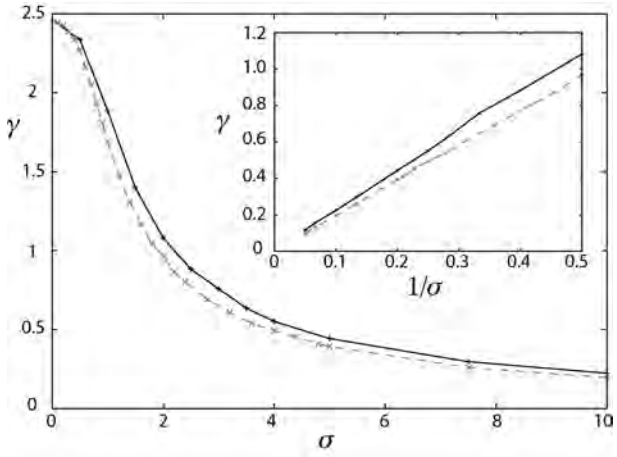

Figure 13.6: γ as a function of σ. Inset: γ as a function of $1/\sigma$. The black solid, dark grey dashed and light grey dashed curves have $\mu = 3$, and $s = 0.5$, 1, and 2, respectively.

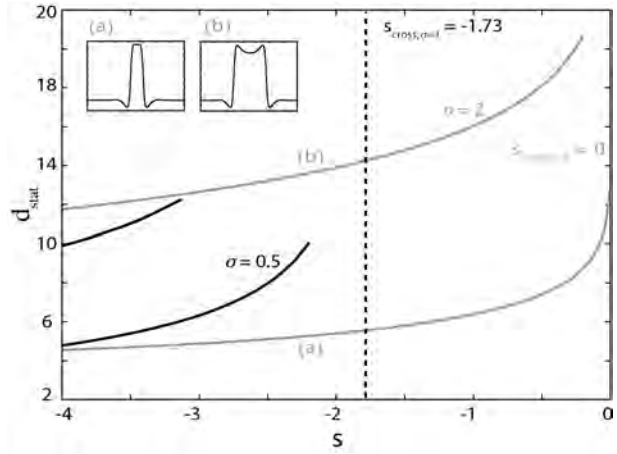

Figure 13.7: Stationary widths of stable localized structures for the nonlocal GLE ($\mu = 3$). Black (grey) line corresponds to $\sigma = 0.5$ ($\sigma = 2$). Insets show examples of localized structure profiles for $\sigma = 2$. $s_{cross,\sigma}$, given by line B in Figure 13.4, indicates the point where the spatial eigenvalues go from being complex conjugate to purely real.

(13.10), no longer holds. Nevertheless, the magnitude of the envelope of the front velocity is still dominated qualitatively by (13.10), as shown in Figure 13.5. In this case, the velocity becomes zero at regular intervals of the distance d between two fronts. This qualitative difference is not unexpected as our study of the spatial eigenvalues of the non-zero HSSs showed that for $s < 0$ oscillatory tails appear (see Figure 13.4). Therefore, at the positions of zero velocity the fronts are locked leading to the formation of LSs. This can be seen in Figure 13.7 where the stationary widths of stable LSs are shown for the nonlocal GLE with $\mu = 3$. The black and grey line correspond to $\sigma = 0.5$ and $\sigma = 2$, respectively. The insets show examples of LS profiles for $\sigma = 2$. One can see that the branches of LSs for a larger spatial interaction $\sigma = 2$ are created immediately for a minimal interaction strength s, while the LSs with a smaller $\sigma = 0.5$ seem to require a larger interaction strength s to come into existence. This behavior is confirmed by the value $s_{cross,\sigma}$, given by line B in Figure 13.4, indicating the point where the spatial eigenvalues go from being complex conjugate to purely real. These LSs, not present in the GLE are thus closely related to the creation of a MI of the non-zero HSSs due to the repulsive nonlocal interaction. The combination of temporal linearly stable HSSs and oscillatory tails provide all necessary ingredients for LSs to exist.
To describe the interaction of fronts with oscillatory tails Eq. (13.10) must be modified. An appropriate ansatz is the following:

$$v = \dot{d} = c\cos[\zeta(s,\sigma)d]e^{-\gamma(s,\sigma)d}\,, \tag{13.11}$$

where $\zeta(s,\sigma)$ is determined by the complex part of the most underdamped spatial eigenvalue of Eq. (13.6), such that $\zeta = 0$ in the region of monotonic tails. Eq. (13.11) adequately describes the dependence of the velocity with the distance indicated in Figure 13.5.

13.2.4 Influence of the nonlocal kernel

For the sake of simplicity, we have considered up to now a Gaussian kernel to describe the nonlocal spatial interaction. We have verified that the results presented above do not depend qualitatively on the precise shape of the kernel, provided it is positively defined.
In this Section, we shortly discuss the effects of a qualitatively different kernel: the mexican-hat shaped kernel [see Figure 13.8(b)]. Up to a scaling factor, it is related to the second derivative of the Gaussian function and we will use it in the following form as our nonlocal kernel:

$$\theta(x) = \sqrt{\frac{2}{\pi}}(1 - \frac{x^2}{2\sigma^2})e^{\frac{x^2}{2\sigma^2}}, \tag{13.12}$$

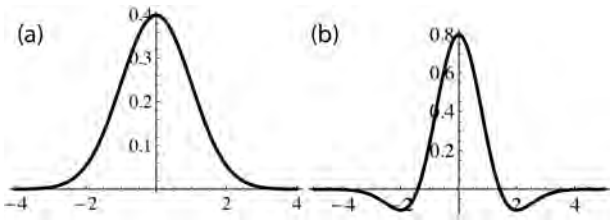

Figure 13.8: Examples of a (a) Gaussian shaped and a (b) mexican-hat shaped nonlocal kernel. $\sigma = 1$.

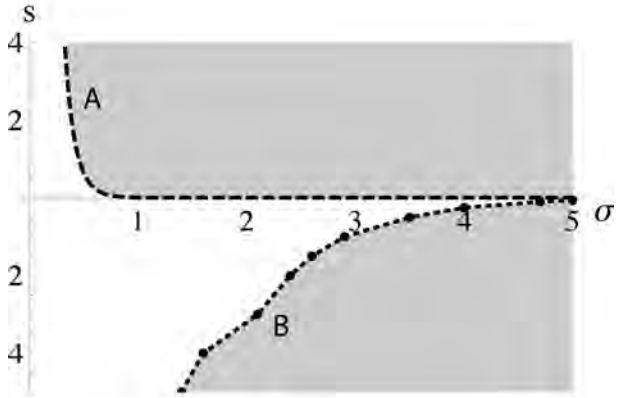

Figure 13.9: Boundaries in the (σ, s)-plane separating the regions of monotonic and oscillatory tails when using a mexican-hat shaped kernel.

where σ is again a measure for the spatial interaction width. Unlike the Gaussian kernel shown in Figure 13.8(a), the mexican-hat shaped kernel does not have the same sign over the entire spatial domain that is considered. In view of the important influence of having either repulsive or attractive interactions as discussed in the previous Sections, it is all but obvious that the mexican-hat shaped kernel would show similar results.

One can repeat the stability analysis of Sections 13.2.1-13.2.2 again by replacing terms of the form $\exp[x^2/(2\sigma^2)]$ by $(1 - \lambda^2\sigma^2)\exp[x^2/(2\sigma^2)]$. Rather than repeating this analysis entirely, we limit ourselves to looking into the influence of the mexican-hat shape on the location in the (s, σ)-plane of the boundary separating the monotonic tails from the oscillatory tails. The result of this analysis is shown in Figure 13.9. The upper boundary A is calculated by determining the point

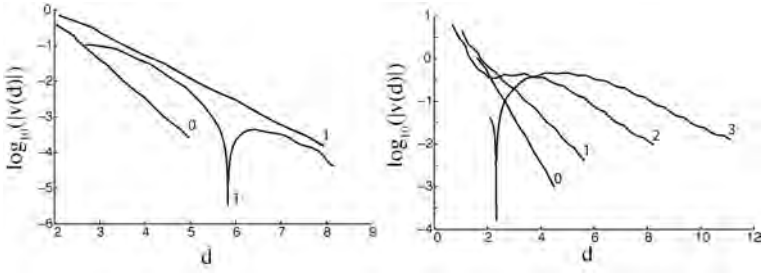

Figure 13.10: Front velocity as a function of the width d for a mexican-hat shaped kernel. $\mu = 3, |s| = 1$, and σ is taken to be 0, 1, 2 and 3, depicted in the figure as $\sigma^{\mathrm{sgn}(s)}$.

where the dominant spatial eigenvalues go from being complex conjugate to purely real. One can notice that this boundary is now flipped with respect to the Gaussian kernel case (see Figure 13.4). As this boundary lies now in the upper half plane, a transition from monotonic to oscillatory tails now occurs by increasing the positive nonlocal interaction strength s. However, when increasing the negative interaction strength $-s$ one can now also observe transition from monotonic to oscillatory tails. In this region, it is interesting to see that the dominant eigenvalue is still real, such that one would in principle expect monotonic tails. Due to other complex conjugate eigenvalues that acquire a real part very close — yet still larger — to the dominant eigenvalue oscillatory tails are created at the lower boundary B[5].

In Figure 13.10 the front velocity is shown as a function of the width d for a mexican-hat shaped kernel with $\mu = 3$ and $|s| = 1$. When taking $\sigma = 1$ and $s = -1$, it is clear that a similar exponential law Eq. (13.10) holds. For comparison the front velocity in the local case $\sigma = 0$ is also shown. Increasing the interaction strength s from -1 to 1, one can see that for values of s such that one crosses the line A in Figure 13.9 LSs come into existence. Hence, at certain widths d the front velocity becomes zero. Taking again $s = -1$, but now increasing the spatial interaction length σ from 0 to 3, one notices that the exponential law starts to break down as one approaches the boundary B in Figure 13.9. When crossing the line B, oscillatory tails are created and corresponding LSs are consequently created as well.

In summary, for the real GLE one finds an enhancement of the interaction due to nonlocality independent of the kernel shape, leading to the appearance of oscil-

[5]The boundary line B is determined by numerical time evolution simulations instead of calculations of the spatial eigenvalues.

latory tails and LSs for a repulsive interaction and increase of the front velocity if the interaction is attractive. In the next Section, we check the generality of these findings for the Parametrically forced complex Ginzburg Landau Equation (PCGLE) whose fronts show oscillatory tails already in the local case and form LSs [32, 33].

13.3 The nonlocal Parametrically forced complex Ginzburg Landau Equation

The parametrically forced complex Ginzburg Landau Equation (PCGLE) is the generic amplitude equation for oscillatory systems parametrically forced at twice the natural frequency [34]. The nonlocal version of the PCGLE can be written as:

$$\begin{aligned}\frac{\partial A(x)}{\partial t} = (1+\mathrm{i}\alpha)\frac{\partial^2 A(x)}{\partial x^2} + [(\mu+\mathrm{i}\nu) - se^{\mathrm{i}\phi_s}]A(x) \\ -(1+\mathrm{i}\beta)|A(x)|^2 A(x) + pA^*(x) + se^{\mathrm{i}\phi_s}F(x),\end{aligned} \tag{13.13}$$

where μ measures the distance from the oscillatory instability threshold, ν is the detuning between the driving and the natural frequencies, $p > 0$ is the forcing amplitude, α and β represent the linear and nonlinear dispersion. The term $se^{\mathrm{i}\phi_s}F(x)$ describes the nonlocal response of the material taking the same form as in the study of the GLE (13.3). Here we consider $s > 0$ with $\phi_s = 0$ and $\phi_s = \pi$ in correspondence with attractive and repulsive interactions discussed previously. Again, the linear contribution has been compensated in the term $-se^{\mathrm{i}\phi_s}A(x)$.

13.3.1 Linear stability

We start by studying the linear stability of the HSSs A_s of Eq. (13.13), as we did for the nonlocal GLE in Section 13.2.1. Writing $A_s = Re^{i\phi}$ allows to separate the real and imaginary component of this equation. Besides the trivial zero solution $R = 0$, a second non-zero solution exists and is given by:

$$\begin{aligned}(\beta R^2 - \nu)\cos\phi + (p + R^2 - \mu)\sin\phi &= 0 \\ (p - R^2 + \mu)\cos\phi + (\beta R^2 - \nu)\sin\phi &= 0\end{aligned} \tag{13.14}$$

An expression for R can easily be found by solving the first equation for $\tan\phi$ and substituting this in the second equation:

$$R^2 = \frac{\mu + \beta\nu + \pm\sqrt{p^2(1+\beta^2) - (\nu - \beta\mu)^2}}{1+\beta^2}. \tag{13.15}$$

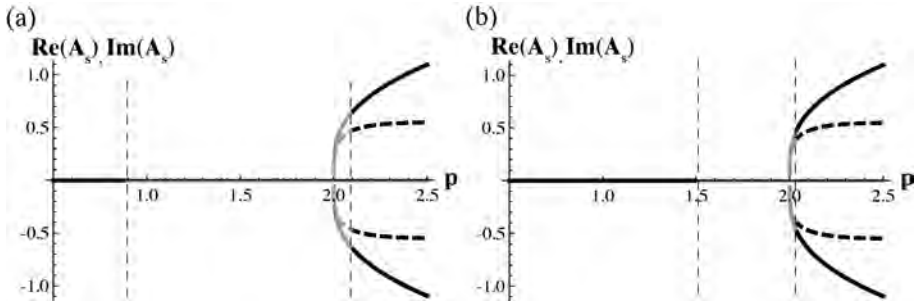

Figure 13.11: Bifurcation diagram of the homogeneous solutions A_s of the nonlocal PCGLE for (a) $s = 0$ (local case), (b) $s = 1$ (nonlocal case). Other parameters are: $\alpha = 0$, $\beta = 0$, $\mu = 0$, $\nu = 2$, $\sigma = 2$, $\phi_s = 0$. Stable solution are shown in a black line, unstable ones in a grey line. The real part of A_s is depicted by the solid line and the imaginary part of A_s by the dashed line.

From R and ϕ, the real and imaginary part of A_s can be easily calculated. In Figure 13.11, the homogeneous solutions A_s are shown for a parameter set such that two equivalent non-zero solutions are born, like in the GLE (13.2), in a pitchfork bifurcation at $\sqrt{\mu^2 + \nu^2}$. In the remainder of this Section, we will work with the same parameter set as in Figure 13.11 and only study the effect of the nonlocal parameters (s, ϕ_s, σ).[6]
In order to gain insight into the influence of the nonlocal coupling term on the temporal stability of the HSSs A_s, we study the linear stability of the HSSs with respect to perturbations $a(t)$ of the form

$$A(x,t) = A_s + a(t)e^{ikx}. \tag{13.16}$$

Opposite to the local GLE (13.2), the local version of the PCGLE already has two MI points destabilizing the HSSs as shown in Figure 13.11(a). When adding the nonlocal term one can see in Figure 13.11(b) that the MI points shift. A more detailed analysis of how the MI point shift in function of the nonlocal parameters (s, ϕ_s, σ) is summarized in Figure 13.12. As in the case of the nonlocal GLE, an increase in the coupling strength s and in the kernel width σ lead to a stronger shift in the MI points. More interestingly, one now observes a large influence of the coupling phase ϕ_s [see Figure 13.12(c),(f)]. The HSSs are most strongly destabilized for a coupling phase $\phi_s \approx \pi$, similar as in the case of negative interaction terms in the GLE (13.2), while the HSSs are stabilized most strongly

[6] For different parameter sets of the PCGLE, the non-zero solutions can originate e.g. in a subcritical bifurcation. We refer to Ref. [35] for a complete study of the local PCGLE.

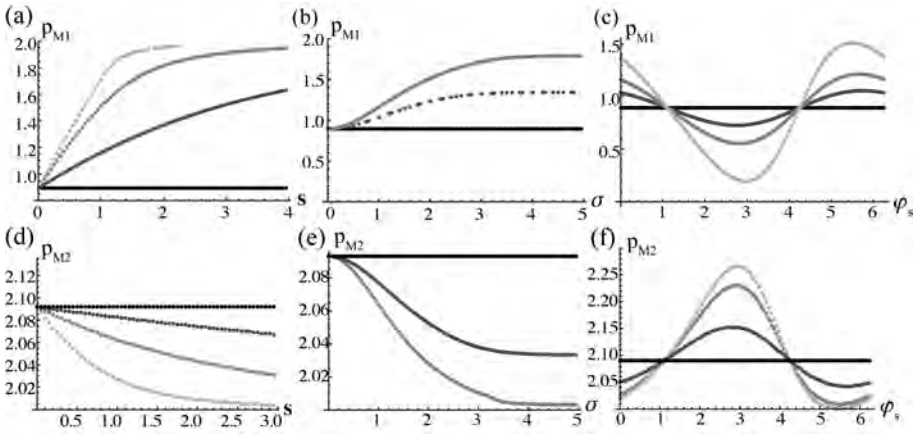

Figure 13.12: The evolution of the modulational instability points of the (a)-(c) zero homogeneous solutions and (d)-(f) of the non-zero homogeneous solutions. The evolution as a function of the nonlocal strength s is shown in (a),(d). $\phi_s = 0$ and σ increases from black to light grey. In (a): $\sigma = 0, 1, 2, 3$, while in (d) $\sigma = 0, 0.5, 1, 2$. The evolution of the modulational instability points as a function of σ for $\phi_s = 0$ is shown in (b),(e). s increases from black to light grey: $s = 0, 0.5, 1$. The evolution of the modulational instability points as a function of ϕ_s is shown in (c),(f). σ increases from black to light grey: $s = 0, 0.5, 1, 2$ (c), $s = 0, 0.5, 1, 1.2$ (f).

for coupling phases around $\phi_s = 0$. The behavior for intermediate values of ϕ_s is exemplified in Figure 13.12(c),(f).

13.3.2 Spatial dynamics

In Section 13.2.2, we have demonstrated for the nonlocal GLE (13.2) that the MI points introduced by the nonlocal coupling also had a big influence on the spatial dynamics of the system. More in particular, oscillatory tails were created leading to the formation of LSs, not present in the local case. As now the HSSs in the local version of the PCGLE already contain MI points, it is natural to ask ourselves whether the shift of the MI points due to nonlocality also have a large impact on the LSs present in the system.
Figure 13.13 shows the width of the stable LSs locked at the first and second oscillations as a function of the nonlocal strength s. The insets show the LS spatial profile. Whereas in the real GLE, LSs existed only for $s < 0$ (see Figure

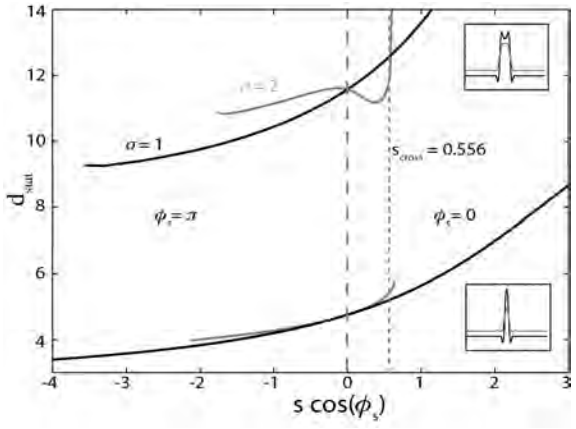

Figure 13.13: Stationary widths of stable LS for $\alpha = 1$, $\beta = 0$, $\mu = 0$, $\nu = 2$ and $p = 2.7$. $\sigma = 1$ (black line) and 2 (grey line). Insets show the transverse profile of the LS.

13.7), in the PCGLE, LSs also exist for a finite range of positive values of $s\cos(\phi_s)$ ($\phi_s = 0$). This is shown in Figure 13.13 for $\sigma = 2$ where the bifurcation branch abruptly ends around $s_{cross} = 0.556$. This can be understood by studying the spatial eigenvalues of the system.

In this case there are two pairs of complex conjugate eigenvalues with small real part λ_l and λ_{nl} which play a relevant role. Figure 13.14(a) shows the dependence of the real and imaginary parts of these two eigenvalues for $\sigma = 1.3$ and 2 as a function of s. For small s the spatial dynamics is dominated by λ_l, the eigenvalue already present in the local case. Increasing s the real part of this eigenvalue becomes slightly larger while the real part of λ_{nl} clearly decreases. For $\sigma = 2$, the real part of the two eigenvalues crosses at $s_{cross} = 0.556$. Beyond that value the spatial dynamics is governed by λ_{nl} whose corresponding spatial length scale [Im(λ_{nl})] is an order of magnitude larger than the one corresponding to λ_l. As a result, the branch of LS experiences dramatic sharpening in Figure 13.13, as the LS broaden with an order of magnitude. Figure 13.14(b) shows the locus of the crossing point in the (σ, s) plane for $\phi_s = 0$. For large values of σ, the crossing point moves towards $s = 0$, while for $\sigma < 1.43$ the crossing never takes place and the spatial dynamics is always dominated by λ_l.

For $\phi_s = \pi$, nonlocality only modifies slightly the preexisting oscillatory tails of the PCGLE. The branches of LS end for negative values of $s\cos(\phi_s)$ close to the modulational instability point of the background states (that for $\sigma = 2$ is at $s\cos(\phi_s) \sim -3$). This MI point, that was originated by the nonlocality in the GLE,

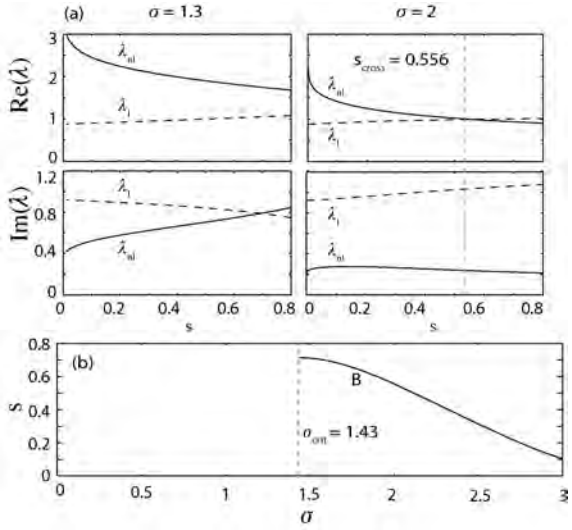

Figure 13.14: (a) Dependence of the absolute value of the real and imaginary parts of the two dominant complex quartets of spatial eigenvalues in the nonlocal PCGLE for $\sigma = 1.3$ and $\sigma = 2$ as a function of s. Other parameters as in Figure 13.13. (b) The curve B depicts the locus in the (σ, s) plane of the points where the absolute values of the real parts of λ_l and λ_{nl} cross.

is already present in the local form of the PCGLE but is enhanced by the nonlocal interactions.

13.3.3 Nonlocal effects in two spatial dimensions

To demonstrate the impact of nonlocality on the dynamics of a more broad class of systems, we turn to the PCGLE in two spatial dimensions. In this case, in general, the front dynamics is governed by curvature effects and it has been shown, both experimentally and theoretically, that the evolution of the radius R of a circular domain wall can be described by [25, 32]:

$$v = \dot{R} = c\cos[\zeta(\phi_s, s, \sigma)R]e^{-\gamma(\phi_s,s,\sigma)R} - \eta_1\frac{1}{R} - \eta_3\frac{1}{R^3}\,. \tag{13.17}$$

In principle one could expect that the reduction of the exponent γ due to the nonlocal interactions would also have implications for the 2D structures, but

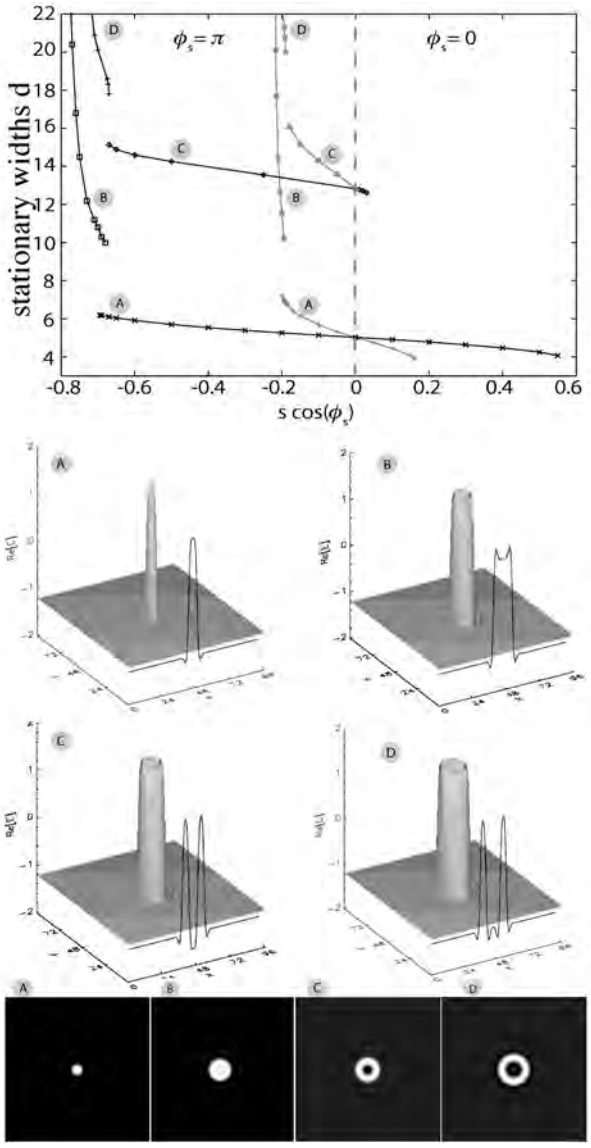

Figure 13.15: The stationary widths of several stable two-dimensional localized structures are depicted for $\alpha = 1$, $\beta = 0$, $\mu = 0$, $\nu = 2$ and $p = 2.7$ for varying values of the nonlocal strength s and this for $\sigma = 1$ (black line) and 2 (grey line). All results have been obtained with temporal numerical simulations.

the dynamics of fronts in 2D is mainly dominated by the curvature, whose intensity decreases much slower ($1/R$) than the exponential, no matter what the value of γ is. We do observe however that the nonlocal coupling affects also the intensity of the curvature η_1. This is demonstrated in Figure 13.15, where the stationary widths of several stable 2D LSs are depicted for varying values of the nonlocal strength s and for $\sigma = 1$ (black line) and $\sigma = 2$ (grey line). All results have been obtained with temporal numerical simulations. For positive values of $s\cos(\mathrm{i}\phi_s)$ we observe the disappearance of LSs much faster than in the 1D case (see Figure 13.13). This is so not because of changes in the front profile or γ, but in the value of η_1, which increases with the strength and range of the nonlocality, overcoming any locking due to tail interactions. For negative values of $s\cos(\mathrm{i}\phi_s)$, η_1 decreases and even changes sign, leading to the formation of large stable droplets due to higher order curvature effects [32]. This phenomenon is associated to the MI of the background mentioned above and enhanced by the nonlocality. We conjecture that a similar change of sign of η_1 occurs in the 2D nonlocal GLE for negative values of s. Otherwise, in the local GLE η_1 is always positive and LSs do not exist in two spatial dimensions.

13.4 Conclusion

In conclusion, we have demonstrated the large impact of a linear nonlocal term on the interaction of fronts connecting two equivalent states. The most striking result is the possibility of obtaining a novel class of self-organized stable localized structures in systems exhibiting fronts with no tails, like the real Ginzburg-Landau equation. This is achieved through a nonlocal repulsive interaction that modifies the profile of the fronts introducing or damping out oscillations. In addition, we have observed an order of magnitude increase of the front velocity due to an enhancement of the interaction between two fronts. Finally we have shown that nonlocal interactions can also smooth out the front oscillations greatly increasing their wavelength such that the localized states become much wider and eventually disappear.

The characterization of the effects of nonlocal coupling on the front properties and dynamics can allow the identification, from both theoretical and experimental data, of different sources of nonlocality. For instance, domain walls have long been studied in photorefractive media [36, 37], which have a large nonlocal response, but its effects on the front dynamics have never been identified. Nonlocal interactions are also common in Biology, Chemistry, and other fields, and they can have a constructive role by enhancing the propagation of information between distant parts of the system.

References

[1] L. Gelens, D. Gomila, G. Van der Sande, M. Matías, and P. Colet, "Nonlocality induced front interaction enhancement," *Phys. Rev. Lett.* **104**, 154101, 2010.

[2] Y. Kuramoto, *Chemical Oscillations, Waves and Turbulence*, Springer Series in Synergetics, 3rd edition, Berlin, 1984.

[3] M. Cross and P. Hohenberg, "Pattern formation outside of equilibrium," *Rev. Mod. Phys.* **65**, 186–206, 1993.

[4] J. Phillips, C. Pérez-Vicente, F. Ritort, and J. Soler, "Influence of induced magnetic fields on the static properties of josephson-junction arrays," *Phys. Rev. B* **47**, 5219–5229, 1993.

[5] Y. Kuramoto, D. Battogtokh, and H. Nakao, "Multiaffine chemical turbulence," *Phys. Rev. Lett.* **81**, 3543–3546, 1998.

[6] S.-I. Shima and Y. Kuramoto, "Rotating spiral waves with phase-randomized core in nonlocally coupled oscillators," *Phys. Rev. E* **69**, 036213, 2004.

[7] J. Murray, *Mathematical Biology*, Springer (3rd edition), New York, 2002.

[8] B. Ermentrout, J. Campbell, and G. Oster, "A model for shell patterns based on neural activity," *The Veliger* **28**, 369, 1986.

[9] S. Coombes, "Waves, bumps, and patterns in neural field theories," *Biological Cybernetics* **93**(2), 91–108, 2005.

[10] B. Ermentrout, "Neural networks as spatio-temporal pattern-forming systems," *Rep. Prog. Phys* **61**, 353, 1998.

[11] E. Hernández-García and C. López, "Clustering, advection, and patterns in a model of population dynamics with neighborhood-dependent rates," *Phys. Rev. E* **70**, 016216, 2004.

[12] P. Pedri and L. Santos, "Two-dimensional bright solitons in dipolar Bose-Einstein condensates," *Phys. Rev. Lett.* **95**, 20404, 2005.

[13] Y. Kuramoto, "Scaling behavior of turbulent oscillators with nonlocal interaction," *Prog. Theor. Phys.* **94**, 321, 1995.

[14] D. Tanaka and Y. Kuramoto, "Complex Ginzburg-Landau equation with nonlocal coupling," *Phys. Rev. E* **68**, 026219, 2003.

[15] Y. Kuramoto and H. Nakao, "Complex Ginzburg-Landau equation with nonlocal coupling," *Phys. Rev. Lett.* **76**, 4352, 1996.

[16] D. Abrams and S. Strogatz, "Chimera states for coupled oscillators," *Phys. Rev. Lett.* **93**, 174102, 2004.

[17] G. Sethia, A. Sen, and F. M. Atay, "Clustered chimera states in delay-coupled oscillator systems," *Phys. Rev. Lett.* **100**, 144102, 2008.

[18] W.J.Firth, L. Columbo, and A. Scroggie, "Proposed resolution of theory-experiment discrepancy in homoclinic snaking," *Phys. Rev. Lett.* **99**, 104503, 2007.

[19] L. Gelens, G. Van der Sande, P. Tassin, M. Tlidi, P. Kockaert, D. Gomila, I. Veretennicoff, and J. Danckaert, "Impact of nonlocal interactions in dissipative systems: towards minimal-sized localized structures," *Phys. Rev. A* **75**(6), 063812, 2007.

[20] L. Gelens, D. Gomila, G. Van der Sande, J. Danckaert, P. Colet, and M. Matías, "Dynamical instabilities of dissipative solitons in nonlinear optical cavities with nonlocal materials," *Phys. Rev. A* **77**, 033841, 2008.

[21] R. Zambrini and F. Papoff, "Convective instability induced by nonlocality in nonlinear diffusive systems," *Phys. Rev. Lett.* **94**, 243903, 2005.

[22] S. Skupin, M. Saffman, and W. Krolikowski, "Nonlocal stabilization of nonlinear beams in a self-focusing atomic vapor," *Phys. Rev. Lett.* **98**, 263902, 2007.

[23] A. Dreischuh, D. Neshev, D. Petersen, O. Bang, and W. Krolikowski, "Observation of attraction between dark solitons," *Phys. Rev. Lett.* **96**, 042901, 2006.

[24] M. Maruvka and M. Shnerb, "Nonlocal competition and front propagation in branching-coalescence systems," *Phys. Rev. E* **75**, 042901, 2007.

[25] M. Pesch, W. Lange, D. Gomila, T. Ackemann, W. Firth, and G.-L. Oppo, "Two-dimensional front dynamics and spatial solitons in a nonlinear optical system," *Phys. Rev. Lett.* **99**, 153902, 2007.

[26] U. Alon, *An Introduction to Systems Biology : Design Principles of Biological Circuits*, Chapman & Hall/CRC, Boca Raton, FL, 2007.

[27] I. Aranson and L. Kramer, "The world of the complex Ginzburg-Landau equation," *Rev. Mod. Phys.* **74**, 99–143, 2002.

[28] A. Boettiger, B. Ermentrout, and G. Oster, "The neural origins of shell structure and pattern in aquatic mollusks," *Proc. Natl. Acad. Sci. USA* **106**, 6837, 2009.

[29] E. Hernández-García, C. López, S. Pigolotti, and K.H.Andersen, "Species competition: coexistence, exclusion and clustering," *Phil. Trans. R. Soc. A* **367**, 3183–3195, 2009.

[30] B. Hellwig, "A quantitative analysis of the local connectivity between pyramidal neurons in layers 2/3 of the rat visual cortex," *Biol. Cybern.* **82**, 111, 2000.

[31] P. Coullet, C. Elphick, and D. Repaux, "Nature of spatial chaos," *Phys. Rev. Lett.* **58**, 431, 1987.

[32] D. Gomila, P. Colet, G. Oppo, and M. S. Miguel, "Stable droplets and growth laws close to the modulational instability of a domain wall," *Phys. Rev. Lett.* **87**, 194101, 2001.

[33] A. Yochelis, J. Burke, and E. Knobloch, "Reciprocal oscillons and nonmonotonic fronts in forced nonequilibrium systems," *Phys. Rev. Lett.* **97**, 254501, 2006.

[34] P. Coullet, J. Lega, B. Houchmandzadeh, and J. Lajzerowicz, "Breaking chirality in nonequilibrium systems," *Phys. Rev. Lett.* **65**, 1352, 1990.

[35] J. Burke, A. Yochelis, and E. Knobloch, "Classification of spatially localized oscillations in periodically forced dissipative systems," *SIAM J. Appl. Dyn. Syst.* **7**, 651–711, 2008.

[36] V. Taranenko, K. Staliunas, and C. Weiss, "Pattern formation and localized structures in degenerate optical parametric mixing," *Phys. Rev. Lett.* **81**, 2236, 1998.

[37] A. Esteban-Martin, V. Taranenko, J. Garcia, E. Roldan, and G. De Valcarcel, "Experimental characterization of domain walls dynamics in a photorefractive oscillator," *Appl. Phys. B* **85**, 117, 2006.

CHAPTER 14

Conclusions to part II

In the second part of this thesis, we have studied emergent structures in spatially-extended systems. We have focused our attention on non-equilibrium systems that are internally dissipative and externally driven. Emergent structures are patterns that appear spontaneously due to the interaction of each part with its immediate surroundings in space. Such patterns do not exist if the various parts are simply coexisting. Therefore, the presence and nature of the spatial coupling between the interacting parts is essential. We have presented an investigation of the formation and dynamics of spatially localized structures, which are emergent structures where one state is "embedded" in a background consisting of a different state. Such spatially localized structures in systems out of equilibrium are also referred to as *dissipative solitons* (DSs). DSs are commonplace and have been shown to arise in a wide variety of pattern forming systems, such as e.g. chemical reactions, neural systems, granular media, binary-fluid convection, vegetation patterns and nonlinear optics. We have studied different types of DSs in several relevant model equations admitting DS solutions: the Lugiato-Lefever equation, the Swift-Hohenberg equation and the Ginzburg-Landau equation. Whereas the Lugiato-Lefever equation has been specifically derived to model the mean electric field in a nonlinear optical cavity, the Swift-Hohenberg equation and the Ginzburg-Landau equation are generic amplitude equations that describe the universal behavior of a system near a bifurcation point.
In the case of photonics, due to recent advances in the fabrication of metamaterials and photonic crystal fibers, it is now possible to conceive nonlinear systems that allow for diffraction and/or dispersion management. In the case of low diffraction and/or dispersion, higher order spatial/temporal effects have to be

taken into account as well. In **Chapter 9**, we have investigated the snaking behavior of one-dimensional bright and dark DSs in a nonlinear optical cavity with diffraction and/or dispersion compensation. Such structures are also called cavity solitons. A stability analysis of a Lugiato-Lefever equation with fourth-order spatial derivatives has been carried out, which has shown that the higher order spatial contribution can stabilize the system under certain conditions. The existence and the snaking bifurcation structure of both bright and dark DSs has been studied in the presence of a subcritical modulational instability towards patterns, evaluating the influence of the higher order spatial derivatives. A stabilization of dark DSs has been demonstrated and a "classical' homoclinic snaking structure has been shown to exist for these dark cavity solitons in the monostable regime, while in the bistable regime a more involved snaking structure has been observed. The bright cavity solitons are organized in intricate stacks of isolas. We have cautiously alluded to the possibility that the creation of stacks of such isolas is attributed to the interplay of two distinct wave numbers in the system, created at the first modulational instability of the homogeneous solution. A more careful analysis is needed, however, in order to elucidate the more complex snaking structure observed for bright DSs and dark DSs.
In **Chapter 10**, we have studied the nonlinear dynamical behavior of two-dimensional cavity solitons in the same Lugiato-Lefever equation with higher order spatial derivatives. Our study has confirmed the possibility to reduce the size of cavity solitons beyond the diffraction limit by using diffraction compensation techniques. However, we have revealed that higher order spatial interactions not only hinder this size reduction, but also alter the stability of cavity solitons in a manifest way, imposing a new limit on their size. We have unveiled the existence of regions with stationary, oscillating and excitable DSs. Furthermore, we have shown that the different bifurcation lines originate from two Takens-Bogdanov codimension-2 points, which is a strong signature for the presence of a homoclinic bifurcation. This homoclinic bifurcation offers a route to the excitable behavior of the two-dimensional DSs. Moreover, two other regimes have been uncovered: one region of tristability and one of conditional excitability.
In **Chapter 11**, we have presented an in-depth study of the complex Swift-Hohenberg equation with real coefficients. The Swift-Hohenberg equation was shown to admit phase-winding solutions in which the real and imaginary parts of the order parameter oscillate periodically in space but with a constant phase difference between them. Such solutions can be unstable to a long-wave instability. We have demonstrated that, depending on the parameters of the equation, the evolution of this instability may or may not conserve phase. In the former case the system undergoes slow coarsening, while in the latter it undergoes repeated phase-slips leading either to a stable phase-winding state or to a faceted

state consisting of an array of frozen defects connecting phase-winding states with equal and opposite phase. When the intrinsic wave number in the system is small, numerical simulations have revealed coarsening dynamics. A theoretical analysis of the stability of the zero phase gradient state with respect to long wavelength perturbations have shown that the observed coarsening is described by the Cahn-Hilliard equation for the perturbation phase gradient. For a larger characteristic wave number in the system, numerical simulations of the complex Swift-Hohenberg equation have revealed the formation of defects that shift the wavenumber of the phase-winding state towards increased stability, behavior that is familiar from existing studies of the Eckhaus instability. We have quantified the parameter regimes where this type of evolution leads to stable phase-winding states and where the final state consists of two or more time-independent defects. The resulting phase defects are reflected as DSs in the amplitude of the complex field as well. In future work, we will confront these predictions with direct numerical simulations of the Maxwell-Bloch equations for lasers or the equations modeling non-degenerate optical parametric oscillators, as these sets of equations can been reduced to the complex Swift-Hohenberg equation.

Chapter 12 offers an expansion of the study of the complex Swift-Hohenberg in Chapter 11 by allowing the coefficients to be complex. This breaks the variational structure of the model equation and leads to time-dependent solutions. The phase-winding states are replaced by traveling wave solutions. The nonlinear dynamical behavior of these traveling waves has been explored in parameter space uncovering a great complexity. Similar behavior as in the (coupled) complex Ginzburg-Landau equation has been observed, such as e.g. stationary or drifting source-sink pairs, spatio-temporal intermittency, bimodal chaos, time-periodic coherent structures and turbulence. However, other dynamical behavior has also been uncovered, which to the best of our knowledge has not been observed in other systems. An example of such behavior was given by the presence of a stable stationary sink and a chaotic source, where the sink was destroyed at certain times to be recreated at another random position. We have derived a convective Cahn-Hilliard type equation to describe the evolution of long-wavelength instabilities in the system, allowing to understand a part of the observed dynamics. In the future, a more systematic study of the influence of all terms in the Cahn-Hilliard type nonlinear phase equation will be carried out, and a direct comparison of numerical simulations of the CSHE with simulations of the phase equation will provide more insight into the dynamical behavior in the complex Swift-Hohenberg equation.

Finally, in **Chapter 13**, we have demonstrated that a nonlocal spatial coupling strongly influences the dynamics of fronts connecting two equivalent states. The most striking result is the possibility of obtaining a novel class of self-organized

stable DSs in systems exhibiting fronts with no tails, like the real Ginzburg-Landau equation. This is achieved through a nonlocal repulsive interaction that modifies the profile of the fronts introducing or damping out oscillations. In addition, we have observed an order of magnitude increase of the front velocity due to an enhancement of the interaction between two fronts. Finally we have shown that nonlocal interactions can also smooth out the front oscillations in systems which already have oscillatory tails in their local form. This greatly increases their wavelength such that the DSs become much wider and eventually disappear. A confrontation between our theoretical predictions and experimental data would allow us to identify different sources of nonlocality. We refer e.g. to domain walls in photorefractive media, which have been shown to have a large nonlocal response, but its effects on the front dynamics remain to be characterized.

Appendices

APPENDIX A

Nonlinear dynamics and bifurcation theory: a Toolbox

As throughout the whole thesis, we use concepts from the field of nonlinear dynamics and bifurcation theory, we provide the reader here with a brief overview of some standard concepts in the field.

A.1 Dynamics and bifurcations

In the field of dynamics, the aim is to study the qualitative (not the quantitative) behavior of a system described by several first order differential equations. The general description of such a system is

$$\begin{aligned} \dot{x}_1 &= f_1(x_1, x_2, \ldots, x_n; \vec{p}) \\ \dot{x}_2 &= f_2(x_1, x_2, \ldots, x_n; \vec{p}) \\ &\vdots \\ \dot{x}_n &= f_n(x_1, x_2, \ldots, x_n; \vec{p}) \end{aligned} \tag{A.1}$$

or in shorthand notation

$$\dot{\vec{x}} = \vec{f}(\vec{x}; \vec{p}) \tag{A.2}$$

where the dot denotes a time derivative and $\vec{p}$ is a vector containing all the parameters influencing the system's behavior. The space made up of the dynamical variables $x_1, x_2, \ldots, x_n$ is called the *phase-space*. In this phase-space, equation (A.2)

can be visualized as a vector field indicating the direction in which the system will evolve in time, just as if it were a velocity vector of a moving particle in a mechanical system. But the particle must then be imagined as moving in an extremely viscous fluid. If we let the system evolve in time, it will cover a trajectory in the phase-space which is tangent to this vector field $\dot{\vec{x}}$.[1] A point $\vec{x^*}$ where the vector field has zero amplitude ($\vec{f}(\vec{x^*}) = \vec{0}$) is called a *fixed point*, because if the system is prepared in $\vec{x^*}$, it would reside there forever.[2]

A fixed point is (asymptotically) *stable* when it is both *attracting* and *Lyapunov stable*. These stability types are defined a follows [1]:

Attracting A point $\vec{x^*}$ is attracting if there is a $\delta > 0$ such that

$$\lim_{t\to\infty} \vec{x}(t) = \vec{x^*}$$

whenever $\left\|\vec{x}(0) - \vec{x^*}\right\| < \delta$. In other words, any trajectory that starts within a distance δ of $\vec{x^*}$ is guaranteed to converge to $\vec{x^*}$ eventually.

Lyapunov stable A point $\vec{x^*}$ is Lyapunov stable if for each $\varepsilon > 0$, there is a $\delta > 0$ such that $\left\|\vec{x}(t) - \vec{x^*}\right\| < \varepsilon$ whenever $t \geq 0$ and $\left\|\vec{x}(0) - \vec{x^*}\right\| < \delta$. Thus, trajectories that start within δ of $\vec{x^*}$ remain within ε of $\vec{x^*}$ for all positive time.

On the other hand, a fixed point $\vec{x^*}$ is *unstable* when it is neither attracting nor Lyapunov stable. Besides stable and unstable fixed points there is one more important type of fixed points: a *saddle*. If $\vec{x^*}$ is a saddle, some initial conditions in the neighborhood of $\vec{x^*}$ will actually converge to $\vec{x^*}$ while slightly different initial conditions will veer away from it. The set of initial conditions such that $\vec{x}(t) \to \vec{x^*}$ as $t \to \infty$, is called the *stable manifold* of $\vec{x^*}$. Likewise, the set of initial conditions such that $\vec{x}(t) \to \vec{x^*}$ as $t \to -\infty$, is called the *unstable manifold* of $\vec{x^*}$. Note that a typical trajectory asymptotically approaches the unstable manifold as $t \to \infty$, and approaches the stable manifold as $t \to -\infty$ [1]. The three different types of fixed points discussed here are summarized in Fig. A.1.

Fixed points, either attracting or repelling trajectories for $t \to \infty$, are not the only possible structures governing the dynamics in the phase-space. Another possibility is a trajectory following a fixed path throughout the phase-space, and returning to its starting point after a fixed amount of time. In other words, a

[1] A trajectory which is not tangent to $\dot{\vec{x}} = \vec{f}$ is not a solution of equation (A.2).
[2] In the absence of possible perturbations such as noise.

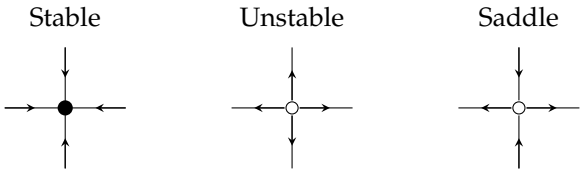

Figure A.1: Illustration of a stable, an unstable and a saddle fixed point (illustrated with straight line trajectories, for the sake of simplicity)

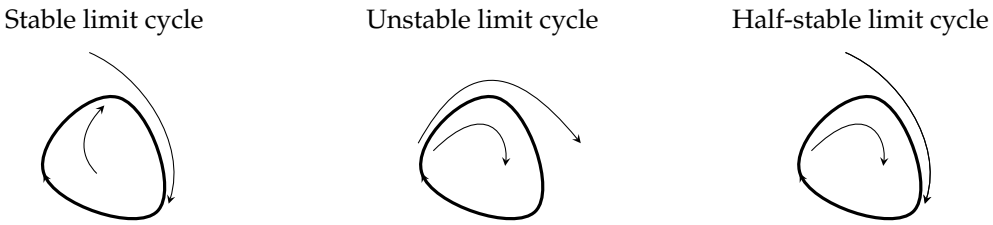

Figure A.2: Illustration of a stable, an unstable and a half-stable limit cycle

closed trajectory or periodic solution. A *limit cycle* is the most common closed trajectory. It is an isolated closed trajectory in phase-space, where isolated means that neighboring trajectories are not closed [1]. They spiral either toward or away from the limit cycle (see Fig. A.2). Scientifically, stable limit cycles are very important since they model systems that exhibit self-sustained oscillations, e.g. the beating of a heart, dangerous self-excited vibrations in bridges and airplane wings, etc. [1].

For different values of $\vec{p}$, we obtain different vector fields in phase-space. In most cases, this will only locally change the direction and magnitude, without qualitatively changing the vector field. But for some special cases, we obtain radical changes in the topology of the vector field. These qualitative changes in the dynamics are called *bifurcations*, and the parameter values at which they occur are called *bifurcation points* [1]. An illuminating example is provided by the buckling of a beam. If the weight placed on top of the beam is small enough, it is able to remain vertical. Even slight perturbations will not buckle the beam, since the vertical position is stable. But once the load becomes too heavy, the vertical position gets unstable and the beam may buckle (see Fig. A.3).

The knowledge of the type and the location of these bifurcations yields a profound understanding of the system's dynamical behavior and enables us to manipulate it as we wish. Below, we will describe the most important types of

Figure A.3: Beam buckling. At a certain mass M, the vertical position becomes unstable and the beam may buckle (figure based on [1])

bifurcations. For the sake of clarity, most of them will be described as bifurcations in a one-dimensional phase-space.[3] But first, we need to address the notion of linear stability.

A.2 Linear stability

The most important property of a fixed point is its stability, because this dictates how the system will behave whenever it comes close to it. A straightforward stability analysis is possible if we first linearize the system at hand. Assuming that $\vec{x^*}$ is a fixed point ($\vec{f}(\vec{x^*}) = \vec{0}$), we can write $\vec{u} = \vec{x} - \vec{x^*}$ for the deviation from the fixed point. The linearized time evolution of $\vec{u}$ then yields

$$\dot{\vec{u}} = J\vec{u} \tag{A.3}$$

where J is the Jacobian matrix of $\vec{f}$ in equation (A.2), evaluated at the fixed point $\vec{x^*}$. The general solution of equation (A.3) is[4]

$$\vec{u}(t) = \sum_{i=1}^{n} c_i e^{\lambda_i t}\vec{v}_i \tag{A.4}$$

where $\vec{v}_i$ are the eigenvectors of the Jacobian matrix J, and λ_i the corresponding eigenvalues. The (complex) constants c_i are uniquely determined by the initial conditions. Since the characteristic equation only has real coefficients (J is assumed to be real), the eigenvalues can only be real or complex conjugates. When they are complex, $\vec{u}(t)$ involves linear combinations of $e^{(\alpha \pm i\omega)t}$ (write $\lambda_{1,2} = \alpha \pm i\omega$). Such terms represent exponentially decaying oscillations if $\alpha = \Re(\lambda) < 0$ and

[3] This is no restriction, as will be explained in section A.2.

[4] This can easily be seen by substituting the solution $\vec{u}(t) = e^{\lambda t}\vec{v}$ in equation (A.3), which then reduces to an eigenvector-eigenvalue problem.

Type	Eigenvalues
Stable node	$\Re(\lambda_i) < 0, \forall\, i = 1, \ldots, n$
Unstable node	$\Re(\lambda_i) > 0, \forall\, i = 1, \ldots, n$
Saddle point	$\exists\, i, j : \Re(\lambda_i)\Re(\lambda_j) < 0$

Table A.1: Classification of a fixed point with eigenvalues $\lambda_1, \ldots, \lambda_n$ (i.e. different stability types), where $\Re(\lambda)$ denotes the real part of the complex number λ

growing oscillations if $\alpha > 0$. Hence the corresponding fixed points are stable and unstable spirals (in a two-dimensional subspace), respectively [1].

So the nature of the eigenvalues (negative or positive real part, zero or nonzero imaginary part etc.) fully determines the type of fixed point we are faced with (see Table A.1). Fortunately, we can go a long way with this linearized theory. The Hartman-Grobman theorem tells us that the stability type of the fixed point is faithfully captured by the linearization, as long as $\Re(\lambda_i) \neq 0$ for $i = 1, \ldots, n$ [1].

Note that equation (A.4) implies that a fixed point can only be stable when the eigenvalues of the Jacobian all lie in the left half-plane $\Re(\lambda) < 0$. If this were not the case, the slightest perturbation along the corresponding eigenvector for which $\Re(\lambda) < 0$ is not satisfied will make the system flow away from the fixed point. In that case the fixed point is unstable.[5]

As mentioned before, bifurcations yield a qualitative or topological change of the phase-space. When a fixed point changes stability, trajectories near the fixed point will reverse direction. The fixed point has then bifurcated. During this bifurcation, some eigenvalue(s) cross(es) the imaginary axis so that their real part becomes positive. When one single eigenvalue goes through zero at this bifurcation (*zero-eigenvalue bifurcations* [1]), the center manifold theorem tells us that all action takes place in a one-dimensional subspace. This center manifold theorem allows us to reduce the dimension of a given system to n_0 near a local bifurcation, where n_0 is the number of eigenvalues with zero real part at the bifurcation point [2, 3].[6]

We will now explain zero-eigenvalue bifurcations (s.a. saddle-node, transcritical, pitchfork) using a one-dimensional system, without any loss of generality.

[5] If $\Re(\lambda) = 0$, the fixed point is *marginally stable*. Perturbations will neither grow nor decay, they will remain invariant.

[6] All the other eigendirections quickly relax to the bifurcating eigenvector(s) because of their negative real parts, and are hence irrelevant for the local bifurcation dynamics.

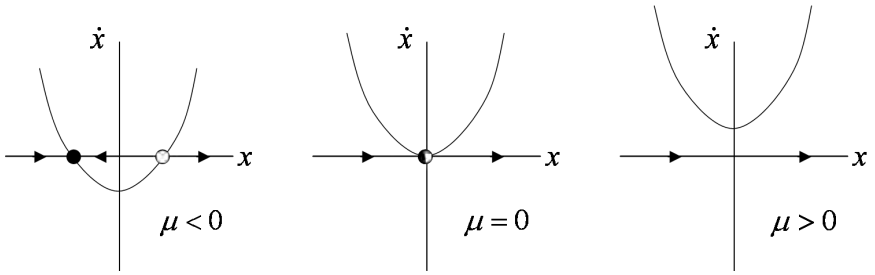

Figure A.4: Normal form of the saddle node bifurcation $\dot{x} = \mu + x^2$. The direction of the vector field is drawn on the horizontal axis (figure based on [1])

A.3 Saddle-Node bifurcation

The first example of a bifurcation type is the saddle-node bifurcation, which is the basic mechanism by which fixed points are created and destroyed. Consider the normal (one-dimensional) form for the saddle node bifurcation

$$\dot{x} = \mu + x^2 \tag{A.5}$$

For $\mu < 0$ we have two fixed points ($\dot{x} = 0 \Leftrightarrow x_1^* = \sqrt{-\mu}$ and $x_2^* = -\sqrt{-\mu}$, x_1^* is unstable and x_2^* is stable, see Fig. A.4). As r increases, the fixed points move towards each other. At $\mu = 0$ (the bifurcation point) both points coincide and we end up with a half-stable fixed point. If we further increase μ, the fixed points disappear into thin air.

So in a saddle-node bifurcation two fixed points (one stable and one unstable fixed point) move towards each other, collide and mutually annihilate when a parameter is varied in a certain direction. In the other direction, two fixed points suddenly appear [1].

When a system is close to a saddle-node bifurcation — just before the fixed points appear or just after they have collided — a saddle-node remnant or *ghost* leads to slow passage through a bottleneck [1]. This can be understood from Fig. A.4, since $\dot{x}$ is very small near the origin when we are close to the bifurcation. Hence, it will take quite some time for the system to get past the origin, which in this case takes on the role of the saddle-node ghost.

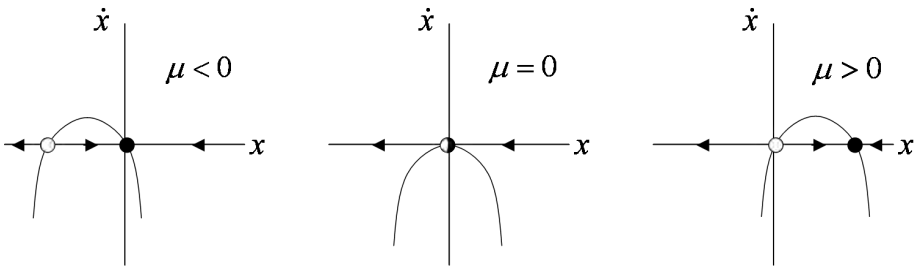

Figure A.5: Normal form of the transcritical bifurcation $\dot{x} = \mu x - x^2$. The direction of the vector field is drawn on the horizontal axis (figure based on [1])

A.4 Transcritical bifurcation

The transcritical bifurcation is the standard mechanism for changes in stability of fixed points. It does not involve any creation or destruction of fixed points. The normal form for the transcritical bifurcation is

$$\dot{x} = \mu x - x^2 \tag{A.6}$$

For $\mu < 0$ we have an unstable fixed point at $x_1^* = \mu$ and a stable fixed point at $x_2^* = 0$ (see Fig. A.5). As we increase μ, the unstable fixed point approaches the origin. At $\mu = 0$ (bifurcation point) both fixed points coincide. When $\mu > 0$ the origin has become unstable, while $x_1^* = \mu$ is now stable. You can say that the two fixed points "exchanged" their stability. The threshold pump value in Fig. **??** is an example of a transcritical bifurcation [1].

A.5 Pitchfork bifurcation

The pitchfork bifurcation is — just as the saddle-node bifurcation — a mechanism to create or destroy fixed points. It is a characteristic bifurcation for systems with inversion symmetry. Hence it often occurs in physical problems that have an intrinsic symmetry. Fixed points then tend to appear and disappear in symmetrical pairs. The buckling beam in Fig. A.3 is an excellent example of a pitchfork bifurcation. Once the load is large enough, the vertical position gets unstable and the beam might buckle to the left or to the right. These are two new symmetrical fixed points.

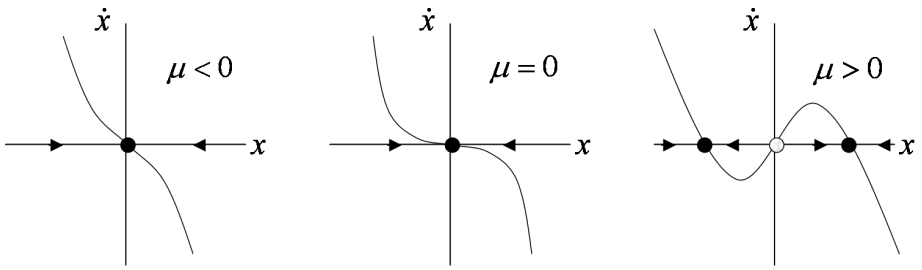

Figure A.6: Normal form of the pitchfork bifurcation $\dot{x} = \mu x - x^3$. The direction of the vector field is drawn on the horizontal axis (figure based on [1])

There are two different types of pitchfork bifurcations, the supercritical and the subcritical pitchfork bifurcation.

The normal form for the supercritical pitchfork bifurcation is

$$\dot{x} = \mu x - x^3 \tag{A.7}$$

Note that this equation is invariant under the transformation $x \to -x$. When $\mu < 0$, the origin is the only fixed point, and it is stable (see Fig. A.6). When $\mu = 0$, the origin is still stable but not as stable as when $\mu < 0$. When $\mu > 0$, the origin has become unstable and two new stable fixed points appear symmetrically around the origin at $x^* = \pm\sqrt{\mu}$.

The normal form for the subcritical pitchfork bifurcation is

$$\dot{x} = \mu x + x^3 \tag{A.8}$$

so that the cubic term is no longer stabilizing (pulling $x(t)$ back toward $x = 0$), but destabilizing. By changing $\mu \to -\mu$, $\dot{x}$ in equation (A.8) becomes exactly $-\dot{x}$ from equation (A.7). So by inverting the μ-axis and inverting the stability of every fixed point of the supercritical case, we obtain the subcritical case.

A.6 Hopf bifurcation

As mentioned in section A.2, a fixed point loses stability when one or more eigenvalues cross the imaginary axis into the right half-plane $\Re(\lambda) > 0$. In all the previous bifurcations real eigenvalues passed through $\lambda = 0$, thus they were all zero-eigenvalue bifurcations. But the Hopf bifurcation is quite different. At a

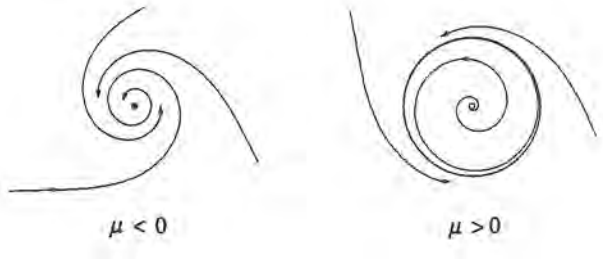

Figure A.7: Phase portrait of the normal form of the supercritical Hopf bifurcation, above and below the bifurcation point $\mu = 0$. When $\mu > 0$, the origin has become unstable and the trajectories flow outward to the new stable limit cycle with amplitude $\sqrt{\mu}$ (figure from [1])

Hopf bifurcation two complex conjugate eigenvalues cross the imaginary axis at the same time. So at the bifurcation the eigenvalues are purely imaginary. This means that at a Hopf bifurcation, a time-periodic solution appears or disappears near a steady state [4].

The Hopf bifurcation is only possible in two or more dimensional systems. It has no one-dimensional counterpart, as opposed to the previous bifurcations which can all occur in a one-dimensional system.

There are two different types: supercritical and subcritical Hopf bifurcations.

A.6.1 Supercritical Hopf bifurcation

At a supercritical Hopf bifurcation, the fixed point becomes unstable and gets surrounded by a stable limit cycle. The normal form (in polar coordinates) is

$$\dot{r} = \mu r - r^3 \tag{A.9}$$
$$\dot{\theta} = \omega \tag{A.10}$$

where the radial equation is identical to the supercritical pitchfork equation (A.7). The resulting phase portrait is shown in Fig. A.7.

A.6.2 Subcritical Hopf bifurcation

At a subcritical Hopf bifurcation, a fixed point gets unstable after colliding with an unstable limit cycle. The trajectories close to the fixed point simply flow to a

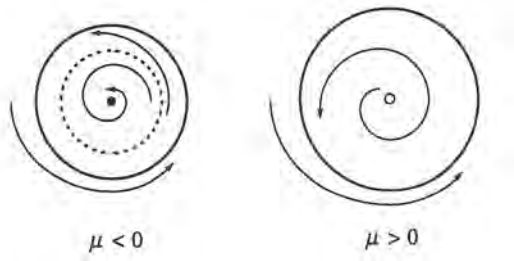

Figure A.8: Phase portrait of the normal form of the subcritical Hopf bifurcation, above and below the bifurcation point $\mu = 0$. The unstable limit cycle surrounding the origin for $\mu < 0$, shrinks continuously with increasing μ until it collides with the origin ($\mu = 0$), after which the origin becomes unstable and the trajectories flow to some distant attractor ($\mu > 0$). In this case the distant attractor is the large stable limit cycle on the outside, generated by the extra $-r^5$ term in equation (A.11) (figure from [1])

distant attractor[7] after the bifurcation has occurred. The normal form is

$$\dot{r} = \mu r + r^3 - r^5 \tag{A.11}$$
$$\dot{\theta} = \omega \tag{A.12}$$

where the radial equation is almost identical to the subcritical putchfork equation (A.8). The term $-r^5$ (stabilizing term) is added to play the role of distant attractor to which the trajectories can evolve after the origin becomes unstable. The typical phase portrait of a two-dimensional subcritical Hopf bifurcation is shown in Fig. A.8.

References

[1] S. Strogatz, *Nonlinear Dynamics And Chaos: With Applications To Physics, Biology, Chemistry, And Engineering*, Westview Press, 1st edition, 2001.

[2] Y. Kuznetsov, *Elements of Applied Bifurcation Theory*, Springer, 3rd edition, New York, 2004.

[3] J. Guckenheimer and P. Holmes, *Nonlinear Oscillations, Dynamical Systems, and Bifurcations of Vector Fields*, Springer-Verlag, New York, 2002.

[7] An attractor is a set to which all neighboring trajectories converge, e.g. a stable fixed point or a stable limit cycle [1].

[4] T. Erneux and P. Glorieux, *Laser Dynamics*, Cambridge University Press, 1st edition, 2010.

APPENDIX B

Numerical integration schemes

We provide the reader with a brief overview of the numerical techniques that have been used in this PhD thesis. In the first Section, we introduce the integration scheme that is used in the first part of the thesis to integrate stochastic ordinary differential equations. Secondly, we explain a numerical method to integrate partial differential equations, which are studied throughout the second part of this thesis.

B.1 Numerical integration of stochastic ordinary differential equations

Throughout the first part of this thesis we have backed up our theoretical and topological predictions with numerical simulations of a general rate-equation model for semiconductor ring lasers (1.1)-(1.3). This set of ordinary differential equations models the time evolution of the slowly varying amplitudes of the counter-propagating waves and the carrier number in a semiconductor ring laser. In order to study stochastic mode-hopping between different attractors and excitability in the ring laser (see Chapters 4 and 6), we have included spontaneous emission noise. This motivates the need to numerically integrate stochastic ordinary differential equations (ODEs) [1].
Consider several fields $A_i(t)$ with $i = 1, 2, \ldots$, which are a function of time, that

satisfy coupled stochastic ODEs of the form:

$$\frac{\partial A_i}{\partial t} = G([A]; \xi_i(t)), \tag{B.1}$$

where G is a given function of the set of fields $[A] = (A_1, A_2, \ldots, A_N)$. For the stochastic field $\xi_i(t)$ usually a white noise approximation is used, i.e. a Gaussian process of zero mean and delta-correlated in time:

$$\langle \xi_i(t)\xi_j(t')\rangle = \delta_{ij}\delta(t-t'). \tag{B.2}$$

In most occasions, Eq. (B.1) takes the form of a generalized Langevin equation:

$$\frac{\partial A_i}{\partial t} = K_i([A]) + \sum_j \sigma_{ij}([A])\xi_j(t), \tag{B.3}$$

with $K_i([A])$, $\sigma_{ij}([A])$ given functions, possibly depending explicitly on time and $[A]$. The numerical integration of Eq. (B.3) proceeds by developing integral algorithms [2]. In the most general case, however, it is very difficult to accurately generate the necessary stochastic variables appearing in the algorithms. This is the reason why we do not go beyond Euler's modification of Milshtein's method:

$$\begin{aligned} A_i(t+h) &= A_i(t) + h^{1/2}\sum_j \sigma_{ij}([A(t)])u_j(t) \\ &\quad + h[K_i([A(t)]) + \frac{1}{2}\sum_{j,k}\sigma_{jk}([A(t)])\frac{\partial \sigma_{ik}([A(t)])}{\partial A_j(t)}u_k(t)u_j(t)], \end{aligned} \tag{B.4}$$

where $u_i(t)$ are a set of independent random variables defined for the time $0, h, 2h, \ldots$ of the recurrence relation, with zero mean and variance one:

$$\langle u_i(t)\rangle = 0, \tag{B.5}$$

$$\langle u_i(t)u_j(t)\rangle = \delta_{ij}, \tag{B.6}$$

$$\langle u_i(t)u_j(t')\rangle = 0, \tag{B.7}$$

with $t \neq t'$. An important case in which one can use straightforward generalizations of the Milshtein and Heun methods is that of diagonal noise, i.e. one in which the noise term does not couple different field variables:

$$A_i(t+h) = A_i(t) + h^{1/2}\sigma_i(A_i(t))u_i(t) + h[K_i(A_i(t)) + \frac{1}{2}\sigma_i(A_i(t))\sigma_i'(A_i(t))u_i(t)^2]. \tag{B.8}$$

In the first part of this thesis, we assume such diagonal noise, which also allows an easy implementation of the Heun method, which is the one we use throughout

this work [1]:

$$k_i = hK_i([A(t)]) \tag{B.9}$$

$$l_i = h^{1/2}u_i(t)\sigma_i([A(t)]) \tag{B.10}$$

$$A_i(t+h) = A_i(t) + \frac{h}{2}[K_i([A(t)]) + K_i([A(t)+l+k])] + \tag{B.11}$$

$$\frac{h^{1/2}u_i(t)}{2}[\sigma_i(A_i(t)) + \sigma_i(A_i(t)+k_i+l_i)] \tag{B.12}$$

B.2 Numerical integration of partial differential equations

In this Section, we describe the numerical method used to integrate partial differential equations (PDEs), studied in the second part of this thesis. The PDEs that have been considered in this work can be written in the following form:

$$\partial_t A(\vec{x},t) = aA(\vec{x},t) + b\nabla^2 A(\vec{x},t) + F(A(\vec{x},t)), \tag{B.13}$$

where $\vec{x} = (x, y)$ and $F(A(\vec{x},t))$ is a nonlinear function of the field $A(\vec{x},t)$.
The time evolution of A subjected to periodic boundary conditions is obtained by numerically solving Eq. (B.13) in Fourier space. This method is pseudospectral and accurate up to second order in time. We start by computing the Fourier transform of Eq. (B.13), giving the evolution in time of each Fourier mode $\tilde{A}(\vec{q},t)$:

$$\partial_t \tilde{A}(\vec{q},t) = -\alpha_{\vec{q}}\tilde{A}(\vec{q},t) + \tilde{F}(\tilde{A}(\vec{q},t)), \tag{B.14}$$

where $\alpha_{\vec{q}} = -(a + b\vec{q}^2)$. At any time, the amplitude $\tilde{F}(\tilde{A}(\vec{q},t))$ is calculated by taking the inverse Fourier transform of $\tilde{A}(\vec{q},t)$, computing the nonlinear term in real space and then calculating the Fourier transform of this term (using e.g. a standard FFT subroutine). Eq. (B.14) is integrated numerically in time with a two-step method. For reasons of convenience, we define the time step to increase by $2\delta t$ at each iteration.
In order to solve the system numerically, the field A needs to be discretized in space with a sufficiently large spatial resolution. Due to the corresponding small spatial step size, the range of values $|\vec{q}|$ is large such that the linear time scales $\alpha_{\vec{q}}$ can take a wide range of values. This stiffness problem is circumvented by treating the linear terms exactly by using the formal solution:

$$\partial_t \tilde{A}(t) = e^{-\alpha_{\vec{q}}t}\left(\tilde{A}(t_0)e^{\alpha_{\vec{q}}t_0} + \int_{t_0}^{t}\tilde{F}(\tilde{A}(s))e^{\alpha_{\vec{q}}s}ds\right), \tag{B.15}$$

where for simplicity the dependence of $\vec{q}$ on the field A has been omitted in the notation. From Eq. B.15, the following relation is found:

$$\frac{\tilde{A}(t+\delta t)}{e^{-\alpha_{\vec{q}}\delta t}} - \frac{\tilde{A}(t-\delta t)}{e^{\alpha_{\vec{q}}\delta t}} = e^{-\alpha_{\vec{q}}t}\int_{t-\delta t}^{t+\delta t}\tilde{F}(\tilde{A}(s))e^{\alpha_{\vec{q}}s}ds. \tag{B.16}$$

The term on the right-hand side is then simplified using a Taylor expansion around $s = t$ assuming small values of δt:

$$\tilde{F}(\tilde{A}(t))\frac{e^{\alpha_{\vec{q}}\delta t} - e^{-\alpha_{\vec{q}}\delta t}}{\alpha_{\vec{q}}} + O(\delta t^3). \tag{B.17}$$

Substituting this result into the evolution equation (B.16) leads to

$$\tilde{A}(n+1) = e^{-2\alpha_{\vec{q}}\delta t}\tilde{A}(n-1) + \frac{1-e^{-2\alpha_{\vec{q}}\delta t}}{\alpha_{\vec{q}}}\tilde{F}(\tilde{A}(n)) + O(\delta t^3), \tag{B.18}$$

where n is used for $n\delta t$. This expression is called the *slaved leap frog* scheme [3]. In order for this scheme to be stable, a corrective algorithm is needed. Following steps similar to the ones before, the following auxiliary expression can be found:

$$\tilde{A}(n) = e^{-\alpha_{\vec{q}}\delta t}\tilde{A}(n-1) + \frac{1-e^{-\alpha_{\vec{q}}\delta t}}{\alpha_{\vec{q}}}\tilde{F}(\tilde{A}(n-1)) + O(\delta t^2). \tag{B.19}$$

Using Eqs. (B.18)-(B.19), we use the numerical method below, also referred to as the two-step method [4, 5]:

1. Compute $\tilde{F}(\tilde{A}(n-1))$ from $\tilde{A}(n-1)$ by going to real space.
2. Eq. (B.19) is used to obtain an approximation for $\tilde{A}(n)$.
3. Using this approximated $\tilde{A}(n)$, the nonlinear term $\tilde{F}(\tilde{A}(n))$ is calculated.
4. $\tilde{A}(n+1)$ is obtained using Eq. (B.18).

At each iteration $\tilde{A}(n+1)$ is thus obtained from $\tilde{A}(n-1)$ as time advances by $2\delta t$. The total error is of order $O(\delta t^3)$ despite the fact that the intermediate step is accurate to $O(\delta t^2)$.

References

[1] M. San Miguel and R. Toral, *Stochastic effects in physical systems*, Instabilities and Nonequilibrium Structures VI, Kluwer Academic Publishers, Dordrecht, 2000.

[2] P. Kloeden and E. Platen, *Numerical solution of stochastic differential equations*, Springer-Verlag, 1992.

[3] U. Frisch, Z. S. She, , and O. Thual, "Viscoelastic behavior of cellular solutions to the Kuramoto-Sivashinsky model," *J. Fluid. Mech.* **168**, 221, 1986.

[4] R. Montagne, E. Hernández-García, A. Amengual, and M. San Miguel, "Wound-up phase turbulence in the complex ginzburg-landau equation," *Phys. Rev. E* **56**, 151–167, 1997.

[5] A. Jacobo, *Spatial structures and information processing in nonlinear optical cavities*, PhD thesis, Universitat de les Illes Balears, 2009.

List of Abbreviations

1D	one-dimensional
2D	two-dimensional
AO	alternate oscillations
Ba	Bautin
BF	Benjamin-Feir
BI	bidirectional
BS	bound state
C	coarsening
CW	clockwise
CCW	counterclockwise
CGLE	complex Ginzburg-Landau equation
CSHE	complex Swift-Hohenberg equation
CH	Cahn-Hilliard
DS	dissipative soliton
E	Eckhaus
EC	Eckhaus - coarsening
EF	Eckhaus - faceting
EEL	edge-emitting laser
FC	fold of cycles
FPE	Fokker-Planck equation
GLE	Ginzburg-Landau equation
H	Hopf
HSS	homogeneous steady state

List of Abbreviations

IPAS	in-phase asymmetric solution
IPSS	in-phase symmetric solution
ISI	inter-spike-interval
KS	Kuramoto-Sivashinsky
LLE	Lugatio-Lefever equation
LS	localized structure
MI	modulational instability
MPEP	most probable escape path
MW	modulated wave
NLSE	nonlinear Schrödinger equation
OPAS	out-of-phase asymmetric solution
OPO	optical parametric oscillator
OPSS	out-of-phase symmetric solution
PCGLE	parametrically forced complex Ginzburg-Landau equation
PCF	photonic crystel fiber
PDE	partial differential equation
PIC	photonic integrated circuit
LHM	left-handed material
RGLE	real Ginzburg-Landau equation
RHM	right-handed material
RO	relaxation oscillation
RSHE	real Swift-Hohenberg equation
RTD	residence time distribution
RW	rotating wave
SHE	Swift-Hohenberg equation
SN	saddle-node
SL	saddle-loop
SRL	semiconductor ring laser
SW	standing wave
TB	Takens-Bogdanov
TW	traveling wave
QW	quantum well
U	unidirectional
VCSEL	vertical-cavity surface-emitting laser
WKB	Wentzel-Kramers-Brillouin

List of Publications

Published in international peer-reviewed journals

- L. Gelens and E. Knobloch,
"Coarsening and frozen faceted structures in the supercritical complex Swift-Hohenberg equation",
Eur. Phys. J. D (in press).

- L. Gelens, S. Beri, G. Van der Sande, G. Verschaffelt and J. Danckaert,
"Multistable and excitable behavior in semiconductor ring lasers with broken Z_2-symmetry",
Eur. Phys. J. D, doi: 10.1140/epjd/e2010-00042-7 (in press).

- L. Gelens, D. Gomila, G. Van der Sande, M. A. Matías and P. Colet,
"Nonlocality induced front interaction enhancement",
Phys. Rev. Lett. **104**, 154101 (2010).

- W. Coomans, S. Beri, G. Van der Sande, L. Gelens and J. Danckaert,
"Optical injection in semiconductor ring lasers",
Phys. Rev. A **81**, 033802 (2010).

- S. Beri, L. Mashall, L. Gelens, G. Van der Sande, G. Mezosi, M. Sorel, J. Danckaert and G. Verschaffelt,
"Excitability in optical systems close to Z_2-symmetry",
Phys. Lett. A **374**, 739-743 (2010).

List of Publications

- M. Tlidi and L. Gelens,
"High-order dispersion stabilizes dark dissipative solitons in all-fiber cavities",
Opt. Lett. **35**, 306–308 (2010).

- L. Gelens and E. Knobloch,
"Faceting and coarsening dynamics in the complex Swift-Hohenberg equation ",
Phys. Rev. E **80**, 046221 (2009).

- S. Beri, L. Gelens, G. Van der Sande and J. Danckaert,
"An asymptotic approach to the analysis of mode-hopping in semiconductor ring lasers ",
Phys. Rev. A **80**, 013823 (2009).

- L. Gelens, S. Beri, G. Van der Sande, G. Mezosi, M. Sorel, J. Danckaert and G. Verschaffelt,
"Exploring multistability in semiconductor ring lasers: Theory and experiment",
Phys. Rev. Lett. **102**, 193904 (2009).

- L. Gelens, G. Van der Sande, S. Beri, and J. Danckaert,
"Phase-space approach to directional switching in semiconductor ring lasers",
Phys. Rev. E **79**, 016213 (2009).

- S. Beri,L. Gelens, M. Mestre, G. Van der Sande, G. Verschaffelt, A. Sciré, G. Mezosi, M. Sorel and J. Danckaert,
"Topological insight into the non-Arrhenius mode hopping of semiconductor ring lasers",
Phys. Rev. Lett. **101**, 093903 (2008).

- L. Gelens, S. Beri, G. Van der Sande, J. Danckaert, N. Calabretta, H. J. .S. Dorren, R. Nötzel, E. A. .J. M. Bente and M. K. Smit,
"Optical injection in semiconductor ring lasers: backfire dynamics",
Opt. Express **16**, 16968-16974 (2008).

- G. Van der Sande, L. Gelens, P. Tassin, A. Sciré and J. Danckaert,
"Two-dimensional phase-space analysis and bifurcation study of the dynamical behavior of a semiconductor ring laser",
J. Phys. B: At. Mol. Opt. Phys. **41**, 095402 (2008).

- L. Gelens, D. Gomila, G. Van der Sande, J. Danckaert, P. Colet and M. A. Matías,
"Dynamical instabilities of dissipative solitons in nonlinear optical cavities

with nonlocal materials",
Phys. Rev. A 77, 033841 (2008).

- P. Tassin, L. Gelens, J. Danckaert, I. Veretennicoff, G. Van der Sande, P. Kockaert, and M. Tlidi,
"Dissipative structures in left-handed material cavity optics",
Chaos **17**, 037116 (2007).

- L. Gelens, G. Van der Sande, P. Tassin, M. Tlidi, P. Kockaert, D. Gomila, I. Veretennicoff and J. Danckaert,
"Impact of nonlocal interactions in dissipative systems: Towards minimal-sized localized structures",
Phys. Rev. A **75**, 32767 (2007).

Piled Higher and Deeper ***by Jorge Cham*** **www.phdcomics.com**

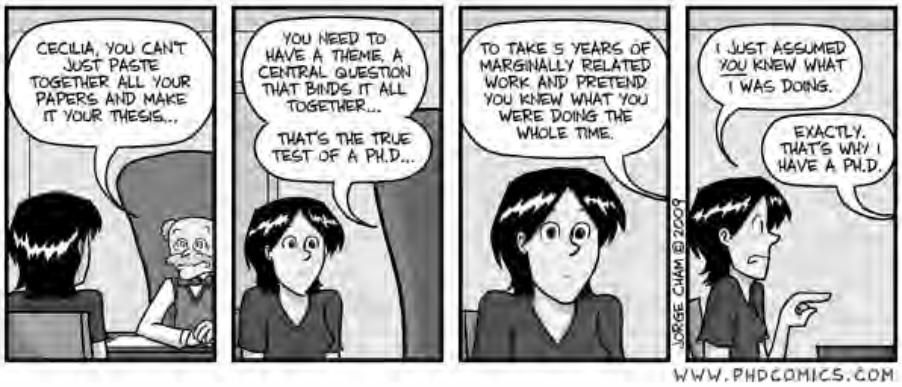

title: "Paste together" - originally published 4/24/2009

Contributions to international conferences

- L. Gelens, S. Beri, G. Van der Sande, G. Mezosi, M. Sorel, J. Danckaert and G. Verschaffelt,
"Analysis of multistability in semiconductor ring lasers",
Photonics Europe (SPIE Brussels) (2010).

- L. Mashal, S.Beri, L. Gelens, G. Van der Sande, G. Mezosi, M. Sorel, G. Verschaffelt and J. Danckaert,
"Study of excitability in semiconductor ring lasers: theory and experiment",
Photonics Europe (SPIE Brussels) (2010).

- W. Coomans, S. Beri, G. Van der Sande, L. Gelens and J. Danckaert,
"Dynamical regimes in an optically injected semiconductor ring laser",
Photonics Europe (SPIE Brussels) (2010).

- S. Beri, L. Gelens, M. Mestre, G. Van der Sande, G. Mezosi, M. Sorel, G. Verschaffelt and J. Danckaert,
"Theoretical and experimental investigation of mode-hopping in semiconductor ring lasers",
Photonics Europe (SPIE Brussels) (2010).

- S. Beri, L. Gelens, L. Mashal, M. Mestre, G. Van der Sande, G. Mezosi, M. Sorel, J. Danckaert, G. Verschaffelt,
"Stochastic and Nonlinear Dynamics in Semiconductor Ring Lasers",
Rio De La Plata Workshop on Laser Dynamics, Piriapolis, Uruguay (2009).

- S. Beri, L. Gelens, L. Mashal, G. Van der Sande, J. Danckaert, G. Verschaffelt, G. Mezosi and M. Sorel,
"Excitability in Semiconductor Ring Lasers",
European Semiconductor Laser Workshop (ESLW), Vienna, Austria (2009).

- W. Coomans, S. Beri, L. Gelens, G. Van der Sande and J. Danckaert,
"Optical Injection in Semiconductor Ring Lasers",
European Semiconductor Laser Workshop (ESLW), Vienna, Austria (2009).

- L. Gelens and E. Knobloch,
"Localized states in the complex Swift-Hohenberg equation",
Localized Excitations in Nonlinear Complex Systems (LENCOS), Sevilla, Spain (2009).

- G. Van der Sande, S. Beri, L. Gelens, G. Mezosi, M. Sorel, G. Verschaffelt, and J. Danckaert,

"Dynamics of semiconductor ring lasers: theory and experiment",
LPHYS'09, 18th International Laser Physics Workshop, Barcelona (2009).

- S. Beri, L. Gelens, G. Van der Sande, G. Verschaffelt, G. Mezosi, M. Sorel and J. Danckaert,
"Directional Mode Hopping in Semiconductor Ring Lasers",
European Conference on Lasers and Electro-Optics and the XIth European Quantum Electronics Conference (CLEO/Europe-EQEC), Munich, Germany (2009).

- G. Van der Sande, L. Gelens, S. Beri, G. Verschaffelt and J. Danckaert,
"Topology of the Asymptotic Two-dimensional Phase Space of a Semiconductor Ring Laser",
SIAM Conference on Applications of Dynamical Systems, Snowbird, Utah, USA (2009).

- L. Gelens, G. Van der Sande, S. Beri and J. Danckaert,
"Directional Mode Switching in Semiconductor Ring Lasers: Deterministic and Stochastic Effects",
XVI Conference on Non-equilibrium Statistical Mechanics & Nonlinear Physics (MEDYFINOL), Punta del Este, Uruguay (2008).

- S. Beri, L. Gelens, M. Mestre, G. Van der Sande, G. Verschaffelt, J. Danckaert, A. Sciré, G. Mezosi and M. Sorel,
"Topological features of the directional mode-hopping in semiconductor ring lasers: Arrhenius and non-Arrhenius events",
European Semiconductor Laser Workshop (ESLW), Eindhoven, Nederland (2008).

- L. Gelens, G. Van der Sande, S. Beri and J. Danckaert,
"Directional switching in semiconductor ring lasers: phase space design",
European Semiconductor Laser Workshop (ESLW), Eindhoven, Nederland (2008).

- S. Beri, L. Gelens, M. Mestre, G. Van der Sande, G. Verschaffelt, G. Mezosi, M. Sorel and J. Danckaert,
"Directional mode hopping in a semiconductor ring laser: non-Arrhenius features",
Dynamics Days, Delft, Nederland (2008).

- N. Calabretta, S. Beri, L. Gelens, R. Nötzel, E. Bente, J. Danckaert, M. Smit, and H. Dorren,
"Experimental investigation of bistable operation of semiconductor ring lasers under optical injection",
CLEO/QELS, San Jose, USA (2008).

- G. Van der Sande, L. Gelens, P. Tassin, A. Sciré and J. Danckaert,
"The dynamical behaviour of a semiconductor ring laser",
Photonics Europe (SPIE Strasbourg) (2008).

- L. Gelens, G. Van der Sande, P. Tassin, D. Gomila, P. Colet, M.A. Matías, M. Tlidi, P. Kockaert, I. Veretennicoff and J. Danckaert,
"Sub-Diffraction-Limited Localized Structures: Influence of linear nonlocal interactions",
Photonics Europe (SPIE Strasbourg) (2008).

- L. Gelens, G. Van der Sande, S. Beri, P. Tassin, A. Sciré and J. Danckaert,
"A reduced phase space description for deterministic and stochastic features in the dynamical behaviour of a semiconductor ring laser",
Workshop on Nonlinear dynamics in semiconductor lasers (WIAS), Berlin, Germany (2007).

- L. Gelens, G. Van der Sande, P. Tassin, A. Sciré and J. Danckaert,
"Bifurcation analysis of the dynamical behavior of a semiconductor ring laser",
European Semiconductor Laser Workshop Berlin (ESLW), Berlin, Germany (2007).

- L. Gelens, P. Tassin, G. Van der Sande, I. Veretennicoff, P. Kockaert, M. Tlidi, D. Gomila and J. Danckaert,
"Influence of nonlocal interactions on the formation and stability of cavity solitons",
International Workshop on Instabilities, Patterns and Optical Solitons (IPSSO), Metz, France, pp. 37-37 (2007).

- L. Gelens, G. Van der Sande, P. Tassin, P. Kockaert, M. Tlidi, D. Gomila, I. Veretennicoff and J. Danckaert,
"Sub-Diffraction-Limited Cavity Solitons",
EOS topical meeting on nonlinear optics: from sources to guided waves, Paris, France (2006).

Contributions to Benelux conferences

- L. Gelens, S. Beri, L. Mashal, G. Van der Sande, M. Sorel, G. Mezosi, J. Danckaert and G. Verschaffelt,
"Theoretical and experimental investigation of excitability in semiconductor ring lasers",
Annual Symposium IEEE Photonics Benelux Chapter, pp. 181-185 (2009).

- W. Coomans, S. Beri, G. Van der Sande, L. Gelens and J. Danckaert, "Optical injection in semiconductor ring lasers", *Annual Symposium IEEE Photonics Benelux Chapter*, pp. 145-149 (2009).
- I.V. Ermakov, G. Van der Sande, L. Gelens, A. Sciré, P. Colet, C.R. Mirasso and J. Danckaert, "Numerical investigation of semiconductor ring lasers with two external cavities", *Thirteenth Annual Symposium of the IEEE/LEOS Benelux Chapter* (2008).
- L. Gelens, G. Van der Sande, P. Tassin, S. Beri, A. Sciré and J. Danckaert, "Bifurcation Analysis of the Dynamical Behaviour of Semiconductor Ring Lasers", *IEEE/LEOS Benelux Workshop* (2008).
- L. Gelens, G. Van der Sande, P. Tassin, A. Sciré and J. Danckaert, "Bifurcation Analysis of the Dynamical Behaviour of Semiconductor Ring Lasers", *IEEE/LEOS Benelux Annual Workshop, Brussels, Belgium*, pp. 207-210 (2007).
- P. Tassin, L. Gelens, G. Van der Sande, M. Tlidi, P. Kockaert, J. Danckaert and I. Veretennicoff, "Cavity Solitons in Diffraction-Managed Optical Resonators", *IEEE/LEOS Benelux Annual Workshop, Brussels, Belgium*, pp. 21-22 (2007).
- L. Gelens, G. Van der Sande, P. Tassin, P. Kockaert, M. Tlidi, D. Gomila, I. Veretennicoff and J. Danckaert, "Beyond the Size Limit on Cavity Solitons with Left-Handed Materials", *IEEE/LEOS Benelux Annual Workshop, Eindhoven, Netherlands* (2006).